Macroscopic Description of Rarefied Gas Flows in the Transition Regime

by

Peyman Taheri Bonab

B.Sc., Azad University, 1999

M.Sc., Tarbiat Modares University, 2002

A Dissertation Submitted in Partial Fulfillment of the
Requirements for the Degree of

DOCTOR OF PHILOSOPHY

in the Department of Mechanical Engineering

University of Victoria

Macroscopic Description of Rarefied Gas Flows in the Transition Regime

by

Peyman Taheri Bonab
B.Sc., Azad University, 1999
M.Sc., Tarbiat Modares University, 2002

Supervisory Committee

Dr. H. Struchtrup, Supervisor
(Department of Mechanical Engineering)

Dr. S. Dost, Departmental Member
(Department of Mechanical Engineering)

Dr. P. Oshkai, Departmental Member
(Department of Mechanical Engineering)

Dr. B. Khouider, Outside Member
(Department of Mathematics and Statistics, University of Victoria)

Supervisory Committee

Dr. H. Struchtrup, Supervisor
(Department of Mechanical Engineering)

Dr. S. Dost, Departmental Member
(Department of Mechanical Engineering)

Dr. P. Oshkai, Departmental Member
(Department of Mechanical Engineering)

Dr. B. Khouider, Outside Member
(Department of Mathematics and Statistics, University of Victoria)

ABSTRACT

The fast–paced growth in microelectromechanical systems (MEMS), microfluidic fabrication, porous media applications, biomedical assemblies, space propulsion, and vacuum technology demands accurate and practical transport equations for rarefied gas flows. It is well–known that in rarefied situations, due to strong deviations from the continuum regime, traditional fluid models such as Navier–Stokes–Fourier (NSF) fail. The shortcoming of continuum models is rooted in nonequilibrium behavior of gas particles in miniaturized and/or low–pressure devices, where the Knudsen number (Kn) is sufficiently large.

Since kinetic solutions are computationally very expensive, there has been a great desire to develop macroscopic transport equations for dilute gas flows, and as a result, several sets of extended equations are proposed for gas flow in nonequilibrium states. However, applications of many of these extended equations are limited due to their instabilities and/or the absence of suitable boundary conditions.

In this work, we concentrate on regularized 13–moment (R13) equations, which are a set of macroscopic transport equations for flows in the transition regime, i.e., $\mathrm{Kn} \lesssim 1$. The R13 system provides a stable set of equations in Super–Burnett order, with a great potential to be a powerful CFD tool for rarefied flow simulations at moderate Knudsen numbers.

The goal of this research is to implement the R13 equations for problems of practical interest in arbitrary geometries. This is done by transformation of the R13 equations and boundary conditions into general curvilinear coordinate systems. Next steps include adaptation of the transformed equations in order to solve some of the popular test cases, i.e., shear–driven, force–driven, and temperature–driven flows in both planar and curved flow passages. It is shown that inexpensive analytical solutions of the R13 equations for the considered problems are comparable to expensive numerical solutions of the Boltzmann equation. The new results present a wide range of linear and nonlinear rarefaction effects which alter the classical flow patterns both in the bulk and near boundary regions. Among these, multiple Knudsen boundary layers (mechanocaloric heat flows) and their influence on mass and energy transfer must be highlighted. Furthermore, the phenomenon of temperature dip and Knudsen paradox in Poiseuille flow; Onsager's reciprocity relation, two–way flow pattern, and thermomolecular pressure difference in simultaneous Poiseuille and transpiration flows are described theoretically. Through comparisons it is shown that for Knudsen numbers up to 0.5 the compact R13 solutions exhibit a good agreement with expensive solutions of the Boltzmann equation.

Contents

List of Tables

List of Figures

ACKNOWLEDGEMENTS

I would like to express my most sincere gratitude to my teacher and my Ph.D. advisor, Dr. Henning Struchtrup, whose encouragement, guidance, and support during my study and research at University of Victoria, from the initial to the final step, enabled me to develop an understanding of the subject. I would have been lost without him. In addition, he kindly included me in teaching activities with his students, that made the research life more rewarding for me.

I was delighted to interact with Dr. Manuel Torrilhon (Seminar for Applied Mathematics, ETH Zürich), whose passion and insights to the subject enlightened new ideas for this research.

I am indebted to many student colleagues at University of Victoria, especially at the Department of Mechanical Engineering, for making it a convivial place to work and live. In particular, I would like to thank my colleagues Yingsong Zheng, Gwynn Elfring, Adel Younis, and Anirudh Rana for providing a stimulating and fun environment in which I learned and grew. Thank you for your friendship and help in the past four years.

I offer my regards and blessings to all of those who supported me in any respect during the completion of the course, including the secretaries and staff in the department for assisting me in many different ways. Dorothy Burrows, Erin Robinson, Arthur Makosinski, and Barry Kent deserve special mention.

Lastly, I owe my loving thanks to my parents and my brother Ali. Without their encouragement, understanding, and loving support it would have been impossible for me to finish this work.

The financial support of Natural Sciences and Engineering Research Council of Canada (NSERC) is gratefully acknowledged.

Peyman Taheri Bonab

Victoria, BC

August 2010

For Atousa

Chapter 1

Introduction

1.1 Overview

From the historical point of view, fluid mechanics is one of the oldest subjects in the realm of physical sciences. The Euler equations for inviscid flows were obtained by Euler in 1757, and it has been over a century that Navier–Stokes equations for viscous flows have been studied. Fluid dynamics is a sub–discipline of fluid mechanics that deals with liquids and gases in motion. It has several sub–disciplines itself, one of them is *hydrodynamics*. Although, the terminology of hydrodynamics usually corresponds to the study of liquids in motion, it can also be used for gas dynamics, when sufficiently dense gases are considered [21, 25, 53, 98, 106].

Classical hydrodynamics is governed by the set of basic conservation laws; conservation of mass (continuity equation), balance of momentum for dissipative flows, and conservation of energy (the first law of thermodynamics). The traditional closure for these equations correspond to *constitutive laws*—Newton's law for shear stress and Fourier's law for heat conduction. In addition, in order to relate temperature to the conserved quantities (mass, momentum, and energy) an appropriate equation of state is required, and sometimes, depending on the flow regime, other complimentary models need to be incorporated, e.g. turbulence models.

Although the basic equations of the classical hydrodynamics, which in this thesis are referred to as "Navier–Stokes–Fourier (NSF)" equations, suffices to successfully describe transport fields in liquids and sufficiently dense gases, experimental observations show that NSF fails to properly describe gas flows in rarefied conditions. This short–coming is addressed to the inability of the NSF system to capture *nonequilibrium effects* in rarefied gases.

Nonequilibrium effects, also called *rarefaction effects*, occur in microscale and/or low density flows, which are common scenarios in miniaturized and low pressure devices, e.g. microelectromechanical systems (MEMS), microscale thermofluidic devices, porous media, biomedical assemblies, high–altitude aerodynamics, and vacuum instruments. In rarefied situations, due to the lack of sufficient collisions between the gas molecules, the continuum assumption collapses and the medium (gas) needs to be treated as a collection of individual particles.

Kinetic theory has a special rule in the subject of nonequilibrium gas dynamics. It is a branch of statistical physics dealing with the dynamics of nonequilibrium processes and their relaxation to thermodynamic equilibrium. The *Boltzmann equation* is the cornerstone in all kinetic based approaches. A rarefied gas is well described by the Boltzmann kinetic equation, which describes the gas on the microscopic level by accounting for the translation and collisions of the gas molecules. The primary goal in kinetic theory of gases is to find solutions for the Boltzmann equation. However, it is important to emphasize that despite the maturity of kinetic theory, rigorous numerical solutions for the Boltzmann equation are unavailable, and approximate solutions are accessible only for simple flows, which of course are computationally very expensive.

While NSF equations determine the macroscopic quantities of mass density $\rho\left(x_i,t\right)$, velocity $v_k\left(x_i,t\right)$ and energy $e\left(x_i,t\right)$, at all locations x_i and all times t, the Boltzmann equation governs the evolution of the particle velocity distribution function $f\left(x_i,t,c_i\right)$, where c_i denotes the microscopic velocity of the particles. The macroscopic quantities of interest, i.e., ρ, v_k, and e, follow from suitable averaging over the distribution function f. Obviously, the NSF equations pose a mathematically less challenging problem than the Boltzmann equation. Indeed, even for simple flow problems, for which NSF can be solved analytically, the Boltzmann equation must be solved numerically.

Kinetic theory bridges microscopic and macroscopic flow behavior. Over the years, this feature has been used to derive macroscopic transport equations for nonequilibrium flows from the Boltzmann kinetic equation. The macroscopic transport equations present a collective behavior of particles and are usually referred to as *extended hydrodynamics* or *extended macroscopic transport equations*, since they govern the behavior of macroscopic quantities, i.e., density, velocity, energy, temperature, pressure etc.

At the limit of sufficiently small Knudsen numbers, the derivation of the well–known Navier–Stokes–Fourier equations from the Boltzmann equation is well documented—in literature usually referred as *asymptotic theory of the Boltzmann equation* [22, 25, 53, 98, 106]. While the NSF equations are capable of describing only low–order rarefaction effects, namely, Navier–Stokes shear stress and Fourier heat flow, there are many other sets of (extended) macroscopic transport equations which are proposed to explain higher–order rarefaction effects outside the standard hydrodynamics (NSF) limit.

In this thesis we concentrate on the regularized 13–moment equations (R13 equations) that are recognized as the regularized version of the original Grad's 13–moment system. Through analytical and numerical solutions for fundamental gas dynamics problems, it is shown that R13 equations in some extent avoid the short–comings of the traditional NSF equations. The solution of fundamental gas dynamics problem with the R13 equations shows that they are promising equations for moderately rarefied gas flows, where traditional gas dynamics equations are inaccurate.

1.2 Outline

This thesis is divided into two parts with twelve chapters. Part I covers the required background theory and presents an introduction to the moment method and moment equations. Part II includes the author's contribution to the subject, and containes the simulation results from the regularized 5–moment equations (Navier–Stokes–Fourier equations) and the regularized 13–moment equations for the boundary value problems of interest. Moreover, the NSF and R13 results are compared to available kinetic solutions in the literature.

Macroscopic and microscopic derivations of basic conservation laws are briefly discussed in Chap. 2. Also, the basic concepts of the kinetic theory of gases are presented where the Boltzmann equation, velocity distribution function and its moments—the macroscopic quantities—are introduced.

Chapter 3 briefly introduces the derivation of the general moment equation from the Boltzmann equation. This is followed by introducing a well–established approach for providing closure for the moment equations, known as classical Grad's method for 13–moment and 26–moment systems. Moreover, the derivation of the Euler equations for inviscid and adiabatic flows is discussed with respect to a low–order moment system, i.e., Grad's 5–moment equations.

Chapter 4 presents the regularization of the moment equations. Regularized 5–moment equations, that are equivalent to Navier–Stokes–Fourier equations, and regularized 13–moment equations that are particularly used in our simulations are discussed in detail. Furthermore, transformed equations in cylindrical coordinates are introduced, and non–dimensionalization and linearization of the equations are explained.

A recently developed strategy to obtain wall boundary conditions for the moments is rigorously discussed in Chap. 5. The obtained boundary conditions are required to solve the boundary value problems discussed in the following chapters. Additionally, the boundary conditions for high–order moments are used to derive second–order velocity slip and temperature conditions for classical hydrodynamics. The scaling approach to obtain velocity and temperature discontinuities over flat and curved boundaries is also included in the chapter. It will be shown that the second–order slip and jump conditions can improve the Navier–Stokes–Fourier solutions effectively.

Through Chap. 6 to Chap. 11, a collection of standard boundary value problems for different geometries and processes are solved both analytically and numerically. Solutions for the selected problems are obtained by solving the NSF and R13 systems, and are compared to available kinetic solutions of the Boltzmann equation. Through these comparisons, advantages of higher–order moment equations (particularly, regularized 13–moment equations) over Navier–Stokes–Fourier equations to describe rarefied gas flow is proved.

Finally, concluding comments and recommendations are listed in Chap. 12.

Part I

THEORY

Chapter 2

Background Theory

2.1 Macroscopic and Microscopic Gas Dynamics

There are two distinct approaches to derive gas dynamics equations; *macroscopic* and *microscopic*.

In the macroscopic approach conservation principles are understood and their application to an infinitely small (control) volume of gas yields a system of partial differential equations, which, with the help of constitutive laws, can describe the macroscopic flow behavior, i.e., the temporal and spatial evolution of density, velocity, temperature, etc. For instance, the Euler and Navier–Stokes–Fourier equations, which are the well–known equations for ideal and dissipative flows, respectively, can be derived through the macroscopic approach. Details of the classical macroscopic approach are discussed in Sec. 2.2.

Alternatively, in microscopic approaches, referred to as *kinetic approaches*, the gas is treated as a domain consisting of molecules (particles) whose motion obey Newtonian mechanics. Accordingly, a kinetic equation is required to describe the evolution of particles distribution due to their advection (free flight) and interaction (collision). In the context of microscopic fluid dynamics, the Boltzmann equation is the governing kinetic equation that combines the laws of mechanics with probability theory to describe a gas at the microscopic level. More discussion on the Boltzmann equation is provided in Sec. 2.3.

The Knudsen number, Kn, is the key parameter in gas dynamics. It is defined as the ratio of the molecular mean free path λ, the average distance that a gas molecule travels between successive collisions, to a relevant characteristic length scale of the flow $\mathcal{L}$,

$$\mathrm{Kn} = \frac{\lambda}{\mathcal{L}}. \tag{2.1}$$

The Knudsen number is recognized as the dimensionless measure of the gas rarefaction. Nonequilibrium (rarefaction) effects dominate the gas flows when the Knudsen number is sufficiently large. This can happen either when the mean free path becomes large, for low density gas flows, or when the length scale $\mathcal{L}$ becomes small, e.g., for micro–scale flows.

For very small Knudsen numbers, where the gas is sufficiently dense, due to the many collisions between molecules any disturbance is rapidly distributed between the molecules. Hence, molecules behave as a continuum and not as individuals, and the gas is treated as a continuum, described by some variables which depend on spatial position x_i and time t. In contrast, in dilute gases where the Knudsen number is large, due to lack of sufficient collisions, the gas cannot be considered in equilibrium and requires to be treated particlewise. Rarefied condition is the case where kinetic approaches are on demand.

Figure 2.1 shows the classification of gas flow regimes based on the Knudsen number[1]. As depicted, the Boltzmann equation embraces the entire range of Knudsen numbers from continuum (hydrodynamic) flow regime up to the collisionless free molecular flow. In certain ranges of the Knudsen number, macroscopic transport equations such as Euler and Navier–Stokes–Fourier equations, can be used. Albeit, compared to the Boltzmann equation, these equations provide less details of the gas behavior.

The Euler equations are applicable for flows with $\mathrm{Kn} \lesssim 0.001$ in which heat conduction and stress are ignored. Navier–Stokes–Fourier equations that include heat conduction and the viscous effect, are generally valid for weak nonequilibrium flows, $\mathrm{Kn} \lesssim 0.1$. For $\mathrm{Kn} \gtrsim 0.01$ higher–order boundary conditions are necessary for the NSF equations to account for nonequilibrium effects at the boundary owing to gas–surface interaction.

In the transition regime where $0.1 \lesssim \mathrm{Kn} \lesssim 10$ the NSF equations fail, since a more detailed description of flow is required. Flows at these moderate Knudsen numbers require either kinetic approaches or extended macroscopic transport equations (extended hydrodynamics).

---

[1] We emphasize that liquids are excluded from our discussion, since mean free path cannot be defined for liquids.

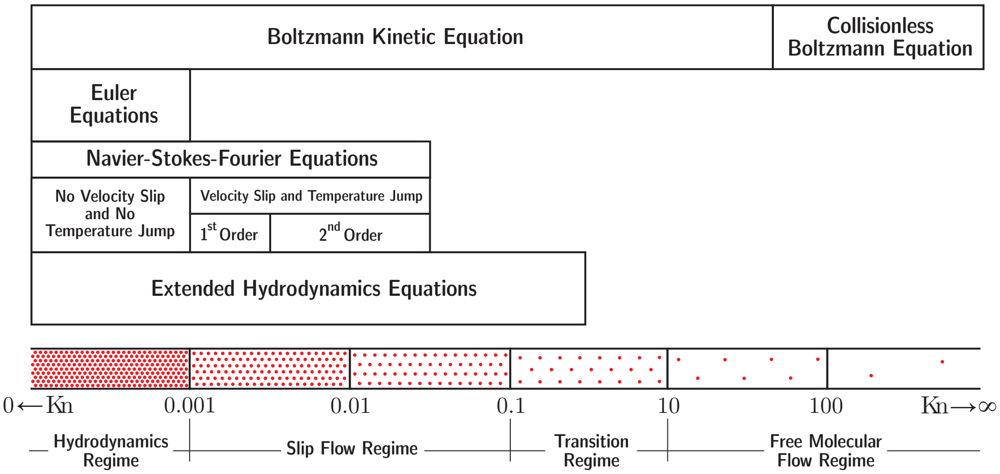

Figure 2.1: Classification of gas flow regimes based on the Knudsen number, Kn. The lower and upper limits of Knudsen number correspond to hydrodynamics regime and free molecular flow regime, respectively. While the Boltzmann equation embraces all flow regimes, classical fluid dynamics equations are applicable only at small Knudsen numbers. For moderate Knudsen numbers the Boltzmann equation can be replaced with simpler set of extended hydrodynamic equations.

2.2 Continuum Description of Gas Dynamics

In this section, we introduce classical hydrodynamics equations in a continuum. Macroscopic approaches use the concept of (small material) control volume to derive fundamental transport equations of gas dynamics. As shown in Fig. 2.2, we consider a thermodynamic system consisting of some matter (gas here) in a stationary[2] volume V. The surface of the fixed volume is S. The components of the gas velocity vector in Cartesian coordinates are $v_i(x_k, t)$, with x_k and t as Cartesian space coordinates and time.

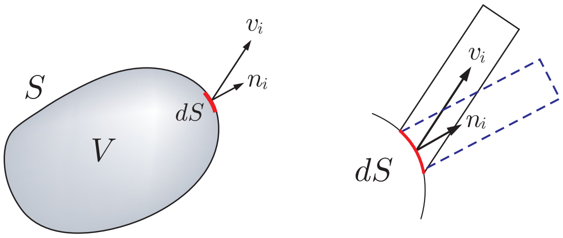

Figure 2.2: Schematic presentation of a stationary control volume in a flow. The volume and its penetratable surface are denoted by V and S. On a small surface element dS, velocity of the flow is v_i. The dashed line represents the normal component of swept volume (solid line), where n_i is the normal vector of the surface element.

---

[2] Instead of a stationary control volume, a moving control volume can be considered too. The assumption of a moving control volume leads to transport equations in Lagrangian frame work.

In the control volume, quantities of mass M , momentum J_i , and total energy E are

$$M = \int_V \rho\, dV, \qquad J_i = \int_V \rho\, v_i\, dV, \qquad E = \int_V \rho\, e\, dV. \tag{2.2}$$

Here ρ, v_i, and e are mass density, components of the velocity vector, and density of total energy, respectively. Densities of total energy e, and internal energy u, are related via

$$e = u + \frac{1}{2} v^2. \tag{2.3}$$

Internal energy is associated with the motion of particles (translational, rotational, vibrational), and is a function of temperature. The integrals in (2.2) can be presented in general notation as

$$X = \int_V \rho\, \varPhi\, dV, \tag{2.4}$$

where $\varPhi = \left\{1, v_i, u + v^2/2\right\}$ and $X = \{M, J_i, E\}$.

The general balance law implies that the change of any quantity inside the system, during time dt, is equal to the net flux of that quantity crossing the boundaries, and also the production inside the system during the considered time step.

The amount of a quantity X transported through dS during dt is $\rho \varPhi v_i\, n_i\, dS\, dt$, where $v_i\, dS\, dt$ is the volume pass through dS during time dt. The outward normal vector of the surface element dS is n_i and $v_i\, n_i\, dS\ dt$ is the normal component of the volume $v_i\, dS\, dt$. Accordingly, the mathematical expression of balance law in general form reads

$$\frac{d}{dt}\left[\int_V \rho \varPhi\, dV\right] = -\oint_S \rho \varPhi v_i\, n_i\, dS - \oint_S \varUpsilon_i n_i\, dS + \int_V \rho \mathscr{P}\, dV + \int_V \rho \mathscr{S}\, dV, \tag{2.5}$$

where the first and second terms on the right–hand side describe convective and non–convective fluxes ($\varUpsilon_i$ is non–convective flux parameter). The third term is responsible for production of $\varPhi$ in V, e.g. absorption, emission or radiation. The last term is the supply of $\varPhi$ in V. Minus signs are applied for convective and non–convective terms, as conventionally we take positive direction for the surface normal vector n_i to be outward.

Gauss' theorem can be applied to convert the integrals over surface to volume integrals,

$$\int_V \left[\frac{\partial\left(\rho \varPhi\right)}{\partial t} + \frac{\partial\left(\rho \varPhi v_i + \varUpsilon_i\right)}{\partial x_i} - \rho\left(\mathscr{P} + \mathscr{S}\right)\right] dV = 0. \tag{2.6}$$

Since this equation must hold for any arbitrary volume (localization assumption), the integral must vanish,

$$\frac{\partial\left(\rho \mathit{\Phi}\right)}{\partial t}+\frac{\partial\left(\rho \mathit{\Phi} v_i+\mathit{\Upsilon}_i\right)}{\partial x_i}-\rho\left(\mathscr{P}+\mathscr{S}\right)=0. \tag{2.7}$$

The principal equations in hydrodynamical systems are the conservation laws for mass, momentum, and energy. The parameters of balance law for these quantities are presented in Table 2.1.

Table 2.1: Parameters for principal conservation laws.

$\int_V \rho \mathit{\Phi}\, dV$	Convective Flux ($\mathit{\Phi}$)	Non–convective Flux ($\mathit{\Upsilon}_i$)	Production ($\mathscr{P}$)	Supply ($\mathscr{S}$)
M	1	0	0	0
J_i	v_i	p_{ij}	0	G_i
E	$u+v^2/2$	$p_{ij}v_j+q_i$	0	$G_j v_j+\dot{e}_{\mathrm{Rad}}$

We assume conservation laws, thus all production terms are zero, $\mathscr{P}=0$. The quantities p_{ij}, G_i, and q_i are Cartesian components of pressure tensor, external body–force vector, and heat–flux vector, respectively. The radiative energy supply is denoted by $\dot{e}_{\mathrm{Rad}}$. The pressure tensor for Newtonian fluids reads

$$p_{ij}=p\delta_{ij}+\sigma_{ij}, \tag{2.8}$$

where σ_{ij} denotes the dissipative viscous part (nonequilibrium part) of the pressure tensor, δ_{ij} is the Kronecker delta, and $p=\frac{1}{3}p_{kk}$ is the pressure. As shown in Table 2.1, the external body force corresponds to supply terms for momentum, ρG_i, and power term for energy $\rho G_j v_j$.

According to Table 2.1 and Eq. (2.8), the conservation laws for mass, momentum, and energy densities are

$$\frac{\partial\rho}{\partial t}+\frac{\partial(\rho v_i)}{\partial x_i}=0, \tag{2.9a}$$

$$\frac{\partial(\rho v_j)}{\partial t}+\frac{\partial(\rho v_i v_j+p\delta_{ij}+\sigma_{ij})}{\partial x_i}=\rho G_j, \tag{2.9b}$$

$$\frac{\partial(\rho e)}{\partial t}+\frac{\partial(\rho e v_i+p_{ij}v_j+q_i)}{\partial x_i}=\rho(v_j G_j+\dot{e}_{\mathrm{Rad}}). \tag{2.9c}$$

In the momentum equation (2.9b) the total momentum flux is

$$\Pi_{ij}=\rho v_i v_j+p\delta_{ij}+\sigma_{ij}, \tag{2.10}$$

where $\rho v_i v_j$ is the convective part. In a dissipative flow, viscosity effects which appears in the viscous stress tensor σ_{ij}, cause irreversible momentum transfer. Similarly, in the energy balance the energy flux is

$$\Theta_i = \rho e v_i + p_{ij} v_j + q_i, \tag{2.11}$$

where the heat–flux vector q_i represents the irreversibility in energy transfer.

Furthermore, in order to find temperature with respect to other quantities, an equation of state is required. In this thesis we only consider monatomic ideal gases where $p = \rho\theta$ and $u = \frac{3}{2}\theta$ hold as "thermal" and "caloric" equations of state, respectively. The quantity θ is the temperature in energy units $\theta = \mathcal{R}T$, where T is the thermodynamic temperature, and $\mathcal{R}$ is the gas constant $\mathcal{R} = k_\mathrm{B}/m$, with k_B and m as the Boltzmann constant[3] and mass of the gas molecules, respectively.

For inviscid and adiabatic flows $\sigma_{ij} = q_i = 0$, then Eqs. (2.9a)–(2.9c) describe ideal flows, also known as equilibrium flows. In this case we call the set of balance equations as *Euler* equations.

To introduce the effects of viscosity and heat transfer, additional equations are required, which are referred as *constitutive relations.* In classical hydrodynamics stress and heat conduction are given by Navier–Stokes and Fourier's (NSF) laws,

$$\sigma_{ij}^{\mathrm{NSF}} = \mu \left(\frac{\partial v_i}{\partial x_j} + \frac{\partial v_j}{\partial x_i} \right) - \frac{2}{3}\,\mu\,\frac{\partial v_k}{\partial x_k}\,\delta_{ij}, \tag{2.12}$$

$$q_i^{\mathrm{NSF}} = -\kappa\,\frac{\partial \theta}{\partial x_i}, \tag{2.13}$$

where μ is the shear viscosity and κ is the thermal conductivity coefficients. These transport coefficients for stress and heat conduction depend on the internal structure of the fluid itself and not the flow. Since macroscopic analysis provides no detail about the internal structure of the fluid, then experimental methods and/or kinetic theory must be applied to determine these transport coefficients.

The stress tensor [cf. Eq. (2.12)] can be written in a compact notation as

$$\sigma_{ij}^{\mathrm{NSF}} = -2\mu \frac{\partial v_{\langle i}}{\partial x_{j\rangle}}, \tag{2.14}$$

where $\partial v_{\langle i}/\partial x_{j\rangle}$ is the trace–free part of the symmetric velocity gradient tensor,

$$\frac{\partial v_{\langle i}}{\partial x_{j\rangle}} = \frac{1}{2} \left(\frac{\partial v_i}{\partial x_j} + \frac{\partial v_j}{\partial x_i} \right) - \frac{1}{3}\frac{\partial v_k}{\partial x_k}\,\delta_{ij}. \tag{2.15}$$

---

[3] The value for Boltzmann's constant is $k_\mathrm{B} = 1.38066 \times 10^{-23}$ J/K.

In our notation we consider σ_{ij} as a symmetric trace–free tensor, and drop the angular brackets for better appearance.

The conservation laws in Eqs. (2.9a)–(2.9c) with the use of Navier–Stokes and Fourier equations [Eqs. (2.12) and (2.13)] provides the transport equations for dissipative flows. They introduce the effects of viscosity and heat transfer in the momentum and energy content of the system, which makes them suitable transport equations for near–equilibrium flows. In this thesis we refer to this set of equations as *Navier–Stokes–Fourier* (NSF) equations.

Indeed, Navier–Stokes–Fourier is a nonequilibrium theory, since it describes heat flux, shear stress, and has entropy generation. The difference between Navier–Stokes–Fourier and rarefied gas theories is non–locality. In NSF what happens in point x_i depends only on the close vicinity of the point (gradients of v and θ in the constitutive laws). However, in rarefied gases, large distance effects play a role, i.e., when the mean free path is large, particles bring energy and momentum from far away. Accordingly, the models which go beyond NSF has higher–order derivatives or extra equations. Also, linear irreversible thermodynamics [34] indicates that a NSF gas is in local equilibrium, but that does not mean it is an equilibrium theory; neighboring points are in different local equilibria, hence we have nonequilibrium processes.

2.3 Boltzmann Equation

In the kinetic theory a gas is defined as a collection of many interacting particles. In such a microscopic scale, where the collective dynamics of particles describes the macroscopic state of the gas, an appropriate kinetic equation is required to precisely describe the underlying microdynamics.

Theoretically, the state of a gas can be specified if both spatial position x_k and velocity c_k of each individual particle are known at time t. In the three–dimensional Cartesian coordinates where position and velocity are defined through their three orthogonal components, they form a six–dimensional space spanned by $\{x_k, c_k\}$ which is called *phase space.*

The key variable in kinetic equations is the velocity distribution function, $f(x_k, t, c_k)$, that is a continuous function in the gas and is defined by

$$N_V = \int_{\text{all } c_k \text{ and all } x_k} f(x_k, t, c_k)\, d\mathbf{c}\, d\mathbf{x}, \tag{2.16}$$

where N_V is the number of particles that occupy a fixed volume $\varOmega = \int d\mathbf{c}\, d\mathbf{x}$ of the phase space at time t.

The main task of a kinetic equation is to predict the evolution of the velocity distribution function due to collision and free flight of particles. The Boltzmann equation is the relevant kinetic equation for gases that reads

$$\frac{\partial f}{\partial t} + c_k \frac{\partial f}{\partial x_k} + G_k \frac{\partial f}{\partial c_k} = \mathcal{Q}\left(f, f\right). \tag{2.17}$$

The only variable in the Boltzmann equation is the velocity distribution function $f\left(x_k, t, c_k\right)$. The left–hand side of the Boltzmann equation describes the effects of particles' free flight. It describes the variation of f with respect to independent variables $\{x_k, t, c_k\}$, where G_k is the external–force vector [the same body–force which appears in Eq. (2.9)]. On the right–hand side of Eq. (2.17), $\mathcal{Q}\left(f, f\right)$ is collision term that describes the variation of f due to interaction (collision) of particles.

For gases consisting of a single type of molecules which undergo *binary collisions*, the collision term in general form reads [98]

$$\mathcal{Q}\left(f, f\right) = \int_{\text{all } \phi_k \text{ and all } c_{k*}} \left(f^{'} f^{'}_{*} - f f_{*}\right) \mathscr{B}\left(\xi_k, \phi_k\right)\, d\Lambda\left(\boldsymbol{\phi}\right)\, d\mathbf{c}_{*}, \tag{2.18}$$

where $\{f, f_*\}$ and $\{f^{'}, f^{'}_{*}\}$ are pre–collision and post–collision velocity distributions of two colliding particles, respectively. The velocity difference between particles before the collision is $\xi_k = c_k - c_{k*}$. The vector ϕ_k is the unit vector that describes the variation of the direction of the molecular velocity owing to a collision; $d\Lambda$ is the solid–angle element in the direction of ϕ_k; $\mathscr{B}\left(\xi_k, \phi_k\right)$ is a non–negative function describing binary collisions. This nonlinear integral form of the collision term makes the solution of the Boltzmann equation very difficult to achieve.

The collision function $\mathscr{B}$, strongly depends on particles' interaction potential. In Fig. 2.3 four different models for molecular interaction are presented, where r and d represent the distance between the center of two colliding particles, and their diameter, respectively. The actual molecular interaction is schematically depicted in plot (a). At large distances, the force between the molecules tends to zero, $F \rightarrow 0$. However, at shorter distances there is a weak attraction force, which changes to a strong repulsive force as a results of molecular intermingling. Due to complexity of analysis with the actual molecular interaction, simplified models are introduced. In the Sutherland model, plot (b), variations of attraction and repulsion forces with respect to the distance between the particles are simplified. In the Maxwell model the attraction force is ignored, see plot (c). The simplest model considers molecules as rigid elastic spheres with no attractive force, when apart, and infinite repulsive force at the instance of contact, see plot (d). It is important to emphasize that despite the simplicity of hard–sphere model it yields fairly accurate results [126].

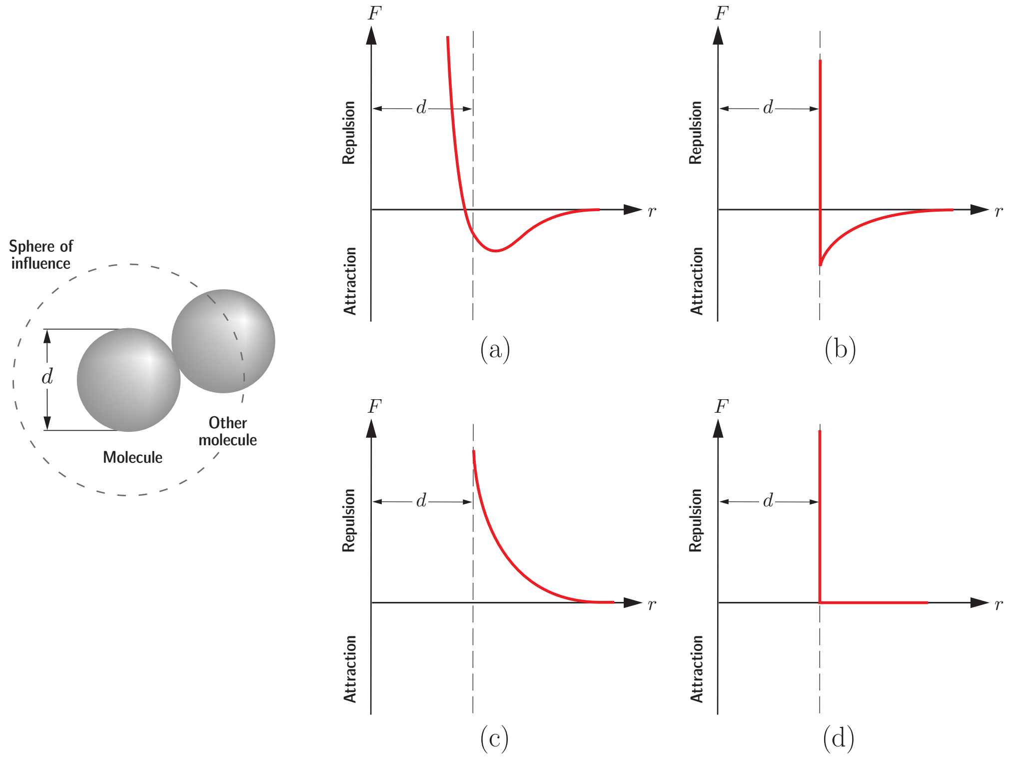

(a) (b) (c) (d)

Figure 2.3: Molecular interaction force as a function of distance between the center of molecules are shown, where d is the diameter of molecules. Plot (a) represents true intermolecular interaction. For $r < d$ electron orbits of molecules intermingle, that results a strong repulsive force. Other plots show simplified molecular interaction models. Plot (b) is known as Sutherland model. Power potential model, shown in plot (c), gives pure repulsive potential. Maxwell molecules are of power potential type. Plot (d), corresponds to hard–sphere molecules, with no attraction force and infinite repulsive force during the collision.

An exact solution for the Boltzmann equation can be obtained for the important and special case of a gas in *equilibrium*. If we restrict our attention to situations without external force fields, $G_k = 0$, at equilibrium all position and time derivatives must be zero, $\partial f/\partial t = \partial f/\partial x_k = 0$, and with regards to Eqs. (2.17) and (2.18) the *local* equilibrium distribution function is the solution of $f' f'_* - f f_* = 0$, which yields

$$f_{\mathrm{E}} = \frac{\rho}{\sqrt{2\pi\theta}^3} \exp\left[-\frac{(c_k - v_k)^2}{2\theta} \right]. \tag{2.19}$$

The above solution for the Boltzmann equations is also referred as the local Maxwellian distribution function.

2.4 Velocity Distribution Function and Macroscopic Variables

The solution of the Boltzmann equation gives the velocity distribution function $f\left(x_k, t, c_k\right)$, that includes detailed information in microscopic level. For science and engineering applications, we are interested in measurable macroscopic quantities, e.g., density, pressure, temperature, heat–flux, and stress. These macroscopic quantities can be expressed as the moments of f. Moments are weighted averages of the distribution function.

Convective moments and *central moments* of f are defined based on particle velocity c_i and *peculiar* velocity C_i, respectively,

$$\mathscr{M}^{\alpha}_{i_1 i_2\, \cdots\, i_n} = \int c^{2\alpha}\, c_{i_1} c_{i_2}\, \cdots\, c_{i_n}\, f\, d\mathbf{c}, \tag{2.20}$$

$$M^{\alpha}_{i_1 i_2\, \cdots\, i_n} = \int C^{2\alpha}\, C_{i_1} C_{i_2}\, \cdots\, C_{i_n}\, f\, d\mathbf{c}, \tag{2.21}$$

where

$$c = \sqrt{c_1^2 + c_2^2 + c_3^3} \quad \text{and} \quad C = \sqrt{C_1^2 + C_2^2 + C_3^3}.$$

The peculiar velocity is the difference between the particle velocity and mean velocity of the gas v_i,

$$C_i = c_i - v_i. \tag{2.22}$$

Analogously, for a matter of convenience, we define trace–free central moments as

$$\mathcal{M}^{\alpha}_{i_1 i_2\, \cdots\, i_n} = M^{\alpha}_{\langle i_1 i_2\, \cdots\, i_n \rangle} = \int C^{2\alpha}\, C_{\langle i_1} C_{i_2}\, \cdots\, C_{i_n \rangle}\, f\, d\mathbf{c}, \tag{2.23}$$

and equilibrium residue scalar moments as

$$\mathcal{W}^{\alpha} = \int C^{2\alpha}\, \left(f - f_{\mathrm{E}}\right)\, d\mathbf{c}. \tag{2.24}$$

In Eq. (2.23), the indices inside the angular brackets indicate the trace–free and symmetric part of a tensor. Symmetric trace–free part of the matrix A_{ij} is $A_{\langle ij \rangle} = (A_{ij} + A_{ji})/2 - A_{kk}\delta_{ij}/3$, for instance see Eq. (2.15) for trace–free part of the symmetric velocity gradient matrix. Details of how the angular brackets can be expanded for tensors (moments) with higher ranks are well documented in Ref. [106, App. A]. In the equilibrium residue scalar moments $\mathcal{W}^{\alpha}$, given by Eq. (2.24), f_{E} is the

Maxwellian (equilibrium) distribution function, Eq. (2.19).

The following well–known macroscopic quantities are the moments of distribution function,

$$\rho = \mathscr{M}^0 = M^0 = \int f \, d\mathbf{c}, \tag{2.25a}$$

$$v_i = \frac{1}{\rho}\mathscr{M}^0_i = \frac{1}{\rho}\int c_i \, f \, d\mathbf{c}, \tag{2.25b}$$

$$e = \frac{1}{2\rho}\mathscr{M}^1 = \frac{1}{2\rho}\int c^2 \, f \, d\mathbf{c}, \tag{2.25c}$$

$$u = \frac{1}{2\rho}M^1 = \frac{1}{2\rho}\int C^2 \, f \, d\mathbf{c}, \tag{2.25d}$$

$$\theta = \frac{1}{3\rho}M^1 = \frac{1}{3\rho}\int C^2 \, f \, d\mathbf{c}, \tag{2.25e}$$

$$p = \frac{1}{3}M^1 = \frac{1}{3}\int C^2 \, f \, d\mathbf{c}, \tag{2.25f}$$

$$p_{ij} = M^0_{ij} = \int C_i C_j \, f \, d\mathbf{c}, \tag{2.25g}$$

$$\sigma_{ij} = \mathcal{M}^0_{ij} = \int C_{\langle i} C_{j\rangle} \, f \, d\mathbf{c}, \tag{2.25h}$$

$$q_i = \frac{1}{2}M^1_i = \frac{1}{2}\int C^2 C_i \, f \, d\mathbf{c}. \tag{2.25i}$$

Describing gas flows with the above moments is the primary goal in practical simulations. These moments represent measurable macroscopic quantities. However, according to Eqs. (2.20) and (2.21) there are many other moments, so–called high–order moments, which represent macroscopic quantities without intuitive physical interpretation, for these the general notation of moments as in (2.20)–(2.24) will be used unless otherwise stated.

2.5 Kinetic Methods for the Boltzmann Equation

Providing both analytical and numerical solutions for the Boltzmann equation is a challenging task. Despite considerable achievements in numerics and computational facilities, direct solution of the Boltzmann equation for practical applications remains formidable, due to the complex structure of the collision term [cf. Eq. (2.18)] and high dimensionality of the microscopic velocity field [21, 98]. Accordingly, in the context of kinetic theory approximate solutions for the Boltzmann equation are reported by using simplified collision models and/or by restricting the magnitude and directions of particles' velocity.

Nowadays, the direct simulation Monte Carlo (DSMC) method [17] is the most successful method for the solution of the Boltzmann equation. The DSMC method was originally developed for supersonic and hypersonic rarefied gas flows in which the product of Knudsen number and Mach number, Kn × Ma, is large. However, the method has been extended to cover near–continuum flows with small Mach numbers.

In the DSMC approach, flow is modeled using simulation molecules, which represent a large number of real molecules, while molecular collisions are calculated using probabilistic (Monte Carlo) simulation. The fundamental assumption of the DSMC method is that the molecular movement and collision can be decoupled over time periods that are smaller than the mean collision time, which makes it suitable for highly rarefied flow simulations.

In general, DSMC simulations are computationally expensive, particularly, when a large number of representative particles is employed, and unsteady processes are considered. Moreover, due to the statistical nature of the method, the results contain stochastic noise, that is known as the main drawback of the DSMC method.

An early kinetic model for the Boltzmann equation is Bhatnagar–Gross–Krook (BGK) model [15] that replaces the collision integral with

$$\mathcal{Q}\left(f,f\right)=\bar{\nu}\left(f_{\mathrm{E}}-f\right), \tag{2.26}$$

where $\bar{\nu}$ is the mean collision frequency of molecules, and f_{E} is the local Maxwellian distribution given in Eq. (2.19).

The BGK approximation for the collision term considerably simplifies the mathematics but retains many of the qualitative features of the true collision integral [22]. Although it describes the right hydrodynamical limit, it does not give the Navier–Stokes equation with correct transport coefficients in the Chapman–Enskog expansion; the major disadvantage of BGK model is its failure to predict the correct Prandtl number. This shortcoming makes it erroneous in describing isothermal and nonisothermal flows simultaneously. Consequently, modified BGK models are proposed which yield the correct Prandtl number, i.e., the ellipsoidal model [43].

Another choice to reduce the complexity of the collision term is to linearize it by assuming

$$f\left(x_k,t,c_k\right)=f_{\mathrm{E}_0}\left(1+h\left(x_k,t,c_k\right)\right), \qquad |h|\ll 1, \tag{2.27}$$

where f_{E_0} represents a global Maxwellian with ρ_0 and θ_0,

$$f_{\mathrm{E}_0} = \frac{\rho_0}{\sqrt{2\pi\theta_0}^3} \exp\left[-\frac{(c_k - v_k)^2}{2\theta_0}\right]. \tag{2.28}$$

Replacing f from (2.27) into Eqs. (2.17) and (2.18), and then neglecting nonlinear terms leads to the linearized Boltzmann equation,

$$\frac{\partial h}{\partial t} + c_k \frac{\partial h}{\partial x_k} = \mathscr{Q}(h, h), \tag{2.29}$$

where the linearized collision term now reads [98]

$$\mathscr{Q}(h, h) = \int_{\text{all } \phi_k \text{ and all } c_{k*}} \left(h' + h'_* - h - h_*\right) \mathscr{B}(\xi_k, \phi_k)\, d\Lambda(\boldsymbol{\phi})\, d\mathbf{c}_*. \tag{2.30}$$

Equation (2.29) is still an integro–differential equation, that demands extensive computational effort. The appropriate numerical approach for this problem is described in [22, 98]. The linearized Boltzmann equation is applicable only to the case where the Reynolds number is very small [22, 98].

The Lattice Boltzmann Method (LBM) is a relatively new simulation technique for complex fluid systems. The idea of lattice Boltzmann method is borrowed from the Boltzmann kinetic equation—free flights and collisions change the velocity distribution function and state of the gas. In LBM the gas is defined through fictitious particles and discrete velocity distribution functions on a lattice, where direction and magnitude of particles' velocity are limited by the lattice.

The original LBM yields Navier–Stokes solution [26], and not the Boltzmann equation itself. These days, LB models are very popular, thanks to their welcoming practical features and simplicity, but they are valid for small Knudsen numbers only and still suffer from instabilities when compressibility and heat transfer come into account [111, 128]. Recently, it was shown [5, 49] that inclusion of high–order moments in isothermal LB methods and increasing the number of discrete velocities can shift the ability of LB methods beyond the hydrodynamics regime.

2.6 Extended Hydrodynamics

Once a microscopic kinetic equation (here the Boltzmann equation) is given, the corresponding macroscopic transport equations can be extracted. This is done in kinetic theory by reducing the degrees of freedom of the velocity distribution function, to the degrees of freedom of a finite set of macroscopic variables. The *Chapman–Enskog (CE) expansion* [25] and *Grad's moment expansion* [32, 33] are the classical methods to extract hydrodynamic–like equations from the Boltzmann equation.

The Chapman–Enskog method replaces the velocity distribution function in the Boltzmann equation by its expansion in the Knudsen number [25],

$$f_{\mathrm{CE}} = \sum_{n=0}^{\infty} \mathrm{Kn}^n f^{(n)} = f^{(0)} + \mathrm{Kn} f^{(1)} + \mathrm{Kn}^2 f^{(2)} + \cdots , \tag{2.31}$$

with $f^{(0)} = f_{\mathrm{E}}$ given in Eq. (2.19). In the Boltzmann equation [cf. Eq. (2.17)] substitution of f with f_{CE}, and equating the terms of the same powers in Kn yields, after tedious manipulation, explicit expressions for heat–flux vector, q_i, and stress tensor, σ_{ij}, as derivatives of the main hydrodynamic variables $\{\rho, T, v_i\}$. Through a standard procedure, the Euler and Navier–Stokes–Fourier equations follow from the zeroth– and first–order expansions, while the second– and third–order expansions yield the Burnett and super–Burnett equations, respectively [25, 106].

Attempts at solving the Burnett–type equations have uncovered many physical and numerical difficulties. As proved in [18, 86], the classical Burnett equations are vulnerable to instabilities, and in many cases (transient flows) give unphysical results. Consequently, several modified versions of these equations are proposed papers have been devoted to this problem, and authors have suggested different techniques to stabilize the equations, including the augmented Burnett equations [134], the regularized Burnett equations [44], consistently ordered extended thermodynamics [76], hyperbolic Burnett equations [19], and hybrid Burnett equations [97].

Even more, it is important to highlight the lack of any systematic approach to derive boundary conditions for the Burnett–type equations, which requires evaluation of higher–order derivatives of the primary quantities on the boundary.

Quite differently compared to the Chapman–Enskog method, in the Grad's moment method the velocity distribution function is constructed by an expansion of the Maxwellian into Hermite polynomials [32, 33] as

$$f_{\mathrm{G}} = \left(a + a_i \frac{\partial}{\partial C_i} + a_{ij} \frac{\partial^2}{\partial C_i \partial C_j} + a_{ijk} \frac{\partial^3}{\partial C_i \partial C_j \partial C_k} + \cdots \right) f_{\mathrm{E}}, \tag{2.32}$$

where $a_{i_1 i_2 \, \cdots \, i_n}$ are the expansion coefficients, and C_k is the peculiar particle velocity as defined in (2.22).

The moments of the distribution function construct a list of macroscopic quantities [Eq. (2.25)], and the set of macroscopic quantities can be expanded based on the approximated polynomial. In Grad's moment method, the moment equations which are obtained from the Boltzmann equation govern the evolution of the moments. Details about the moment method will be presented in Chap. 3.

The prominent advantage of Grad's moment over Chapman–Enskog method is that it yields a stable set of equations: moment equations avoid those instabilities that are inherent in the Burnett–type equations. Moreover, based on Maxwell's kinetic boundary conditions for the Boltzmann equation [74], a rational strategy can be established in order to obtain boundary conditions for the moments. Such strategies have been rigorously discussed in Refs. [35, 121]. For detailed discussion on boundary conditions for the moments see Chap. 5.

Chapter 3

Moment Method for Boltzmann Equation

3.1 General Moment Equation

The moment method is a branch of kinetic theory in which the moments of the velocity distribution function are the key quantities. The evolution equation for the moments follows by multiplying the Boltzmann equation [Eq. (2.17)] with $c^{2\alpha}c_{i_1}c_{i_2}\ \ldots\ c_{i_n}$, and then integrating over the velocity space $\mathbf{c}$. This gives the general moment equation,

$$\frac{\partial \mathscr{M}^{\alpha}_{i_1 i_2\ \cdots\ i_n}}{\partial t} + \frac{\partial \mathscr{M}^{\alpha}_{i_1 i_2\ \cdots\ i_n k}}{\partial x_k} = \mathscr{P}^{\alpha}_{i_1 i_2\ \cdots\ i_n} + \mathscr{S}^{\alpha}_{i_1 i_2\ \cdots\ i_n}, \tag{3.1}$$

where $\mathscr{M}^{\alpha}_{i_1 i_2\ \cdots\ i_n}$ denotes the convective moments, introduced in Eq. (2.20). For the moments, the production term due to collision $\mathscr{P}^{\alpha}_{i_1 i_2\ \cdots\ i_n}$ and supply term $\mathscr{S}^{\alpha}_{i_1 i_2\ \cdots\ i_n}$ are [106]

$$\mathscr{P}^{\alpha}_{i_1 i_2\ \cdots\ i_n} = \int c^{2\alpha} c_{i_1} c_{i_2}\ \cdots\ c_{i_n}\ \mathcal{Q}\left(f,f\right)\, d\mathbf{c}, \tag{3.2}$$

$$\mathscr{S}^{\alpha}_{i_1 i_2\ \cdots\ i_n} = n\mathscr{M}^{\alpha}_{(i_1 i_2\ \cdots\ i_{n-1}} G_{i_n)} + 2\alpha \mathscr{M}^{\alpha-1}_{i_1 i_2 \cdots\ i_n k} G_k, \tag{3.3}$$

where $n = 0, 1, 2, \cdots$ refers to the tensor rank of the moments. The vector G_i is the body–force vector, and indices inside the round brackets denote the symmetric part of a tensor.

The structure of the above equations shows that change of any moment with respect to time

$\partial \mathscr{M}^{\alpha}_{i_1 i_2 \cdots i_n}/\partial t$, depends on the divergence of the next higher–order moment, i.e., $\partial \mathscr{M}^{\alpha}_{i_1 i_2 \cdots i_n k}/\partial x_k$, and the next lower–order moment in the supply term $\mathscr{M}^{\alpha}_{(i_1 i_2 \cdots i_{n-1}} G_{i_n)}$. This implies a successive coupling between moment equations. Consequently, the system of differential equations in (3.1) is not closed. In Sec. 3.2 the classical Grad closure for moment equations is introduced.

In Eq. (3.1), the first term represents the local variation of the moments, while the second term corresponds to the flux of the moments. To provide an abstracted form of the moment equations, we define $\varPsi_A = c^{2\alpha} c_{i_1} c_{i_2} \ \ldots \ c_{i_n}$ as a polynomial of the particles' velocity. Then, Eq. (3.1) recasts as

$$\frac{\partial \mathscr{U}_A}{\partial t} + \frac{\partial \mathscr{F}_{Ak}}{\partial x_k} = \mathscr{P}_A + \mathscr{S}_A, \tag{3.4}$$

with

$$\mathscr{U}_A = \int \varPsi_A \, f \, d\mathbf{c}, \qquad \mathscr{F}_{Ak} = \int \varPsi_A c_k \, f \, d\mathbf{c}. \tag{3.5}$$

In the above equations $\mathscr{U}_A$ are the macroscopic variables (moments) with their corresponding fluxes $\mathscr{F}_{Ak}$, production $\mathscr{P}_A$, and supply $\mathscr{S}_A$.

3.2 Grad's Classical Closure for Moment Equations

As shown in Sec. 3.1, the moment equations construct a coupled set of infinitely many equations. In order to provide a solution for the moment equations, first, a finite set of moment equations should be selected, then a closure is required. To meet these requirements, Grad [32, 33] proposed a velocity distribution function f_{G}, by expanding the equilibrium distribution function (2.19) into Hermite polynomials [Eq. (2.32)]. This expansion can be written as [33, 106]

$$f_{\mathrm{G}} = f_{\mathrm{E}} \sum \vartheta_A \, \varPsi_A, \tag{3.6}$$

where ϑ_A are the expansion coefficients. These coefficients need to be determined such that the replacement of f_{G} in Eq. (3.5) yields macroscopic variables $\mathscr{U}_A$ and their corresponding fluxes $\mathscr{F}_{Ak}$.

3.2.1 Grad's 5–moment (G5) Equations: Euler Equations

As given in Eqs. (2.25a)–(2.25c) the conserved quantities of mass, momentum, and total energy correspond to the moments $\mathscr{M}^0$, $\mathscr{M}^0_i$, and $\mathscr{M}^1$, respectively. Accordingly, multiplication of the Boltzmann equation with $\varPsi_A = \{1, c_i, \frac{1}{2}c^2\}$, and then integrating over the velocity space yields the moment equations,

$$\frac{\partial \mathscr{M}^0}{\partial t}+\frac{\partial \mathscr{M}^0_k}{\partial x_k}=\mathscr{P}^0+\mathscr{S}^0, \tag{3.7a}$$

$$\frac{\partial \mathscr{M}^0_i}{\partial t}+\frac{\partial \mathscr{M}^0_{ik}}{\partial x_k}=\mathscr{P}^0_i+\mathscr{S}^0_i, \tag{3.7b}$$

$$\frac{1}{2}\frac{\partial \mathscr{M}^1}{\partial t}+\frac{1}{2}\frac{\partial \mathscr{M}^1_k}{\partial x_k}=\frac{1}{2}\mathscr{P}^1+\frac{1}{2}\mathscr{S}^1. \tag{3.7c}$$

Since mass, momentum, and energy are conserved during the collision process, then, production terms in the above equations vanish,

$$\mathscr{P}^0=\mathscr{P}^0_i=\mathscr{P}^1=0. \tag{3.8}$$

Moreover, evaluation of the supply terms from Eq. (3.3) gives

$$\mathscr{S}^0=0,\qquad \mathscr{S}^0_i=\rho G_i,\qquad \frac{1}{2}\mathscr{S}^1=\rho v_i G_i. \tag{3.9}$$

By replacing the moments from (2.25), the moment equations in (3.7) read as

$$\frac{\partial \rho}{\partial t}+\frac{\partial(\rho v_k)}{\partial x_k}=0, \tag{3.10a}$$

$$\frac{\partial(\rho v_i)}{\partial t}+\frac{\partial(\rho v_i v_k+p\delta_{ik}+\sigma_{ik})}{\partial x_k}=\rho G_i, \tag{3.10b}$$

$$\frac{\partial(\rho e)}{\partial t}+\frac{\partial(\rho e v_k+p_{ik}v_i+q_k)}{\partial x_k}=\rho v_i G_i, \tag{3.10c}$$

that are equivalent to basic conservation laws as in Eq. (2.9)—without the radiation contribution, $\dot{e}_{\mathrm{Rad}}$, in the energy supply term. The second terms on the left–hand side of Eqs. (3.7b) and (3.7c) represent total fluxes of momentum and energy [cf. Eqs. (2.10) and (2.11)], which are expressed through the following *convective* moments

$$\mathscr{M}^0_{ik}=\rho v_i v_k+p\delta_{ik}+\sigma_{ik}=\Pi_{ik},\qquad \frac{1}{2}\mathscr{M}^1_k=\rho e v_k+p_{ik}v_i+q_k=\Theta_k. \tag{3.11}$$

In order to close the system in (3.10), stress tensor σ_{ik}, and heat–flux vector q_k must be expressed with respect to the main variables, $\{\rho,\rho v_i,\rho e\}$. For this purpose, Grad's distribution function (3.6) must be employed that takes the following form

$$f_{\mathrm{G5}} = f_{\mathrm{E}} \left(\vartheta^0 + \vartheta_i^0 c_i + \frac{1}{2} \vartheta^1 c^2 \right). \tag{3.12}$$

The unknown coefficients in the above equation must be chosen so that f_{G5} reproduces the main variables, i.e.,

$$(\rho, \rho v_i, \rho e)^{\mathrm{T}} = \int \left(1, c_i, \frac{1}{2} c^2 \right)^{\mathrm{T}} f_{\mathrm{G5}} \, d\mathbf{c}. \tag{3.13}$$

After straightforward integration the coefficients read $\vartheta^0 = 1$ and $\vartheta_i^0 = \vartheta^1 = 0$. Therefore, the Maxwellian distribution function [Eq. (2.19)] is recovered

$$f_{\mathrm{G5}} = f_{\mathrm{E}} = \frac{\rho}{\sqrt{2\pi\theta}^3} \exp\left(-\frac{C^2}{2\theta} \right), \tag{3.14}$$

that describes an equilibrium state. With f_{G5} the stress tensor σ_{ik}, and heat–flux vector q_k, can be calculated from their corresponding moment equations [Eqs. (2.25h) and (2.25i)],

$$\sigma_{ik|5} = \int C_{\langle i} C_{k\rangle} \, f_{\mathrm{G5}} \, d\mathbf{c} = 0, \qquad q_{k|5} = \int C^2 C_k \, f_{\mathrm{G5}} \, d\mathbf{c} = 0. \tag{3.15}$$

Finally, Grad's 5–moment system reduces to Euler's hydrodynamic system

$$\frac{D\rho}{Dt} + \rho \frac{\partial v_k}{\partial x_k} = 0, \tag{3.16a}$$

$$\rho \frac{Dv_i}{Dt} + \frac{\partial (\rho\theta)}{\partial x_i} = \rho G_i, \tag{3.16b}$$

$$\rho \frac{De}{Dt} + \frac{\partial (\rho\theta v_k)}{\partial x_k} = \rho v_i G_i, \tag{3.16c}$$

that describes ideal flows without viscous dissipation and heat conduction, through five equilibrium moments $\mathscr{U}_A^{[5]} = \{\rho, \rho v_i, \rho e\}$. In the above equations, the convective (or material) derivative is defined as

$$\frac{D}{Dt} = \frac{\partial}{\partial t} + v_k \frac{\partial}{\partial x_k}. \tag{3.17}$$

3.2.2 Grad's 13–moment (G13) Equations

By choosing $\Psi_A = \{1, c_i, \frac{1}{2}c^2, C_i C_j, \frac{1}{2} C^2 C_i\}$, the corresponding moments are $\mathscr{U}_A = \{\rho, \rho v_i, \rho e, \sigma_{ij}, q_i\}$. As shown in Sec. 3.2.1, for $\Psi_A = \{1, c_i, \frac{1}{2}c^2\}$ the moment equations give conservation laws[1] [cf. Eq.

---

[1] In Ψ_A, the choice of $\frac{1}{2}C^2$ instead of $\frac{1}{2}c^2$ gives the balance (and not conservation) of internal energy, u.

(3.10)]. The remained elements in $\mathit{\Psi}_A$ lead to balance equations for heat–flux vector and stress tensor,

$$\frac{\partial \sigma_{ij}}{\partial t} + v_k \frac{\partial \sigma_{ij}}{\partial x_k} + \frac{\partial \mathcal{M}^0_{ijk}}{\partial x_k} + \frac{4}{5}\frac{\partial q_{\langle i}}{\partial x_{j\rangle}} + 2\sigma_{k\langle i}\frac{\partial v_{j\rangle}}{\partial x_k} + \sigma_{ij}\frac{\partial v_k}{\partial x_k} + 2\rho\theta\frac{\partial v_{\langle i}}{\partial x_{j\rangle}} = \mathscr{P}^0_{ij}, \tag{3.18}$$

$$\begin{aligned}\frac{\partial q_i}{\partial t} + v_k\frac{\partial q_i}{\partial x_k} + \frac{5}{2}\rho\theta\frac{\partial \theta}{\partial x_i} - \sigma_{ik}\frac{\partial \theta}{\partial x_k} - \frac{\theta\sigma_{ik}}{\rho}\frac{\partial \rho}{\partial x_k} - \frac{\sigma_{ik}}{\rho}\frac{\partial \sigma_{kl}}{\partial x_l} - \frac{5}{2}\theta\frac{\partial \sigma_{ik}}{\partial x_k}& \\ + \frac{1}{6}\frac{\partial \mathcal{W}^2}{\partial x_i} + \frac{1}{2}\frac{\partial \mathcal{M}^1_{ik}}{\partial x_k} + \mathcal{M}^0_{ikl}\frac{\partial v_k}{\partial x_l} + \frac{7}{5}q_i\frac{\partial v_k}{\partial x_k} + \frac{7}{5}q_k\frac{\partial v_i}{\partial x_k} + \frac{2}{5}q_k\frac{\partial v_k}{\partial x_i} &= \frac{1}{2}\mathscr{P}^1_i.\end{aligned} \tag{3.19}$$

In the above equations there are unknown moments $\{\mathcal{W}^2, \mathcal{M}^1_{ik}, \mathcal{M}^0_{ikl}\}$, plus the production terms, $\mathscr{P}^0_{ij}$ and $\mathscr{P}^1_i$. For Maxwell molecules the production terms can be computed independent of distribution function [106, 122],

$$\mathscr{P}^0_{ij} = -\frac{\rho\theta}{\mu}\sigma_{ij}, \qquad \mathscr{P}^1_i = -\frac{4}{3}\frac{\rho\theta}{\mu}q_i. \tag{3.20}$$

Even more, to obtain a closed system of equations, we need to express the unknown moments $\{\mathcal{W}^2, \mathcal{M}^1_{ik}, \mathcal{M}^0_{ikl}\}$ as a function of variables $\mathscr{U}_A = \{\rho, \rho v_i, \rho e, \sigma_{ij}, q_i\}$. Similar to the G5 case, a velocity distribution function as in Eq. (3.6) suffices to provide a closure for the system,

$$f_{\mathrm{G13}} = f_{\mathrm{E}}\left(\vartheta^0 + \vartheta^0_i c_i + \frac{1}{2}\vartheta^1 c^2 + \vartheta^0_{ij}C_iC_j + \frac{1}{2}\vartheta^1_i C^2 C_i\right). \tag{3.21}$$

The unknown coefficients in the above equation must be determined such that

$$(\rho, \rho v_i, \rho e, \sigma_{ij}, q_i)^{\mathrm{T}} = \int \left(1, c_i, \frac{1}{2}c^2, C_iC_j, \frac{1}{2}C^2C_i\right)^{\mathrm{T}} f_{\mathrm{G13}}\, d\mathbf{c}. \tag{3.22}$$

After evaluation of the coefficients, the velocity distribution function (3.21) takes the following form

$$f_{\mathrm{G13}} = f_{\mathrm{E}}\left[1 + \left(\frac{C^2}{5\rho\theta^3} - \frac{1}{\rho\theta^2}\right)C_jq_j + \frac{1}{2\rho\theta^2}C_iC_j\sigma_{ij}\right]. \tag{3.23}$$

With f_{G13} the unknown moments in Eqs. (3.18) and (3.19) read as

$$\mathcal{W}^2_{|\mathrm{G13}} = \int C^4 (f_{\mathrm{G13}} - f_{\mathrm{E}})\, d\mathbf{c} = M^2 - 15\rho\theta^2 = 0, \tag{3.24a}$$

$$\mathcal{M}^1_{ik|\mathrm{G13}} = \int C^2 C_{\langle i}C_{k\rangle}\, f_{\mathrm{G13}}\, d\mathbf{c} = 7\theta\sigma_{ik}, \tag{3.24b}$$

$$\mathcal{M}^0_{ikl|\mathrm{G13}} = \int C_{\langle i}C_kC_{l\rangle}\, f_{\mathrm{G13}}\, d\mathbf{c} = 0. \tag{3.24c}$$

Then, the balance equations for stress and heat–flux are

$$\frac{D\sigma_{ij}}{Dt}+\frac{4}{5}\frac{\partial q_{\langle i}}{\partial x_{j\rangle}}+\sigma_{ij}\frac{\partial v_k}{\partial x_k}+2\sigma_{k\langle i}\frac{\partial v_{j\rangle}}{\partial x_k}=-2\rho\theta\frac{\partial v_{\langle i}}{\partial x_{j\rangle}}-\frac{\rho\theta}{\mu}\sigma_{ij}, \tag{3.25}$$

$$\begin{aligned}\frac{Dq_i}{Dt}+\frac{5}{2}\sigma_{ik}\frac{\partial\theta}{\partial x_k}-\frac{\theta\sigma_{ik}}{\rho}\frac{\partial\rho}{\partial x_k}-\frac{\sigma_{ik}}{\rho}\frac{\partial\sigma_{kl}}{\partial x_l}+\theta\frac{\partial\sigma_{ik}}{\partial x_k}&\\ +\frac{7}{5}q_k\frac{\partial v_i}{\partial x_k}+\frac{7}{5}q_i\frac{\partial v_k}{\partial x_k}+\frac{2}{5}q_k\frac{\partial v_k}{\partial x_i}&=-\frac{5}{2}\rho\theta\frac{\partial\theta}{\partial x_i}-\frac{2}{3}\frac{\rho\theta}{\mu}q_i.\end{aligned} \tag{3.26}$$

The collection of conservation laws (3.10) and moment equations for stress (3.25) and heat flux (3.26), describe the evolution of thirteen macroscopic variables $\mathscr{U}_A^{[13]}=\{\rho,\rho v_i,\rho e,\sigma_{ij},q_i\}$. The name *13–moment* refers to the number of moments which are included as variables in the equations.

3.2.3 Grad's 26–moment (G26) Equations

The G26 system adds the unknown moments of G13 [cf. Eqs. (3.24)] to the list of variables $\mathscr{U}_A^{[26]}$, and considers thirteen additional equations for those thirteen variables (moments).

For Grad's 26–moment system we choose $\varPsi_A=\{1,c_i,\frac{1}{2}c^2,C_iC_j,\frac{1}{2}C^2C_i,C_iC_jC_k,C^2C_iC_j,C^4\}$ where the corresponding variables are $\mathscr{U}_A^{[26]}=\{\rho,\rho v_i,\rho e,\sigma_{ij},q_i,\mathcal{M}^0_{ijk},\mathcal{M}^1_{ij},M^2\}$. The moment equations for $\mathcal{M}^0_{ijk}$, $\mathcal{M}^1_{ij}$, and M^2 (which are not shown here) contain additional moments $\mathcal{M}^0_{ijkl}$, $\mathcal{M}^1_{ijk}$, and M^2_i that must, again, be expressed with respect to the variables in $\mathscr{U}_A^{[26]}$.

The proper form of Grad–type distribution function [Eq. (3.6)] for 26–moment system is

$$\begin{aligned}f_{\mathrm{G26}}=f_{\mathrm{E}}\Bigg[1+\left(\frac{C^2}{5\rho\theta^3}-\frac{1}{\rho\theta^2}\right)C_jq_j+\frac{1}{2\rho\theta^2}C_iC_j\sigma_{ij}+\frac{\mathcal{W}^2}{8\rho\theta^2}\left(1-\frac{2C^2}{3\theta}+\frac{C^4}{15\theta^2}\right)&\\ +\left(\frac{1}{4\rho\theta^3}-\frac{C^2}{28\rho\theta^4}\right)C_iC_j\left(7\theta\sigma_{ij}-\mathcal{M}^1_{ij}\right)+\frac{1}{6\rho\theta^3}C_iC_jC_k\mathcal{M}^0_{ijk}\Bigg]&,\end{aligned}$$

that gives the unknown moments as

$$\mathcal{M}^0_{ijkl|\mathrm{G26}}=\int C_{\langle i}C_jC_kC_{l\rangle}\,f_{\mathrm{G26}}\,d\mathbf{c}=0, \tag{3.27a}$$

$$\mathcal{M}^1_{ijk|\mathrm{G26}}=\int C^2C_{\langle i}C_jC_{k\rangle}\,f_{\mathrm{G26}}\,d\mathbf{c}=9\theta\mathcal{M}^0_{ijk}, \tag{3.27b}$$

$$M^2_{i|\mathrm{G26}}=\int C^4C_i\,f_{\mathrm{G26}}\,d\mathbf{c}=28\theta q_i. \tag{3.27c}$$

The relevant production terms in the G26 system can be obtained for Maxwell molecules [106],

$$\mathscr{P}^0_{ijk} = -\frac{3}{2}\frac{\rho\theta}{\mu}\mathcal{M}^0_{ijk}, \qquad \mathscr{P}^1_{ij} = -\frac{7}{6}\frac{\rho\theta}{\mu}\left(\mathcal{M}^1_{ij} - \theta\sigma_{ij} + \frac{4}{7}\frac{\sigma_{k\langle i}\sigma_{j\rangle k}}{\rho}\right),$$

$$\mathscr{P}^2 = -\frac{2}{3}\frac{\rho\theta}{\mu}\left(\mathcal{W}^2 + \frac{\sigma_{ij}\sigma_{ij}}{\rho}\right). \tag{3.28}$$

The closure given by Eqs. (3.27) and (3.28) gives the final form of moment equations for $\mathcal{M}^0_{ijk}$, $\mathcal{M}^1_{ij}$, and $\mathcal{W}^2$ as

$$\frac{D\mathcal{M}^0_{ijk}}{Dt} - 3\sigma_{\langle ij}\left(\frac{1}{\rho}\frac{\partial\sigma_{k\rangle l}}{\partial x_l} + \frac{\theta}{\rho}\frac{\partial\rho}{\partial x_{k\rangle}} + \frac{\partial\theta}{\partial x_{k\rangle}}\right) + \frac{3}{7}\frac{\partial\mathcal{M}^1_{\langle ij}}{\partial x_{k\rangle}}$$

$$+ 3\mathcal{M}^0_{l\langle ij}\frac{\partial v_{k\rangle}}{\partial x_l} + \mathcal{M}^0_{ijk}\frac{\partial v_l}{\partial x_l} + \frac{12}{5}q_{\langle i}\frac{\partial v_j}{\partial x_{k\rangle}} = -\frac{3}{2}\frac{\rho\theta}{\mu}\mathcal{M}^0_{ijk}, \tag{3.29}$$

$$\frac{D\mathcal{M}^1_{ij}}{Dt} - 2\mathcal{M}^0_{ijk}\left(\frac{1}{\rho}\frac{\partial\sigma_{kl}}{\partial x_l} + \frac{\theta}{\rho}\frac{\partial\rho}{\partial x_k}\right) + 7\mathcal{M}^0_{ijk}\frac{\partial\theta}{\partial x_k} - \frac{28}{5}q_{\langle i}\left(\frac{1}{\rho}\frac{\partial\sigma_{j\rangle k}}{\partial x_k} + \frac{\theta}{\rho}\frac{\partial\rho}{\partial x_{j\rangle}}\right)$$

$$+ \frac{28}{5}q_{\langle i}\frac{\partial\theta}{\partial x_{j\rangle}} + 9\theta\frac{\partial\mathcal{M}^0_{ijk}}{\partial x_k} + \frac{56}{5}\theta\frac{\partial q_{\langle i}}{\partial x_{j\rangle}} + \frac{6}{7}\mathcal{M}^1_{\langle ij}\frac{\partial v_{k\rangle}}{\partial x_k} + \frac{4}{5}\mathcal{M}^1_{k\langle i}\frac{\partial v_k}{\partial x_{j\rangle}} + 2\mathcal{M}^1_{k\langle i}\frac{\partial v_{j\rangle}}{\partial x_k}$$

$$+ \mathcal{M}^1_{ij}\frac{\partial v_k}{\partial x_k} + \frac{14}{15}\mathcal{W}^2\frac{\partial v_{\langle i}}{\partial x_{j\rangle}} + 14\rho\theta^2\frac{\partial v_{\langle i}}{\partial x_{j\rangle}} = -\frac{7}{6}\frac{\rho\theta}{\mu}\left(\mathcal{M}^1_{ij} - \theta\sigma_{ij} + \frac{4}{7}\frac{\sigma_{k\langle i}\sigma_{j\rangle k}}{\rho}\right), \tag{3.30}$$

and

$$\frac{D\mathcal{W}^2}{Dt} + 8\theta\frac{\partial q_k}{\partial x_k} - 20\theta\sigma_{kl}\frac{\partial v_k}{\partial x_l} + 4\mathcal{M}^1_{kl}\frac{\partial v_k}{\partial x_l} + 20q_k\frac{\partial\theta}{\partial x_k} - 8\frac{\theta q_k}{\rho}\frac{\partial\rho}{\partial x_k}$$

$$- 8\frac{q_k}{\rho}\frac{\partial\sigma_{kl}}{\partial x_l} + \frac{7}{3}\mathcal{W}^2\frac{\partial v_k}{\partial x_k} = -\frac{2}{3}\frac{\rho\theta}{\mu}\left(\mathcal{W}^2 + \frac{\sigma_{ij}\sigma_{ij}}{\rho}\right). \tag{3.31}$$

The collection of fundamental conservation laws (3.10), and moment equations (3.18), (3.19), (3.29)–(3.31) construct the G26 system, which govern the evolution of *26–moments* (macroscopic variables) in $\mathscr{U}^{[26]}_A$.

3.2.4 On Larger Sets of Grad–type Moment Equations

Extending the Grad–type moment equations to 45, 71, 105, 148, 201, 265, $\cdots$ moment systems, follows in the same fashion as discussed for G13 and G26 cases. By following the described strategy, larger systems of partial differential equations can be constructed, which provide more refined description of nonequilibrium flows due to inclusion of more moments.

High–order moments in large moment systems do not present any physical quantity, however, they express nonequilibrium effects in rarefied gas flows [106]. As the Knudsen number increases, nonequilibrium effects alter the flow pattern more strongly, and employment of large moment systems is desired.

In general, the purpose of using moment equations is to save computational time by avoiding the solution of the Boltzmann equation. When a large system of moment equations is considered, the required computational effort to solve the system might be comparable (or even exceed) to kinetic approaches, since the equations become quite complex. Thus, no profit remains to solve the moment system instead of the kinetic equation.

In Part II of this thesis it will be shown that for moderate Knudsen numbers, that correspond to flows in transition regime, 13–moment system offers a reasonable accuracy compared to required computational investment. Due to this welcoming feature it is considered as a useful tool to study transport phenomenon in moderately rarefied flows.

Chapter 4

Regularized Moment Equations

For the Maxwellian distribution function (2.19), the Grad's method corresponds to a 5–moment system, which is equivalent to the Euler equations through $\mathcal{O}(\mathrm{Kn}^0)$, governing the evolution of the five equilibrium moments $\{\rho, \theta, v_i\}$ in inviscid flows without heat conduction.

In Grad's classical 13–moment (G13) system the variables are extended to include the heat–flux vector and stress tensor. According to the Chapman–Enskog method, the G13 equations are second–order in the Knudsen number, $\mathcal{O}(\mathrm{Kn}^2)$. Analogously, in Grad's 26–moment equations inclusion of higher–order moments promote the system to be of super–Burnett order, $\mathcal{O}(\mathrm{Kn}^3)$. A quick glance to Eqs. (3.15), (3.24), and (3.27) shows that Grad's classical moment method provides algebraic expressions for closure of the moment systems. Thus, the moment equations remain as first–order partial differential systems.

Systems of first–order partial differential equations are mostly associated with hyperbolic equations, which are suitable to describe advective processes. It is well–known that hyperbolic equations, for instance, Euler equations, imply finite wave speeds, and thus cannot describe shock structures correctly. Indeed, the absence of diffusion terms in Euler equations is the reason for this shortcoming. As opposed to advective processes, diffusive processes can be properly described by second–order partial differential equations, which are associated with parabolic systems, e.g. the heat equation.

Regularization is a method to add some parabolic terms to hyperbolic (or conditionally hyperbolic) equations [108]. It changes the character of equations leading to correct shock structures. The idea of regularization goes back to Grad [33] and was later revived by Karlin *et al.* [45] who derived a set of linear transport equations, but did not provide numerical values for the various transport coefficients.

Although regularization was initially motivated by high–speed flows, it extends the accuracy of equations for low speed flows as well. Details of the regularization processes are not concerned in this thesis, as they are rigorously explained in the textbook [106].

In this chapter, regularized closures for G5 and G13 equations are presented. Moreover, Navier–Stokes–Fourier (NSF or R5) and regularized 13–moment (R13) equations in cylindrical coordinates system are given in Sec. 4.3. These regularized equations and their corresponding boundary conditions will be used in Part II to solve the considered boundary value problems.

4.1 Regularized 5 (R5) Moment Equations

All macroscopic transport equations are based on the fundamental conservation laws for mass, momentum, and energy densities [cf. Eq. (3.10)] that for ideal gases reads as,

$$\frac{D\rho}{Dt}+\rho\frac{\partial v_i}{\partial x_i}=0, \tag{4.1a}$$

$$\rho\frac{Dv_i}{Dt}+\frac{\partial p}{\partial x_i}+\frac{\partial \sigma_{ij}}{\partial x_j}=\rho G_i, \tag{4.1b}$$

$$\frac{3}{2}\rho\frac{D\theta}{Dt}+\frac{\partial q_i}{\partial x_i}=-\left(p\,\delta_{ij}+\sigma_{ij}\right)\frac{\partial v_i}{\partial x_j}. \tag{4.1c}$$

The above equations are respective moment equations for equilibrium quantities—density ρ, velocity v_i, and temperature θ. Note that Eq. (4.1c) is the balance equation for internal energy, which for ideal gases is related to temperature through the caloric equation of state, $u=\frac{3}{2}\theta$. The right–hand side of Eq. (4.1c) represents the production of internal energy due to viscous heating effects.

Now, we consider moment equations for stress and heat flux as given by the G13 system for Maxwellian molecules [Eqs. (3.25) and (3.26)]

$$\frac{D\sigma_{ij}}{Dt}+[\cdots\text{ space derivatives of moments }\cdots]=-\frac{1}{\epsilon}\frac{p}{\mu}\sigma_{ij}, \tag{4.2a}$$

$$\frac{Dq_i}{Dt}+[\cdots\text{ space derivatives of moments }\cdots]=-\frac{1}{\epsilon}\frac{2}{3}\frac{p}{\mu}q_i, \tag{4.2b}$$

where the dimensionless smallness parameter ϵ indicates how fast the moments σ_{ij} and q_i change. We emphasize that when Eqs. (3.25) and (3.26) are presented in dimensionless form the smallness parameter ϵ is equivalent to the Knudsen number [106]. Next, σ_{ij} and q_i are expanded similar to the Chapman–Enskog expansion

$$\sigma_{ij} = \sigma_{ij}^{(0)} + \epsilon\,\sigma_{ij}^{(1)} + \cdots\,, \qquad q_i = q_i^{(0)} + \epsilon\,q_i^{(1)} + \cdots\,, \tag{4.3}$$

and replaced back in (4.2). When terms with equal powers in ϵ are equated, we obtain

$$\sigma_{ij}^{(0)} = q_i^{(0)} = 0, \tag{4.4}$$

which means the zeroth–order expansion results in the Euler equations (3.16).

Analogously, the first–order expansion yields Navier–Stokes and Fourier's laws for shear stress and heat conduction [106],

$$\sigma_{ij}^{(1)} = -2\mu\frac{\partial v_{\langle i}}{\partial x_{j\rangle}}, \qquad q_i^{(1)} = -\frac{15}{4}\mu\frac{\partial \theta}{\partial x_i}. \tag{4.5}$$

With the above closure for conservation laws (4.1), the classical hydrodynamics equations, namely, the Navier–Stokes and Fourier laws, are obtained. On account of the Chapman–Enskog method, the Navier–Stokes–Fourier equations are first–order in the Knudsen number $\mathcal{O}(\mathrm{Kn}^1)$.

Based on the above discussion, the Navier–Stokes–Fourier system can be considered as the regularized version of the Euler equations. This means that the first–order nonequilibrium quantities, i.e., Navier–Stokes shear stress and Fourier heat conduction, which appear in 13–moment system, are included in the regularized 5–moment system only to some extent—the relations in (4.5) are given on the right–hand side of Eqs. (3.25) and (3.26).

Substitution of (4.5) into (4.1) yields second–order derivatives, that makes the Navier–Stokes–Fourier equations of mixed parabolic–hyperbolic type.

4.2 Regularized 13 (R13) Moment Equations

Despite the welcoming feature of stability, Grad's 13–moment equations yield unphysical shock structures for large Mach numbers [106, 127], and are unable to capture Knudsen layer effects.

The regularization of Grad's 13–moment equations follows to the same concept that was briefly described in the previous section for the 5–moment case, however, more complex calculations are involved [105, 106, 108].

The balance equations for stress and heat–flux follow from their corresponding moment equations

[Eqs. (3.18) and (3.19)]

$$\frac{D\sigma_{ij}}{Dt} + \frac{4}{5}\frac{\partial q_{\langle i}}{\partial x_{j\rangle}} + \sigma_{ij}\frac{\partial v_k}{\partial x_k} + 2\sigma_{k\langle i}\frac{\partial v_{j\rangle}}{\partial x_k} + \frac{\partial m_{ijk}}{\partial x_k} = -2\rho\theta\frac{\partial v_{\langle i}}{\partial x_{j\rangle}} - \frac{\rho\theta}{\mu}\sigma_{ij}, \tag{4.6}$$

$$\begin{aligned}\frac{Dq_i}{Dt} + \frac{5}{2}\sigma_{ik}\frac{\partial\theta}{\partial x_k} - \frac{\theta\sigma_{ik}}{\rho}\frac{\partial\rho}{\partial x_k} - \frac{\sigma_{ik}}{\rho}\frac{\partial\sigma_{kl}}{\partial x_l} + \theta\frac{\partial\sigma_{ik}}{\partial x_k} + \frac{7}{5}\left(q_k\frac{\partial v_i}{\partial x_k} + q_i\frac{\partial v_k}{\partial x_k}\right)&\\ + \frac{2}{5}q_k\frac{\partial v_k}{\partial x_i} + \frac{1}{6}\frac{\partial\mathit{\Delta}}{\partial x_i} + \frac{1}{2}\frac{\partial R_{ik}}{\partial x_k} + m_{ijk}\frac{\partial v_j}{\partial x_k} = -\frac{5}{2}\rho\theta\frac{\partial\theta}{\partial x_i} - \mathrm{Pr}\frac{\rho\theta}{\mu}q_i,&\end{aligned} \tag{4.7}$$

where the collision terms are evaluated for Maxwellian molecules, see Eq. (3.20). The constant Pr in the heat–flux equation is the Prandtl number, that is $\mathrm{Pr} = \frac{2}{3}$ for Maxwellian molecules.

For the sake of better appearance, in the above equations the notation $\{\mathit{\Delta}, R_{ij}, m_{ijk}\}$ is employed to present the moments $\{\mathcal{W}^2, \mathcal{M}^1_{ij} - 7\theta\sigma_{ij}, \mathcal{M}^0_{ijk}\}$, respectively. The Grad's original closure in (3.24) yields $\mathit{\Delta} = R_{ij} = m_{ijk} = 0$, that turn the them to be of second–order, $\mathcal{O}(\mathrm{Kn}^2)$ [106].

To regularize the G13 system, we recast the moment equations for $\mathit{\Delta}$, R_{ij}, and m_{ijk} in G26 system (3.29)–(3.31) as,

$$\frac{Dm_{ijk}}{Dt} + [\cdots \text{ space derivatives of moments } \cdots] = -\frac{1}{\epsilon}\frac{3}{2}\frac{p}{\mu}m_{ijk}, \tag{4.8a}$$

$$\frac{DR_{ij}}{Dt} + [\cdots \text{ space derivatives of moments } \cdots] = -\frac{1}{\epsilon}\frac{7}{6}\frac{p}{\mu}\left(R_{ij} + \frac{4}{7}\frac{\sigma_{k\langle i}\sigma_{j\rangle k}}{\rho}\right), \tag{4.8b}$$

$$\frac{D\mathit{\Delta}}{Dt} + [\cdots \text{ space derivatives of moments } \cdots] = -\frac{1}{\epsilon}\frac{2}{3}\frac{p}{\mu}\left(\mathit{\Delta} + \frac{\sigma_{ij}\sigma_{ij}}{\rho}\right), \tag{4.8c}$$

and expand the G26 moments as

$$m_{ijk} = m^{(0)}_{ijk} + \epsilon\, m^{(1)}_{ijk} + \cdots, \qquad R_{ij} = R^{(0)}_{ij} + \epsilon\, R^{(1)}_{ij} + \cdots, \qquad \mathit{\Delta} = \mathit{\Delta}^{(0)} + \epsilon\,\mathit{\Delta}^{(1)} + \cdots. \tag{4.9}$$

Balancing the terms of order $\mathcal{O}\left(\epsilon^0\right)$ gives

$$m^{(0)}_{ijk} = R^{(0)}_{ij} + \underline{\frac{4}{7}\frac{\sigma_{k\langle i}\sigma_{j\rangle k}}{\rho}} = \mathit{\Delta}^{(0)} + \underline{\frac{\sigma_{ij}\sigma_{ij}}{\rho}} = 0, \tag{4.10}$$

where the underlined terms are nonlinear production terms [Eq. (3.28)].

The first–order contributions, $\mathcal{O}\left(\epsilon^1\right)$, give regularization of the G13 system [105, 106, 108] with the following closure,

$$\varDelta = \mathcal{W}^2 = M^2 - 15\rho\theta^2 = \mathsf{A}_1 \frac{\sigma_{ij}\sigma_{ij}}{\rho} + \mathsf{A}_2 \frac{\mu}{\rho\theta}\left(\theta\frac{\partial q_k}{\partial x_k} + \frac{5}{2}q_k\frac{\partial\theta}{\partial x_k} - \frac{\theta q_k}{\rho}\frac{\partial\rho}{\partial x_k} + \theta\sigma_{kl}\frac{\partial v_k}{\partial x_l}\right), \tag{4.11}$$

$$R_{ij} = \mathcal{M}^1_{ij} - 7\theta\sigma_{ij} = \mathsf{B}_1 \frac{\sigma_{k\langle i}\sigma_{j\rangle k}}{\rho} + \mathsf{B}_2 \frac{\mu}{\rho\theta}\left(\theta\frac{\partial q_{\langle i}}{\partial x_{j\rangle}} + q_{\langle i}\frac{\partial\theta}{\partial x_{j\rangle}} - \frac{\theta q_{\langle i}}{\rho}\frac{\partial\rho}{\partial x_{j\rangle}} + \frac{10}{7}\theta\sigma_{k\langle i}S_{j\rangle k}\right), \tag{4.12}$$

$$m_{ijk} = \mathcal{M}^0_{ijk} = \mathsf{C}\,\frac{\mu}{\rho\theta}\left(\theta\frac{\partial\sigma_{\langle ij}}{\partial x_{k\rangle}} - \frac{\theta\sigma_{\langle ij}}{\rho}\frac{\partial\rho}{\partial x_{k\rangle}} + \frac{4}{5}q_{\langle i}\frac{\partial v_j}{\partial x_{k\rangle}}\right), \tag{4.13}$$

where for a compact presentation we defined

$$S_{jk} = \frac{\partial v_{\langle j}}{\partial x_{k\rangle}}, \qquad \text{and} \qquad \sigma_{k\langle i}S_{j\rangle k} = \frac{1}{2}\left(\sigma_{k\langle i}\frac{\partial v_k}{\partial x_{j\rangle}} + \sigma_{k\langle i}\frac{\partial v_{j\rangle}}{\partial x_k}\right) - \frac{1}{3}\sigma_{ij}\frac{\partial v_k}{\partial x_k}. \tag{4.14}$$

For Maxwellian molecules the constants in (4.7)–(4.13) are

$$\mathrm{Pr}^{\mathrm{M}} = \frac{2}{3}, \quad \mathsf{A}_1^{\mathrm{M}} = -1, \quad \mathsf{A}_2^{\mathrm{M}} = -12, \quad \mathsf{B}_1^{\mathrm{M}} = -\frac{4}{7}, \quad \mathsf{B}_2^{\mathrm{M}} = -\frac{24}{5}, \quad \mathsf{C}^{\mathrm{M}} = -2, \tag{4.15}$$

while for the Bhatnagar–Gross–Krook (BGK) kinetic model one must use the following coefficients [106]

$$\mathrm{Pr}^{\mathrm{BGK}} = 1, \quad \mathsf{A}_1^{\mathrm{BGK}} = 0, \quad \mathsf{A}_2^{\mathrm{BGK}} = -8, \quad \mathsf{B}_1^{\mathrm{BGK}} = 0, \quad \mathsf{B}_2^{\mathrm{BGK}} = -\frac{28}{5}, \quad \mathsf{C}^{\mathrm{BGK}} = -3. \tag{4.16}$$

As denoted by the above coefficients, the BGK kinetic model fails to predict the correct Prandtl number. The quadratic terms without gradients in (4.11) and (4.12) result from the collision term for Maxwell molecules, which vanish in the BGK model.

Constitutive equations in (4.11)–(4.13) promote the Grad's 13–moment equations to be of super–Burnett order, $\mathcal{O}(\mathrm{Kn}^3)$.

4.3 R13 Equations in Cylindrical Coordinates

In practical applications, due to the system design and/or the type of the process, particular flow geometries might be utilized, see Fig. 4.1. Some examples are bend pipes, nozzles/diffusers, converging–diverging channels, and porous media meanders. Moreover, flows in highly symmetric geometries such as cylindrical or spherical systems is another popular scenario. Flow simulation through these arbitrary geometries is the major challenge in design of fuel cells, microfluidics assemblies, space

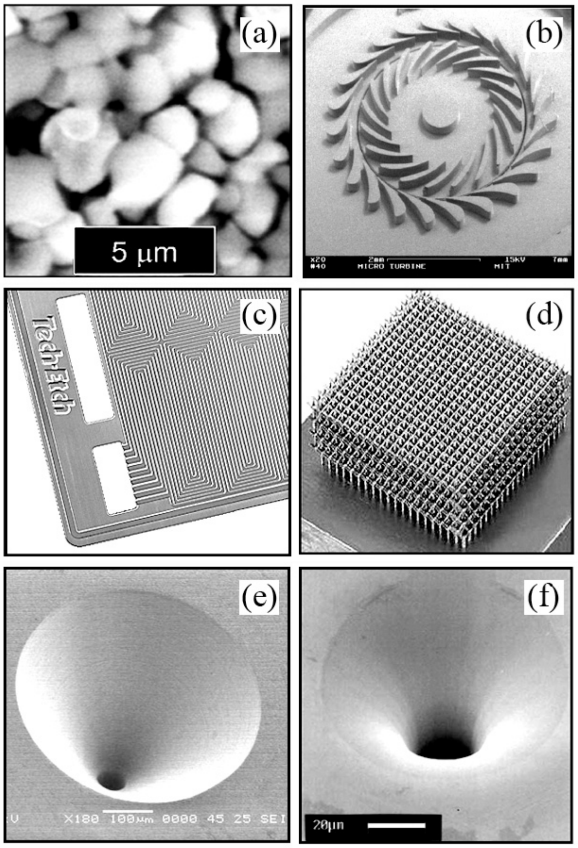

Figure 4.1: Some examples of arbitrary geometries in micro–scale devices. (a) Porous media (Ni+YSXZ) in solid oxide fuel cells. (b) Blades of a micro–turbine. (c) Bipolar plate for micro fuel cells. (d) Micro–structured heat sink for micro–electronic cooling. (e,f) Micro–scale nozzles.

propulsion systems, Knudsen pumps, and super–vacuum pumps. Investigating the behavior of rarefied gas flows through these curved passages is a new subject for the R13 system.

So far all moment equations were presented in rectangular Cartesian coordinates, $x_i = \{x_1, x_2, x_3\}$, which allow to present abstracted form of three–dimensional equations in index notation. Unfortunately, this advantageous feature of index notation is lost when equations are presented in curvilinear coordinate systems.

This section is devoted to transformation of R13 (and NSF) equations into a specific case of curvilinear coordinates, i.e., cylindrical coordinates system. The transformed equations will be used to investigate rotary and axial flows inside channels with circular cross section.

The transformation starts with writing the equations in symbolic notation. Accordingly, the principal conservation laws (4.1) read

$$\frac{D\rho}{Dt} + \rho \operatorname{div} \mathbf{v} = 0, \tag{4.17}$$

$$\rho \frac{D\mathbf{v}}{Dt} + \operatorname{grad} p + \operatorname{div} \boldsymbol{\sigma} = \rho \mathbf{G}, \tag{4.18}$$

$$\frac{3}{2}\rho \frac{D\theta}{Dt} + \operatorname{div} \mathbf{q} = -\mathbf{P} : \operatorname{grad} \mathbf{v}, \tag{4.19}$$

where $\mathbf{v}$, $\mathbf{G}$, and $\mathbf{q}$ are velocity, body–force, and heat–flux vectors, respectively. The stress and pressure tensors are denoted with $\boldsymbol{\sigma}$ and $\mathbf{P}$. Furthermore, moment equations for stress (4.6) and heat flux (4.7) are recast to

$$\frac{D\boldsymbol{\sigma}}{Dt} + \frac{4}{5}\left\langle \operatorname{grad} \mathbf{q} \right\rangle + \boldsymbol{\sigma} \operatorname{div} \mathbf{v} + 2\left\langle \boldsymbol{\sigma} \cdot \operatorname{grad} \mathbf{v} \right\rangle + \operatorname{div} \mathbf{m} = -2\rho\theta \left\langle \operatorname{grad} \mathbf{v} \right\rangle - \frac{\rho\theta}{\mu}\boldsymbol{\sigma}, \tag{4.20}$$

$$\begin{aligned} \frac{D\mathbf{q}}{Dt} + \frac{5}{2}\boldsymbol{\sigma} \cdot \operatorname{grad} \theta - \frac{\theta}{\rho}\boldsymbol{\sigma} \cdot \operatorname{grad} \rho - \frac{1}{\rho}\boldsymbol{\sigma} \cdot \operatorname{div} \boldsymbol{\sigma} + \theta \operatorname{div} \boldsymbol{\sigma} + \frac{7}{5}\left(\mathbf{q} \cdot \operatorname{grad} \mathbf{v} + \mathbf{q} \operatorname{div} \mathbf{v}\right) \\ + \frac{2}{5}\mathbf{q} \cdot \left(\operatorname{grad} \mathbf{v}\right)^{\mathrm{T}} + \frac{1}{6}\operatorname{grad} \mathit{\Delta} + \frac{1}{2}\operatorname{div} \mathbf{R} + \mathbf{m} : \operatorname{grad} \mathbf{v} = -\frac{5}{2}\rho\theta \operatorname{grad} \theta - \mathrm{Pr}\frac{\rho\theta}{\mu}\mathbf{q}. \end{aligned} \tag{4.21}$$

The terms inside angular brackets are symmetric and trace–free part of tensors, that for a rank–2 tensor $\mathbf{T}$, reads

$$\left\langle \mathbf{T} \right\rangle = \frac{1}{2}\left(\mathbf{T} + \mathbf{T}^{\mathrm{T}}\right) - \frac{1}{3}\operatorname{tr} \mathbf{T}\ \mathbf{I},$$

with $\mathbf{I}$ as the unit matrix. The bold face $\mathbf{R}$ and $\mathbf{m}$ correspond to their counterparts R_{ij} and m_{ijk}, which now take the following form

$$\mathit{\Delta} = \mathsf{A}_1 \frac{\boldsymbol{\sigma} : \boldsymbol{\sigma}}{\rho} + \mathsf{A}_2 \frac{\mu}{p}\left(\theta \operatorname{div} \mathbf{q} + \frac{5}{2}\mathbf{q} \cdot \operatorname{grad} \theta - \frac{\theta}{\rho}\mathbf{q} \cdot \operatorname{grad} \rho + \theta\boldsymbol{\sigma} \colon \operatorname{grad} \mathbf{v}\right), \tag{4.22}$$

$$\mathbf{R} = \mathsf{B}_1 \frac{\left\langle \boldsymbol{\sigma} \cdot \boldsymbol{\sigma} \right\rangle}{\rho} + \mathsf{B}_2 \frac{\mu}{p}\left(\theta \left\langle \operatorname{grad} \mathbf{q} \right\rangle + \left\langle \mathbf{q} \operatorname{grad} \theta \right\rangle - \frac{\theta}{\rho}\left\langle \mathbf{q} \operatorname{grad} \rho \right\rangle + \frac{10}{7}\theta \left\langle \sigma \cdot \left\langle \operatorname{grad} \mathbf{v} \right\rangle \right\rangle\right), \tag{4.23}$$

$$\mathbf{m} = \mathsf{C}\,\frac{\mu}{p}\left(\theta \left\langle \operatorname{grad} \boldsymbol{\sigma} \right\rangle - \frac{\theta}{\rho}\left\langle \boldsymbol{\sigma} \operatorname{grad} \rho \right\rangle + \frac{4}{5}\left\langle \mathbf{q} \operatorname{grad} \mathbf{v} \right\rangle\right). \tag{4.24}$$

In order to express the above equations in any coordinate system, it suffices to define the divergence and gradient operators in the desired coordinate system. For cylindrical geometry, gradient and divergence operators on scalers, vectors, and tensors are presented in Appendix A.

Spatial coordinates in cylindrical geometry are known as $\mathbf{x} = \{r, \varphi, z\}$, which correspond to radial, azimuthal, and axial directions, respectively. By using the transformation rules [cf. Appendix A] continuity and momentum balance equations in cylindrical coordinates read as

$$\frac{D\rho}{Dt}+\rho\frac{\partial v_r}{\partial r}+\frac{\rho}{r}\frac{\partial v_\varphi}{\partial \varphi}+\frac{\rho v_r}{r}+\rho\frac{\partial v_z}{\partial z}=0, \tag{4.25}$$

and

$$\rho\frac{Dv_r}{Dt}+\frac{\partial(\rho\theta)}{\partial r}+\frac{\partial\sigma_{rr}}{\partial r}+\frac{1}{r}\frac{\partial\sigma_{r\varphi}}{\partial\varphi}+\frac{\partial\sigma_{rz}}{\partial z}+\frac{\sigma_{rr}-\sigma_{\varphi\varphi}}{r}=\rho G_r, \tag{4.26a}$$

$$\rho\frac{Dv_\varphi}{Dt}+\frac{1}{r}\frac{\partial(\rho\theta)}{\partial\varphi}+\frac{\partial\sigma_{r\varphi}}{\partial r}+\frac{1}{r}\frac{\partial\sigma_{\varphi\varphi}}{\partial\varphi}+\frac{\partial\sigma_{\varphi z}}{\partial z}+\frac{2\sigma_{r\varphi}}{r}=\rho G_\varphi, \tag{4.26b}$$

$$\rho\frac{Dv_z}{Dt}+\frac{\partial(\rho\theta)}{\partial z}+\frac{\partial\sigma_{rz}}{\partial r}+\frac{1}{r}\frac{\partial\sigma_{\varphi z}}{\partial\varphi}+\frac{\partial\sigma_{zz}}{\partial z}+\frac{\sigma_{rz}}{r}=\rho G_z. \tag{4.26c}$$

In the same manner, the balance of internal energy follows as

$$\begin{aligned}\frac{3}{2}\rho\frac{D\theta}{Dt}+\frac{\partial q_r}{\partial r}+\frac{1}{r}\frac{\partial q_\varphi}{\partial\varphi}+\frac{q_r}{r}+\frac{\partial q_z}{\partial z}=&-\rho\theta\left(\frac{\partial v_r}{\partial r}+\frac{1}{r}\frac{\partial v_\varphi}{\partial\varphi}+\frac{v_r}{r}+\frac{\partial v_z}{\partial z}\right)-\frac{\sigma_{r\varphi}}{r}\left(\frac{\partial v_r}{\partial\varphi}-v_\varphi\right)\\&-\sigma_{rr}\frac{\partial v_r}{\partial r}-\sigma_{rz}\frac{\partial v_r}{\partial z}-\sigma_{r\varphi}\frac{\partial v_\varphi}{\partial r}-\frac{\sigma_{\varphi\varphi}}{r}\left(\frac{\partial v_\varphi}{\partial\varphi}+v_r\right)\\&-\sigma_{\varphi z}\frac{\partial v_\varphi}{\partial z}-\sigma_{rz}\frac{\partial v_z}{\partial r}-\frac{\sigma_{\varphi z}}{r}\frac{\partial v_z}{\partial\varphi}-\sigma_{zz}\frac{\partial v_z}{\partial z},\end{aligned} \tag{4.27}$$

where all terms on the right–hand side are related to viscous dissipation.

Equations (4.20)–(4.24) in cylindrical coordinates yield lengthy expressions, and, hence, are presented in Appendix B.

4.4 Linearized Three–dimensional Equations in Dimensionless Form

The merit of linearization is brevity of the equations, that makes the analytical solution accessible. Indeed, coupling between variables are discarded through the linearized equations; for instance, viscous heating effects which link the velocity and temperature fields are not included in the linearized equations.

Knudsen layers which are interesting rarefaction effects in our considered problems [cf. Part. II], can be computed from the linearized equations. In slow rarefied flows, e.g., microflows, Knudsen layers are dominant rarefaction effects. Inclusion of nonlinear terms in the equations leads to more accuracy in prediction of Knudsen layers and bulk effects, which of course demands numerical solution. It is shown in Chap. 11 that some nonlinear effects can be described in analytical solutions [114, 115].

The reference equilibrium state is defined by $\{\rho_0, \theta_0, v_i^0\}$, which is used for non–dimensionalization and linearization. Dimensionless density and temperature are defined as their deviations from the reference equilibrium state,

$$\tilde{\rho} = \frac{\rho - \rho_0}{\rho_0} = \frac{\rho}{\rho_0} - 1, \qquad \tilde{\theta} = \frac{\theta - \theta_0}{\theta_0} = \frac{\theta}{\theta_0} - 1. \tag{4.28}$$

The tilde signs indicate dimensionless quantities. The isothermal speed of sound, $\sqrt{\theta_0}$, is employed as the velocity scale. The dimensionless spatial position, time, and external force are defined as

$$\tilde{x}_i = \frac{x_i}{\mathcal{L}}, \qquad \tilde{t} = \frac{t}{t_0} = \frac{t}{\mathcal{L}/\sqrt{\theta_0}}, \qquad \tilde{G}_i = \frac{\mathcal{L}}{\theta_0} G_i, \tag{4.29}$$

where $\mathcal{L}$ is an arbitrary macroscopic length scale of the considered flow, e.g. the radius of a circular channel.

The rest of the variables in proper dimensionless form are

$$\tilde{v}_i = \frac{v_i}{\sqrt{\theta_0}}, \quad \tilde{\sigma}_{ij} = \frac{\sigma_{ij}}{\rho_0 \theta_0}, \quad \tilde{q}_i = \frac{q_i}{\rho_0 \sqrt{\theta_0}^3}, \quad \tilde{\Delta} = \frac{\Delta}{\rho_0 \theta_0^2}, \quad \tilde{R}_{ij} = \frac{R_{ij}}{\rho_0 \theta_0^2}, \quad \tilde{m}_{ijk} = \frac{m_{ijk}}{\rho_0 \sqrt{\theta_0}^3}. \tag{4.30}$$

Furthermore, $\tilde{\mu} = \mu/\mu_0 - 1$ is the dimensionless viscosity deviation with $\mu_0 = \mu(\theta_0)$. In the reference equilibrium state all nonequilibrium moments in (4.30) vanish.

In the standard linearization, only terms that are linear in deviations from the ground equilibrium state are included within the equations. For instance, by using Eq. (4.28) the equation of state for ideal gases reads

$$p = \rho\theta = \rho_0(1 + \tilde{\rho})\theta_0(1 + \tilde{\theta}) = \rho_0\theta_0(1 + \tilde{\rho} + \tilde{\theta} + \tilde{\rho}\tilde{\theta}), \tag{4.31}$$

in which, removing $\tilde{\rho}\tilde{\theta}$ leads to the linearized equation of state. Accordingly, the pressure in dimensionless form follows $\tilde{p} = p/p_0 - 1 = \tilde{\rho} + \tilde{\theta}$, where $p_0 = \rho_0\theta_0$.

4.4.1 Dimensionless and Linearized Equations in Planar Geometry

NSF and R13 equations in dimensionless form are obtained by introducing the dimensionless quantities from Eqs. (4.28)–(4.30) into the moment equations (4.1)–(4.13). After omitting nonlinear terms, the linearized balance laws (4.1) read

$$\frac{\partial \tilde{\rho}}{\partial \tilde{t}} + \frac{\partial \tilde{v}_i}{\partial \tilde{x}_i} = 0, \tag{4.32}$$

$$\frac{\partial \tilde{v}_i}{\partial \tilde{t}} + \frac{\partial \tilde{\rho}}{\partial \tilde{x}_i} + \frac{\partial \tilde{\theta}}{\partial \tilde{x}_i} + \frac{\partial \tilde{\sigma}_{ij}}{\partial \tilde{x}_j} = \tilde{G}_i, \tag{4.33}$$

$$\frac{3}{2}\frac{\partial \tilde{\theta}}{\partial \tilde{t}} + \frac{\partial \tilde{q}_i}{\partial \tilde{x}_i} = 0, \tag{4.34}$$

The linearized moment equations for stress [Eq. (4.6)] and heat flux [Eq. (4.7)] are

$$\frac{\partial \tilde{\sigma}_{ij}}{\partial \tilde{t}} + \frac{4}{5}\frac{\partial \tilde{q}_{\langle i}}{\partial \tilde{x}_{j\rangle}} + \frac{\partial \tilde{m}_{ijk}}{\partial \tilde{x}_k} = -2\frac{\partial \tilde{v}_{\langle i}}{\partial \tilde{x}_{j\rangle}} - \frac{1}{\mathrm{Kn}}\tilde{\sigma}_{ij}, \tag{4.35}$$

$$\frac{\partial \tilde{q}_i}{\partial \tilde{t}} + \frac{\partial \tilde{\sigma}_{ik}}{\partial \tilde{x}_k} + \frac{1}{6}\frac{\partial \tilde{\Delta}}{\partial \tilde{x}_i} + \frac{1}{2}\frac{\partial \tilde{R}_{ik}}{\partial \tilde{x}_k} = -\frac{5}{2}\frac{\partial \tilde{\theta}}{\partial \tilde{x}_i} - \frac{\mathrm{Pr}}{\mathrm{Kn}}\tilde{q}_i, \tag{4.36}$$

with the following linear regularization

$$\tilde{\Delta} = \mathsf{A}_2\,\mathrm{Kn}\frac{\partial \tilde{q}_k}{\partial \tilde{x}_k}, \qquad \tilde{R}_{ij} = \mathsf{B}_2\,\mathrm{Kn}\frac{\partial \tilde{q}_{\langle i}}{\partial \tilde{x}_{j\rangle}}, \qquad \tilde{m}_{ijk} = \mathsf{C}\,\mathrm{Kn}\frac{\partial \tilde{\sigma}_{\langle ij}}{\partial \tilde{x}_{k\rangle}}. \tag{4.37}$$

Here, Kn is the Knudsen number [cf. Eq. (2.1)] at the reference state, defined as the ratio of the mean free path at the reference equilibrium state $\lambda_0 = \mu_0\sqrt{\theta_0}/p_0$ to a characteristic length $\mathcal{L}$,

$$\mathrm{Kn} = \frac{\lambda_0}{\mathcal{L}} = \frac{\mu_0}{\rho_0\sqrt{\theta_0}\mathcal{L}}. \tag{4.38}$$

In dimensionless form, the linear Navier–Stokes and Fourier laws for the conservation laws are

$$\tilde{\sigma}_{ij}^{\mathrm{NSF}} = -2\,\mathrm{Kn}\frac{\partial \tilde{v}_{\langle i}}{\partial \tilde{x}_{j\rangle}}, \qquad \tilde{q}_i^{\mathrm{NSF}} = -\frac{5}{2}\frac{\mathrm{Kn}}{\mathrm{Pr}}\frac{\partial \tilde{\theta}}{\partial \tilde{x}_i}. \tag{4.39}$$

4.4.2 Dimensionless and Linearized Equations in Cylindrical Geometry

The continuity equation in cylindrical coordinates [Eq. (4.25)] takes the following linear form,

$$\frac{\partial \tilde{\rho}}{\partial \tilde{t}} + \frac{\partial \tilde{v}_r}{\partial \tilde{r}} + \frac{1}{\tilde{r}}\frac{\partial \tilde{v}_\varphi}{\partial \varphi} + \frac{\tilde{v}_r}{\tilde{r}} + \frac{\partial \tilde{v}_z}{\partial \tilde{z}} = 0, \tag{4.40}$$

while the linearized momentum equations are

$$\frac{\partial \tilde{v}_r}{\partial \tilde{t}} + \frac{\partial \tilde{\rho}}{\partial \tilde{r}} + \frac{\partial \tilde{\theta}}{\partial \tilde{r}} + \frac{\partial \tilde{\sigma}_{rr}}{\partial \tilde{r}} + \frac{1}{\tilde{r}}\frac{\partial \tilde{\sigma}_{r\varphi}}{\partial \tilde{\varphi}} + \frac{\partial \tilde{\sigma}_{rz}}{\partial \tilde{z}} + \frac{\tilde{\sigma}_{rr} - \tilde{\sigma}_{\varphi\varphi}}{\tilde{r}} = \tilde{G}_r, \tag{4.41}$$

$$\frac{\partial \tilde{v}_\varphi}{\partial \tilde{t}} + \frac{1}{\tilde{r}}\frac{\partial \tilde{\rho}}{\partial \tilde{\varphi}} + \frac{1}{\tilde{r}}\frac{\partial \tilde{\theta}}{\partial \tilde{\varphi}} + \frac{\partial \tilde{\sigma}_{r\varphi}}{\partial \tilde{r}} + \frac{1}{\tilde{r}}\frac{\partial \tilde{\sigma}_{\varphi\varphi}}{\partial \tilde{\varphi}} + \frac{\partial \tilde{\sigma}_{\varphi z}}{\partial \tilde{z}} + \frac{2\tilde{\sigma}_{r\varphi}}{\tilde{r}} = \tilde{G}_\varphi, \tag{4.42}$$

$$\frac{\partial \tilde{v}_z}{\partial \tilde{t}} + \frac{\partial \tilde{\rho}}{\partial \tilde{z}} + \frac{\partial \tilde{\theta}}{\partial \tilde{z}} + \frac{\partial \tilde{\sigma}_{rz}}{\partial \tilde{r}} + \frac{1}{\tilde{r}}\frac{\partial \tilde{\sigma}_{\varphi z}}{\partial \tilde{\varphi}} + \frac{\partial \tilde{\sigma}_{zz}}{\partial \tilde{z}} + \frac{\tilde{\sigma}_{rz}}{\tilde{r}} = \tilde{G}_z. \tag{4.43}$$

In the energy balance [Eq. (4.27)] all viscous heating terms vanish due to linearization, thus, in linear form it reads

$$\frac{3}{2}\frac{\partial \tilde{\theta}}{\partial \tilde{t}} + \frac{\partial \tilde{q}_r}{\partial \tilde{r}} + \frac{1}{\tilde{r}}\frac{\partial \tilde{q}_\varphi}{\partial \tilde{\varphi}} + \frac{\tilde{q}_r}{\tilde{r}} + \frac{\partial \tilde{q}_z}{\partial \tilde{z}} = -\left(\frac{\partial \tilde{v}_r}{\partial \tilde{r}} + \frac{1}{\tilde{r}}\frac{\partial \tilde{v}_\varphi}{\partial \tilde{\varphi}} + \frac{\tilde{v}_r}{\tilde{r}} + \frac{\partial \tilde{v}_z}{\partial \tilde{z}}\right). \tag{4.44}$$

Additionally, the linearized moment equations for the stress tensor, which in their fully nonlinear form are presented in Eqs. (B.2)–(B.7) in Appendix B, take the following form,

$$\begin{aligned}\frac{\partial \tilde{\sigma}_{rr}}{\partial \tilde{t}} + \frac{8}{15}\frac{\partial \tilde{q}_r}{\partial \tilde{r}} - \frac{4}{15}\frac{\tilde{q}_r}{\tilde{r}} - \frac{4}{15}\frac{1}{\tilde{r}}\frac{\partial \tilde{q}_\varphi}{\partial \tilde{\varphi}} - \frac{4}{15}\frac{\partial \tilde{q}_z}{\partial \tilde{z}} + \frac{\partial \tilde{m}_{rrr}}{\partial \tilde{r}} + \frac{1}{\tilde{r}}\frac{\partial \tilde{m}_{rr\varphi}}{\partial \tilde{\varphi}}& \\ + \frac{\partial \tilde{m}_{rrz}}{\partial \tilde{z}} + \frac{\tilde{m}_{rrr} - 2\tilde{m}_{r\varphi\varphi}}{\tilde{r}} &= -\frac{4}{3}\frac{\partial \tilde{v}_r}{\partial \tilde{r}} + \frac{2}{3}\frac{1}{\tilde{r}}\frac{\partial \tilde{v}_\varphi}{\partial \tilde{\varphi}} + \frac{2}{3}\frac{\tilde{v}_r}{\tilde{r}} + \frac{2}{3}\frac{\partial \tilde{v}_z}{\partial \tilde{z}} - \frac{1}{\mathrm{Kn}}\tilde{\sigma}_{rr},\end{aligned} \tag{4.45}$$

$$\begin{aligned}\frac{\partial \tilde{\sigma}_{r\varphi}}{\partial \tilde{t}} + \frac{2}{5}\frac{1}{\tilde{r}}\frac{\partial \tilde{q}_r}{\partial \tilde{\varphi}} - \frac{2}{5}\frac{\tilde{q}_\varphi}{\tilde{r}} + \frac{2}{5}\frac{\partial \tilde{q}_\varphi}{\partial \tilde{r}} + \frac{\partial \tilde{m}_{rr\varphi}}{\partial \tilde{r}} + \frac{1}{\tilde{r}}\frac{\partial \tilde{m}_{r\varphi\varphi}}{\partial \tilde{\varphi}} + \frac{\partial \tilde{m}_{r\varphi z}}{\partial \tilde{z}}& \\ + \frac{2\tilde{m}_{rr\varphi} - \tilde{m}_{\varphi\varphi\varphi}}{\tilde{r}} &= -\frac{1}{\tilde{r}}\frac{\partial \tilde{v}_r}{\partial \tilde{\varphi}} + \frac{\tilde{v}_\varphi}{\tilde{r}} - \frac{\partial \tilde{v}_\varphi}{\partial \tilde{r}} - \frac{1}{\mathrm{Kn}}\tilde{\sigma}_{r\varphi},\end{aligned} \tag{4.46}$$

$$\frac{\partial \tilde{\sigma}_{rz}}{\partial \tilde{t}} + \frac{4}{5}\frac{\partial \tilde{q}_r}{\partial \tilde{z}} + \frac{\partial \tilde{m}_{rrz}}{\partial \tilde{r}} + \frac{1}{\tilde{r}}\frac{\partial \tilde{m}_{r\varphi z}}{\partial \tilde{\varphi}} + \frac{\partial \tilde{m}_{rzz}}{\partial \tilde{z}} + \frac{\tilde{m}_{rrz} - \tilde{m}_{\varphi\varphi z}}{\tilde{r}} = -2\frac{\partial \tilde{v}_r}{\partial \tilde{z}} - \frac{1}{\mathrm{Kn}}\tilde{\sigma}_{rz}, \tag{4.47}$$

$$\begin{aligned}\frac{\partial \tilde{\sigma}_{\varphi\varphi}}{\partial \tilde{t}} + \frac{4}{5}\frac{\tilde{q}_r}{\tilde{r}} - \frac{4}{15}\frac{\partial \tilde{q}_r}{\partial \tilde{r}} - \frac{4}{15}\frac{\tilde{q}_r}{\tilde{r}} + \frac{4}{5}\frac{1}{\tilde{r}}\frac{\partial \tilde{q}_\varphi}{\partial \tilde{\varphi}} - \frac{4}{15}\frac{1}{\tilde{r}}\frac{\partial \tilde{q}_\varphi}{\partial \tilde{\varphi}} - \frac{4}{15}\frac{\partial \tilde{q}_z}{\partial \tilde{z}} + \frac{\partial \tilde{m}_{r\varphi\varphi}}{\partial \tilde{r}} + \frac{1}{\tilde{r}}\frac{\partial \tilde{m}_{\varphi\varphi\varphi}}{\partial \tilde{\varphi}}& \\ + \frac{\partial \tilde{m}_{\varphi\varphi z}}{\partial \tilde{z}} + 3\frac{\tilde{m}_{r\varphi\varphi}}{\tilde{r}} &= -\frac{4}{3}\frac{1}{\tilde{r}}\frac{\partial \tilde{v}_\varphi}{\partial \tilde{\varphi}} - \frac{4}{3}\frac{\tilde{v}_r}{\tilde{r}} + \frac{2}{3}\frac{\partial \tilde{v}_r}{\partial \tilde{r}} + \frac{2}{3}\frac{\partial \tilde{v}_z}{\partial \tilde{z}} - \frac{1}{\mathrm{Kn}}\tilde{\sigma}_{\varphi\varphi},\end{aligned} \tag{4.48}$$

$$\frac{\partial \tilde{\sigma}_{\varphi z}}{\partial \tilde{t}} + \frac{2}{5}\frac{1}{\tilde{r}}\frac{\partial \tilde{q}_z}{\partial \tilde{\varphi}} + \frac{2}{5}\frac{\partial \tilde{q}_\varphi}{\partial \tilde{z}} + \frac{\partial \tilde{m}_{r\varphi z}}{\partial \tilde{r}} + \frac{1}{\tilde{r}}\frac{\partial \tilde{m}_{\varphi\varphi z}}{\partial \tilde{\varphi}} + \frac{\partial \tilde{m}_{\varphi zz}}{\partial \tilde{z}} + 2\frac{\tilde{m}_{r\varphi z}}{\tilde{r}} = -\frac{\partial \tilde{v}_\varphi}{\partial \tilde{z}} - \frac{1}{\tilde{r}}\frac{\partial \tilde{v}_z}{\partial \tilde{\varphi}} - \frac{1}{\mathrm{Kn}}\tilde{\sigma}_{\varphi z}, \tag{4.49}$$

$$\frac{\partial \tilde{\sigma}_{zz}}{\partial \tilde{t}} - \frac{4}{15}\frac{\partial \tilde{q}_r}{\partial \tilde{r}} - \frac{4}{15}\frac{\tilde{q}_r}{\tilde{r}} - \frac{4}{15}\frac{1}{\tilde{r}}\frac{\partial \tilde{q}_\varphi}{\partial \tilde{\varphi}} + \frac{8}{15}\frac{\partial \tilde{q}_z}{\partial \tilde{z}} + \frac{\partial \tilde{m}_{rzz}}{\partial \tilde{r}} + \frac{1}{r}\frac{\partial \tilde{m}_{\varphi zz}}{\partial \tilde{\varphi}}$$
$$+ \frac{\partial \tilde{m}_{zzz}}{\partial \tilde{z}} + \frac{\tilde{m}_{rzz}}{\tilde{r}} = -\frac{4}{3}\frac{\partial \tilde{v}_z}{\partial \tilde{z}} + \frac{2}{3}\frac{\partial \tilde{v}_r}{\partial \tilde{r}} + \frac{2}{3}\frac{1}{\tilde{r}}\frac{\partial \tilde{v}_\varphi}{\partial \tilde{\varphi}} + \frac{2}{3}\frac{\tilde{v}_r}{\tilde{r}} - \frac{1}{\mathrm{Kn}}\tilde{\sigma}_{zz}. \quad (4.50)$$

The terms on the right–hand side of Eqs. (4.45)–(4.50) are of the order of classical hydrodynamics $\mathcal{O}(\mathrm{Kn})$, which relate stress components to velocity gradients, i.e., the Navier–Stokes law.

The full moment equations for the components of heat–flux vector in cylindrical coordinates are presented in Eqs. (B.9)–(B.11) in Appendix B. These equations in linear form are

$$\frac{\partial \tilde{q}_r}{\partial \tilde{t}} + \frac{\partial \tilde{\sigma}_{rr}}{\partial \tilde{r}} + \frac{1}{\tilde{r}}\frac{\partial \tilde{\sigma}_{r\varphi}}{\partial \tilde{\varphi}} + \frac{\partial \tilde{\sigma}_{rz}}{\partial \tilde{z}} + \frac{\tilde{\sigma}_{rr} - \tilde{\sigma}_{\varphi\varphi}}{\tilde{r}} + \frac{1}{6}\frac{\partial \tilde{\mathit{\Delta}}}{\partial \tilde{r}} + \frac{1}{2}\frac{\partial \tilde{R}_{rr}}{\partial \tilde{r}}$$
$$+ \frac{1}{2}\frac{1}{\tilde{r}}\frac{\partial \tilde{R}_{r\varphi}}{\partial \tilde{\varphi}} + \frac{1}{2}\frac{\partial \tilde{R}_{rz}}{\partial \tilde{z}} + \frac{1}{2}\frac{\tilde{R}_{rr} - \tilde{R}_{\varphi\varphi}}{\tilde{r}} = -\frac{5}{2}\frac{\partial \tilde{\theta}}{\partial \tilde{r}} - \frac{\mathrm{Pr}}{\mathrm{Kn}}\tilde{q}_r, \quad (4.51)$$

$$\frac{\partial \tilde{q}_\varphi}{\partial \tilde{t}} + \frac{\partial \tilde{\sigma}_{r\varphi}}{\partial \tilde{r}} + \frac{1}{\tilde{r}}\frac{\partial \tilde{\sigma}_{\varphi\varphi}}{\partial \tilde{\varphi}} + \frac{\partial \tilde{\sigma}_{\varphi z}}{\partial \tilde{z}} + 2\frac{\tilde{\sigma}_{r\varphi}}{\tilde{r}} + \frac{1}{6}\frac{1}{\tilde{r}}\frac{\partial \tilde{\mathit{\Delta}}}{\partial \tilde{\varphi}}$$
$$+ \frac{1}{2}\frac{\partial \tilde{R}_{r\varphi}}{\partial \tilde{r}} + \frac{1}{2}\frac{1}{\tilde{r}}\frac{\partial \tilde{R}_{\varphi\varphi}}{\partial \tilde{\varphi}} + \frac{1}{2}\frac{\partial \tilde{R}_{\varphi z}}{\partial \tilde{z}} + \frac{\tilde{R}_{r\varphi}}{\tilde{r}} = -\frac{5}{2}\frac{1}{\tilde{r}}\frac{\partial \tilde{\theta}}{\partial \tilde{\varphi}} - \frac{\mathrm{Pr}}{\mathrm{Kn}}\tilde{q}_\varphi, \quad (4.52)$$

$$\frac{\partial \tilde{q}_z}{\partial \tilde{t}} + \frac{\partial \tilde{\sigma}_{rz}}{\partial \tilde{r}} + \frac{1}{\tilde{r}}\frac{\partial \tilde{\sigma}_{\varphi z}}{\partial \tilde{\varphi}} + \frac{\partial \tilde{\sigma}_{zz}}{\partial \tilde{z}} + \frac{\tilde{\sigma}_{rz}}{\tilde{r}} + \frac{1}{6}\frac{\partial \tilde{\mathit{\Delta}}}{\partial \tilde{z}} + \frac{1}{2}\frac{\partial \tilde{R}_{rz}}{\partial \tilde{r}}$$
$$+ \frac{1}{2}\frac{1}{\tilde{r}}\frac{\partial \tilde{R}_{\varphi z}}{\partial \tilde{\varphi}} + \frac{1}{2}\frac{\partial \tilde{R}_{zz}}{\partial \tilde{z}} + \frac{1}{2}\frac{\tilde{R}_{rz}}{\tilde{r}} = -\frac{5}{2}\frac{\partial \tilde{\theta}}{\partial \tilde{z}} - \frac{\mathrm{Pr}}{\mathrm{Kn}}\tilde{q}_z. \quad (4.53)$$

The terms on the right–hand side of Eqs. (4.51)–(4.53) are of the order of classical hydrodynamics $\mathcal{O}(\mathrm{Kn})$, which relate the heat–flux components to temperature gradients, i.e., the Fourier law.

Regularized closure in cylindrical geometry in fully nonlinear form are given in Eqs. (B.13)–(B.32), which in linear form reduce to

$$\tilde{\mathit{\Delta}} = \mathsf{A}_2\,\mathrm{Kn}\left(\frac{\partial \tilde{q}_r}{\partial \tilde{r}} + \frac{\tilde{q}_r}{\tilde{r}} + \frac{1}{\tilde{r}}\frac{\partial \tilde{q}_\varphi}{\partial \tilde{\varphi}} + \frac{\partial \tilde{q}_z}{\partial \tilde{z}}\right), \quad (4.54)$$

$$\tilde{R}_{rr} = \frac{\mathsf{B}_2}{3}\,\mathrm{Kn}\left(2\frac{\partial \tilde{q}_r}{\partial \tilde{r}} - \frac{\tilde{q}_r}{\tilde{r}} - \frac{1}{\tilde{r}}\frac{\partial \tilde{q}_\varphi}{\partial \tilde{\varphi}} - \frac{\partial \tilde{q}_z}{\partial \tilde{z}}\right), \tag{4.55}$$

$$\tilde{R}_{r\varphi} = \frac{\mathsf{B}_2}{2}\,\mathrm{Kn}\left(\frac{1}{\tilde{r}}\frac{\partial \tilde{q}_r}{\partial \tilde{\varphi}} - \frac{\tilde{q}_\varphi}{\tilde{r}} + \frac{\partial \tilde{q}_\varphi}{\partial \tilde{r}}\right), \tag{4.56}$$

$$\tilde{R}_{rz} = \mathsf{B}_2\,\mathrm{Kn}\frac{\partial \tilde{q}_r}{\partial \tilde{z}}, \tag{4.57}$$

$$\tilde{R}_{\varphi\varphi} = \frac{\mathsf{B}_2}{3}\,\mathrm{Kn}\left(2\frac{1}{\tilde{r}}\frac{\partial \tilde{q}_\varphi}{\partial \tilde{\varphi}} + 2\frac{\tilde{q}_r}{\tilde{r}} - \frac{\partial \tilde{q}_r}{\partial \tilde{r}} - \frac{\partial \tilde{q}_z}{\partial \tilde{z}}\right), \tag{4.58}$$

$$\tilde{R}_{\varphi z} = \frac{\mathsf{B}_2}{2}\,\mathrm{Kn}\left(\frac{\partial \tilde{q}_\varphi}{\partial \tilde{z}} + \frac{1}{\tilde{r}}\frac{\partial \tilde{q}_z}{\partial \tilde{\varphi}}\right), \tag{4.59}$$

$$\tilde{R}_{zz} = \frac{\mathsf{B}_2}{3}\,\mathrm{Kn}\left(2\frac{\partial \tilde{q}_z}{\partial \tilde{z}} - \frac{\partial \tilde{q}_r}{\partial \tilde{r}} - \frac{1}{\tilde{r}}\frac{\partial \tilde{q}_\varphi}{\partial \tilde{\varphi}} - \frac{\tilde{q}_r}{\tilde{r}}\right), \tag{4.60}$$

$$\tilde{m}_{rrr} = \mathsf{C}\,\mathrm{Kn}\left[\frac{3}{5}\frac{\partial \tilde{\sigma}_{rr}}{\partial \tilde{r}} - \frac{2}{5}\left(\frac{1}{\tilde{r}}\frac{\partial \tilde{\sigma}_{r\varphi}}{\partial \tilde{\varphi}} + \frac{\tilde{\sigma}_{rr} - \tilde{\sigma}_{\varphi\varphi}}{\tilde{r}} + \frac{\partial \tilde{\sigma}_{rz}}{\partial \tilde{z}}\right)\right], \tag{4.61}$$

$$\tilde{m}_{rr\varphi} = \frac{\mathsf{C}}{3}\,\mathrm{Kn}\left[\frac{8}{5}\frac{\partial \tilde{\sigma}_{r\varphi}}{\partial \tilde{r}} + \frac{1}{\tilde{r}}\frac{\partial \tilde{\sigma}_{rr}}{\partial \tilde{\varphi}} - \frac{14}{5}\frac{\tilde{\sigma}_{r\varphi}}{\tilde{r}} - \frac{2}{5}\left(\frac{1}{\tilde{r}}\frac{\partial \tilde{\sigma}_{\varphi\varphi}}{\partial \tilde{\varphi}} + \frac{\partial \tilde{\sigma}_{\varphi z}}{\partial \tilde{z}}\right)\right], \tag{4.62}$$

$$\tilde{m}_{rrz} = \frac{\mathsf{C}}{3}\,\mathrm{Kn}\left[\frac{8}{5}\frac{\partial \tilde{\sigma}_{rz}}{\partial \tilde{r}} + \frac{\partial \tilde{\sigma}_{rr}}{\partial \tilde{z}} - \frac{2}{5}\left(\frac{1}{\tilde{r}}\frac{\partial \tilde{\sigma}_{\varphi z}}{\partial \tilde{\varphi}} + \frac{\tilde{\sigma}_{rz}}{\tilde{r}} + \frac{\partial \tilde{\sigma}_{zz}}{\partial \tilde{z}}\right)\right], \tag{4.63}$$

$$\tilde{m}_{r\varphi\varphi} = \frac{\mathsf{C}}{3}\,\mathrm{Kn}\left[\frac{\partial \tilde{\sigma}_{\varphi\varphi}}{\partial \tilde{r}} + \frac{8}{5}\left(\frac{1}{\tilde{r}}\frac{\partial \tilde{\sigma}_{r\varphi}}{\partial \tilde{\varphi}} + \frac{\tilde{\sigma}_{rr} - \tilde{\sigma}_{\varphi\varphi}}{\tilde{r}}\right) - \frac{2}{5}\left(\frac{\partial \tilde{\sigma}_{rr}}{\partial \tilde{r}} + \frac{\partial \tilde{\sigma}_{rz}}{\partial \tilde{z}}\right)\right], \tag{4.64}$$

$$\tilde{m}_{r\varphi z} = \frac{\mathsf{C}}{3}\,\mathrm{Kn}\left[\frac{\partial \tilde{\sigma}_{\varphi z}}{\partial \tilde{r}} + \frac{1}{\tilde{r}}\frac{\partial \tilde{\sigma}_{rz}}{\partial \tilde{\varphi}} - \frac{\tilde{\sigma}_{\varphi z}}{\tilde{r}} + \frac{\partial \tilde{\sigma}_{r\varphi}}{\partial \tilde{z}}\right], \tag{4.65}$$

$$\tilde{m}_{rzz} = \frac{\mathsf{C}}{3}\,\mathrm{Kn}\left[\frac{\partial \tilde{\sigma}_{zz}}{\partial \tilde{r}} + \frac{8}{5}\frac{\partial \tilde{\sigma}_{rz}}{\partial \tilde{z}} - \frac{2}{5}\left(\frac{\partial \tilde{\sigma}_{rr}}{\partial \tilde{r}} + \frac{1}{\tilde{r}}\frac{\partial \tilde{\sigma}_{r\varphi}}{\partial \tilde{\varphi}} + \frac{\tilde{\sigma}_{rr} - \tilde{\sigma}_{\varphi\varphi}}{\tilde{r}}\right)\right], \tag{4.66}$$

$$\tilde{m}_{\varphi\varphi\varphi} = \frac{\mathsf{C}}{5}\,\mathrm{Kn}\left[3\frac{1}{\tilde{r}}\frac{\partial \tilde{\sigma}_{\varphi\varphi}}{\partial \tilde{\varphi}} + 6\frac{\tilde{\sigma}_{r\varphi}}{\tilde{r}} - 2\left(\frac{\partial \tilde{\sigma}_{r\varphi}}{\partial \tilde{r}} + \frac{\partial \tilde{\sigma}_{\varphi z}}{\partial \tilde{z}}\right)\right], \tag{4.67}$$

$$\tilde{m}_{\varphi\varphi z} = \frac{\mathsf{C}}{3}\,\mathrm{Kn}\left[\frac{8}{5}\frac{1}{\tilde{r}}\frac{\partial \tilde{\sigma}_{\varphi z}}{\partial \tilde{\varphi}} + 2\frac{\tilde{\sigma}_{rz}}{\tilde{r}} + \frac{\partial \tilde{\sigma}_{\varphi\varphi}}{\partial \tilde{z}} - \frac{2}{5}\left(\frac{\partial \tilde{\sigma}_{rz}}{\partial \tilde{r}} + \frac{\tilde{\sigma}_{rz}}{\tilde{r}} + \frac{\partial \tilde{\sigma}_{zz}}{\partial \tilde{z}}\right)\right], \tag{4.68}$$

$$\tilde{m}_{\varphi zz} = \frac{\mathsf{C}}{3}\,\mathrm{Kn}\left[\frac{1}{\tilde{r}}\frac{\partial \tilde{\sigma}_{zz}}{\partial \tilde{\varphi}} + 2\left(\frac{1}{\tilde{r}}\frac{\partial \tilde{\sigma}_{\varphi z}}{\partial \tilde{\varphi}} + \frac{\tilde{\sigma}_{rz}}{\tilde{r}}\right) - \frac{2}{5}\left(\frac{\partial \tilde{\sigma}_{r\varphi}}{\partial \tilde{r}} + \frac{1}{\tilde{r}}\frac{\partial \tilde{\sigma}_{\varphi\varphi}}{\partial \tilde{\varphi}} + 2\frac{\tilde{\sigma}_{r\varphi}}{\tilde{r}} + \frac{\partial \tilde{\sigma}_{\varphi z}}{\partial \tilde{z}}\right)\right], \tag{4.69}$$

$$\tilde{m}_{zzz} = \frac{\mathsf{C}}{5}\,\mathrm{Kn}\left[3\frac{\partial \tilde{\sigma}_{zz}}{\partial \tilde{z}} - 2\left(\frac{\partial \tilde{\sigma}_{rz}}{\partial \tilde{r}} + \frac{1}{\tilde{r}}\frac{\partial \tilde{\sigma}_{\varphi z}}{\partial \tilde{\varphi}} + \frac{\tilde{\sigma}_{rz}}{\tilde{r}}\right)\right]. \tag{4.70}$$

It is important to emphasize on the terms which are multiplied with the curvature $\not{c} = r^{-1}$. These terms introduce the curvature effects into the equations. In the limit of $r \to \infty$ Eqs. (4.40)–(4.70) reduce to the linear R13 equations in slab geometry, that is Eqs. (4.32)–(4.37).

Chapter 5

Kinetic Boundary Conditions for Moments

The low–order moments, i.e., density, velocity, temperature, stress, and heat flux, which construct the classical Navier–Stokes–Fourier system, and their corresponding boundary conditions, all have meaningful physical interpretations, and can be measured on the boundary. However, there are not such obvious physical interpretations for higher–order moments which appear in larger moment systems. For large systems of moment equations, due to their size and the intercoupling between the equations, prescription of boundary conditions is a challenging task. Therefore, great care must be taken in deriving and implementing boundary conditions, as ill posed boundary conditions lead to unphysical results.

For all transport equations, boundary conditions are necessary to find a unique solution. All extended systems that go beyond the Navier–Stokes–Fourier require extended boundary conditions, compared to the NSF boundary conditions. For Burnett–type equations boundary conditions must be given for higher–order gradients of density, velocity, and temperature at the boundary. For Grad–type moment equations, on the other hand, boundary conditions for moments are required.

For a long time, the nonavailability of proper boundary conditions for high–order moments was the major obstacle in rendering the R13 equations (and other sets of extended moment systems) into an engineering tool. The first attempt to understand the structure of boundary conditions for R13 moments appeared in [109], where by employment of the principles of classical nonequilibrium thermodynamics, it was shown that the linearized R13 equations and their boundary conditions lead to positive entropy production, i.e., the H theorem is fulfilled both for the gas and the gas–wall interface. Only recently, building up on Grad's discussion of the problem [32, 33] boundary conditions for the R13 equations were derived from the boundary conditions of the Boltzmann equation by Gu and Emerson [35] and by Torrilhon and Struchtrup [121]. The results in [35] show spurious boundary layers, due to prescription of more boundary conditions than mathematically required. Torrilhon and Struchtrup [121] checked both physical and mathematical consistencies of their boundary conditions on Couette and Poiseuille flows within microchannels. Their numerical solutions show excellent agreement with the DSMC simulations.

In this section, the strategy to derive boundary conditions for the moments in R13 system is presented, the technique can be extended to larger systems of moments. In Ref. [36] a similar strategy is employed to obtain boundary conditions for the regularized 26–moment equations.

5.1 Maxwell's Diffusive–reflective Model for Kinetic Boundary Conditions

Consider a wall with temperature θ_W and velocity v_k^W, which is exposed to a rarefied gas flow, in which velocity of the gas close to the wall is v_k, and its temperature is θ, see Fig. 5.1a. From experimental observations it is well–known that the gas can slide over a surface. Also, a temperature difference remains at the gas–surface interface, if the temperatures of the gas and surface are different. These discontinuities in velocity and temperature at the boundary are known as slip velocity $\mathcal{V}_k$, and temperature jump $\mathcal{T}$,

$$\mathcal{V}_k = v_k - v_k^W, \tag{5.1}$$

$$\mathcal{T} = \theta - \theta_W. \tag{5.2}$$

Slip velocity and temperature jump can drastically affect the flow character in internal and external rarefied gas flows [92]. As will be seen, their influence is proportional to the rarefaction degree [22, 98], and they vanish as Kn → 0.

We assume an impermeable surface (wall), then, $v_k n_k = \mathcal{V}_k n_k = 0$, where n_k is the normal vector of the wall pointing towards the gas. As shown in Fig. 5.1a, for an arbitrary gas particle close to the wall c_k and $C_k = c_k - v_k$ are the particle's velocity and its peculiar velocity, respectively. For simplicity, we set a frame in which the wall is at rest (the observer rests with the wall), see Fig. 5.1b. In the rest frame, denoted by superscript 'W', the velocities of the gas particle are $c_k^W = c_k - v_k^W$ and $C_k^W = c_k^W - \mathcal{V}_k = C_k$, while $C_k^W n_k = c_k^W n_k$. For particles which depart from the wall $c_k^W n_k \geqslant 0$, and for particles moving to hit the wall $c_k^W n_k \leqslant 0$.

The distribution function f_g is assigned to the gas particles inside the flow, see Fig. 5.1c, and $\bar{f}$ is the distribution function for particles in front of the wall. Kinetic boundary conditions are required to relate f_g to $\bar{f}$.

In theory $\bar{f}$ is known if details of the gas–surface interaction are precisely understood. In the absence of such a detailed information, a simple argument going back to Maxwell [74] can be utilized to derive the required boundary conditions. In the context of kinetic theory Maxwell's boundary condition is widely used as the boundary condition for Boltzmann equation [22, 53, 98] and also in DSMC simulations [17]. Maxwell's boundary condition is based on the assumption that particles interact with the wall only in two ways, *specular reflection* and *thermalization* (perfect diffuse interaction).

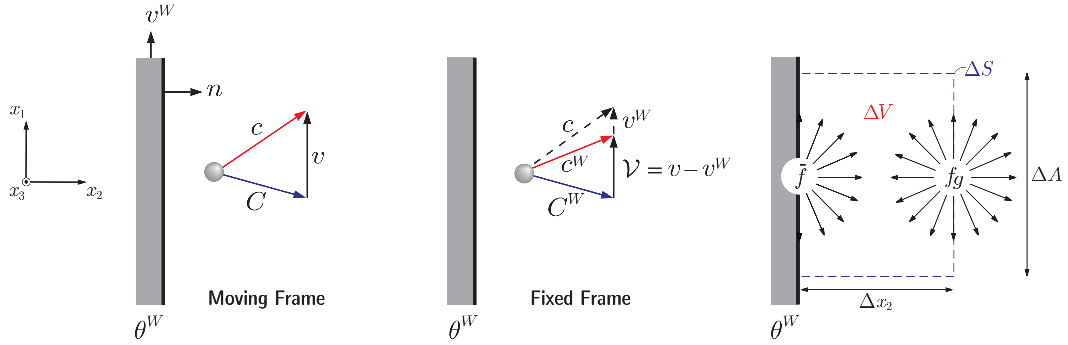

(a) (b) (c)

Figure 5.1: On kinetic boundary conditions.

In the rest frame, $f_g(c_k^W, x_k, t)$ is the velocity distribution function of the gas close to the wall. In order to simplify the following discussion, it is useful to present f_g as a function of tangential velocity $c_i^W - c_k^W n_k n_i$ and normal velocity $c_k^W n_k$, then $f_g = f_g(c_k^W n_k, c_i^W - c_k^W n_k n_i, x_i, t)$.

In specular reflection the tangential velocity remains unchanged, while the sign of normal velocity changes. For those particles which fly to hit the wall $c_k^W n_k \leqslant 0$ and their phase density is $f_g(c_k^W n_k, c_i^W - c_k^W n_k n_i, x_i, t)$. Hence, for elastically reflected particles $c_k^W n_k \geqslant 0$ and $f_R = f_g(-c_k^W n_k, c_i^W - c_k^W n_k n_i, x_i, t)$.

In perfectly diffusive gas–surface interaction (thermalization), the particles leave the wall in a

Maxwellian distribution which is based on temperature and velocity at the wall, that reads[1]

$$f_W = \frac{\rho^W}{\sqrt{2\pi\theta^W}^3} \exp\left(-\frac{c_W^2}{2\theta^W}\right) \quad \text{with} \quad c_W^2 = c_k^W c_k^W. \tag{5.3}$$

Since both specular reflection and thermalization are too simple to describe the realistic gas–surface interaction, Maxwell combined them by means of introducing the accommodation coefficient χ, such that

$$\bar{f} = \begin{cases} \chi f_W + (1-\chi) f_R = \chi f_W + (1-\chi) f_g(-c_k^W n_k, c_i^W - c_k^W n_k n_i, x_i, t), & c_k^W n_k \geqslant 0 \\ f_g(c_k^W n_k, c_i^W - c_k^W n_k n_i, x_i, t). & c_k^W n_k \leqslant 0, \end{cases} \tag{5.4}$$

Here, $\bar{f}$ is the velocity distribution function of the gas in an infinitesimal neighborhood of the wall. The accommodation factor χ, describes the wall characteristics and must be given or measured. In Maxwell's diffusive–reflective boundary condition [Eq. (5.4)] $\chi = 0$ and $\chi = 1$ describe fully reflective (smooth) and fully diffusive (rough) surfaces, respectively. Walls with $\chi = 0$, are also known as adiabatic walls. Equation (5.4) shows that a discontinuity in velocity distribution function exists on the wall, which leads to nonequilibrium effects on the wall, e.g. discontinuity of moments and formation of Knudsen boundary layers.

In specular reflection of particles on the wall the normal velocity of particles is inversed. In thermalization ρ^W must be obtained such that particles accumulation does not occur on the wall. This condition implies that net normal momentum, $\rho v_k n_k$, for all particles colliding on the wall is zero, i.e.,

$$\int c_k^W n_k \, \bar{f} \, d\mathbf{c} = 0 \quad \text{or} \quad \int\limits_{c_k^W n_k \geq 0} c_k^W n_k \, \bar{f} \, d\mathbf{c} + \int\limits_{c_k^W n_k \leq 0} c_k^W n_k \, \bar{f} \, d\mathbf{c} = 0. \tag{5.5}$$

Substituting Eq. (5.4) into (5.5) gives

$$\int\limits_{c_k^W n_k \geq 0} c_k^W n_k \left[\chi f_W + (1-\chi) f_g \left(-c_k^W n_k\right)\right] d\mathbf{c} + \int\limits_{c_k^W n_k \leq 0} c_k^W n_k \, f_g \left(c_k^W n_k\right) d\mathbf{c} = 0, \tag{5.6}$$

---

[1] Note that in the wall rest frame, in the Maxwellian distribution function we have the particle velocity c instead of the peculiar velocity C.

or

$$\chi \int\limits_{c_k^W n_k \geq 0} c_k^W n_k \, f_W \, d\mathbf{c} + \underline{\int\limits_{c_k^W n_k \geq 0} c_k^W n_k \, f_g \left(-c_k^W n_k\right) d\mathbf{c}} - \chi \int\limits_{c_k^W n_k \geq 0} c_k^W n_k \, f_g \left(-c_k^W n_k\right) d\mathbf{c} = \\ \underline{- \int\limits_{c_k^W n_k \leq 0} c_k^W n_k \, f_g \left(c_k^W n_k\right) d\mathbf{c}}.$$

The underlined terms cancel, and we get

$$\int\limits_{c_k^W n_k \geq 0} c_k^W n_k \, f_W \, d\mathbf{c} = - \int\limits_{c_k^W n_k \leq 0} c_k^W n_k \, f_g \left(c_k^W n_k\right) d\mathbf{c}. \tag{5.7}$$

Since the normal velocity vanishes, we have

$$0 = \int c_k^W n_k \, f_g \left(c_k^W n_k\right) d\mathbf{c} = \int\limits_{c_k^W n_k \leq 0} c_k^W n_k \, f_g \left(c_k^W n_k\right) d\mathbf{c} + \int\limits_{c_k^W n_k \geq 0} c_k^W n_k \, f_g \left(c_k^W n_k\right) d\mathbf{c}, \tag{5.8}$$

then Eq. (5.7) reads

$$\int\limits_{c_k^W n_k \geq 0} c_k^W n_k \, f_W \, d\mathbf{c} = \int\limits_{c_k^W n_k \geq 0} c_k^W n_k \, f_g \left(c_k^W n_k\right) d\mathbf{c}. \tag{5.9}$$

Here, in the integrals over f_g we replace c_k^W with $C_k^W + \mathcal{V}_k$, where C_k^W is the peculiar velocity of particles[2], then

$$\int\limits_{c_k^W n_k \geq 0} c_k^W n_k \, f_W \, d\mathbf{c} = \int\limits_{c_k^W n_k \geq 0} \left(C_k^W + \mathcal{V}_k\right) n_k \, f_g \left(c_k^W n_k\right) d\mathbf{c}. \tag{5.10}$$

Since $\mathcal{V}_k n_k = 0$ then

$$\int\limits_{c_k^W n_k \geq 0} c_k^W n_k \, f_W \, d\mathbf{c} = \int\limits_{C_k^W n_k \geq 0} C_k^W n_k \, f_g \, d\mathbf{c}. \tag{5.11}$$

5.2 Flux Boundary Conditions in General Form

As depicted in Fig. 5.1 c, we consider a constant volume of gas adjacent to the wall where its volume and surface are $\Delta V = \Delta x_1 \Delta x_2 \Delta x_3$ and ΔS, respectively. We integrate the moment equation (3.4)

---

[2] Note that the normal component of peculiar velocities in both original and rest frames are equal, $C_k^W n_k = C_k n_k$, however, to keep the generality and to emphasize that all calculations are carried in the rest frame, the superscript 'W' is applied.

over ΔV and apply the divergence theorem to get

$$\frac{\partial}{\partial t}\int\limits_{\Delta V} \mathscr{U}_A \, dV + \oint\limits_{\Delta S} \mathscr{F}_{Ak} n_k \, dS = \int\limits_{\Delta V} \mathscr{P}_A \, dV + \int\limits_{\Delta V} \mathscr{S}_A \, dV, \tag{5.12}$$

where $\mathscr{U}_A$ and $\mathscr{F}_{Ak}$ are macroscopic variables (moments) and their corresponding fluxes, respectively. If a thin layer of gas is assumed $\Delta x_2 \to 0$, then $\Delta V \to 0$, and the volume integrals in Eq. (5.12) vanish. Furthermore, when $\Delta x_2 \to 0$, those particles (and their corresponding fluxes) passing through lower, upper, front and back surfaces of the control volume can be neglected, and the surface integral in Eq. (5.12) reduces to

$$\oint\limits_{\Delta A} \left(\bar{\mathscr{F}}_{Ak} - \mathscr{F}^g_{Ak}\right) n_k \, dA = 0 \quad \text{or} \quad \oint\limits_{\Delta A} \mathscr{F}^g_{Ak} n_k \, dA = \oint\limits_{\Delta A} \bar{\mathscr{F}}_{Ak} n_k \, dA, \tag{5.13}$$

where $\Delta A = \Delta x_1 \Delta x_3$ is the surface which allows normal fluxes into ΔV. The fluxes $\mathscr{F}^g_{Ak}$ and $\bar{\mathscr{F}}_{Ak}$ correspond to fluxes in the gas and fluxes on the wall, respectively, and $(\bar{\mathscr{F}}_{Ak} - \mathscr{F}^g_{Ak})n_k$ is the net normal flux. Equation (5.13) holds for all ΔA, then

$$\left(\bar{\mathscr{F}}_{Ak} - \mathscr{F}^g_{Ak}\right) n_k = 0. \tag{5.14}$$

On account of Eq. (3.5) the normal fluxes in (5.14) at the considered rest frame are

$$\mathscr{F}^g_{Ak} = \int \mathit{\Psi}_A c^W_k \, f_g \, d\mathbf{c} \quad \text{and} \quad \bar{\mathscr{F}}_{Ak} = \int \mathit{\Psi}_A c^W_k \, \bar{f} \, d\mathbf{c}, \tag{5.15}$$

where $\mathit{\Psi}_A$ are polynomials of particles' velocity, c^W_i. For later discussions it is useful to use $\mathit{\Psi}_A\left(c^W_k n_k\right)$ instead of $\mathit{\Psi}_A$.

Substitution of fluxes from Eq. (5.15) into Eq. (5.14) and decomposing the integral for incoming an outgoing particles yields

$$\int\limits_{c^W_k n_k \geq 0} \mathit{\Psi}_A\left(c^W_k n_k\right) c^W_k n_k \left(\bar{f} - f_g\right) d\mathbf{c} + \int\limits_{c^W_k n_k \leq 0} \mathit{\Psi}_A\left(c^W_k n_k\right) c^W_k n_k \left(\bar{f} - f_g\right) d\mathbf{c} = 0. \tag{5.16}$$

This integral equation relates gas and wall distribution functions, and their moments. Based on

Eq. (5.4) the second integral in the above equation is zero and the first integral recasts to

$$\int\limits_{c_k^W n_k \geq 0} \mathit{\Psi}_A \left(c_k^W n_k\right) c_k^W n_k \left[\chi\, f_W + (1-\chi)\, f_g\left(-c_k^W n_k\right) - f_g\left(c_k^W n_k\right)\right] d\mathbf{c} = 0. \tag{5.17}$$

Further manipulation gives

$$\int\limits_{c_k^W n_k \geq 0} \mathit{\Psi}_A \left(c_k^W n_k\right) c_k^W n_k \left[\chi\left(f_W - f_g\left(c_k^W n_k\right)\right) + (1-\chi)\left(f_g\left(-c_k^W n_k\right) - f_g\left(c_k^W n_k\right)\right)\right] d\mathbf{c} = 0. \tag{5.18}$$

The half–space integral over f_g can be written as

$$\begin{aligned}\int\limits_{c_k^W n_k \geq 0} \mathit{\Psi}_A \left(c_k^W n_k\right) c_k^W n_k\, f_g\left(c_k^W n_k\right) d\mathbf{c} &= \int \mathit{\Psi}_A \left(c_k^W n_k\right) c_k^W n_k\, f_g\left(c_k^W n_k\right) d\mathbf{c}\\ &\quad - \int\limits_{c_k^W n_k \leq 0} \mathit{\Psi}_A \left(c_k^W n_k\right) c_k^W n_k\, f_g\left(c_k^W n_k\right) d\mathbf{c}\\ &= \int \mathit{\Psi}_A \left(c_k^W n_k\right) c_k^W n_k\, f_g\left(c_k^W n_k\right) d\mathbf{c}\\ &\quad + \int\limits_{c_k^W n_k \geq 0} \mathit{\Psi}_A \left(-c_k^W n_k\right) c_k^W n_k\, f_g\left(-c_k^W n_k\right) d\mathbf{c}.\end{aligned} \tag{5.19}$$

Replacement of the half–space integrals over f_g from Eq. (5.19) into (5.18), after some rearrangement, gives

$$\begin{aligned}(1-\chi)\int \mathit{\Psi}_A \left(c_k^W n_k\right) c_k^W n_k\, f_g d\mathbf{c} &= \chi \int\limits_{c_k^W n_k \geq 0} \mathit{\Psi}_A \left(c_k^W n_k\right) c_k^W n_k \left[f_W - f_g\left(c_k^W n_k\right)\right] d\mathbf{c}\\ &\quad + (1-\chi) \int\limits_{c_k^W n_k \geq 0} \left[\mathit{\Psi}_A \left(c_k^W n_k\right) - \mathit{\Psi}_A \left(-c_k^W n_k\right)\right] c_k^W n_k\, f_g\left(-c_k^W n_k\right) d\mathbf{c}.\end{aligned} \tag{5.20}$$

Equation (5.20) is the central equation to obtain boundary conditions for the moments. Integrating this equation yields a relation between moments in the gas and wall properties, that serves as boundary conditions for the moments. This strategy is used in the next chapters to derive boundary conditions for regularized 13–moment equations.

5.3 Grad's Hypothesis for Boundary Conditions for Moments

When deriving moment equations Grad also discussed boundary conditions, see [32, 33]. The idea was to take the accommodation model (5.20) and compute boundary conditions for moments from it. Equation (5.20) can be evaluated by assuming a specific model for the distribution function, and different polynomials for $\varPsi_A$.

Based on Grad's observation [32], in order to get meaningful boundary conditions, velocity function $\varPsi_A$ should be even in the normal component of the particle velocity $c_k^W n_k$. When $\varPsi_A$ is an odd function in $c_k^W n_k$, i.e., $\varPsi_A\left(-c_k^W n_k\right) = -\varPsi_A\left(c_k^W n_k\right)$, then Eq. (5.20) reads

$$\begin{aligned}(1-\chi)\int \varPsi_A\left(c_k^W n_k\right) c_k^W n_k\, f_g d\mathbf{c} = \chi \int\limits_{c_k^W n_k \geq 0} \varPsi_A\left(c_k^W n_k\right) c_k^W n_k \left[f_W - f_g\left(c_k^W n_k\right)\right] d\mathbf{c} \\ + 2(1-\chi) \int\limits_{c_k^W n_k \geq 0} \varPsi_A\left(c_k^W n_k\right) c_k^W n_k\, f_g\left(-c_k^W n_k\right) d\mathbf{c}. \qquad (5.21)\end{aligned}$$

As illustrated in Fig. 5.1, since the distribution function in the gas is assumed to be symmetric, i.e., $f_g\left(c_k^W n_k\right) = f_g\left(-c_k^W n_k\right)$, the above equation further simplifies to

$$\begin{aligned}(1-\chi)\int \varPsi_A\left(c_k^W n_k\right) c_k^W n_k\, f_g d\mathbf{c} = \chi \int\limits_{c_k^W n_k \geq 0} \varPsi_A\left(c_k^W n_k\right) c_k^W n_k \left[f_W - 3 f_g\left(c_k^W n_k\right)\right] d\mathbf{c} \\ + 2 \int\limits_{c_k^W n_k \geq 0} \varPsi_A\left(c_k^W n_k\right) c_k^W n_k\, f_g\left(c_k^W n_k\right) d\mathbf{c}. \qquad (5.22)\end{aligned}$$

In an asymptotic limit when $\chi \to 0$, Eq. (5.22), in which $\varPsi_A\left(-c_k^W n_k\right) = -\varPsi_A\left(c_k^W n_k\right)$, yields

$$\int\limits_{c_k^W n_k \geq 0} \varPsi_A\left(c_k^W n_k\right) c_k^W n_k\, f_g\left(c_k^W n_k\right) d\mathbf{c} = \int\limits_{c_k^W n_k \geq 0} \varPsi_A\left(c_k^W n_k\right) c_k^W n_k\, f_g\left(c_k^W n_k\right) d\mathbf{c}, \qquad (5.23)$$

which is an identity, but not a boundary condition.

In conclusion, Eq. (5.20) can be used to obtain boundary conditions for moment when $\varPsi_A$ is an even function in $c_k^W n_k$, that is $\varPsi_A\left(-c_k^W n_k\right) = \varPsi_A\left(c_k^W n_k\right)$. Accordingly, the proper form of Eq. (5.20), which in the next section is used to derive boundary condition for the R13 equations, reads

$$(1-\chi)\int \Psi_A\left(c_k^W n_k\right) c_k^W n_k\, f_g d\mathbf{c} = \chi \int\limits_{c_k^W n_k \geq 0} \Psi_A\left(c_k^W n_k\right) c_k^W n_k\left[f_W - f_g\left(c_k^W n_k\right)\right] d\mathbf{c}. \qquad (5.24)$$

5.4 Boundary Conditions for R13 Equations

To perform integrations in Eq. (5.24) velocity distribution functions f_W and f_g, and velocity function $\Psi_A\left(c_k^W n_k\right)$ are required.

The Maxwellian–type distribution function f_W, that accounts for the wall properties $\{\rho^W, \theta^W\}$, is given in Eq. (5.3). According to the Chapman–Enskog expansion, R13 equations are of third order, hence, a third–order approximation of the velocity distribution function is required. Therefore, for the R13 system it suffices to set $f_g = f_{\mathrm{G26}}$ [Eq. (3.27a)]

$$f_g = f_{\mathrm{G26}} = f_{\mathrm{E}}\left(1+\mathcal{F}_1+\mathcal{F}_2+\mathcal{F}_3\right), \qquad (5.25)$$

with

$$\begin{aligned}
\mathcal{F}_1 &= \frac{1}{2\rho\theta^2} C_i C_j \sigma_{ij} + \left(\frac{1}{5\rho\theta^3}C^2 - \frac{1}{\rho\theta^2}\right) C_j q_j, \\
\mathcal{F}_2 &= \frac{1}{6\rho\theta^3} C_i C_j C_k m_{ijk}, \\
\mathcal{F}_3 &= \frac{\Delta}{\rho\theta^2}\left(\frac{1}{8} - \frac{1}{12\theta}C^2 + \frac{1}{120\theta^2}C^4\right) - \left(\frac{1}{4\rho\theta^3} - \frac{1}{28\rho\theta^4}C^2\right) C_i C_j R_{ij}.
\end{aligned} \qquad (5.26)$$

Expansion of $\mathcal{F}_1$ reads

$$\begin{aligned}
\mathcal{F}_1 = & \frac{1}{2\rho\theta^2}\left(C_1^2\sigma_{11} + 2C_1C_2\sigma_{12} + 2C_1C_3\sigma_{13} + C_2^2\sigma_{22} + 2C_2C_3\sigma_{23} + C_3^2\sigma_{33}\right) \\
& + \left(\frac{1}{5\rho\theta^3}C^2 - \frac{1}{\rho\theta^2}\right)\left(C_1q_1 + C_2q_2 + C_3q_3\right),
\end{aligned} \qquad (5.27)$$

where $C^2 = C_1^2 + C_2^2 + C_3^2$ and for symmetric trace–free stress tensor $\sigma_{ij} = \sigma_{ji}$. Similarly, expansions for $\mathcal{F}_2$ and $\mathcal{F}_3$ are,

$$\begin{aligned}
\mathcal{F}_2 = \frac{1}{6\rho\theta^3} & \left(C_1^3 m_{111} + 3C_1^2C_2 m_{112} + 3C_1^2C_3 m_{113} + 3C_1C_2^2 m_{122} + 6C_1C_2C_3 m_{123}\right. \\
& \left. + 3C_1C_3^2 m_{133} + C_2^3 m_{222} + 3C_2^2C_3 m_{223} + 3C_2C_3^2 m_{233} + C_3^3 m_{333}\right),
\end{aligned} \qquad (5.28)$$

and

$$\mathcal{F}_3 = \frac{\Delta}{\rho\theta^2}\left(\frac{1}{8} - \frac{1}{12\theta}C^2 + \frac{1}{120\theta^2}C^4\right) - \left(\frac{1}{4\rho\theta^3} - \frac{1}{28\rho\theta^4}C^2\right)\left(C_1^2 R_{11} + 2C_1C_2R_{12} + 2C_1C_3R_{13}\right.$$
$$\left. + C_2^2R_{22} + 2C_2C_3R_{23} + C_3^2R_{33}\right), \tag{5.29}$$

where symmetry conditions for m_{ijk} and R_{ij} were applied.

Furthermore, the velocity function $\varPsi_A\left(c_k^W n_k\right)$ must be selected such that integrals in Eq. (5.24) yield the flux of moments which occur in the R13 equations, that are $\{v_i, \sigma_{ij}, q_i, m_{ijk}, R_{ij}\}$.

As used in Eqs. (5.27)–(5.29) the microscopic velocity field is three–dimensional $\mathbf{C} = (C_1, C_2, C_3)^{\mathrm{T}}$. However, here, we consider two–dimensional boundary conditions in the x_1–x_2 plane [see Fig. (5.1)], that means, macroscopic quantities (moments) and their corresponding fluxes are considered in the x_1–x_2 plane. To keep some generality, we introduce a new notation $\mathbf{C} = (C_n, C_t, C_\tau)^{\mathrm{T}}$, where subscript n denotes its normal direction, $\{t, \tau\}$ refer to the tangential directions, and t–n plate is equivalent to x_1–x_2 plane.

According to Grad's hypothesis $\varPsi_A\left(c_k^W n_k\right)$ must be even in $c_k^W n_k$, therefore, we assume

$$\varPsi_A\left(c_k^W n_k\right) = \left\{1, C_t, C^2, C_nC_n, C_tC_t, C^2C_t\right\}, \tag{5.30}$$

which respectively correspond to fluxes

$$\int \varPsi_A\left(c_k^W n_k\right) c_k^W n_k\, f_g d\mathbf{c} = \{\rho v_n, \sigma_{tn}, q_n, m_{nnn}, m_{ttn}, R_{tn}\}. \tag{5.31}$$

For $\varPsi_A = 1$ Eq. (5.24) governs the conservation of mass at the wall, and then a relation for ρ^W is obtained as

$$\mathcal{P} = \rho_W\sqrt{\theta\,\theta_W} = p + \frac{1}{2}\sigma_{nn} - \frac{1}{120}\frac{\Delta}{\theta} - \frac{1}{28}\frac{R_{nn}}{\theta}. \tag{5.32}$$

Boundary condition for shear stress is obtained for $\varPsi_A = C_t$ as

$$\sigma_{tn} = \frac{-\chi}{2-\chi}\sqrt{\frac{2}{\pi\theta}}\left(\mathcal{P}\mathcal{V}_t + \frac{1}{5}q_t + \frac{1}{2}m_{tnn}\right). \tag{5.33}$$

For heat flux, boundary condition is available only for its normal component q_n, which corresponds to $\Psi_A = C^2$

$$q_n = \frac{\chi}{2-\chi}\sqrt{\frac{2}{\pi\theta}}\left(\frac{1}{2}\mathcal{P}\mathcal{V}_t^2 - 2\mathcal{P}\mathcal{T} - \frac{1}{2}\theta\sigma_{nn} - \frac{1}{15}\Delta - \frac{5}{28}R_{nn}\right). \tag{5.34}$$

For $\Psi_A = \{C_nC_n, C_tC_t\}$ one obtains

$$m_{nnn} = \frac{-\chi}{2-\chi}\sqrt{\frac{2}{\pi\theta}}\left(\frac{3}{5}\mathcal{P}\mathcal{V}_t^2 - \frac{2}{5}\mathcal{P}\mathcal{T} + \frac{7}{5}\theta\sigma_{nn} - \frac{1}{75}\Delta + \frac{1}{14}R_{nn}\right), \tag{5.35a}$$

$$m_{ttn} = \frac{\chi}{2-\chi}\sqrt{\frac{2}{\pi\theta}}\left(\frac{4}{5}\mathcal{P}\mathcal{V}_t^2 - \frac{1}{5}\mathcal{P}\mathcal{T} - \theta\sigma_{tt} + \frac{1}{5}\theta\sigma_{nn} - \frac{1}{150}\Delta - \frac{1}{14}R_{tt}\right). \tag{5.35b}$$

It is important to mention that regarding to the Grad's hypothesis, the velocity function C_tC_τ exists in (5.30), where the subscript τ refers to the other tangential direction, i.e., direction x_3 in Fig. 5.1. However, $C_tC_\tau C_n$ leads to a boundary condition for $m_{t\tau n}$ that is required only for three–dimensional calculations—which is beyond the scope of this thesis.

Finally, the other components in (5.30), i.e., $\Psi_A = C^2C_t$ yields

$$R_{tn} = \frac{-\chi}{2-\chi}\sqrt{\frac{2}{\pi\theta}}\left(\mathcal{P}\mathcal{V}_t^3 - \mathcal{P}\mathcal{V}_t\theta - 6\mathcal{P}\mathcal{T}\mathcal{V}_t + \frac{11}{5}\theta q_t + \frac{1}{2}\theta m_{tnn}\right). \tag{5.36}$$

5.5 Second–order Boundary Conditions for Navier–Stokes–Fourier Equations

The R13 boundary conditions presented in (5.32)–(5.36) include a range of first– , second– and third–order moments—with respect to the Chapman–Enskog scaling. Therefore, they can be used to derive high–order slip velocity and temperature jump conditions for Navier–Stokes–Fourier equations. The strategy to obtain these high–order boundary conditions for Couette and Poiseuille flows in planar geometry is presented in Ref. [110]. In this thesis, the same strategy is employed to obtain second–order contributions of high–order moments to slip velocity and temperature jump in other flow settings.

Explicit expressions for slip velocity $\mathcal{V}_t$, and temperature jump $\mathcal{T}$, can be obtained form Eqs. (5.33) and (5.34)

$$\mathcal{V}_t = \underline{-\frac{2-\chi}{\chi}\sqrt{\frac{\pi\theta}{2}}\frac{\sigma_{tn}}{\mathcal{P}} - \frac{1}{5}\frac{q_t}{\mathcal{P}}} - \frac{1}{2}\frac{m_{tnn}}{\mathcal{P}}, \tag{5.37}$$

$$\mathcal{T} = \underline{-\frac{2-\chi}{\chi}\sqrt{\frac{\pi\theta}{2}}\frac{q_n}{2\mathcal{P}}} + \frac{1}{4}\mathcal{V}_t^2 - \frac{1}{4}\frac{\theta\sigma_{nn}}{\mathcal{P}} - \frac{1}{30}\frac{\Delta}{\mathcal{P}} - \frac{5}{56}\frac{R_{nn}}{\mathcal{P}}. \tag{5.38}$$

The above boundary conditions are of third–order, $\mathcal{O}\left(\mathrm{Kn}^3\right)$. The underlined terms correspond to the well–known first–order slip velocity and temperature jump conditions [106], where σ_{tn} and q_n require the Navier–Stokes–Fourier (NSF) relations [cf. Eq. (4.5)], and $\mathcal{P}^{\mathrm{NSF}} = p$. In Eq. (5.37) the first–order contribution of tangential (streamwise) heat flux q_t remains only for thermally–driven flows, which is postulated by Fourier's law—based on the streamwise temperature gradient.

According to the Chapman–Enskog expansion the moments in (5.37) and (5.38) need to be scaled as $M = \mathrm{Kn}^{\alpha}\overset{\circ}{M}$, where the rescaled moment $\overset{\circ}{M}$ is of order unity and α is the order of the moment M. The scaling allows to identify the higher–order contributions to slip and jump. Since the order of moments depend on the flow setting, for each problem we must derive higher–order slip and jump conditions separately. For flows, which are favored in practical applications, second–order slip and jump conditions are presented below. For details of the calculations see Appendix C.

5.6 Linearized and Dimensionless Boundary Conditions for R13 Equations

In order to obtain a unique solution for linearized R13 equations, linearized boundary conditions must be employed. As discussed in Sec. 4.4, by introducing dimensionless variables [cf. Eqs. (4.28) and (4.30)] and dropping nonlinear terms, the boundary conditions (5.33)–(5.36) reduce to

$$\tilde{\sigma}_{tn} = \frac{-\chi}{2-\chi}\sqrt{\frac{2}{\pi}}\left(\tilde{\mathcal{V}}_t + \frac{1}{5}\tilde{q}_t + \frac{1}{2}\tilde{m}_{tnn}\right), \tag{5.39a}$$

$$\tilde{q}_n = \frac{\chi}{2-\chi}\sqrt{\frac{2}{\pi}}\left(-2\tilde{\mathcal{T}} - \frac{1}{2}\tilde{\sigma}_{nn} - \frac{1}{15}\tilde{\Delta} - \frac{5}{28}\tilde{R}_{nn}\right), \tag{5.39b}$$

$$\tilde{m}_{nnn} = \frac{-\chi}{2-\chi}\sqrt{\frac{2}{\pi}}\left(-\frac{2}{5}\tilde{\mathcal{T}} + \frac{7}{5}\tilde{\sigma}_{nn} - \frac{1}{75}\tilde{\Delta} + \frac{1}{14}\tilde{R}_{nn}\right), \tag{5.39c}$$

$$\tilde{m}_{ttn} = \frac{\chi}{2-\chi}\sqrt{\frac{2}{\pi}}\left(-\frac{1}{5}\tilde{\mathcal{T}} - \tilde{\sigma}_{tt} + \frac{1}{5}\tilde{\sigma}_{nn} - \frac{1}{150}\tilde{\Delta} - \frac{1}{14}\tilde{R}_{tt}\right), \tag{5.39d}$$

$$\tilde{R}_{tn} = \frac{-\chi}{2-\chi}\sqrt{\frac{2}{\pi}}\left(-\tilde{\mathcal{V}}_t + \frac{11}{5}\tilde{q}_t + \frac{1}{2}\tilde{m}_{tnn}\right). \tag{5.39e}$$

Part II

BOUNDARY VALUE PROBLEMS

In this part of the dissertation, a collection of internal and external rarefied gas flows, which are favored in engineering applications, are solved using both the classical Navier–Stokes–Fourier (NSF) fluid dynamics equations, and the regularized 13–moment (R13) equations. Comparison of the solutions for both systems renders a lucid analysis on shortcomings of the traditional NSF equations. Moreover, flows in both planar and curvilinear (cylindrical) geometries are considered to discern the influence of curvature on rarefaction effects. Also, for completeness of the study, unsteady rarefaction effects in oscillatory flows are discussed as well.

For the selected problems, NSF and R13 equations along with their corresponding boundary conditions lead to a set of boundary value problems, that are solved in their linear, weakly nonlinear (semilinear), and fully nonlinear forms. Based on comparisons with kinetic theory data, it is shown that the linearized R13 equations suffice to fairly approximate rarefaction effects in slow and moderately rarefied gas flows. Also, through semilinear analysis, it is shown that when more nonlinear terms are included within the equations, a more refined presentation of nonequilibrium effects can be achieved.

Chapter 6

Linear Theory for Half–space Flows in Planar Geometry

Linearized R13 equations in planar geometry were presented in Sec. 4.4.1. In this chapter these linear equations are adapted to describe linear rarefaction effects in half–space flows over a flat surface[1]. Simplicity of the flow geometry in the half–space problems leads to compact solutions which offer a valuable insight into the nonequilibrium effects. It will be shown that the theoretical description for dominant rarefaction effects is available through the linearized R13 equations, while some accuracy is lost due to linearization of the equations.

6.1 Viscous Velocity Slip, Thermal Creep, and Force–driven Flows Over a Flat Surface

The problem of viscous (velocity) slip, also called *Kramer's problem* [22], concerns half–space ($x_2 > 0$) gas flow over a flat solid surface at $x_2 = 0$, see Fig. 6.1a. The uniform temperature of the wall (surface) θ_W, is kept constant at θ_0, which is taken as the reference temperature. Far from the wall the temperature and density of the gas are constant (θ_0 and ρ_0), however, there is a gas flow parallel to the wall, whose velocity is a linear function of x_2; $\partial v_1/\partial x_2 = A$ with A as the constant velocity gradient (shear rate) in the bulk.

While in Kramer's problem the surface temperature is uniform, in thermal creep flow a constant

---

[1] The presented materials in this chapter are published in Ref. [112].

streamwise temperature gradient $\partial\theta/\partial x_1 = B$ is applied in the wall, Fig. 6.1b. This boundary treatment induces a tangential velocity in the gas close to the surface such that the gas flows in direction of the temperature gradient, i.e., from cold to hot. Also, it is assumed that the length of the plate, L, is sufficiently large that the creep layer is fully developed. This implies that the same temperature gradient is established in the gas, and far from the surface pressure remains constant in the x_1–direction [80, 114].

Additionally, as illustrated in Fig. 6.1c, a gas flow over the surface can be induced by a constant external body force, G_1. This constant force can be described as a homogeneous pressure gradient, $\partial p/\partial x_1 \equiv G_1$.

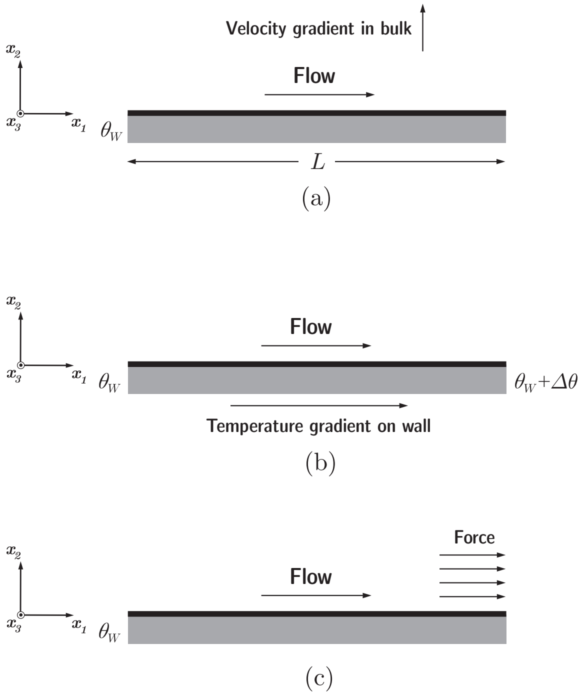

Figure 6.1: (a) Viscous slip flow, known as Kramer's problem, is a one–dimensional viscous flow over a stationary flat wall, where temperatures of the wall θ_W and flow are the same. In the bulk flow, there is a constant velocity gradient normal to the wall in x_2 direction, which sweeps the gas over the surface. (b) In thermal creep flow a non–uniform temperature distribution in a flat plate induces a tangential velocity in the adjacent gas. This thermally induced flow is in the direction of the temperature gradient, i.e., in the opposite direction of heat flow. (c) In force–driven flow, a homogeneous external force is applied to convect the gas.

These steady state flows are independent of the direction x_3, as sufficiently wide plates are considered. The walls act as thermal reservoirs, and are impermeable. We will consider flows in the linear regime, where the viscous slip and force–driven flows will turn out to be isothermal. This means that the wall and gas remain at the same temperature θ_0, since no external energy supply is considered and also viscous heating effects (internal friction) are omitted due to linearization [see Sec. 4.4]. In viscous slip and force–driven flows a unidirectional velocity field parallel to the plates is allowed, $\mathbf{v} = \left(v_1\left(x_2\right), 0, 0\right)^{\mathrm{T}}$, and flow parameters are independent of the stream direction, i.e., $\partial/\partial x_1 = 0$.

In the thermal creep flow, owing to the temperature/density gradient, the constant pressure creep flow is not isothermal. Hence, unidimensional flow is not assured, and the velocity field is two–dimensional, $\mathbf{v} = \left(v_1\left(x_1, x_2\right), v_2\left(x_1, x_2\right), 0\right)^{\mathrm{T}}$. Nevertheless, we realized when the streamwise temperature gradient B is small, the compressibility effects can be discarded, which leads to $v_2 = 0$. In the following calculations for the creep flow we superimpose a unidirectional velocity field. It will be shown that this assumption is consistent with the obtained linear results.

Based on the above discussion the velocity vector, heat–flux vector, body–force vector, and symmetric trace–free stress tensor for all the considered flows simplify to

$$v_i = \begin{pmatrix} v_1\left(x_2\right) \\ 0 \\ 0 \end{pmatrix}, \quad q_i = \begin{pmatrix} q_1\left(x_2\right) \\ q_2\left(x_2\right) \\ 0 \end{pmatrix}, \quad G_i = \begin{pmatrix} G_1 \\ 0 \\ 0 \end{pmatrix},$$

$$\sigma_{ij} = \begin{pmatrix} \sigma_{11}\left(x_2\right) & \sigma_{12}\left(x_2\right) & 0 \\ \sigma_{12}\left(x_2\right) & \sigma_{22}\left(x_2\right) & 0 \\ 0 & 0 & -\sigma_{11}\left(x_2\right) - \sigma_{22}\left(x_2\right) \end{pmatrix}. \tag{6.40}$$

6.2 Linearized R13 Equations for Viscous Slip, Thermal Creep, and Force–driven Flows Over a Flat Surface

For the considered flow geometries, illustrated in Fig. 6.1, expansion of linear R13 equations [cf. (4.32)–(4.37)] with regards to the assumptions in (6.40) yields the following sets of differential equations.

■ The velocity problem:

R13 case: In order to find the flow velocity, the following system must be solved

$$\frac{\partial \tilde{\sigma}_{12}}{\partial \tilde{x}_2} = \tilde{G}_1, \tag{6.41a}$$

$$\frac{2}{5}\frac{\partial \tilde{q}_1}{\partial \tilde{x}_2} + \frac{\partial \tilde{m}_{122}}{\partial \tilde{x}_2} = -\frac{\partial \tilde{v}_1}{\partial \tilde{x}_2} - \frac{1}{\mathrm{Kn}}\tilde{\sigma}_{12}, \tag{6.41b}$$

$$\frac{\partial \tilde{\sigma}_{12}}{\partial \tilde{x}_2} + \frac{1}{2}\frac{\partial \tilde{R}_{12}}{\partial \tilde{x}_2} = -\frac{5}{2}\frac{\partial \tilde{\theta}}{\partial \tilde{x}_1} - \frac{\mathrm{Pr}}{\mathrm{Kn}}\tilde{q}_1, \tag{6.41c}$$

that require the following constitutive relations

$$\tilde{R}_{12} = \frac{\mathsf{B}_2}{2}\,\mathrm{Kn}\frac{\partial \tilde{q}_1}{\partial \tilde{x}_2}, \qquad \tilde{m}_{122} = \frac{8\,\mathsf{C}}{15}\,\mathrm{Kn}\frac{\partial \tilde{\sigma}_{12}}{\partial \tilde{x}_2}, \tag{6.42}$$

and linearized boundary conditions [cf. Eq. (5.39)]

$$\tilde{\sigma}_{12} = -\frac{\chi}{2-\chi}\sqrt{\frac{2}{\pi}}\left(\tilde{\mathcal{V}}_1 + \frac{1}{5}\tilde{q}_1 + \frac{1}{2}\tilde{m}_{122}\right)n_2, \tag{6.43a}$$

$$\tilde{R}_{12} = -\frac{\chi}{2-\chi}\sqrt{\frac{2}{\pi}}\left(-\tilde{\mathcal{V}}_1 + \frac{11}{5}\tilde{q}_1 + \frac{1}{2}\tilde{m}_{122}\right)n_2. \tag{6.43b}$$

Classical case: In the Navier–Stokes–Fourier equations, the velocity problem consists of the momentum balance (6.41a) which after substitution of Navier–Stokes law, $\tilde{\sigma}_{12}^{\mathrm{NSF}} = -\mathrm{Kn}\,\partial\tilde{v}_1/\partial\tilde{x}_2$, reads

$$\frac{\partial^2 \tilde{v}_1}{\partial \tilde{x}_2^2} = -\frac{\tilde{G}_1}{\mathrm{Kn}}. \tag{6.44}$$

This equation requires the slip condition [Eq. (C.29)] that in linear form is

$$\tilde{\mathcal{V}}_1^{\mathrm{NSF}} = \frac{2-\chi}{\chi}\sqrt{\frac{\pi}{2}}\frac{\partial \tilde{v}_1}{\partial \tilde{x}_2}\,\mathrm{Kn}\,n_2 + \frac{1}{2\,\mathrm{Pr}}\frac{\partial \tilde{\theta}}{\partial \tilde{x}_1}\,\mathrm{Kn} - \left(\frac{1}{5\,\mathrm{Pr}} - \frac{4\,\mathsf{C}}{15}\right)\frac{\partial^2 \tilde{v}_1}{\partial \tilde{x}_2^2}\,\mathrm{Kn}^2. \tag{6.45}$$

Note that in the above slip condition Navier–Stokes law, $\tilde{\sigma}_{12}^{\mathrm{NSF}} = -\mathrm{Kn}\,\partial\tilde{v}_1/\partial\tilde{x}_2$, and Fourier law, $\tilde{q}_1^{\mathrm{NSF}} = -(5\,\mathrm{Kn}/(2\,\mathrm{Pr}))\partial\tilde{\theta}/\partial\tilde{x}_1$, were used.

■ The temperature problem:

R13 case: The temperature distribution in the gas can be obtained by solving the system

$$\frac{\partial \tilde{q}_2}{\partial \tilde{x}_2} = 0, \tag{6.46a}$$

$$\frac{8}{15}\frac{\partial \tilde{q}_2}{\partial \tilde{x}_2} + \frac{\partial \tilde{m}_{222}}{\partial \tilde{x}_2} = -\frac{1}{\mathrm{Kn}}\tilde{\sigma}_{22}, \tag{6.46b}$$

$$\frac{\partial \tilde{\sigma}_{22}}{\partial \tilde{x}_2} + \frac{1}{2}\frac{\partial \tilde{R}_{22}}{\partial \tilde{x}_2} + \frac{1}{6}\frac{\partial \tilde{\mathit{\Delta}}}{\partial \tilde{x}_2} = -\frac{5}{2}\frac{\partial \tilde{\theta}}{\partial \tilde{x}_2} - \frac{\mathrm{Pr}}{\mathrm{Kn}}\tilde{q}_2, \tag{6.46c}$$

in which

$$\tilde{\mathit{\Delta}} = \mathsf{A}_2\,\mathrm{Kn}\frac{\partial \tilde{q}_2}{\partial \tilde{x}_2}, \qquad \tilde{R}_{22} = \frac{2\,\mathsf{B}_2}{3}\,\mathrm{Kn}\frac{\partial \tilde{q}_2}{\partial \tilde{x}_2}, \qquad \tilde{m}_{222} = \frac{3\,\mathsf{C}}{5}\,\mathrm{Kn}\frac{\partial \tilde{\sigma}_{22}}{\partial \tilde{x}_2}. \tag{6.47}$$

The corresponding linear boundary conditions for the temperature problem are [cf. Eq. (5.39)]

$$\tilde{q}_2 = \frac{\chi}{2-\chi}\sqrt{\frac{2}{\pi}}\left(-2\tilde{\mathcal{T}} - \frac{1}{2}\tilde{\sigma}_{22} - \frac{1}{15}\tilde{\mathit{\Delta}} - \frac{5}{28}\tilde{R}_{22}\right)n_2, \tag{6.48a}$$

$$\tilde{m}_{222} = \frac{\chi}{2-\chi}\sqrt{\frac{2}{\pi}}\left(\frac{2}{5}\tilde{\mathcal{T}} - \frac{7}{5}\tilde{\sigma}_{22} + \frac{1}{75}\tilde{\mathit{\Delta}} - \frac{1}{14}\tilde{R}_{22}\right)n_2. \tag{6.48b}$$

Classical case: In the NSF system the temperature solution can be simply obtained from the energy balance equation (6.46a), in which Fourier's law in x_2–direction is used, so that

$$\frac{\partial^2 \tilde{\theta}}{\partial \tilde{x}_2^2} = 0. \tag{6.49}$$

The corresponding boundary condition for the above equation is the temperature jump condition (C.30) that in linear form is

$$\tilde{\mathcal{T}}^{\mathrm{NSF}} = \frac{2-\chi}{\chi}\frac{5}{4\,\mathrm{Pr}}\sqrt{\frac{\pi}{2}}\frac{\partial \tilde{\theta}}{\partial \tilde{x}_2}\,\mathrm{Kn}\,n_2 + \frac{5}{2\,\mathrm{Pr}}\left(\frac{\mathsf{A}_2}{30} + \frac{5\,\mathsf{B}_2}{84}\right)\frac{\partial^2 \tilde{\theta}}{\partial \tilde{x}_2^2}\,\mathrm{Kn}^2. \tag{6.50}$$

■ The density/pressure problem:

R13 case: To find the density distribution, it suffices to solve the normal momentum equation,

$$\frac{\partial \tilde{\rho}}{\partial \tilde{x}_2} + \frac{\partial \tilde{\theta}}{\partial \tilde{x}_2} + \frac{\partial \tilde{\sigma}_{22}}{\partial \tilde{x}_2} = 0, \tag{6.51}$$

which indeed requires the solution of the temperature problem. For the density problem kinetic boundary condition is not available, however, for flows in finite domains, $0 < x_2 < H$, conservation of mass in the process gives an auxiliary condition,

$$\int_0^{H/L} \tilde{\rho}\, d\tilde{x}_2 = \text{const.}, \tag{6.52}$$

which can be employed to evaluate the density distribution.

Classical case: In the NSF system the density problem simplifies to $\partial\tilde{\rho}/\partial\tilde{x}_2 = -\partial\tilde{\theta}/\partial\tilde{x}_2$, since $\tilde{\sigma}_{22}^{\mathrm{NSF}} = 0$.

■ The remaining:

The balance equation for σ_{11} is the remaining equation in the R13 system, it reads

$$-\frac{4}{15}\frac{\partial\tilde{q}_2}{\partial\tilde{x}_2} + \frac{\partial\tilde{m}_{112}}{\partial\tilde{x}_2} = -\frac{1}{\mathrm{Kn}}\tilde{\sigma}_{11}, \tag{6.53}$$

with

$$\tilde{m}_{112} = \frac{\mathsf{C}}{3}\,\mathrm{Kn}\left(\frac{\partial\tilde{\sigma}_{11}}{\partial\tilde{x}_2} - \frac{2}{5}\frac{\partial\tilde{\sigma}_{22}}{\partial\tilde{x}_2}\right), \tag{6.54}$$

and its corresponding linear boundary condition is [cf. Eq. (5.39)]

$$\tilde{m}_{112} = \frac{\chi}{2-\chi}\sqrt{\frac{2}{\pi}}\left(-\frac{1}{5}\tilde{\mathcal{T}} - \tilde{\sigma}_{11} + \frac{1}{5}\tilde{\sigma}_{22} - \frac{1}{150}\tilde{\Delta} - \frac{1}{14}\tilde{R}_{11}\right)n_2, \tag{6.55}$$

in which $\tilde{R}_{11} = 0$ (for all the considered flows), since $\partial\tilde{q}_1/\partial\tilde{x}_1 = 0$.

For briefness, the governing equations and boundary conditions for the considered boundary value problems are unified in (6.41)–(6.55) where $\mathrm{Kn} = \lambda_0/\mathcal{L} = 1$ is the Knudsen number [cf. Eq. (4.38)]. For the considered half–space problems, the macroscopic length scale is assumed to be the reference mean free path, $\mathcal{L} = \lambda_0$.

The body force $\tilde{G}_1$ must be set to zero except for the force–driven flow, and $\partial\tilde{\theta}/\partial\tilde{x}_1$ is zero except for the creep flow.

If we assume two dimensional flows, then $\tilde{v}_2$ is responsible for the redistribution of mass in the cross section, i.e., in direction $\tilde{x}_1$. In our problems we assumed $\tilde{v}_2 = 0$. This implies that the redistribution of density cannot be described by the continuity equation. Instead, the density follows from the equation for $\tilde{v}_2$, i.e., the balance of momentum in x_2–direction, Eq. (6.51), which describes an instantaneous change of density. For steady thermal creep flow we shall further discuss the continuity equation after we obtained its solution.

In the following we only present solutions for the velocity problem. For the linearized temperature problem [cf. Eqs. (6.46)–(6.48)], in which temperature of wall and gas are the same, a trivial solution can be obtained $\tilde{\theta} = \tilde{q}_2 = \tilde{\sigma}_{22} = 0$, that means the flows are isothermal.

Similarly, trivial solution for the density/pressure problem can be concluded from temperature solution. We emphasize that in the thermal creep flow, streamwise thermal effects can be described by the velocity problem, due to the one–dimensional velocity assumption.

6.3 Solutions for Half–space Flows

6.3.1 Half–space Viscous Slip Flow

For the steady state shear–driven flow over a flat surface, with $\tilde{G}_1 = \partial\tilde{\theta}/\partial\tilde{x}_1 = 0$, the velocity problem (6.41) reads

$$\frac{\partial\tilde{\sigma}_{12}}{\partial\tilde{x}_2} = 0, \qquad \frac{2}{5}\frac{\partial\tilde{q}_1}{\partial\tilde{x}_2} = -\frac{\partial\tilde{v}_1}{\partial\tilde{x}_2} - \frac{1}{\mathrm{Kn}}\tilde{\sigma}_{12}, \qquad \frac{\mathsf{B}_2}{4}\,\mathrm{Kn}\frac{\partial^2\tilde{q}_1}{\partial\tilde{x}_2^2} = -\frac{\mathrm{Pr}}{\mathrm{Kn}}\tilde{q}_1, \tag{6.56}$$

where $\tilde{R}_{12}$ and $\tilde{m}_{122}$ are substituted by the constitutive relations (6.42). We replace B_2 and Pr from Eq. (4.16), since we will compare our results with BGK Boltzmann data. The solution for (6.56) follows by integrating as

$$\tilde{\sigma}_{12} = \underline{\mathbf{C}_1}, \qquad \tilde{v}_1 = \underline{\mathbf{C}_4 - \frac{\tilde{\sigma}_{12}}{\mathrm{Kn}}\,\tilde{x}_2} - \frac{2}{5}\tilde{q}_1, \qquad \tilde{q}_1 = \mathbf{C}_2 \exp\left(\frac{\sqrt{5}}{\sqrt{7}\,\mathrm{Kn}}\tilde{x}_2\right) + \mathbf{C}_3 \exp\left(\frac{-\sqrt{5}}{\sqrt{7}\,\mathrm{Kn}}\tilde{x}_2\right), \tag{6.57}$$

with $\mathbf{C}_1$ to $\mathbf{C}_4$ as the integrating constants, that need to be determined from the boundary conditions (6.43). The constant velocity gradient in the bulk, which drives the process, must be considered as a boundary condition at $\tilde{x}_2 \to \infty$. In dimensionless form we denote this shear rate as $\nu = \partial\tilde{v}_1/\partial\tilde{x}_2|_{\tilde{x}_2\to\infty}$.

The underlined terms represent the solution for the Navier–Stokes–Fourier equations. Note that both R13 and NSF systems yield constant shear stress, $\tilde{\sigma}_{12} = \mathbf{C}_1$, albeit with different values for the constant. The term $\mathbf{C}_4$ is the velocity slip, and $-\tilde{\sigma}_{12}\,\tilde{x}_2/\mathrm{Kn}$ is the bulk solution. Since the NSF system only predicts temperature–gradient driven heat flux, it cannot predict the tangential heat flux, $\tilde{q}_1$, in isothermal flows. Indeed, a heat flow which is not driven by temperature gradient and occurs in opposite direction of mass flow is a pure rarefaction effect [115] that lies beyond the resolution of traditional hydrodynamics.

6.3.2 Half–space Thermal Creep Flow

For steady state thermally–driven flow over a flat wall, with $\tilde{G}_1 = 0$, the proper form of the velocity problem (6.41) is

$$\frac{\partial \tilde{\sigma}_{12}}{\partial \tilde{x}_2} = 0, \qquad \frac{2}{5}\frac{\partial \tilde{q}_1}{\partial \tilde{x}_2} = -\frac{\partial \tilde{v}_1}{\partial \tilde{x}_2} - \frac{1}{\mathrm{Kn}}\tilde{\sigma}_{12}, \qquad \frac{\mathsf{B}_2}{4}\,\mathrm{Kn}\frac{\partial^2 \tilde{q}_1}{\partial \tilde{x}_2^2} = -\frac{5}{2}\tau - \frac{\mathrm{Pr}}{\mathrm{Kn}}\tilde{q}_1, \tag{6.58}$$

where $\tau = \partial\tilde{\theta}/\partial\tilde{x}_1$ is the dimensionless streamwise temperature gradient that drives the process.

Similar to the viscous slip problem, integrating (6.58) for the BGK model leads to

$$\begin{gathered} \tilde{\sigma}_{12} = \underline{\mathbf{C}_1}, \qquad \tilde{v}_1 = \underline{\mathbf{C}_4 - \frac{\tilde{\sigma}_{12}}{\mathrm{Kn}}\,\tilde{x}_2} - \frac{2}{5}\tilde{q}_1, \\ \tilde{q}_1 = \underline{-\frac{5}{2}\,\mathrm{Kn}\,\tau} + \mathbf{C}_2 \exp\left(\frac{\sqrt{5}}{\sqrt{7}\,\mathrm{Kn}}\tilde{x}_2\right) + \mathbf{C}_3 \exp\left(\frac{-\sqrt{5}}{\sqrt{7}\,\mathrm{Kn}}\tilde{x}_2\right), \end{gathered} \tag{6.59}$$

where the underlined terms represent the solution for the Navier–Stokes–Fourier equations. As shown in (6.57) and (6.59), the general solutions for viscous slip and thermal creep problems only differ in the heat–flux solution. In the creep flow, superposition of the Fourier's law, $\tilde{q}_1^{\mathrm{NSF}} = -\frac{5}{2}\,\mathrm{Kn}\,\tau$, and Knudsen layers construct the parallel heat flux. Knudsen layers in thermally–driven flows are also referred as *mechanocaloric heat flow* [70]. In the velocity solution, $\mathbf{C}_4$ and the contribution of the Fourier's law represent the slip velocity (temperature–driven plug flow).

6.3.3 Half–space Force–driven Flow

For steady state force–driven flows, with $\partial\tilde{\theta}/\partial\tilde{x}_1 = 0$, the velocity problem (6.41) recasts to

$$\frac{\partial \tilde{\sigma}_{12}}{\partial \tilde{x}_2} = \tilde{G}_1, \qquad \frac{2}{5}\frac{\partial \tilde{q}_1}{\partial \tilde{x}_2} = -\frac{\partial \tilde{v}_1}{\partial \tilde{x}_2} - \frac{1}{\mathrm{Kn}}\tilde{\sigma}_{12}, \qquad \tilde{G}_1 + \frac{\mathsf{B}_2}{4}\,\mathrm{Kn}\frac{\partial^2 \tilde{q}_1}{\partial \tilde{x}_2^2} = -\frac{\mathrm{Pr}}{\mathrm{Kn}}\tilde{q}_1, \tag{6.60}$$

that for Maxwellian molecules with coefficients (4.15) yields

$$\begin{gathered} \tilde{\sigma}_{12} = \underline{\mathbf{C}_1 + \tilde{G}_1\tilde{x}_2}, \qquad \tilde{v}_1 = \underline{\mathbf{C}_4 - \frac{\tilde{G}_1}{2\,\mathrm{Kn}}\,\tilde{x}_2^2 - \frac{\mathbf{C}_1}{\mathrm{Kn}}\,\tilde{x}_2} - \frac{2}{5}\tilde{q}_1, \\ \tilde{q}_1 = -\frac{3}{2}\,\mathrm{Kn}\,\tilde{G}_1 + \mathbf{C}_2 \exp\left(\frac{\sqrt{5}}{3\,\mathrm{Kn}}\tilde{x}_2\right) + \mathbf{C}_3 \exp\left(\frac{-\sqrt{5}}{3\,\mathrm{Kn}}\tilde{x}_2\right). \end{gathered} \tag{6.61}$$

Again, the underlined terms represent the solution for classical hydrodynamics. In force–driven flow, stress distribution is a linear function of force. Moreover, the term $-\frac{3}{2}\,\mathrm{Kn}\,\tilde{G}_1$ is a high–order bulk heat flux which does not appear in the NSF solution.

It is important to emphasize that in solutions (6.57), (6.59), and (6.61) the exponential functions represent the Knudsen boundary layers. Alternatively, the exponential functions can be written as combination of hyperbolic sine and cosine functions [109, 110, 113, 114].

6.4 Results and Discussion for Half–space Flows

In this section, we provide comparison between our solutions (for viscous slip and thermal creep flows) to published solutions of the Boltzmann equation available in the literature. Kinetic data for force–driven flows over a surface is not available, however, in later sections we will use our solution for this problem to investigate force–driven Poiseuille flows in parallel–plate micro–channels.

6.4.1 Viscous Slip Flow (Kramer's Problem)

Velocity slip and defect in Kramer's problem have been extensively studied using kinetic approaches based on the Boltzmann equation [13, 22, 63, 66, 68, 69, 72, 80].

The integrating constants $\mathbf{C}_1$–$\mathbf{C}_4$ in the solution (6.57) are determined from the boundary conditions (6.43) and (6.45) as

$$\mathbf{C}_1^{\mathrm{R13}} = -\mathrm{Kn}\,\nu, \quad \mathbf{C}_2^{\mathrm{R13}} = 0, \quad \mathbf{C}_3^{\mathrm{R13}} = \frac{5\sqrt{\pi}\,\mathrm{Kn}\,\nu}{2\sqrt{35\pi} + 12\sqrt{2}\,\bar{\chi}}, \quad \mathbf{C}_4^{\mathrm{R13}} = \frac{2\pi\sqrt{35}/\bar{\chi} + 13\sqrt{2\pi}}{2\sqrt{70\pi} + 24\,\bar{\chi}}\,\mathrm{Kn}\,\nu,$$
$$\mathbf{C}_1^{\mathrm{NSF}} = -\mathrm{Kn}\,\nu, \qquad \mathbf{C}_4^{\mathrm{NSF}} = \frac{1}{\bar{\chi}}\sqrt{\frac{\pi}{2}}\,\mathrm{Kn}\,\nu. \tag{6.62}$$

with $\bar{\chi} = \chi/\left(2-\chi\right)$. The constant $\mathbf{C}_1$ follows from the bulk condition where the dimensionless velocity gradient is prescribed by $\partial\tilde{v}_1/\partial\tilde{x}_2 = \nu$. Moreover, $\mathbf{C}_2 = 0$ results from the fact that the heat flux is finite in the far field.

Figure 6.2 shows the R13 and NSF solutions for the velocity distribution in the viscous slip problem, i.e., Eq. (6.57). Solutions for different accommodation factors $\chi = \{0.2, 0.4, 0.6, 0.8, 1.0\}$ are presented, where the diamond symbols represent the BGK Boltzmann equation data of Refs. [13, 72]. The Knudsen number and bulk velocity in [13, 72] are related to our definitions by $\mathrm{Kn} = 1/\sqrt{2}$ and $\nu = 1$, respectively. In Fig. 6.2c the profiles near the wall are magnified, where the effects of Knudsen boundary layers yield curvature in the velocity profiles. The NSF solution is a straight line, while the Knudsen layer in the R13 solution bends the bulk solution towards the Boltzmann solution. We observed a similar agreement when we compared our results with data in [80].

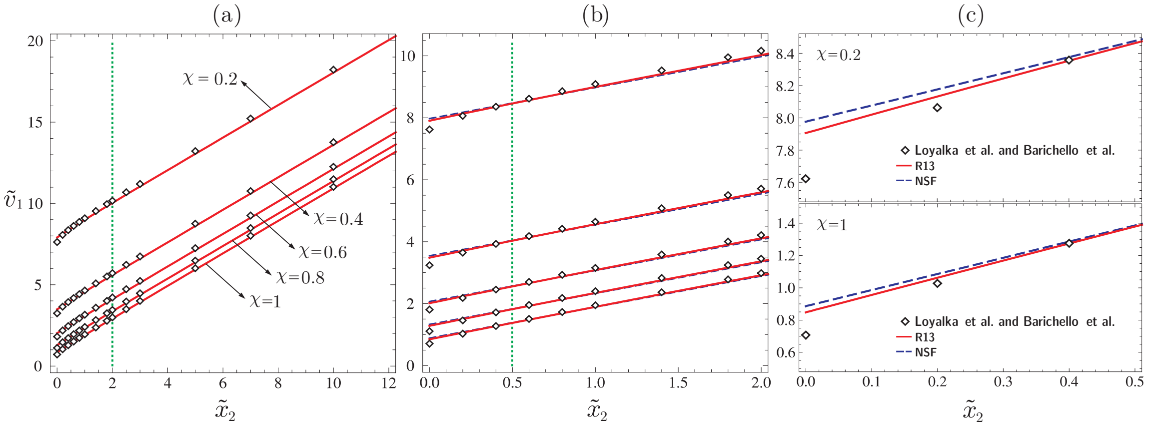

Figure 6.2: Dimensionless velocity profiles in the viscous slip flow (Kramer's problem), obtained for different surface accommodation factors. Solution for the linearized NSF (dashed blue line) and linearized R13 (continuous red line) are compared to the linearized Boltzmann equation data (diamonds). Velocity distributions are shown within different distances from the wall. (*a*) For a large distance from the wall, NSF and R13 look identical, both correctly predict the bulk solution. (b, c) The same velocity profiles near the wall, where the Knudsen layers affect the profiles. Knudsen layers are absent in the Navier–Stokes–Fourier solution (straight line), while they introduce small curvature to the linear R13 solutions.

In Ref. [59], Kramer's problem is solved using several extended systems, including the R13 equations, where the exact boundary value from DSMC computations is forced on solutions of the macroscopic transport equations, and accuracy of the solutions are judged based on their bulk values. A similar comparison is conducted in [55]. Since the curvature of Knudsen boundary layers for the R13 equations is smaller than the actual curvature (from DSMC) this comparison procedure lets the R13 equations appear worse than they actually are. As Fig. 6.2 shows, the lack of curvature is compensated by extra slip, so that the R13 result matches the kinetic result in the bulk.

Knudsen layers in isothermal viscous slip flow, as given by the linear R13 equations, are depicted in Fig. 6.3. They construct the tangential heat flux $\tilde{q}_1$, which is a pure rarefaction effect. In shear–driven flows, larger accommodation factors yield more friction at the boundary and reduce the tangential heat flux.

In Fig. 6.4, the coefficient C_4, which represents the viscous slip velocity, is plotted versus the accommodation factor. The viscous slip velocity does not include the Knudsen layer contribution to slip, and that is why both R13 and NSF yield similar results. The accurate evaluation of C_4

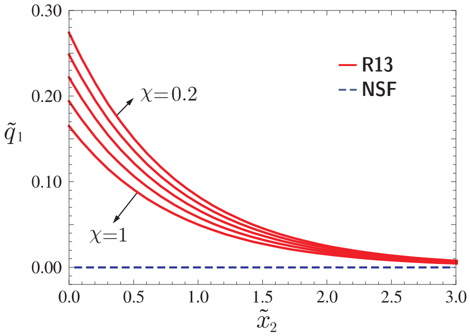

Figure 6.3: Dimensionless parallel heat flux in the viscous slip flow (Kramer's problem), obtained for different surface accommodation factors. The streamwise heat flux is a pure rarefaction effect, thus, it only includes Knudsen layers. This streamwise heat flow which is not forced by temperature gradient is beyond the resolution of the classical NSF equations. Solutions for linearized NSF (dashed blue line) and linearized R13 (continuous red line) are presented.

guaranties convergence of the solution to the bulk values. In the R13 system, the Knudsen layer bridges the boundary values to the bulk solution.

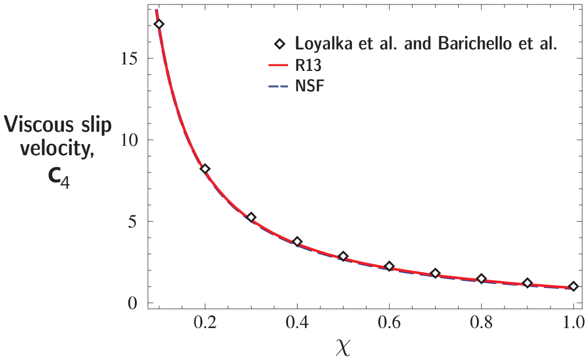

Figure 6.4: Viscous slip velocity vs. momentum accommodation factor of the surface. Contribution of Knudsen boundary layers on slip velocity is not considered in the plot. Larger accommodation factors which represent rough surfaces, reduce the sliding velocity on the surface. The R13 and NSF systems predict the slip velocity with the same accuracy, which shows good agreement with Boltzmann equation data.

6.4.2 Thermal Creep Flow

Rarefaction effects in thermally–driven flow over a surface is widely discussed in kinetic theory, see Refs. [13, 64, 65, 72, 80, 98].

For the thermal creep flow the integrating constants $\mathbf{C}_1$–$\mathbf{C}_4$ in solution (6.59) are determined from the boundary conditions (6.43) and (6.45) as

$$\mathbf{C}_1^{\mathrm{R13}} = \mathbf{C}_2^{\mathrm{R13}} = 0, \qquad \mathbf{C}_3^{\mathrm{R13}} = \frac{15\sqrt{2}\,\bar{\chi}}{\sqrt{35\pi}+6\sqrt{2}\,\bar{\chi}}\mathrm{Kn}\,\tau, \qquad \mathbf{C}_4^{\mathrm{R13}} = \frac{-\sqrt{35\pi}}{2\left(\sqrt{35\pi}+6\sqrt{2}\,\bar{\chi}\right)}\mathrm{Kn}\,\tau,$$
$$\mathbf{C}_1^{\mathrm{NSF}} = 0, \qquad \mathbf{C}_4^{\mathrm{NSF}} = \frac{1}{2}\left(1-2\,\mathrm{Kn}\right)\tau, \tag{6.63}$$

with $\bar{\chi} = \chi/\left(2-\chi\right)$. In the bulk flow, the velocity distribution is uniform ($\partial\tilde{v}_1/\partial\tilde{x}_2 = 0$) and the heat flux is finite. These conditions give $\mathbf{C}_1 = \mathbf{C}_2 = 0$ in the R13 solution.

For different accommodation factors, the creep velocities over the plate, as given by Eq. (6.59), are illustrated in Fig. 6.5. The Knudsen number and wall temperature gradient in [13, 72] are related to our definitions by $\mathrm{Kn} = 1/\sqrt{2}$ and $\tau = \sqrt{2}$, respectively. For all accommodation factors, NSF predicts a constant velocity (plug flow) since the slip condition (6.45) reduces to $\tilde{\mathcal{V}}_1^{\mathrm{NSF}} = \frac{1}{2}\mathrm{Kn}\,\tau$, i.e., slip condition does not depend on χ. R13, however, exhibits a good agreement with the BGK Boltzmann data of Refs. [13, 72]. As depicted in Fig. 6.5a, our simplified R13 model underestimates the bulk velocity specifically for diffusive walls. This difference might be addressed to the assumption of one–dimensional flow in our approach, or, to ambiguities in scaling the Boltzmann solutions. In Fig. 6.5b,c the velocity distribution near the wall is magnified; similar to Kramer's problem, Knudsen layers are visible.

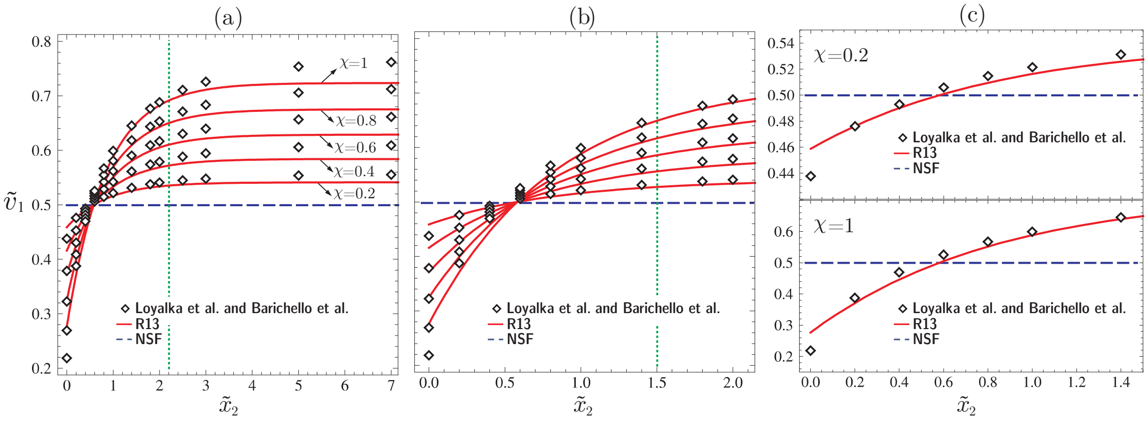

Figure 6.5: Dimensionless velocity profiles in creep flow for different accommodation factors. Solutions for the linearized NSF (dashed blue line) and linearized R13 (continuous red line) are compared to linearized Boltzmann equation data (diamonds). Velocity distributions are shown within different distances from the wall. The NSF solution is a constant, which does not depend on the surface accommodation factor. (*a*) The bulk solution is predicted by the R13 equations with small error (about 3%). (*b, c*) The same velocity profiles near the wall, where the Knudsen layers affect the curvature of the profiles. Knudsen layers are absent in the constant Navier–Stokes–Fourier solution.

In the creep flow, similar to the Kramer's problem, Knudsen layers appear in the tangential heat flux solution, Eq. (6.59). Figure 6.6 depicts the counterstream heat flux for both NSF and R13 systems. In the R13 solution, $\tilde{q}_1$ is a superposition of Knudsen layers and bulk solution (Fourier's law). Diffusive walls reduce the tangential heat flow at the boundary, however, they yield larger velocities in the bulk.

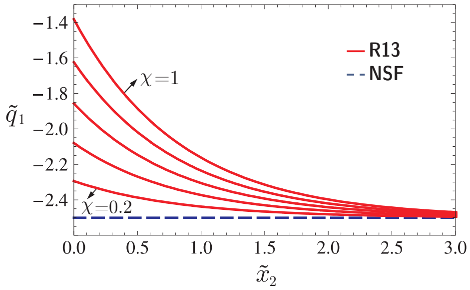

Figure 6.6: Dimensionless parallel heat flux in the thermal creep flow, calculated for different surface accommodation factors. In the NSF equations tangential heat flux is given by Fourier's law (dashed blue line), while in the R13 systems streamwise heat flux is a superposition of bulk solution (Fourier's law) and Knudsen boundary layers (continuous red line).

The constant $\mathbf{C}_4$ versus accommodation factor is plotted in Fig. 6.7. As shown, in contrast to NSF, the R13 system provides an acceptable estimate of the low speed thermal slip on the wall, compared to kinetic data in [65, 72].

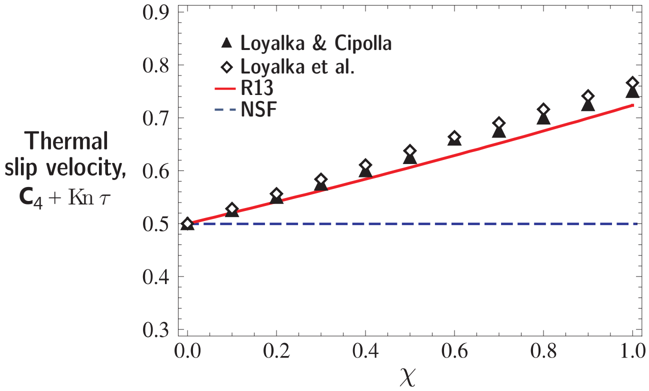

Figure 6.7: Thermal slip velocity vs. momentum accommodation factor of the surface. Contribution of Knudsen boundary layers on slip velocity is not considered in the plot. In contrast to the viscous slip problem, larger accommodation factors which represent rough surfaces, increase the sliding velocity on the surface. The R13 gives outstanding agreement with the linearized Boltzmann equation data. The NSF solution is independent of surface accommodation coefficients and leads to a constant slip velocity.

The assumption of one–dimensional velocity in thermally–driven flow can be justified using the linear solutions (6.59) with the evaluated constants in (6.63). For two–dimensional steady flow the continuity equation can be written as

$$\tilde{\rho}\frac{\partial \tilde{v}_1}{\partial \tilde{x}_1} + \tilde{v}_1 \frac{\partial \tilde{\rho}}{\partial \tilde{x}_1} + \frac{\partial \tilde{\rho}\tilde{v}_2}{\partial \tilde{x}_2} = 0,$$

where, according to the linear solution the first term is zero and the second one is of order τ^2, since $\partial\tilde{\theta}/\partial\tilde{x}_1 = -\partial\tilde{\rho}/\partial_{\tilde{x}_1} = \tau$. Therefore, the last term should be of order τ^2, and thus is zero in the linear limit. This argument gives $\tilde{\rho}\tilde{v}_2 = \text{const.}$, and the boundary condition of impermeable walls yields $\tilde{v}_2 = 0$.

Chapter 7

Linear Theory for Parallel–plate Channel Flows

Linearized R13 equations in planar geometry were presented in Sec. 4.4.1. In this chapter these linear equations are employed to analytically investigate linear rarefaction effects in parallel–plate channel flows[1]. It is straightforward to describe parallel–plate channel flows as a specific case of half–space flows in a finite domain. Accordingly, in this chapter we frequently refer to our results in Chap. 6.

7.1 Couette, Force–driven Poiseuille, and Transpiration Flows in Parallel–plate Channels

The fundamental problems of rarefied Couette and force–driven Poiseuille flows in parallel–plate channels have been investigated form different perspectives. It is well–known that a wealth of nonequilibrium effects exist in dilute Couette and Poiseuille flows, which the Navier–Stokes–Fourier theory cannot describe. Heat flux parallel to flow direction which is not forced by temperature gradient [7, 12, 42, 119, 120, 123], non–uniform pressure profile [7, 73, 117, 118, 123] and characteristic temperature dip in Poiseuille flow [1, 7, 73, 117, 118, 129, 130, 133] are among the most prominent effects. Moreover, in rarefied condition, the formation of Knudsen boundary layers affects the bulk solution [79, 85, 98], and the so–called Knudsen minimum [51] can be observed. In the NSF theory

---

[1] The presented materials in this chapter are published in Refs. [114, 115].

the Knudsen minimum can be captured only with the second–order slip condition on the walls [39, 58].

As discussed for the half–space creep flow, thermal creep phenomena occur in gases when nonuniform temperature distributions are applied in the flow boundaries [98]. In the case of channel flows, when the creep velocity spreads over the whole channel width, the flow is called *thermal transpiration flow* [84]. Experimental observations by Knudsen proved the existence of a pumping effect in transpiration flows; he obtained a ten–fold pressure increase between inlet and outlet of a series of heated tubes [51, 52].

Nowadays, nonuniformly heated channels are used in miniaturized devices as pumps or compressors with no moving parts, referred as Knudsen pumps or compressors, which operate based on thermal transpiration flow [41, 102]. Furthermore, thermally–driven and pressure–driven flows may be combined in order to control mass and energy flow rates in miniaturized devices.

7.2 Linearized R13 Equations for Couette, Force–driven Poiseuille, and Transpiration Flows in Parallel–plate Channels

We assume steady state flows confined between two infinite planar parallel plates, see Fig. 7.1. Comparison of Figs. 6.1 and 7.1 shows that Couette, force–driven Poiseuille, and thermal transpiration flows can be respectively considered as viscous slip flow (Kramer's problem), force–driven flow, and thermal creep flow in a finite domain, H, between the plates. Accordingly, in the linear limit, all the assumptions in (6.40) that we considered for the half–space problems hold for their counterparts in channel problems.

The linearized R13 equations as presented in Eqs. (6.41)–(6.55) and their solutions [cf. Eqs. (6.57), (6.59), and (6.61)] can be directly used to study processes in micro–channels. However, evaluation of the integrating constants requires boundary conditions at both lower and upper walls.

7.3 Solutions for Parallel–plate Channel Flows

Similar to the half–space problems, in the linear limit it suffices to consider the solution of the velocity problem. For convenience, the exponential terms in solutions (6.57), (6.59) with (6.61) are expressed as superposition of hyperbolic sine and cosine functions.

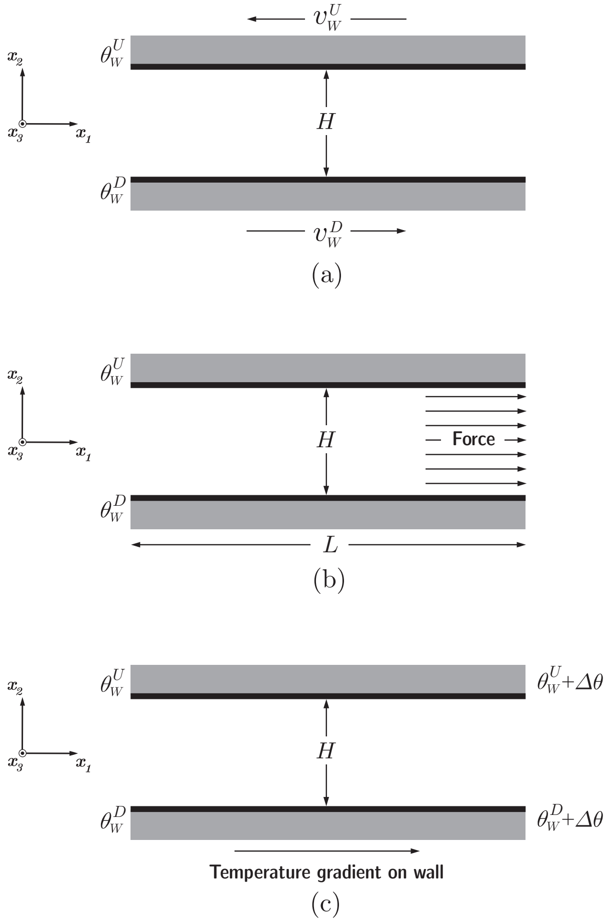

Figure 7.1: (a) In Couette flow the walls of the channel are moving in opposite directions $\pm v_W$, and the gas moves as the result of shear stress diffusion from the walls. (b) In Force–driven Poiseuille flow the gas is driven through the action of an external (body) force. (c) In transpiration flow,gas is accelerated due to the temperature gradients on the walls. Wall temperatures θ_W^U and θ_W^D are symmetric around the centerline, $x_2 = 0$.

For Maxwellian molecules with coefficients (4.15), the general solution of the system (6.41) and (6.42) reads

$$\begin{aligned} \tilde{\sigma}_{12} &= \underline{\mathbf{C}_1 + \tilde{G}_1 \tilde{x}_2}, \qquad \tilde{v}_1 = \underline{\mathbf{C}_4 - \frac{\tilde{G}_1}{2\,\mathrm{Kn}}\,\tilde{x}_2^2 - \frac{\mathbf{C}_1}{\mathrm{Kn}}\,\tilde{x}_2} - \frac{2}{5}\tilde{q}_1, \\ \tilde{q}_1 &= -\frac{3}{2}\,\mathrm{Kn}\,\tilde{G}_1 \underline{- \frac{15}{4}\,\mathrm{Kn}\,\tau} + \mathbf{C}_2 \sinh\left(\frac{\sqrt{5}}{3\,\mathrm{Kn}}\tilde{x}_2\right) + \mathbf{C}_3 \cosh\left(\frac{\sqrt{5}}{3\,\mathrm{Kn}}\tilde{x}_2\right), \end{aligned} \tag{7.1}$$

which holds for all the considered flow problems; the body force $\tilde{G}_1$ must be set zero except for Poiseuille flow, and $\tau = \partial\tilde{\theta}/\partial\tilde{x}_1$ is zero except for transpiration flow. For channel flows, $\mathrm{Kn} = \lambda_0/H$ is the Knudsen number at the reference equilibrium state, with $\lambda_0 = \mu_0\sqrt{\theta_0}/p_0$ as the reference mean free path, i.e.,

$$\mathrm{Kn} = \frac{\mu_0 \sqrt{\theta_0}}{p_0 H}. \tag{7.2}$$

The hyperbolic functions describe Knudsen layer contributions to the solutions. The coefficients $\mathbf{C}_1$–$\mathbf{C}_4$ must be evaluated using the linearized boundary conditions. Since in the Couette flow $v_1(x_2) = -v_1(x_2)$ and $q_1(x_2) = -q_1(x_2)$ then $\mathbf{C}_3 = \mathbf{C}_4 = 0$. In Poiseuille and transpiration flows, due to the symmetry of the solutions with respect to the centerline $\mathbf{C}_1 = \mathbf{C}_2 = 0$. These conditions reduce the number of unknown integrating constants to two, which necessitate the implementation of two boundary conditions [cf. Eq. (6.43)] in one of the channel walls. Application of boundary conditions requires $n_2 = +1$ and $n_2 = -1$ for lower and upper walls, respectively, see Fig. 7.1.

7.4 Results and Discussion for Parallel–plate Channel Flows

In this section, the results of analytical solutions for linearized Couette, force–driven Poiseuille, and transpiration flows are illustrated, and compared to kinetic simulations.

7.4.1 Couette Flow in a Parallel–plate Channel

For Couette flow, solution (7.1) reduces to [compare with (6.57)]

$$\tilde{\sigma}_{12} = \underline{\mathbf{C}_1}, \qquad \tilde{v}_1 = \underline{-\frac{\mathbf{C}_1}{\mathrm{Kn}}\tilde{x}_2} - \frac{2\,\mathbf{C}_2}{5}\sinh\left(\frac{\sqrt{5}}{3\,\mathrm{Kn}}\tilde{x}_2\right), \qquad \tilde{q}_1 = \mathbf{C}_2 \sinh\left(\frac{\sqrt{5}}{3\,\mathrm{Kn}}\tilde{x}_2\right). \tag{7.3}$$

Couette flow, similar to Kramer's problem, leads to a constant shear stress distribution. The structure of the Knudsen layer, $\tilde{q}_1$, is approximated with a hyperbolic sine function. Superpositions of the Knudsen layer and the linear bulk solution $-\mathbf{C}_1\,\tilde{x}_2/\mathrm{Kn}$ yields curvature on the velocity profiles near the wall.

Figure 7.2 shows the dimensionless R13 solutions for the velocity problem for Couette flow. The obtained results are compared to DSMC simulations at $\mathrm{Kn} = \{0.05, 0.1, 0.5\}$ for argon. The DSMC results are obtained for Maxwell molecules based on Bird's code [17], where at standard conditions (101,325 Pa and 0°C) molecular mass, viscosity, and viscosity exponent for argon read $m = 66.3 \times 10^{-27}$ kg, $\mu_0 = 2.117 \times 10^{-5}$ Ns/m^2, and $\varpi = 0.81$. The walls move with $v^W = \pm 100$ m/s ($\tilde{v}^W = \pm 0.4195$) at temperature 273 K ($\tilde{\theta}^W = 1$). As depicted, for small Knudsen numbers, where the case is close to classical hydrodynamics, the profiles are in good agreement with DSMC results.

For larger Knudsen numbers, where the rarefaction effects are strong, some difference to the DSMC results is observed, especially at the boundaries. The tangential heat flux, q_1, which vanish in classical hydrodynamics, is predicted with acceptable accuracy.

For this problem, numerical solutions for the fully nonlinear R13 equations are available in [121].

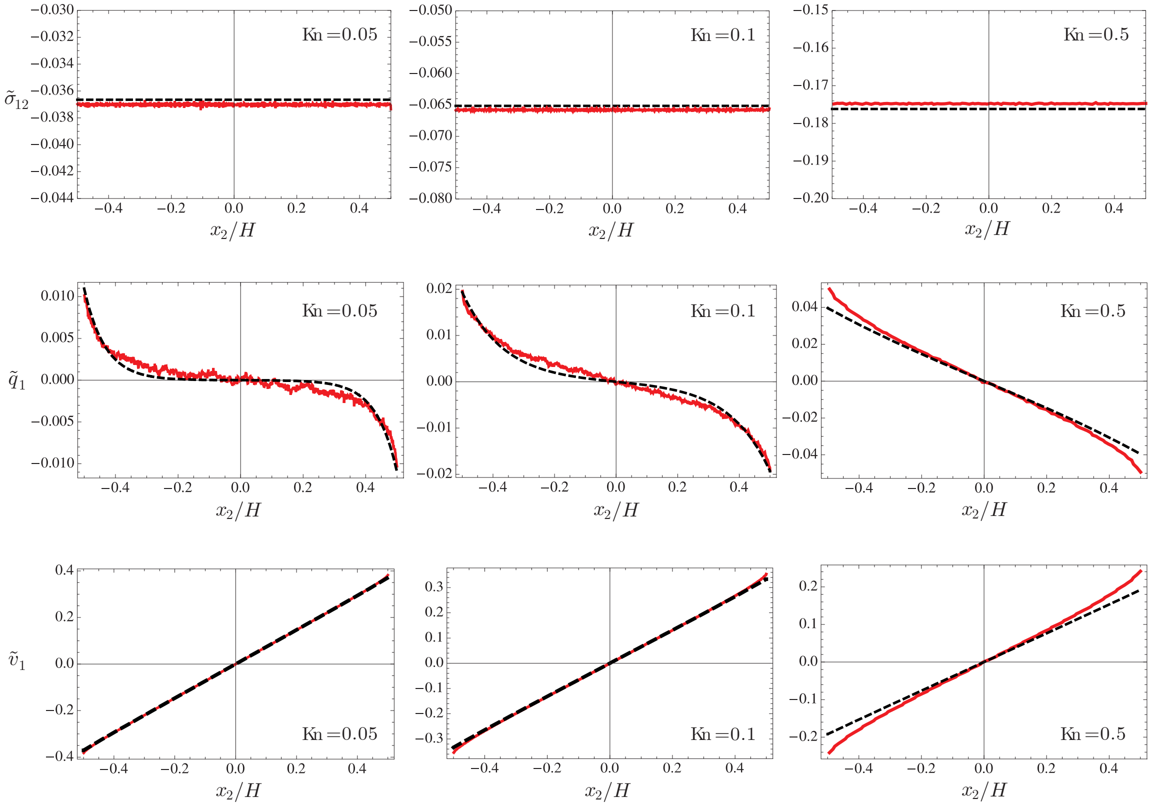

Figure 7.2: Solutions for the linearized velocity problem across the channel for Couette flow with argon. Wall temperature and velocities are 273 K and ±100 m/s. Comparison between linear R13 (dashed lines) and DSMC (solid lines).

7.4.2 Force–driven Poiseuille Flow in a Parallel–plate Channel

For Poiseuille flow, solution (7.1) reduces to [compare with (6.61)]

$$\tilde{\sigma}_{12} = \underline{\tilde{G}_1 \tilde{x}_2}, \qquad \tilde{v}_1 = \underline{\mathbf{C}_4 - \frac{\tilde{G}_1}{2\,\mathrm{Kn}} \tilde{x}_2^2} + \frac{3}{5}\,\mathrm{Kn}\,\tilde{G}_1 - \frac{2\,\mathbf{C}_3}{5} \cosh\left(\frac{\sqrt{5}}{3\,\mathrm{Kn}}\tilde{x}_2\right),$$

$$\tilde{q}_1 = -\frac{3}{2}\,\mathrm{Kn}\,\tilde{G}_1 + \mathbf{C}_3 \cosh\left(\frac{\sqrt{5}}{3\,\mathrm{Kn}}\tilde{x}_2\right). \tag{7.4}$$

Figure 7.3 shows the solution of the linear velocity problem for Poiseuille flow. The dimensionless external force is $\tilde{G}_1 = 0.2355$, and the walls are stationary at 273 K ($\tilde{\theta}^W = 1$). The results for $\mathrm{Kn} = 0.072$ are compared to DSMC simulations [129, 133][2].

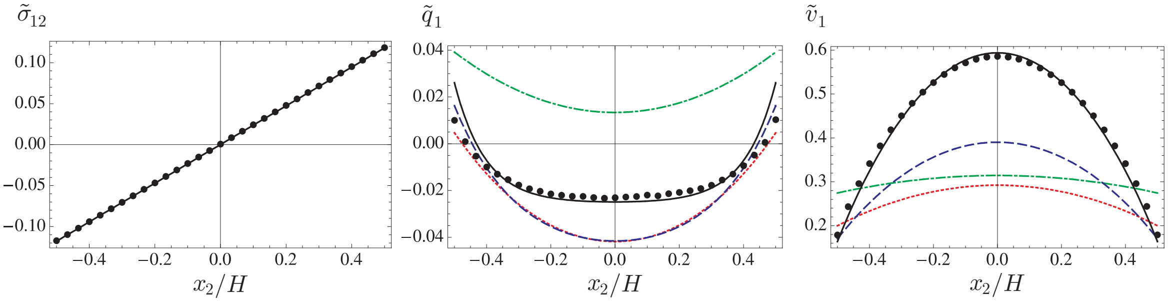

Figure 7.3: Solution of the linear velocity problem for force–driven Poiseuille flow with dimensionless force $\tilde{G}_1 = 0.2355$. Profiles are computed for $\mathrm{Kn} = 0.072$ (solid line), $\mathrm{Kn} = 0.15$ (dashed line), $\mathrm{Kn} = 0.4$ (dotted line), and $\mathrm{Kn} = 1.0$ (dashed–dotted line). For $\mathrm{Kn} = 0.072$ comparison with DSMC simulations (circles) is presented.

The velocity profiles in Fig. 7.3 show a decrease of flow velocity in the middle of the channel as the Knudsen number increases, however, the slip is increasing, due to decrease of friction. That is why the velocity curve for $\mathrm{Kn} = 1$ lies above the curve of $\mathrm{Kn} = 0.4$. Owing to this behavior, the mass flow rate

$$M_P = \sqrt{2}\int_{-1/2}^{1/2} |\tilde{v}_1| \, d\tilde{x}_2, \tag{7.5}$$

as a function of Knudsen number exhibits a minimum around $\mathrm{Kn} = 0.7$, which is known as Knudsen minimum, or Knudsen paradox [51]. For Eq. (7.5) the velocity function in given by (7.4) and the factor $\sqrt{2}$ is used for consistency with the kinetic data.

The normalized mass flow rate $M_P/\tilde{G}_1$ as a function of the Knudsen number is plotted in Fig. 7.4 for linearized R13, linearized Navier–Stokes–Fourier (with first– and second–order slip conditions), and linearized Boltzmann equation [42, 70, 71, 79]. The plots correspond to different accommodation coefficients $\chi = \{0.5, 0.75, 1.0\}$. For all accommodation coefficients a similar pattern is observed, where smooth channel walls, i.e., small χ, allow larger flow rates. As shown, NSF with first–order slip condition fails to capture the minimum, but the second–order slip condition [cf. Eq. (6.45)] yields a minimum around $\mathrm{Kn} = 0.3$. R13 shows good agreement with the kinetic data up to $\mathrm{Kn} = 0.6$, with less than 7% error (= (Data − R13) /R13). Enhancement of the R13 results must be addressed to its third–order boundary conditions and the contribution of the Knudsen layer, $\tilde{q}_1$, to the velocity

---

[2] The author thanks Dr. Kun Xu (Hong Kong University of Science and Technology) for providing the DSMC data for Poiseuille flow.

solution. Comparison of our results with lattice Boltzmann data in [49, 50] shows that our simple theoretical approach provides a more accurate prediction of the Knudsen minimum phenomenon.

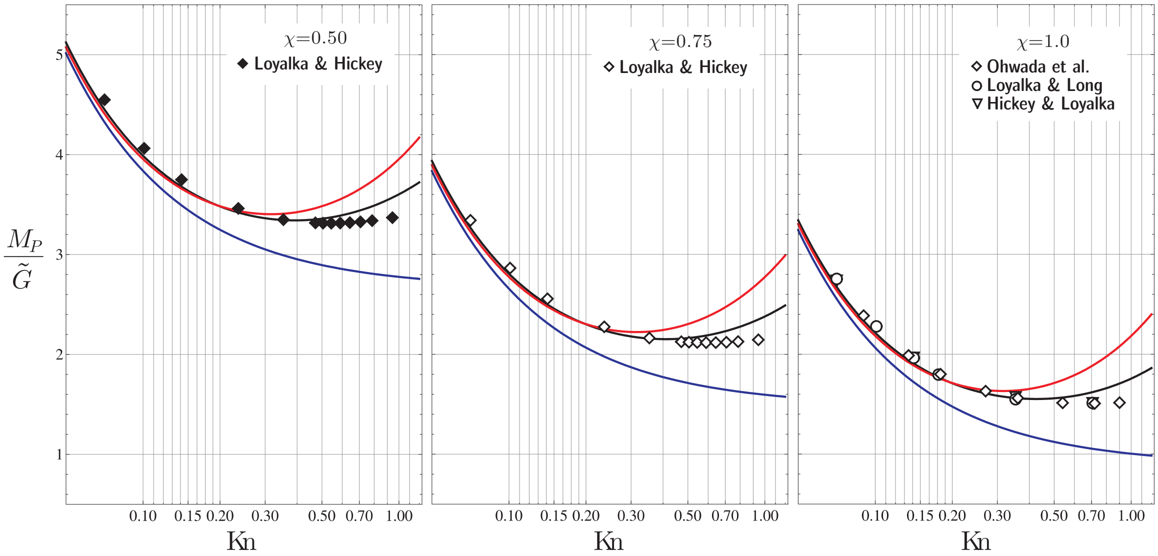

Figure 7.4: The effects of Knudsen number and surface accommodation on the mass flow rate in Poiseuille flow between parallel plates. Navier–Stokes–Fourier with first–order slip condition (long–dashed blue line), Navier–Stokes–Fourier with second–order slip condition (dashed red line), and regularized 13–moment with third–order boundary conditions (solid black line) are compared to kinetic data (symbols) [70, 42, 71, 79] for $\chi = \{0.5, 0.75, 1.0\}$. It is shown that second–order slip condition improves the NSF solution in transition flow regime.

The explicit expression for M_P, obtained from the R13 system, reads

$$M_P = \sqrt{2}\left[-\frac{\tilde{G}_1}{24\,\mathrm{Kn}} + \frac{3\,\tilde{G}_1}{5}\,\mathrm{Kn} - \frac{12\,\mathbf{C}_3}{5\sqrt{5}}\,\mathrm{Kn}\,\sinh\left(\frac{\sqrt{5}}{6\,\mathrm{Kn}}\right) + \mathbf{C}_4\right], \tag{7.6}$$

in which the integrating constants are

$$\mathbf{C}_3 = \frac{5\,\tilde{G}_1}{24}\,\frac{3\sqrt{2\pi} + 56\,\bar{\chi}\,\mathrm{Kn}}{\sqrt{10\pi}\,\sinh\left(\frac{\sqrt{5}}{6\,\mathrm{Kn}}\right) + 6\,\bar{\chi}\cosh\left(\frac{\sqrt{5}}{6\,\mathrm{Kn}}\right)}, \tag{7.7a}$$

$$\mathbf{C}_4 = \tilde{G}_1\frac{\bar{\chi}\left[90\,\bar{\chi} + 195\sqrt{2\pi}\,\mathrm{Kn} + 448\,\bar{\chi}\,\mathrm{Kn}^2\right]\coth\left(\frac{\sqrt{5}}{6\,\mathrm{Kn}}\right) + \sqrt{5}\left[60\pi\,\mathrm{Kn} + \left(15 + 28\,\mathrm{Kn}^2\right)\sqrt{2\pi}\,\bar{\chi}\right]}{120\,\bar{\chi}\,\mathrm{Kn}\left[\sqrt{10\pi} + 6\,\bar{\chi}\coth\left(\frac{\sqrt{5}}{6\,\mathrm{Kn}}\right)\right]}, \tag{7.7b}$$

with $\bar{\chi} = \chi/\left(2-\chi\right)$.

7.4.3 Transpiration Flow in a Parallel–plate Channel

For transpiration flow, the solution (7.1) reads [compare with (6.59)]

$$\tilde{\sigma}_{12} = 0, \qquad \tilde{v}_1 = \underline{\mathsf{C}_4 + \frac{3}{2}\,\mathrm{Kn}\,\tau} - \frac{2\,\mathsf{C}_3}{5}\cosh\left(\frac{\sqrt{5}}{3\,\mathrm{Kn}}\tilde{x}_2\right), \qquad \tilde{q}_1 = \underline{-\frac{15}{4}\,\mathrm{Kn}\,\tau} + \mathsf{C}_3\cosh\left(\frac{\sqrt{5}}{3\,\mathrm{Kn}}\tilde{x}_2\right), \tag{7.8}$$

where $\mathsf{C}_4 + 3\,\mathrm{Kn}\,\tau/2$ in the velocity solution represents the slip velocity (temperature–driven plug flow). The solutions in (7.8) shows that in the linear limit nonequilibrium effects arise only for the tangential heat flux and velocity, while the shear stress remains in the reference state.

With the help of the fully linear boundary conditions [Eq. (6.43)] the unknown integrating constants are found as

$$\mathsf{C}_3 = \tau\,\mathrm{Kn}\,\frac{45\,\bar{\chi}\sqrt{\dfrac{2}{\pi}}}{12\,\bar{\chi}\sqrt{\dfrac{2}{\pi}}\cosh\left(\dfrac{\sqrt{5}}{6\,\mathrm{Kn}}\right) + 4\sqrt{5}\sinh\left(\dfrac{\sqrt{5}}{6\,\mathrm{Kn}}\right)}, \tag{7.9a}$$

$$\mathsf{C}_4 = \tau\,\mathrm{Kn}\,\frac{-3\sqrt{5}\sinh\left(\dfrac{\sqrt{5}}{6\,\mathrm{Kn}}\right)}{12\,\bar{\chi}\sqrt{\dfrac{2}{\pi}}\cosh\left(\dfrac{\sqrt{5}}{6\,\mathrm{Kn}}\right) + 4\sqrt{5}\sinh\left(\dfrac{\sqrt{5}}{6\,\mathrm{Kn}}\right)}. \tag{7.9b}$$

Profiles for normalized velocity and parallel heat flux, according to solution (7.8) are depicted in Fig. 7.5. These results are compared with direct numerical solutions of the linear Boltzmann equation from Ref. [79]. The relation between our Knudsen number [Eq. (7.2)] and the Knudsen number in [79] is $\mathrm{Kn} = 1/(\sqrt{2}\,k)$. The plots are shown for four different Knudsen numbers and perfectly diffusive walls, $\chi = 1$. As postulated by Fourier's law, the tangential heat flow is in the opposite direction of the temperature gradient, i.e., from hot to cold. The decrease of heat flow close to the walls is due to the non–Fourier contribution in the Knudsen layer, i.e., the hyperbolic cosine function in Eq. (7.8). The slip velocity on the walls is predicted with an outstanding accuracy. This gives further evidence of the reliability of the applied boundary conditions. Unlike the heat flux, the velocity plots show that mass flow is in the direction of the temperature gradient. As expected, the R13 system is reliable within the transition regime ($\mathrm{Kn} \lesssim 0.5$), hence, for $k = 0.6$ (or $\mathrm{Kn} = 0.53$) some deviations from the Boltzmann solution appear in the bulk flow.

While in the force–driven Poiseuille flow mass flux versus Knudsen number exhibits the so–called Knudsen minimum, in the temperature–driven flow, mass flux increases with Knudsen number. To

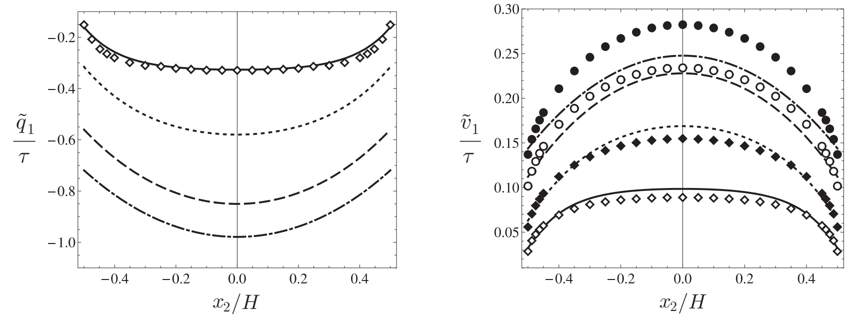

Figure 7.5: Dimensionless distribution of normalized heat flux $\tilde{q}_1/\tau$ and velocity $\tilde{v}_1/\tau$ across the channel are show for transpiration flow. The R13 results (lines) which are obtained for fully diffusive walls $\chi = 1$ in different Knudsen numbers are compared to kinetic data (symbols) from Ref. [79]. For the sake of consistency in comparison, the dimensionless kinetic data are multiplied with $\sqrt{2}$. (Solid line, white diamonds) $\mathrm{Kn} = 0.088$; (dotted line, black diamonds) $\mathrm{Kn} = 0.177$; (dashed line, white circles) $\mathrm{Kn} = 0.353$; (dash–dotted line, black circles) $\mathrm{Kn} = 0.530$.

show this, similar to Refs. [70, 79, 92] we define the mass flow rate M_T as

$$M_T = \sqrt{2} \int_{-1/2}^{+1/2} |\tilde{v}_1| \, d\tilde{x}_2, \tag{7.10}$$

where the required velocity function is given in Eq. (7.8), and the factor $\sqrt{2}$ is used for proper scaling with the kinetic data. This integral yields a linear expression in τ for the mass flow rate,

$$M_T = \tau \, \frac{3\,\mathrm{Kn}}{2\sqrt{2}} \left(2 - \frac{5\sqrt{\pi} + 36\sqrt{2}\,\bar{\chi}\,\mathrm{Kn}}{5\sqrt{\pi} + 3\sqrt{10}\,\bar{\chi}\coth\left(\dfrac{\sqrt{5}}{6\,\mathrm{Kn}}\right)} \right). \tag{7.11}$$

In Fig. 7.6, our results for the normalized mass flow rate M_T/τ are compared with kinetic data from [70, 79] which are the solutions for linearized Boltzmann equation. In the plots, mass flow rates for different surface accommodation coefficients $\chi = \{1.0, 0.75, 0.5\}$ are compared. As illustrated, for larger Knudsen numbers, smooth channels with small accommodation coefficients allow larger mass flow rates. This occurs due to the slip increase on the channel walls. For fully diffuse walls ($\chi = 1$) our results agree with kinetic data for $\mathrm{Kn} < 0.5$ [cf. plot (a)], while for $\chi = 0.5$ the R13 results are valid for $\mathrm{Kn} < 0.7$, see plot (c). As shown previously for Couette and Poiseuille flows [109, 110, 115, 121], the validity of R13 equations within the transition regime is again confirmed here.

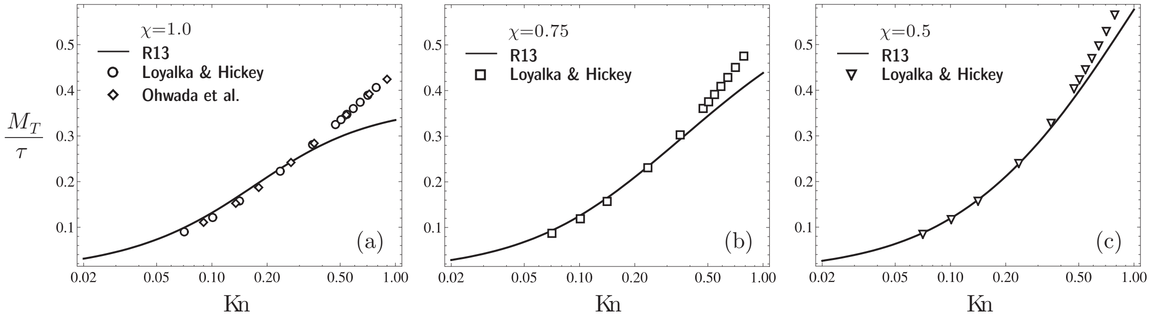

Figure 7.6: The normalized mass flow rate M_T/τ vs. Kn in thermal transpiration flow. The R13 results (solid line) are compared to linearized Boltzmann data (symbols) from Refs. [79, 70]. Dependence of mass flow rate on accommodation coefficient χ are shown in the plots. In transpiration flow mass flow rate diverges infinitely in the free molecular limit when Kn $\to \infty$, and vanishes in the continuum limit, i.e., Kn $\to 0$.

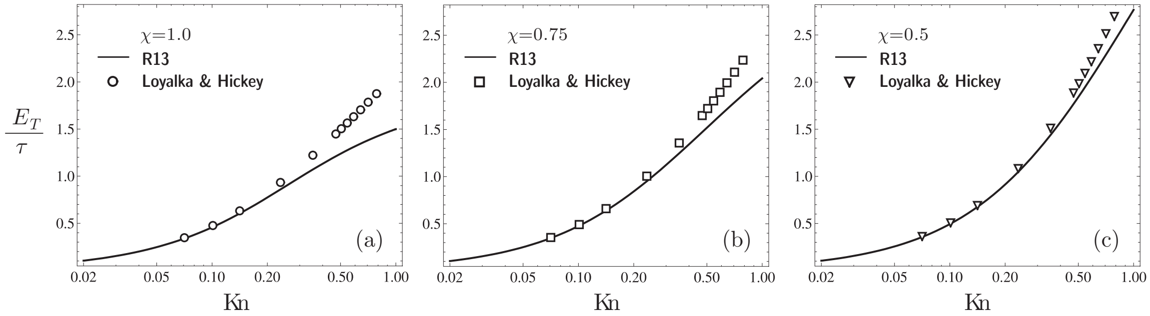

Figure 7.7: The normalized thermal energy flow rate E_T/τ vs. Kn in thermal transpiration flow. The R13 results (solid line) are compared to linearized Boltzmann data (symbols) from Ref. [70]. Dependence of thermal energy flow rate on accommodation coefficient χ are shown in the plots. In transpiration flow energy flow rate diverges infinitely in the free molecular limit when Kn $\to \infty$, and vanishes in the continuum limit, i.e., Kn $\to 0$.

Similar to the mass flow rate, the thermal energy flow rate E_T can be defined as [70, 92]

$$E_T = \sqrt{2} \int_{-1/2}^{+1/2} |\tilde{q}_1| \, d\tilde{x}_2, \tag{7.12}$$

where the required heat flux function is given in Eq. (7.8). This integral yields a linear expression in τ for thermal energy flow rate,

$$E_T = \tau \, \frac{3\,\mathrm{Kn}}{2\sqrt{2}} \left(5 - \frac{36\sqrt{5}\,\bar{\chi}\,\mathrm{Kn}}{\sqrt{10\,\pi} + 6\,\bar{\chi}\,\coth\left(\dfrac{\sqrt{5}}{6\,\mathrm{Kn}}\right)} \right), \tag{7.13}$$

which similar to M_T is a function of dimensionless temperature gradient τ, surface accommodation coefficient χ, and Knudsen number Kn.

In Fig. 7.7, we compare our results for the normalized thermal energy flow rate, E_T/τ, with the kinetic data in [70]. Variations of energy flow rate with respect to χ and Kn is similar to the mass flow rate.

Chapter 8

Linear Theory for Periodically Unsteady Flows in Parallel–plate Channels

8.1 Oscillatory Couette and Pulsating Poiseuille Flows

In oscillatory Couette flow, the gas is confined in a slit between two infinite parallel plates, where one of the plates (upper plate here) oscillates harmonically in its own plane, and the other plate is stationary, see Fig. 8.1a. The velocity of the oscillatory wall is $v_W = V_W \sin(\omega t)$, where ω and V_W are constant frequency and velocity amplitude of the exerted oscillations. The plates are parallel in x_1–direction, separated by distance H, located on $x_2 = \pm H/2$. Both plates are assumed to be isothermal at temperature θ_0.

This flow configuration can be viewed as the limiting case of the classical Stokes' second problem in fluid mechanics, where a semi–infinite expanse of a viscous fluid is bounded by a laterally oscillating flat surface [54]. In Stokes' problem the plate oscillations propagate into the infinite expanse of the surrounding gas. In the oscillatory Couette flow the range of propagation is limited between the walls.

The viscous damping mechanism in oscillatory shear–driven flows is applied in many MEMS designs, including resonant sensors/actuators, microfilters, microaccelerometers, and microbearings

[30].

In pulsating Poiseuille flow both plates of the channel are at rest and a homogeneous oscillating force is driving the process, see Fig. 8.1b. We assume the force to be $g = G \sin(\omega t)$ with amplitude G and frequency ω, acting in x_1–direction. The rest of the setup is equivalent to the oscillatory Couette case. As discussed in the previous section, standard Poiseuille flow without time–depending force is known to exhibit non–intuitive behavior like the Knudsen minimum for small channel widths. Hence, we expect interesting phenomena for the pulsating case.[1],[2]

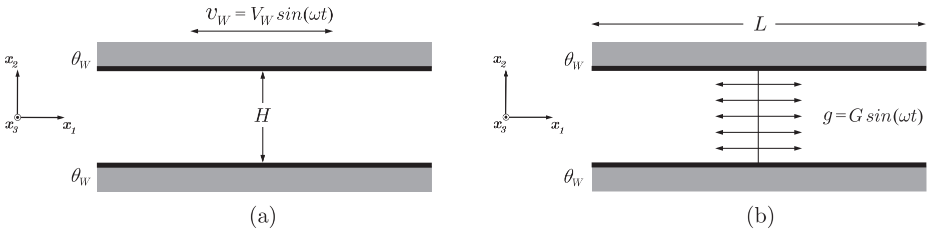

Figure 8.1: (a) In oscillatory Couette flow a viscous fluid between two parallel plates at temperature θ_W, separated by distance H, is excited by lateral oscillations of the top plate. (b) In pulsating Poiseuille flow, plates are stationary and a harmonically pulsating body force is applied. In both problems one–dimensional flows are considered.

8.2 Unsteady and Linearized Velocity Problem for Oscillatory Couette and Pulsating Poiseuille Flows

We assume that in the considered oscillatory problems, the amplitudes are small, hence, nonlinear effects are negligible and the processes can be fairly approximated with linear equations. In the linear limit, similar to the half–space problems and parallel–plate channel flows the assumptions in Eq. (6.40) hold for the considered unsteady problems as well.

For Maxwellian molecules with coefficients in Eq. (4.15) the unsteady velocity problem [cf.

---

[1] The presented materials in this chapter are published in Ref. [112].

[2] Presented materials for pulsating Poiseuille flow stems from a collaboration with Dr. Manuel Torrilhon (ETH Zürich).

Eq. (6.41)] reads

$$\frac{\partial \tilde{v}_1}{\partial \tilde{t}} + \frac{\partial \tilde{\sigma}_{12}}{\partial \tilde{x}_2} = \tilde{G} \sin\left(\tilde{\omega}\tilde{t}\right), \tag{8.1a}$$

$$\frac{\partial \tilde{\sigma}_{12}}{\partial \tilde{t}} + \frac{2}{5}\frac{\partial \tilde{q}_1}{\partial \tilde{x}_2} - \frac{16}{15}\mathrm{Kn}\frac{\partial^2 \tilde{\sigma}_{12}}{\partial \tilde{x}_2^2} = -\frac{\partial \tilde{v}_1}{\partial \tilde{x}_2} - \frac{1}{\mathrm{Kn}}\tilde{\sigma}_{12}, \tag{8.1b}$$

$$\frac{\partial \tilde{q}_1}{\partial \tilde{t}} + \frac{\partial \tilde{\sigma}_{12}}{\partial \tilde{x}_2} - \frac{6}{5}\mathrm{Kn}\frac{\partial^2 \tilde{q}_1}{\partial \tilde{x}_2^2} = -\frac{5}{2}\frac{\partial \tilde{\theta}}{\partial \tilde{x}_1} - \frac{2}{3\,\mathrm{Kn}}\tilde{q}_1, \tag{8.1c}$$

in which the constitutive relations (6.42) are applied. The required boundary conditions are the same as for the steady problems, i.e., Eq. (6.43). The temporal derivatives of $\tilde{v}_1$, $\tilde{\sigma}_{12}$, and $\tilde{q}_1$ are retained within the velocity problem, which introduce the unsteady effects. Two specific dimensionless parameters $\tilde{G}$ and $\tilde{\omega}$ are the force amplitude and frequency. The dimensionless force is introduced in Eq. (4.29), and the dimensionless frequency is defined by

$$\tilde{\omega} = \omega t_0 = \frac{\omega\, H}{\sqrt{\theta_0}}. \tag{8.2}$$

8.3 Solutions for Periodically Unsteady Flows

8.3.1 Oscillatory Couette Flow

For periodically unsteady shear–driven flow the oscillatory force term in (8.1a) is zero. The oscillation velocity at the upper wall is written in complex form as $v_W = V_W \exp(i\omega t)$, where $\Im\left[v_W\right] = V_W \sin(\omega t)$ indicates its imaginary part. As long as the calculations involve only linear operations, we can omit the imaginary sign and proceed with the complex form, taking the imaginary part of the final result.

By using the dimensionless frequency we can write

$$\sin(\omega t) = \sin\left(\tilde{\omega}\tilde{t}\right) = \sin\left(\mathrm{Kn}\,\mathrm{St}^2\,\tilde{t}\right), \tag{8.3}$$

where

$$\mathrm{Kn} = \frac{\mu_0}{\rho_0\sqrt{\theta_0}H}, \qquad \mathrm{St} = H\left(\frac{\rho_0\,\omega}{\mu_0}\right)^{1/2}. \tag{8.4}$$

The parameter St is the Stokes number (at the reference equilibrium state), which is also used in [11, 40, 81, 91]. The Stokes number is defined as the ratio of shear diffusion time scale to the oscillation time scale, and represents the unsteady effects.

R13 case: The long time solutions for (8.1) with $\tilde{G} = 0$ are expected to be plane harmonic waves

$$\tilde{u}\left(\tilde{x}_2, \tilde{t}\right) = \mathcal{U} \exp\left[i\left(\mathrm{Kn}\,\mathrm{St}^2\,\tilde{t} - \tilde{k}\,\tilde{x}_2\right)\right], \qquad \text{where} \qquad \tilde{u} = \left\{\tilde{v}_1, \tilde{q}_1, \tilde{\sigma}_{12}\right\}. \tag{8.5}$$

The constant $\mathcal{U}$ is the complex (dimensionless) amplitude of the waves, $\mathrm{Kn}\,\mathrm{St}^2 = \tilde{\omega}$ is the dimensionless frequency induced by the boundary conditions, and $\tilde{k}$ is the wave number.

After substitution of the harmonic solution into (8.1), it can be written as a homogeneous system,

$$\begin{bmatrix} i\,\mathrm{Kn}\,\mathrm{St}^2 & 0 & -i\,\tilde{k} \\ 0 & i\,\mathrm{Kn}\,\mathrm{St}^2 + \frac{2}{3}\frac{1}{\mathrm{Kn}} + \frac{6}{5}\,\mathrm{Kn}\,\tilde{k}^2 & -i\,\tilde{k} \\ -i\,\tilde{k} & -\frac{2}{5}\,i\,\tilde{k} & i\,\mathrm{Kn}\,\mathrm{St}^2 + \frac{1}{\mathrm{Kn}} + \frac{16}{15}\,\mathrm{Kn}\,\tilde{k}^2 \end{bmatrix} \begin{bmatrix} \tilde{v}_1 \\ \tilde{q}_1 \\ \tilde{\sigma}_{12} \end{bmatrix} = \begin{bmatrix} 0 \\ 0 \\ 0 \end{bmatrix}, \tag{8.6}$$

which serves as an equation for $\tilde{k}$. The dispersion relation, which relates $\tilde{k}$ and $\tilde{\omega}$, results from the requirement that the system (8.6) has nontrivial solutions, $\det[\cdot] = 0$. This gives two pairs of solutions with opposite signs, $\tilde{k} \in \left\{\tilde{k}_\alpha\left(\mathrm{Kn}, \mathrm{St}\right), \alpha = 1, 2, 3, 4\right\}$.

In order to relate the general solution to the boundary conditions, we write (8.5) as

$$\tilde{u}\left(\tilde{x}_2, \tilde{t}\right) = U\left(\tilde{x}_2\right) \exp\left(i\,\mathrm{Kn}\,\mathrm{St}^2\,\tilde{t}\right) \qquad \text{with} \qquad U = \left\{V_1, Q_1, \Sigma_{12}\right\}. \tag{8.7}$$

This form of the solution transforms the PDEs in (8.1) to the ODEs,

$$i\,\mathrm{Kn}\,\mathrm{St}^2\,V_1 + \frac{d\Sigma_{12}}{d\tilde{x}_2} = 0, \tag{8.8a}$$

$$i\,\mathrm{Kn}\,\mathrm{St}^2\,\Sigma_{12} + \frac{2}{5}\frac{dQ_1}{d\tilde{x}_2} + \frac{dV_1}{d\tilde{x}_2} - \frac{16}{15}\,\mathrm{Kn}\frac{d^2\Sigma_{12}}{d\tilde{x}_2^2} = -\frac{1}{\mathrm{Kn}}\Sigma_{12}, \tag{8.8b}$$

$$i\,\mathrm{Kn}\,\mathrm{St}^2\,Q_1 + \frac{d\Sigma_{12}}{d\tilde{x}_2} - \frac{6}{5}\,\mathrm{Kn}\frac{d^2Q_1}{d\tilde{x}_2^2} = -\frac{2}{3\,\mathrm{Kn}}Q_1, \tag{8.8c}$$

which govern the amplitude distribution in the gas between the plates. Based on the solution of the dispersion relation (8.6), the solution for Σ_{12} is a superposition of the solutions

$$\Sigma_{12} = \sum_{\alpha=1}^{4} \mathsf{C}_\alpha \exp\left(-i\,\tilde{k}_\alpha\,\tilde{x}_2\right), \tag{8.9a}$$

where the constants C_α must be determined from boundary conditions. The solutions for velocity and heat–flux follow from (8.8) as

$$V_1 = -\frac{1}{i\,\mathrm{Kn}\,\mathrm{St}^2}\frac{d\Sigma_{12}}{d\tilde{x}_2}, \tag{8.9b}$$

$$Q_1 = -\frac{1}{i\,\mathrm{Kn}\,\mathrm{St}^2 + 2/(3\,\mathrm{Kn})}\left(\frac{6}{5}\,\mathrm{Kn}\frac{d^2Q_1}{d\tilde{x}_2^2} - \frac{d\Sigma_{12}}{d\tilde{x}_2}\right), \tag{8.9c}$$

with

$$\frac{dQ_1}{d\tilde{x}_2} = -\frac{5}{2}\left(\frac{1+i\,\mathrm{Kn}^2\,\mathrm{St}^2}{\mathrm{Kn}}\Sigma_{12} + \frac{dV_1}{d\tilde{x}_2}\right) + \frac{8}{3}\,\mathrm{Kn}\frac{d^2\Sigma_{12}}{d\tilde{x}_2^2}.$$

Classical Case: The oscillatory Couette flow in the Navier–Stokes–Fourier system is simply described by the momentum equation (8.1a) with $\tilde{G} = 0$, which after substitution of the law of Navier and Stokes, $\tilde{\sigma}_{12}^{\mathrm{NSF}} = -\mathrm{Kn}\,\partial\tilde{v}_1/\partial\tilde{x}_2$, changes to the diffusion equation,

$$\frac{\partial\tilde{v}_1}{\partial\tilde{t}} = \mathrm{Kn}\frac{\partial^2\tilde{v}_1}{\partial\tilde{x}_2^2}. \tag{8.10}$$

The assumption of harmonic solution leads to an ODE for the velocity amplitude distribution

$$V_1 = \frac{1}{i\,\mathrm{St}^2}\frac{d^2V_1}{d\tilde{x}_2^2}, \tag{8.11}$$

with the general solution

$$V_1 = \mathbf{C}_1\exp\left(\sqrt{i}\,\mathrm{St}\,\tilde{x}_2\right) + \mathbf{C}_2\exp\left(-\sqrt{i}\,\mathrm{St}\,\tilde{x}_2\right). \tag{8.12}$$

The constants $\mathbf{C}_1$ and $\mathbf{C}_2$ in the NSF solutions will be determined from the velocity slip boundary condition [cf. Eq. (6.45)].

Note that, unlike (6.57), (6.59), and (6.61) in (8.9a) and (8.12) the exponential terms do not explicitly represent the Knudsen boundary layers.

8.3.2 Pulsating Poiseuille Flow

For pulsating Poiseuille flow the oscillating body–force, $\tilde{G}\sin\left(\tilde{\omega}\tilde{t}\right)$, is included in Eq. (8.1a). Due to linearity, the velocity amplitude will be proportional to $\tilde{G}$. In the results below, we will choose $\tilde{G}$ such that for $\mathrm{Kn} \to 0$ the velocity amplitude is unity, which requires $\tilde{G} = \tilde{\omega}$, since in this case $\tilde{\sigma}_{12} \to 0$ and $\partial\tilde{v}_1/\partial\tilde{t} = \tilde{G}\sin\left(\tilde{\omega}\tilde{t}\right)$. Accordingly, the continuum limit is a plug flow with $\tilde{v}_1 = \cos\left(\tilde{\omega}\tilde{t}\right)$ exhibiting a phase shift of $\pi/2$ with respect to the force.

For the solution, we write the force in complex notation as $\tilde{G}\exp\left(i\tilde{\omega}\tilde{t}\right)$. Similar to the oscillatory Couette flow, general solutions are then expected as plane harmonic waves, i.e., Eq. (8.5).

The linear system to determine the wave number $\tilde{k}$ is identical to (8.6), when substituting $\mathrm{Kn}\,\mathrm{St}^2$ by $\tilde{\omega}$. The solutions have the form $\tilde{k} \in \left\{\tilde{k}_\alpha\left(\mathrm{Kn}, \tilde{\omega}\right), \alpha = 1, 2, 3, 4\right\}$. The final solution now includes the force

$$\Sigma_{12} = \sum_{\alpha=1}^{4} \mathsf{C}_\alpha \exp\left(-i\,\tilde{k}_\alpha\,\tilde{x}_2\right), \tag{8.13a}$$

$$V_1 = \tilde{G} - \frac{1}{i\,\tilde{\omega}}\frac{\partial \Sigma_{12}}{\partial \tilde{x}_2}, \tag{8.13b}$$

$$Q_1 = -\frac{1}{i\,\tilde{\omega} + 2/(3\,\mathrm{Kn})}\left(\frac{6}{5}\,\mathrm{Kn}\frac{\partial^2 Q_1}{\partial \tilde{x}_2^2} - \frac{\partial \Sigma_{12}}{\partial \tilde{x}_2}\right), \tag{8.13c}$$

with

$$\frac{\partial Q_1}{\partial \tilde{x}_2} = -\frac{5}{2}\left(\frac{1 + i\,\tilde{\omega}\,\mathrm{Kn}}{\mathrm{Kn}}\Sigma_{12} + \frac{\partial V_1}{\partial \tilde{x}_2}\right) + \frac{8}{3}\,\mathrm{Kn}\frac{\partial^2 \Sigma_{12}}{\partial \tilde{x}_2^2}.$$

8.4 Results and Discussion for Periodically Unsteady Flows

8.4.1 Oscillatory Couette Flow

Figure 8.2 shows analytical solutions of linearized NSF and R13 for velocity and parallel heat flux in oscillatory Couette flow. NSF solutions are given with both first– and second–order boundary conditions. Three pairs of Knudsen and Stokes numbers are selected within the transition regime to investigate the interaction of viscosity and rarefaction effects. The velocity solution is compared to DSMC data of Ref. [40].

Velocity plots show that, as the gas becomes more rarefied, deviations of the macroscopic equations from the DSMC data increase at the boundaries, particularly at the oscillating boundary. For small Knudsen numbers the differences between NSF and R13 are small, but the R13 solutions are more accurate at higher Knudsen numbers. In general, the solution that gives the required curvature at the boundary, and sooner converges to the bulk solution must be considered as the best solution. At the first glance, the NSF solution with the first–order slip condition seems to be very close to the DSMC data. NSF behaves better right on the surface, but due to the absence of Knudsen layers, it under–estimates the curvature and then converges to the bulk solution in a longer distance, compared to the R13 solution, especially for the case of small Knudsen numbers. Second–order slip condition improves the curvature on the boundary such that its bulk solution becomes close to the

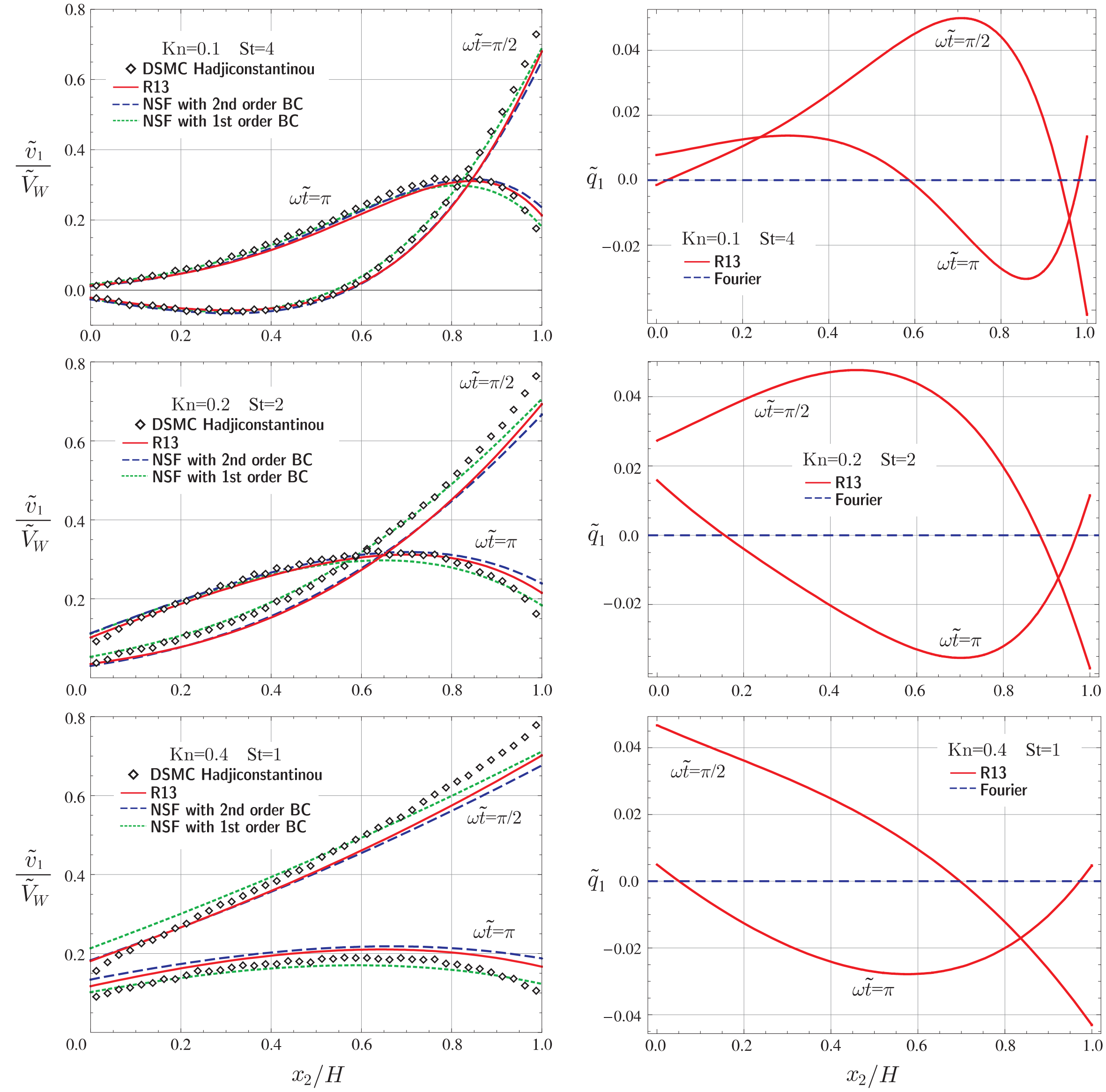

Figure 8.2: Interaction between rarefaction and viscosity effects in oscillatory Couette flow are illustrated using three pairs of Knudsen–Stokes numbers at $\omega\tilde{t} = \{\pi, \pi/2\}$. *Left* Analytical velocity solutions for Navier–Stokes–Fourier and regularized 13–moment equations are compared to direct simulation Monte Carlo data. *Right* Oscillatory Knudsen layers (parallel heat flow) which are zero in Navier–Stokes–Fourier are presented for linear R13 equations.

R13 bulk solution.

Near the oscillating boundary, the curvature of R13 differs from NSF due to Knudsen layers, i.e., parallel heat flux. The oscillating Knudsen layers are shown in the right plots of Fig. 8.2, which are zero in NSF theory.

Our linear approach treats viscosity as a constant, i.e., independent of temperature. Indeed, dependence of viscosity on temperature covers a portion of nonlinear effects, which are excluded in the presented calculations. This can be addressed as the most likely reason for differences between the DSMC and analytical results.

8.4.2 Pulsating Poiseuille Flow

For pulsating Poiseuille flow, kinetic or experimental data could not be found for rarefied conditions. Here, we present the results for the linearized NSF and R13 systems, and demonstrate that large deviations between the models are possible, even for moderate Knudsen numbers. The results for NSF have been computed with full second–order slip boundary conditions.

Figure 8.3 displays the velocity profiles for two different cases, and two time instances $\tilde{\omega}t = 0$, and $\tilde{\omega}t = \pi/2$ within one cycle of the oscillating force. The left plot of the figure uses $\mathrm{Kn} = 0.1$ and a dimensionless frequency of $\tilde{\omega} = 1$. Both results show qualitative agreement, but NSF somewhat overestimates the velocity value in the middle of the channel. The right plot of the figure displays the result for $\mathrm{Kn} = 0.3$ and $\tilde{\omega} = 8$, that is, for a 8–times higher frequency. The differences between NSF and R13 are marked.

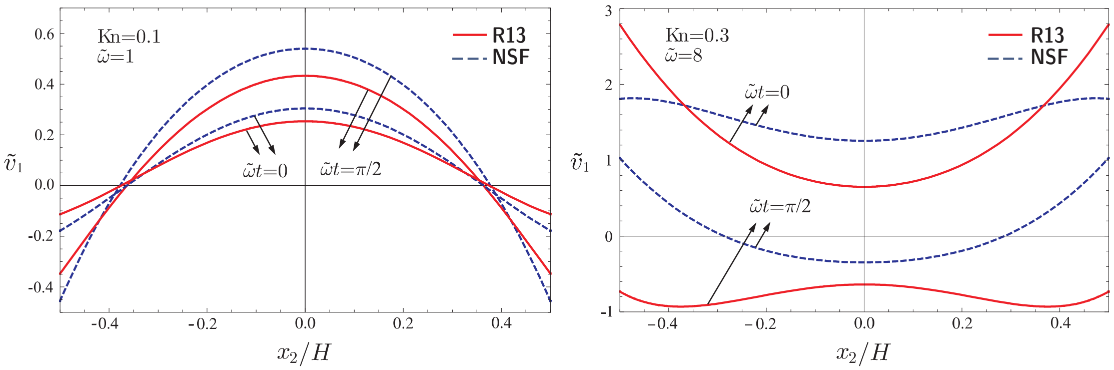

Figure 8.3: Comparison of velocity profiles for pulsating Poiseuille flow computed with NSF and R13 for two different situations: ($\tilde{\omega} = 1$, $\mathrm{Kn} = 0.1$) and ($\tilde{\omega} = 8$, $\mathrm{Kn} = 0.3$). The plots show the two different times $\tilde{\omega}t = 0$ and $\tilde{\omega}t = \pi/2$ within one force cycle.

To obtain more insight into the behavior of the solutions for pulsating Poiseuille flow, we compute the average velocity

$$\int_{-1/2}^{1/2} v_1\left(\tilde{x}_2, \tilde{t}\right) d\tilde{x}_2 = \mathcal{A}\,\sin\left(\tilde{\omega}\tilde{t} + \gamma\right), \tag{8.14}$$

with amplitude $\mathcal{A}$ and phase shift γ. This quantity depends only on Knudsen number and frequency $\tilde{\omega}$, but not on space and time. In Fig. 8.4, we plot the amplitude and phase shift as functions of Kn for two frequencies, $\tilde{\omega} = 1$ (upper plots), and $\tilde{\omega} = 8$ (lower plots).

For very small Knudsen number the amplitude converges to $\mathcal{A} = 1$ and the phase shift becomes $\gamma = \pi/2$, due to the scaling of the force as mentioned above. For larger Knudsen numbers the amplitude and phase shift follow rather complicated curves reflecting the complex interplay of convection, dissipation and boundary conditions in the process.

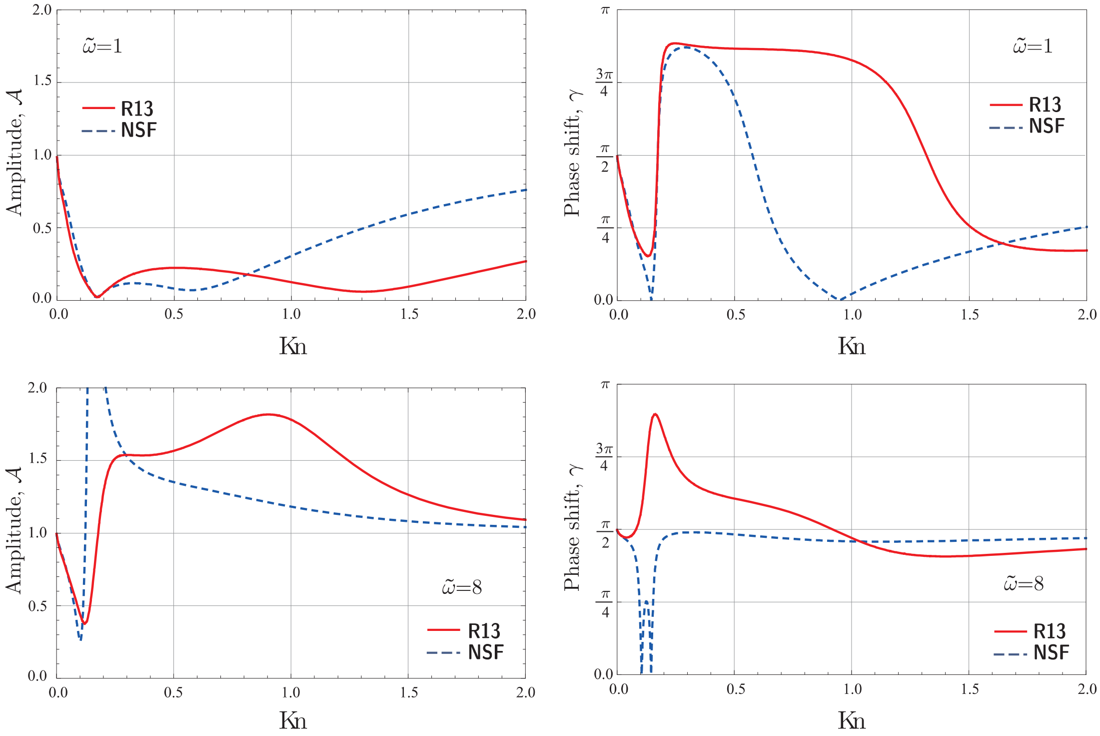

Figure 8.4: Amplitude and phase shift of velocity over Knudsen number in pulsating Poiseuille flow for NSF and R13. This figure shows the frequencies $\tilde{\omega} = \{1, 8\}$ and uses accommodation factor $\chi = 1$. Phase shift converges to $\pi/2$ for large Kn both for NSF and R13. For high–frequency flow $\tilde{\omega} = 8$, the models predict opposite phase shifts for Kn ≈ 0.2.

The case $\tilde{\omega} = 1$ shows differences between NSF and R13 only for relatively large Knudsen numbers, especially in the phase shift. Note that independent of $\tilde{\omega}$ the phase shift converges to $\gamma = \pi/2$ for large Knudsen numbers for both models. For the larger frequency $\tilde{\omega} = 8$, the differences are already very strong for Knudsen numbers as small as Kn $= 0.1$. The NSF equations predict a phase shift smaller than $\pi/2$ while R13 gives clearly $\gamma > \pi/2$ in the range $0.05 < \mathrm{Kn} < 1.0$. Similarly, the amplitude shows much larger values in the NSF result. Due to the higher accuracy of R13 for larger Knudsen numbers and faster processes we expect the R13 result to be superior over the NSF solution. It remains to compare amplitude and phase shift to DSMC solutions or experimental data for pulsating Poiseuille flow.

Chapter 9

Linear Theory for Shear–driven Rotary Flows in Cylindrical Geometry

9.1 Non–isothermal Cylindrical Couette Flow

Circular flow between two concentric cylinders which are at different temperatures and rotate relative to each other, i.e., non–isothermal cylindrical Couette flow, is a basic problem of shear–driven flows in non–planar coordinates[1]. The simple configuration of cylindrical Couette flow allows to study the structure of Knudsen boundary layers over curved boundaries. Microscale cylindrical Couette flows are common in miniaturized turbomachinery designs, e.g. microturbines, where work transfer between a rotor and a fluid is desired [27]. Moreover, they have many applications in micro–tribology, i.e., the science of interacting surfaces in relative motion [31].

Rarefied shear–driven circular flows have been investigated experimentally [2, 3], and numerically [8, 24, 78, 93, 94, 99, 100, 101, 104, 116, 131]. Different aspects of these flows are studied through the kinetic approaches. These include prediction of drag coefficients on the cylinders [2, 24], density minimum phenomenon [78], evaporation and condensation on the cylinders [100, 101], non–Newtonian stress components [94], non–Fourier heat flow [94], flow stability [104, 131], effects of boundary curvature and the velocity inversion phenomenon [8, 99, 116]. The velocity inversion is

---

[1] The presented materials in this chapter are published in Ref. [113].

a non–intuitive phenomenon which happens in cylindrical Couette flows with smooth walls. When the inner cylinder is rotating and the outer one is stationary, the velocity of the gas increases with the distance from the inner cylinder.

In Refs. [28, 77, 132] and also in the present study, it is shown that the classical NSF equations can describe some of the characteristic features of cylindrical Couette flows, e.g. velocity inversion. Even more, they can approximate the effects of velocity slip and temperature jump when higher order boundary conditions are employed. Nevertheless, NSF equations fail to present the high–order rarefaction effects, i.e., Knudsen boundary layers.

In this section, we apply the R13 equations and their corresponding kinetic boundary conditions as a higher–order macroscopic transport model for shear–driven rotary flows in micro–annuli. This model predicts a circumferential non–Fourier heat flow and non–Newtonian stress components which are pure rarefaction effects [110, 115], to which little attention is given in the literature. In addition, we will show that second–order boundary conditions (in cylindrical coordinate) for NSF equations effectively improve the NSF predictions.

In the context of moments method, Khayat and Eu [47, 48] adapted their Grad–type moment equations to investigate cylindrical Couette flow of Lennard–Jones fluids. However, they reduced the governing equations such that NSF boundary conditions were sufficient.

We conclude this introductory section by giving a short remark on stability of shear–driven rotary flows with limited axial length, also called *Taylor–Couette flows.* For liquids, stability of circular Couette flow with finite axial length is rigorously investigated by Andereck *et al.* [4]. Their experiments with water revealed that eighteen flow regimes can be distinguished in two–dimensional cylindrical Couette flows, where the effects of top and bottom ends are prominent. They showed that for fixed flow dimensions, transition between the regimes depends on the Reynolds numbers corresponding to inner and outer cylinders, and the rotation mode (counter–rotating and co–rotating). Experiments in [4] concern only dynamic (and not thermal) behavior of cylindrical Couette flows. To the authors' knowledge there is a lack of similar study for rarefied gas flows, owing to the difficulties of experiments with gases. However, in Refs. [104, 131] DSMC simulations are reported for moderately rarefied cylindrical Couette flows without axial uniformity, where top and bottom boundaries were in effect. For a constant Knudsen number and a fixed flow geometry, three different flow regimes were reported, which only depend on the velocity of the cylinders [131].

9.2 Flow Setting for Cylindrical Couette Flow

We consider a monatomic ideal gas flow in rarefied condition that is confined in an annulus between two coaxial cylinders. The height of the cylinders H is sufficiently large such that top and bottom boundary effects can be neglected. For instance, the ratio of gap to height in the apparatus used by Alfos and Springer [2] was 0.06, where the inner and outer radii were 6.350 cm and 7.112 cm, respectively; the height of the cylinders was 6.350 cm, and for minimizing end effects measurements were made on the center, $H/2$.

The flow setting is depicted in Fig. 9.1. The temperatures of inner and outer cylinders are $\theta^{W,\mathrm{i}}$ and $\theta^{W,\mathrm{o}}$, respectively. The angular velocities of the cylinders are ω_{i} and ω_{o} around the z–axis. We employ cylindrical coordinates $\mathbf{x} = \{r, \varphi, z\}$, where r is the radial coordinate and r_{i} and r_{o} are inner and outer radii of the circular gap, respectively. The gap size is $L = r_{\mathrm{o}} - r_{\mathrm{i}}$. The circumferential velocities of the wall surfaces are $v_{\varphi}^{W,\mathrm{i}} = r_{\mathrm{i}}\,\omega_{\mathrm{i}}$, and $v_{\varphi}^{W,\mathrm{o}} = r_{\mathrm{o}}\,\omega_{\mathrm{o}}$. We investigate steady state behavior of the gas in the absence of body forces.

In general, the considered flows are defined by setting the dimensions $(r_{\mathrm{i}}, r_{\mathrm{o}})$, temperatures $(\theta^{W,\mathrm{i}}, \theta^{W,\mathrm{o}})$, and velocities $(v_{\varphi}^{W,\mathrm{o}}, v_{\varphi}^{W,\mathrm{i}})$ of the cylinders. Moreover, the gas rarefaction is controlled through the mass of the gas in the system (or the mass density at rest).

The walls are impermeable and there is no velocity in radial direction, $v_r = 0$. Also, there is no axial velocity $v_z = 0$; flow is independent of axial direction $\partial/\partial z = 0$, and it is uniform circumferentially, $\partial/\partial\varphi = 0$, i.e., axisymmetric flow. Accordingly, the velocity field reads

$$\mathbf{v} = \begin{pmatrix} 0 \\ v_{\varphi}(r) \\ 0 \end{pmatrix}. \tag{9.1a}$$

Since the flow is assumed to be independent of the z–direction, the symmetric and trace–free stress tensor σ_{ij}, and the heat–flux vector q_i simplify to

$$\boldsymbol{\sigma} = \begin{pmatrix} \sigma_{rr}(r) & \sigma_{r\varphi}(r) & 0 \\ \sigma_{r\varphi}(r) & \sigma_{\varphi\varphi}(r) & 0 \\ 0 & 0 & \sigma_{zz}(r) \end{pmatrix}, \quad \mathbf{q} = \begin{pmatrix} q_r(r) \\ q_{\varphi}(r) \\ 0 \end{pmatrix}, \tag{9.1b}$$

where all components are functions of the radial coordinate r. Trace–free condition for the stress tensor gives $\sigma_{zz}(r) = -\sigma_{rr}(r) - \sigma_{\varphi\varphi}(r)$.

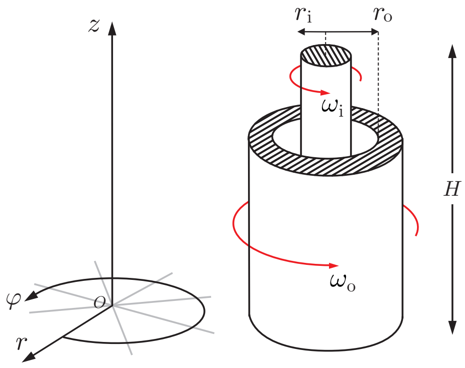

Figure 9.1: Coordinates and flow setting in cylindrical Couette flow. The gas is confined in the gap between the cylinders, which have different temperatures and rotate independently.

9.3 Linearized R13 Equations for Cylindrical Couette Flow

For steady state and unidirectional rotary flows, as illustrated in Fig. 9.1, linearized R13 equations in cylindrical coordinates [Eqs. (4.40)–(4.70)] reduce to the following three sets of differential equations.

■ The velocity problem:

R13 case: The motion of the gas is described by tangential momentum, tangential heat–flux, and tangential stress (shear stress) equations that in their linear form read

$$\frac{\partial \tilde{\sigma}_{r\varphi}}{\partial \tilde{r}} + 2\frac{\tilde{\sigma}_{r\varphi}}{\tilde{r}} = 0, \tag{9.2a}$$

$$\frac{1}{2}\frac{\partial \tilde{R}_{r\varphi}}{\partial \tilde{r}} + \frac{\tilde{R}_{r\varphi}}{\tilde{r}} = -\frac{\mathrm{Pr}}{\mathrm{Kn}}\tilde{q}_{\varphi}, \tag{9.2b}$$

$$\frac{2}{5}\left(\frac{\partial \tilde{q}_{\varphi}}{\partial \tilde{r}} - \frac{\tilde{q}_{\varphi}}{\tilde{r}}\right) + \frac{\partial \tilde{m}_{rr\varphi}}{\partial \tilde{r}} + \frac{2\tilde{m}_{rr\varphi} - \tilde{m}_{\varphi\varphi\varphi}}{\tilde{r}} = -\frac{1}{\mathrm{Kn}}\tilde{\sigma}_{r\varphi} + \frac{\tilde{v}_{\varphi}}{\tilde{r}} - \frac{\partial \tilde{v}_{\varphi}}{\partial \tilde{r}}. \tag{9.2c}$$

For the above equations, the required constitutive relations and linear boundary conditions [Eq. (5.39)] are

$$\tilde{R}_{r\varphi} = \frac{\mathsf{B}_2}{2}\,\mathrm{Kn}\left(\frac{\partial \tilde{q}_{\varphi}}{\partial \tilde{r}} - \frac{\tilde{q}_{\varphi}}{\tilde{r}}\right), \qquad \tilde{m}_{rr\varphi} = -\tilde{m}_{\varphi\varphi\varphi} = -2\,\mathsf{C}\,\mathrm{Kn}\frac{\tilde{\sigma}_{r\varphi}}{\tilde{r}}, \tag{9.3}$$

and

$$\tilde{\sigma}_{r\varphi} = -\frac{\chi}{2-\chi}\sqrt{\frac{2}{\pi}}\left(\tilde{\mathcal{V}}_{\varphi} + \frac{1}{5}\tilde{q}_{\varphi} + \frac{1}{2}\tilde{m}_{rr\varphi}\right) n_r, \tag{9.4a}$$

$$\tilde{R}_{r\varphi} = -\frac{\chi}{2-\chi}\sqrt{\frac{2}{\pi}}\left(-\tilde{\mathcal{V}}_{\varphi} + \frac{11}{5}\tilde{q}_{\varphi} + \frac{1}{2}\tilde{m}_{rr\varphi}\right) n_r. \tag{9.4b}$$

As a pure rarefaction effect, the tangential heat flow $\tilde{q}_{\varphi}$, governed by Eq. (9.2b), is not driven by a temperature gradient, which makes the velocity problem completely independent of temperature.

Classical case: The linearized velocity problem in the Navier–Stokes–Fourier system includes the tangential momentum balance [Eq. (9.2a)],

$$\left(\frac{\partial}{\partial\tilde{r}} + \frac{2}{\tilde{r}}\right)\left(\frac{\partial\tilde{v}_{\varphi}}{\partial\tilde{r}} - \frac{\tilde{v}_{\varphi}}{\tilde{r}}\right) = 0, \tag{9.5}$$

in which the linear Navier–Stokes law for viscous stress was used, i.e.,

$$\tilde{\sigma}_{r\varphi}^{\mathrm{NSF}} = -\mathrm{Kn}\left(\frac{\partial\tilde{v}_{\varphi}}{\partial\tilde{r}} - \frac{\tilde{v}_{\varphi}}{\tilde{r}}\right). \tag{9.6}$$

The linearized second–order velocity slip condition for the NSF system follows from Eq. (C.13), which, after substitution of Navier and Stokes law reads

$$\begin{aligned}\mathcal{V}_{\varphi}^{\mathrm{NSF}} = {}& \frac{2-\chi}{\chi}\sqrt{\frac{\pi}{2}}\left(\frac{\partial\tilde{v}_{\varphi}}{\partial\tilde{r}} - \frac{\tilde{v}_{\varphi}}{\tilde{r}}\right)\mathrm{Kn}\, n_r - \left(\frac{1}{5\,\mathrm{Pr}} - \frac{4\,\mathsf{C}}{15}\right)\left(\frac{\partial^2\tilde{v}_{\varphi}}{\partial\tilde{r}^2} - \frac{1}{\tilde{r}}\frac{\partial\tilde{v}_{\varphi}}{\partial\tilde{r}} + \frac{\tilde{v}_{\varphi}}{\tilde{r}^2}\right)\mathrm{Kn}^2 \\ & - \left(\frac{2}{5\,\mathrm{Pr}} + \frac{7\,\mathsf{C}}{15}\right)\left(\frac{1}{\tilde{r}}\frac{\partial\tilde{v}_{\varphi}}{\partial\tilde{r}} - \frac{\tilde{v}_{\varphi}}{\tilde{r}^2}\right)\mathrm{Kn}^2.\end{aligned} \tag{9.7}$$

■ The temperature problem:

R13 case: The thermal behavior of the stationary gas between two cylinders is governed by

$$\frac{\partial\tilde{q}_r}{\partial\tilde{r}} + \frac{\tilde{q}_r}{\tilde{r}} = 0, \tag{9.8a}$$

$$\frac{4}{15}\left(2\frac{\partial\tilde{q}_r}{\partial\tilde{r}} - \frac{\tilde{q}_r}{\tilde{r}}\right) + \frac{\partial\tilde{m}_{rrr}}{\partial\tilde{r}} + \frac{\tilde{m}_{rrr} - 2\tilde{m}_{r\varphi\varphi}}{\tilde{r}} = -\frac{1}{\mathrm{Kn}}\tilde{\sigma}_{rr}, \tag{9.8b}$$

$$\frac{4}{15}\left(2\frac{\tilde{q}_r}{\tilde{r}} - \frac{\partial\tilde{q}_r}{\partial\tilde{r}}\right) + \frac{\partial\tilde{m}_{r\varphi\varphi}}{\partial\tilde{r}} + 3\frac{\tilde{m}_{r\varphi\varphi}}{\tilde{r}} = -\frac{1}{\mathrm{Kn}}\tilde{\sigma}_{\varphi\varphi}, \tag{9.8c}$$

$$\frac{\partial\tilde{\sigma}_{rr}}{\partial\tilde{r}} + \frac{\tilde{\sigma}_{rr} - \tilde{\sigma}_{\varphi\varphi}}{\tilde{r}} + \frac{1}{6}\frac{\partial\tilde{\Delta}}{\partial\tilde{r}} + \frac{1}{2}\frac{\partial\tilde{R}_{rr}}{\partial\tilde{r}} + \frac{1}{2}\frac{\tilde{R}_{rr} - \tilde{R}_{\varphi\varphi}}{\tilde{r}} = -\frac{5}{2}\frac{\partial\tilde{\theta}}{\partial\tilde{r}} - \frac{\mathrm{Pr}}{\mathrm{Kn}}\tilde{q}_r, \tag{9.8d}$$

with the constitutive relations for its high–order moments

$$\tilde{\mathit{\Delta}} = 0, \qquad \tilde{R}_{rr} = -\tilde{R}_{\varphi\varphi} = -\mathsf{B}_2 \,\mathrm{Kn}\, \frac{\tilde{q}_r}{\tilde{r}}, \qquad \tilde{m}_{rrr} = \mathsf{C}\,\mathrm{Kn}\left(\frac{3}{5}\frac{\partial \tilde{\sigma}_{rr}}{\partial \tilde{r}} - \frac{2}{5}\frac{\tilde{\sigma}_{rr} - \tilde{\sigma}_{\varphi\varphi}}{\tilde{r}}\right),$$
$$\tilde{m}_{r\varphi\varphi} = \frac{\mathsf{C}}{3}\,\mathrm{Kn}\left(\frac{\partial \tilde{\sigma}_{\varphi\varphi}}{\partial \tilde{r}} - \frac{2}{5}\frac{\partial \tilde{\sigma}_{rr}}{\partial \tilde{r}} + \frac{8}{5}\frac{\tilde{\sigma}_{rr} - \tilde{\sigma}_{\varphi\varphi}}{\tilde{r}}\right). \tag{9.9}$$

The boundary conditions for the temperature problems are [Eq. (5.39)]

$$\tilde{q}_r = \frac{\chi}{2-\chi}\sqrt{\frac{2}{\pi}}\left(-2\tilde{\mathcal{T}} - \frac{1}{2}\tilde{\sigma}_{rr} - \frac{1}{15}\tilde{\mathit{\Delta}} - \frac{5}{28}\tilde{R}_{rr}\right) n_r, \tag{9.10a}$$

$$\tilde{m}_{rrr} = \frac{-\chi}{2-\chi}\sqrt{\frac{2}{\pi}}\left(-\frac{2}{5}\tilde{\mathcal{T}} + \frac{7}{5}\tilde{\sigma}_{rr} - \frac{1}{75}\tilde{\mathit{\Delta}} + \frac{1}{14}\tilde{R}_{rr}\right) n_r, \tag{9.10b}$$

$$\tilde{m}_{r\varphi\varphi} = \frac{\chi}{2-\chi}\sqrt{\frac{2}{\pi}}\left(-\frac{1}{5}\tilde{\mathcal{T}} - \tilde{\sigma}_{\varphi\varphi} + \frac{1}{5}\tilde{\sigma}_{rr} - \frac{1}{150}\tilde{\mathit{\Delta}} - \frac{1}{14}\tilde{R}_{\varphi\varphi}\right) n_r. \tag{9.10c}$$

Equation (9.8a) is the linearized energy balance, where the nonlinear viscous heating terms are discarded in the linearization, compare with Eq. (4.27). Linearized balance equations for normal components of the stress tensor and heat–flux vector are given in (9.8b)–(9.8d).

Classical case: The linearized temperature problem in the Navier–Stokes–Fourier system consists of energy balance [Eq. (9.8a)],

$$\left(\frac{\partial}{\partial \tilde{r}} + \frac{1}{\tilde{r}}\right)\frac{\partial \tilde{\theta}}{\partial \tilde{r}} = 0, \tag{9.11}$$

in which the linearized Fourier law for heat conduction was used, i.e.,

$$\tilde{q}_r^{\mathrm{NSF}} = -\frac{5}{2}\frac{\mathrm{Kn}}{\mathrm{Pr}}\frac{\partial \tilde{\theta}}{\partial \tilde{r}}. \tag{9.12}$$

The linearized second–order temperature jump condition for the NSF system follows from Eq. (C.14), which after substitution of Fourier's law reads

$$\mathcal{T}^{\mathrm{NSF}} = \frac{2-\chi}{\chi}\frac{5}{4\,\mathrm{Pr}}\sqrt{\frac{\pi}{2}}\frac{\partial \tilde{\theta}}{\partial \tilde{r}}\,\mathrm{Kn}\, n_r - \frac{5}{2\,\mathrm{Pr}}\left[\left(\frac{5\,\mathsf{B}_2}{168} - \frac{1}{5} - \frac{\mathsf{A}_2}{30}\right)\frac{1}{\tilde{r}}\frac{\partial \tilde{\theta}}{\partial \tilde{r}} - \left(\frac{\mathsf{A}_2}{30} + \frac{5\,\mathsf{B}_2}{84}\right)\frac{\partial^2 \tilde{\theta}}{\partial \tilde{r}^2}\right]\mathrm{Kn}^2. \tag{9.13}$$

■ The density/pressure problem:

R13 case: The radial momentum balance [Eq. (4.26a)] includes the radial density/pressure gradient, that in linear form reads

$$\frac{\partial \tilde{\rho}}{\partial \tilde{r}} + \frac{\partial \tilde{\theta}}{\partial \tilde{r}} + \frac{\partial \tilde{\sigma}_{rr}}{\partial \tilde{r}} + \frac{\tilde{\sigma}_{rr} - \tilde{\sigma}_{\varphi\varphi}}{\tilde{r}} = 0, \tag{9.14}$$

where $\tilde{p} = 1 + \tilde{\rho} + \tilde{\theta}$ is used as the linearized ideal gas law, see Eq. (4.31).

Since kinetic boundary condition is not available for neither density nor pressure, the condition of constant mass in the process can be used to evaluate the radial density/pressure distribution,

$$\int_{\tilde{r}_\mathrm{i}}^{\tilde{r}_\mathrm{o}} (\tilde{\rho} + 1)\, \tilde{r}\, d\tilde{r} = \text{const.} \tag{9.15}$$

The above condition is similar to (6.52) in the case of parallel–plate channel flows.

Classical case: In classical hydrodynamics where non–Newtonian stress components are zero, the density/pressure problem reduces to $\partial\tilde{\theta}/\partial\tilde{r} = -\partial\tilde{\rho}/\partial\tilde{r}$.

9.4 Remarks on Characteristic Parameters

The linearized equations in the previous section are presented in dimensionless form. Detailed information about dimensionless parameters is available in Sec. 4.4. For the prescribed cylindrical geometry, the chosen reference length $\mathcal{L}$, normally is either the radius of the inner cylinder, r_i [8], the radius of the outer cylinder, r_o [94], or the gap width, $(r_\mathrm{o} - r_\mathrm{i})$ [116]. This allows several choices for $\mathcal{L}$, and consequently, the Knudsen number, $\mathrm{Kn} = \lambda_0/\mathcal{L}$, is not uniquely defined. For characterizing the degree of rarefaction one will be inclined to base the definition of Kn on the smallest of these scales, i.e., either r_i or $(r_\mathrm{o} - r_\mathrm{i})$. To present results in dimensionless form, any choice of the reference length might be used. However, one has to be careful about the various definitions used in the literature when results of different sources are compared. When comparing to the results of other authors, we shall follow their choice of definition, otherwise we base the definition of Kn on the radius of the inner cylinder.

Apart from the Knudsen number, the processes depend on the (angular) velocities of the cylinders and their temperatures. The differences in angular velocities $(\omega_\mathrm{o} - \omega_\mathrm{i})$ and in temperatures $\left(\theta^{W,\mathrm{o}} - \theta^{W,\mathrm{i}}\right)$ are the driving forces for the processes. Dimensionless measures, e.g. the Mach number, are useful to indicate the strength of these driving forces. As explained in Eq. (4.30), for the velocity scale we use the isothermal speed of sound, $\sqrt{\theta_0}$, which is proportional to the equilibrium speed of sound, $c_s = \sqrt{\gamma\,\theta_0}$ ($\gamma = 5/3$ is the ratio of specific heats). Thus, the dimensionless velocity is related to the Mach number by $|\tilde{v}| = \mathrm{Ma}\sqrt{\gamma}$.

9.5 Solutions for Cylindrical Couette Flow

9.5.1 Analytical Solution for the Linearized Velocity Problem

Replacement of (9.3) into (9.2b) and (9.2c) leads to a compact form of the velocity problem,

$$\frac{\partial \tilde{\sigma}_{r\varphi}}{\partial \tilde{r}} + 2\frac{\tilde{\sigma}_{r\varphi}}{\tilde{r}} = 0, \qquad \frac{\partial}{\partial \tilde{r}}\left(\frac{\partial \tilde{q}_{\varphi}}{\partial \tilde{r}} + \frac{\tilde{q}_{\varphi}}{\tilde{r}}\right) = -\frac{5}{9\,\mathrm{Kn}^2}\tilde{q}_{\varphi}, \qquad \frac{\partial}{\partial \tilde{r}}\left(\frac{2}{5}\frac{\tilde{q}_{\varphi}}{\tilde{r}} + \frac{\tilde{v}_{\varphi}}{\tilde{r}}\right) = -\frac{1}{\mathrm{Kn}}\frac{\tilde{\sigma}_{r\varphi}}{\tilde{r}}, \tag{9.16}$$

in which Pr, B_2, and C are replaced from Eq. (4.15) for Maxwellian molecules.

From Eq. (9.16), it is a straightforward task to find the general solution for $\tilde{\sigma}_{r\varphi}$. The second equation is a *modified Bessel equation* and its general solution consists of two linearly independent solutions, the *Bessel functions* $\mathcal{I}_{\alpha}$ and $\mathcal{K}_{\alpha}$ (with $\alpha = 1$ in this case). The solution for $\tilde{v}_{\varphi}$ follows by integrating the stress equation and substituting the obtained solutions for $\tilde{\sigma}_{r\varphi}$ and $\tilde{q}_{\varphi}$. Accordingly, the general solutions for the velocity problem are

$$\tilde{\sigma}_{r\varphi} = \underline{\frac{\mathbf{C}_1}{\tilde{r}^2}}, \qquad \tilde{q}_{\varphi} = \mathbf{C}_2\,\mathcal{I}_1\left(\frac{\sqrt{5}}{3\,\mathrm{Kn}}\tilde{r}\right) + \mathbf{C}_3\,\mathcal{K}_1\left(\frac{\sqrt{5}}{3\,\mathrm{Kn}}\tilde{r}\right), \qquad \tilde{v}_{\varphi} = -\frac{2}{5}\tilde{q}_{\varphi} + \underline{\frac{1}{2\,\mathrm{Kn}}\tilde{\sigma}_{r\varphi}\,\tilde{r} + \mathbf{C}_4\,\tilde{r}}, \tag{9.17}$$

where $\mathbf{C}_1$ to $\mathbf{C}_4$ are the integrating constants that must be determined from the boundary conditions. The underlined terms denote the linearized NSF solution, which require the boundary condition (9.7).

As indicated in Eq. (9.17), the linear solutions for the shear stress are the same for both NSF and R13 systems. The Bessel functions $\mathcal{I}_1$ and $\mathcal{K}_1$ represent the Knudsen layers which are pure rarefaction effects. The circumferential heat flow, $\tilde{q}_{\varphi}$, contributes to the velocity solution. In the linear case, the only difference between NSF and R13 arises through the Knudsen boundary layer $\tilde{q}_{\varphi}$, where $\tilde{q}_{\varphi}^{\mathrm{NSF}} = 0$. Slip velocity on the boundaries is given by the coefficient $\mathbf{C}_4$, and the Knudsen layer contribution.

9.5.2 Numerical Solution for the Linearized Temperature Problem

Due to the coupling between σ_{rr} and $\sigma_{\varphi\varphi}$ in Eqs. (9.8b)–(9.8d), an analytical solution for the temperature problem is not accessible. Thus, the linear temperature problem is solved numerically.

The linearized temperature problem given by Eqs. (9.8a)–(9.8d) includes four independent parameters $\{\tilde{\theta}, \tilde{q}_r, \tilde{\sigma}_{rr}, \tilde{\sigma}_{\varphi\varphi}\}$, and five dependent parameters $\{\tilde{\Delta}, \tilde{R}_{rr}, \tilde{R}_{\varphi\varphi}, \tilde{m}_{rrr}, \tilde{m}_{r\varphi\varphi}\}$, all vary only with respect to the radial direction. In the linear case explicit expressions are available for $\{\tilde{\Delta}, \tilde{R}_{rr}, \tilde{R}_{\varphi\varphi}\}$ [see Eq. (9.9)], thus, these dependent parameters can be removed from the parameters list $\mathbf{U}$ as long as they can be expressed by other dependent parameters.

After straightforward manipulations the linearized temperature problem can be written in matrix form,

$$\mathbf{I}\frac{\partial \mathbf{U}}{\partial r} = \mathbf{P}\,\mathbf{U}, \tag{9.18}$$

with the boundary conditions

$$\mathbf{U} = \mathbf{B}\,\mathbf{U} + \mathbf{B}_{\text{inh}}, \tag{9.19}$$

where $\mathbf{I}$ is the unit matrix, and $\mathbf{U}$ is the parameter vector

$$\mathbf{U} = \left(\tilde{q}_r, \tilde{\sigma}_{\varphi\varphi}, \tilde{m}_{r\varphi\varphi}, \tilde{m}_{rrr}, \tilde{\sigma}_{rr}, \tilde{\theta}\right)^{\mathrm{T}}.$$

The vector $\mathbf{B}_{\text{inh}}$ contains the boundary properties, including the temperature and accommodation coefficients of the walls

$$\mathbf{B}_{\text{inh}} = \left(2\beta\,\tilde{\theta}^{W}, 0, \frac{1}{5}\beta\,\tilde{\theta}^{W}, -\frac{2}{5}\beta\,\tilde{\theta}^{W}, 0\right)^{\mathrm{T}}. \tag{9.20}$$

The matrices $\mathbf{P}$ and $\mathbf{B}$ are

$$\mathbf{P} = \begin{pmatrix} -\dfrac{1}{r} & 0 & 0 & 0 & 0 & 0 \\ 0 & \dfrac{4\,\mathrm{Kn}}{3\,r} & -\dfrac{3}{2\,\mathrm{Kn}} & -\dfrac{1}{3\,\mathrm{Kn}} & -\dfrac{4\,\mathrm{Kn}}{3\,r} & 0 \\ -\dfrac{4}{5\,r} & -\dfrac{1}{\mathrm{Kn}} & -\dfrac{3}{r} & 0 & 0 & 0 \\ \dfrac{4}{5\,r} & 0 & \dfrac{2}{r} & -\dfrac{1}{r} & -\dfrac{1}{\mathrm{Kn}} & 0 \\ 0 & -\dfrac{2}{3\,r} & 0 & -\dfrac{5}{6\,\mathrm{Kn}} & \dfrac{2}{3\,r} & 0 \\ -\dfrac{4}{15\,\mathrm{Kn}} & \dfrac{2}{3\,r} & 0 & \dfrac{1}{3\,\mathrm{Kn}} & -\dfrac{2}{3\,r} & 0 \end{pmatrix}, \tag{9.21}$$

and

$$\mathbf{B} = \begin{pmatrix} -\dfrac{6\,\mathrm{Kn}\,\beta}{7\,r} & 0 & 0 & 0 & -\dfrac{\beta}{2} & -2\,\beta \\ 0 & 1 & 0 & 0 & 0 & 0 \\ \dfrac{12\,\mathrm{Kn}\,\beta}{35\,r} & -\beta & 0 & 0 & \dfrac{\beta}{5} & -\dfrac{\beta}{5} \\ -\dfrac{12\,\mathrm{Kn}\,\beta}{35\,r} & 0 & 0 & 0 & -\dfrac{7\,\beta}{5} & \dfrac{2\,\beta}{5} \\ 0 & 0 & 0 & 0 & 1 & 0 \\ 0 & 0 & 0 & 0 & 0 & 1 \end{pmatrix}, \tag{9.22}$$

where for brevity in presentation of the boundary conditions, modified accommodation factors β are introduced as

$$\beta = \frac{\chi}{2-\chi}\sqrt{\frac{2}{\pi}}. \tag{9.23}$$

By using the basic central finite difference method, Eq. (9.18) with the boundary condition (9.19) is solved numerically for $\mathbf{U}$. In the linear case, the parameters in $\mathbf{U}$ change locally, and since both $\mathbf{P}$ and $\mathbf{B}$ matrices are independent of $\mathbf{U}$, no iteration is required in the numerical method, and the accuracy of the numerical results only depends on the grid resolution.

The general solution for Eq. (9.11) is

$$\tilde{\theta}^{\mathrm{NSF}} = \mathsf{C}_5 \ln \tilde{r} + \mathsf{C}_6,$$

that gives the radial temperature distribution for the linear NSF system. The integrating constants C_5 and C_6 must be determined from the boundary condition (9.13).

9.6 Results and Discussion for Cylindrical Couette Flow

In this section, first we present a parametric study on radial distribution of macroscopic properties in the cylindrical Couette flow of a moderately rarefied gas. Furthermore, we compare the accuracy of linear NSF and R13 systems with available DSMC data in the literature.

9.6.1 Results for the Velocity Problem

The linear velocity problem can be characterized by Knudsen number Kn, surface accommodation factor χ, and the wall velocities $\tilde{v}_\varphi^W$, or wall Mach numbers. We shall investigate the radial distributions for $\{\tilde{\sigma}_{r\varphi}, \tilde{q}_\varphi, \tilde{v}_\varphi\}$ given by Eq. (9.17). The radius of the inner cylinder $r_\mathrm{i} = 1$ is taken as the reference length scale, i.e., the Knudsen number is defined based on the radius of the inner cylinder, and a fixed radius ratio is considered $r_\mathrm{o}/r_\mathrm{i} = 2$. The other parameters assume the values $\chi = \{0.02, 0.2, 0.5, 1\}$ and $\mathrm{Kn} = \{0.01, 0.05, 0.1, 0.2\}$. Rotational state of the cylinders are categorized in three modes given in Table 9.1, such that $\tilde{v}_\varphi^{W,\mathrm{i}} + \tilde{v}_\varphi^{W,\mathrm{o}} = 0.5$.

Figure 9.2 presents the radial distribution of shear stress, circumferential heat flux, and velocity in the annulus. The plots are obtained for fully diffusive walls $\chi = 1$, while the effects of different Knudsen numbers and rotational modes are illustrated.

Table 9.1: Rotational modes for cylinders in cylindrical Couette flow.

	$\tilde{v}_{\varphi}^{W,\mathrm{i}}$	$\tilde{v}_{\varphi}^{W,\mathrm{o}}$
Mode 1	0.5	0
Mode 2	0	0.5
Mode 3	0.25	0.25

Distribution of shear stress $\tilde{\sigma}_{r\varphi}$ for both NSF and R13 systems is given by Eq. (9.17), albeit with different values for the constant $\mathbf{C}_1$, which is obtained from different boundary conditions. As shown in the top row of Fig. 9.2, for larger Knudsen numbers we observe larger shear stress on the walls. As expected, plot (a) shows that for rotation mode 1 stress is maximum on the inner rotary cylinder and rapidly decays towards the outer stationary surface. However, this pattern is not observed for rotational mode 2 in plot (b), where the stress is minimum on the rotary outer cylinder and increases towards the inner cylinder. This occurs because of curvature effects (converging geometry), i.e., the volume of flow decreases towards the inner cylinder. Rotation of the inner cylinder in the same direction as of the outer one can change this pattern again, see plot (c).

On the middle row of Fig. 9.2 the circumferential heat flux given in Eq. (9.17) is plotted. This non–Fourier heat flow which is not driven by temperature gradient is a pure rarefaction effect, and is not accessible for classical hydrodynamics, $\tilde{q}_{\varphi}^{\mathrm{NSF}} = 0$. The velocity solution (9.17) indicates that $\tilde{q}_{\varphi}$ gives the Knudsen boundary layer for the velocity problem. It can be seen in Fig. 9.2 that the magnitude of the circumferential heat flow and thickness of the Knudsen layer increases with Kn.

As a consequence of curvature effects, for all the rotational modes the circumferential heat flow is stronger on the inner cylinder, and already for Kn $= 0.2$ this Knudsen layer extends over the whole flow field. For rotational modes 1 and 2 the heat flow direction on the rotary wall is opposite to the wall velocity, and hence, mass flow direction. This is consistent with Couette flow simulations in planar geometry [115]. Nevertheless, in the cylindrical geometry direction of $\tilde{q}_{\varphi}$ is inverted on the stationary walls, see plots (d) and (e) in Fig. 9.2.

The bottom plots in Fig. 9.2 are devoted to the velocity distribution. The obtained results confirm that velocity slip increases in dilute gases. Moreover, for all rotation modes, the inner cylinder has larger slip values owing to more surface curvature.

The Navier–Stokes results obtained from the first– and second–order slip conditions are shown for Kn $= 0.2$. Indeed, the proposed higher–order boundary condition in Eq. (9.7) effectively shift the Navier–Stokes solutions towards the R13 prediction.

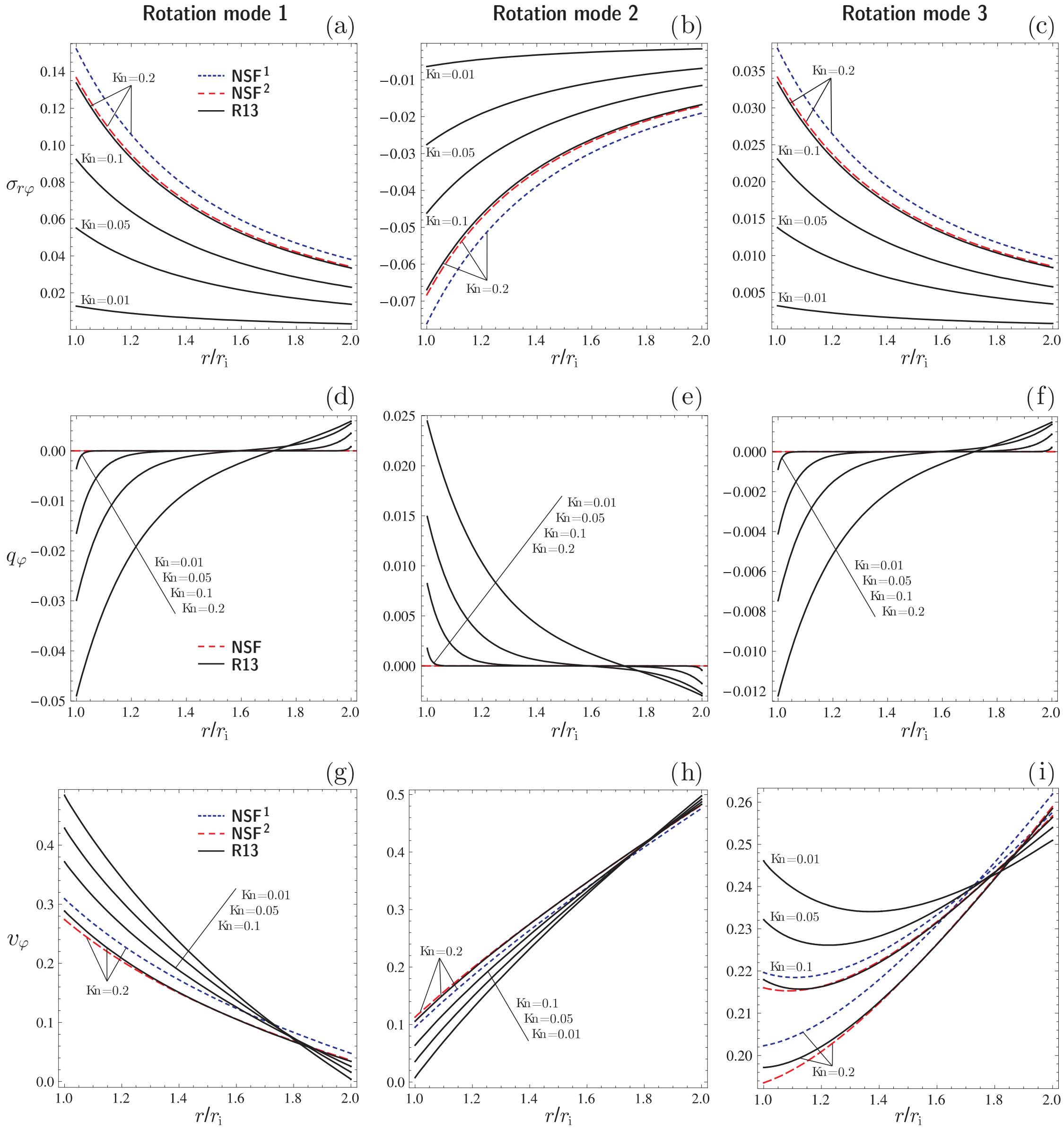

Figure 9.2: Solutions of the linear velocity problem: dashed blue line is NSF with first–order boundary condition; long–dashed red line is NSF with second–order boundary condition; continuous black line is R13 with third–order boundary conditions. Radial distribution of shear stress (top plots), circumferential heat flux (middle plots), and velocity (bottom plots) in the annulus between two fully diffusive cylinders $\chi = 1$, are shown. Plots in left, middle, and right columns correspond to rotational modes 1, 2 and 3, respectively. For each rotational mode, effects of Knudsen number variation are depicted. NSF results with the proposed second–order slip condition show satisfactory agreement with the R13 predictions. For the small Knudsen numbers NSF results are not shown, since they are very close to the R13 predictions.

Velocity differences between R13 and NSF with second–order slip condition are more apparent near the walls. This can be explained by the explicit solution for velocity in Eq. (9.17) which is the superposition of Knudsen layer, bulk velocity, and slip. The R13 equations benefit the Knudsen layer to provide more curvature near the walls, see plots (g) and (i) in Fig. 9.2.

The effects of different accommodation factors and rotational modes for $\mathrm{Kn} = 0.1$ are investigated in Fig. 9.3, where radial distribution for shear stress, circumferential heat flux, and velocity are given. Comparison between Fig. 9.2 and Fig. 9.3 shows that for the same rotational mode, variations of χ and Kn have similar effects on $\tilde{\sigma}_{r\varphi}$ and $\tilde{q}_{\varphi}$ distribution. Smooth walls with small χ values impose less stress and weak Knudsen layers.

In plot (g) velocity inversion is observed, i.e., flow velocity increases close to the stationary wall [8, 28, 116, 132]. The velocity inversion takes place only for rotational mode 1 and for small accommodation coefficients. It is not a rarefaction effect as it can be predicted by NSF system. This phenomenon is the effect of curvature on the slip length, hence it cannot be observed in the planar Couette flows. In other words, cooperation between the wall curvature and wall smoothness on the inner cylinder extensively increases the slip such that velocity inversion occurs.

In Figs. 9.4 and 9.5 we have compared our velocity results with DSMC data from Refs. [8, 116]. In the considered DSMC simulations, molecules are treated as hard–sphere molecules, thus, coefficients for Maxwellian molecules [cf. Eq. (4.15)] have been used in the R13 equations. It is important to emphasize that in Refs. [8] and [116] the Knudsen number is defined based on the gap size $L = r_\mathrm{o} - r_\mathrm{i}$, and inner radius r_i, respectively. Consequently, our solutions are characterized by two different Knudsen numbers.

The DSMC data in Ref. [116] are for argon at $p = 101\,325$ Pa, confined between two isothermal walls at $T = 298.15$ K, where the mean–free path for hard–sphere molecules is $\lambda^{\mathrm{HS}} = 6.25 \times 10^{-8}$ m, and speed of sound is 321.629 m/s. The outer cylinder is stationary while the inner one rotates at $\omega_\mathrm{i} = 5.17 \times 10^{8}$ rad/s. The gap size is $L = r_\mathrm{o} - r_\mathrm{i}$ with $r_\mathrm{i} = 3\lambda^{\mathrm{HS}}$ and $r_\mathrm{o} = 5\lambda^{\mathrm{HS}}$. These conditions give $\mathrm{Kn} = 0.447$ (based on our definition for Knudsen number), while different accommodation factors are employed.

Plots (a) and (b) in Fig. 9.4 present Navier–Stokes results for velocity with first– and second–order slip conditions, respectively. It is shown that the new second–order slip condition improves the Navier–Stokes predictions, and makes them comparable with DSMC, and with the R13 results, which are depicted in Plot (c). This improvement is more apparent near the outer stationary wall.

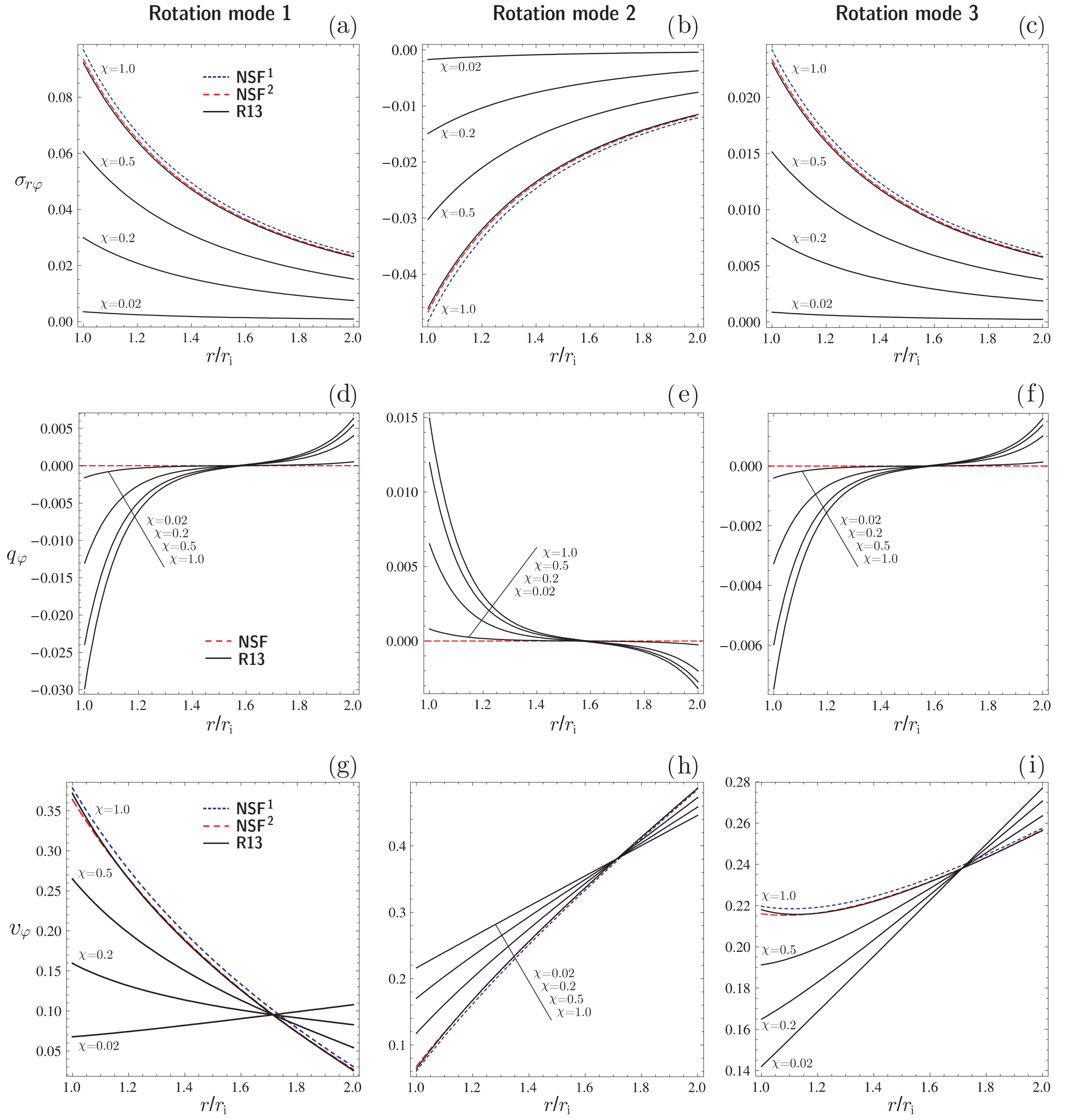

Figure 9.3: Solutions of the linear velocity problem: dashed blue line is NSF with first–order boundary condition; long–dashed red line is NSF with second–order boundary condition; continuous black line is R13 with third–order boundary conditions. Radial distribution of shear stress (top plots), circumferential heat flux (middle plots), and velocity (bottom plots) in the annulus for Kn $= 0.1$ are shown. Plots in left, middle, and right columns correspond to rotational modes 1, 2 and 3, respectively. For each rotational mode, effects of surface accommodation factors are depicted. NSF results with the proposed second–order slip condition show satisfactory agreement with the R13 predictions. For the small Knudsen numbers NSF results are not shown, since they are very close to the R13 predictions.

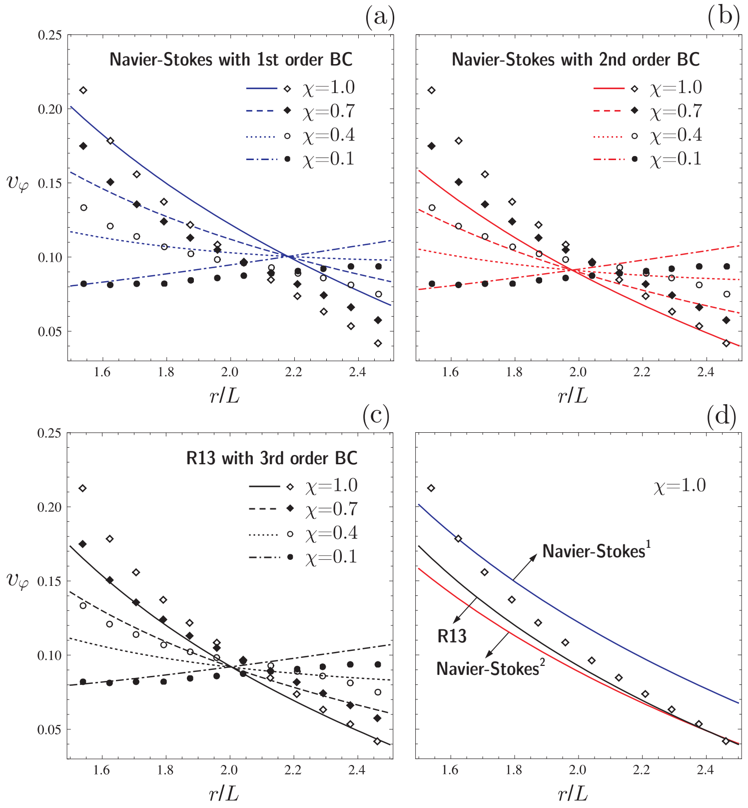

Figure 9.4: Radial velocity distribution for different accommodation factors when $\mathrm{Kn} = 0.447$. Knudsen number is defined based on the gap size, $L = r_\mathrm{o} - r_\mathrm{i}$. Navier–Stokes and R13 results are compared to DSMC data (diamond symbols) from Ref. [116].

For fully diffusive walls, the velocity profiles are compared in plot (d).

We emphasize that in the DSMC simulations of Ref. [116] the size of the gap between the cylinders is $2\lambda^{\mathrm{HS}}$, which is very small. The thickness of Knudsen boundary layers is usually in the order of two mean free paths. Therefore, in the data of Ref. [116] the Knudsen layers affect the whole flow field, specifically for the diffusive walls. So we do not expect excellent agreement with the DSMC results of [116], since the Knudsen number is too large for our method. This motivated another comparison with DSMC data for smaller Knudsen number from Ref. [8].

In Ref. [8], unlike [116], the radius of the inner cylinder r_i is assigned as the characteristic length, and $r_\mathrm{o} = 2r_\mathrm{i}$. The dimensionless surface velocity of the inner cylinder is $\tilde{v}_\varphi^{W,\mathrm{i}} = \sqrt{2}/2$, and the outer cylinder is at rest. The Knudsen number k used in [8] is related to our definition by $k = 8\sqrt{2}\,\mathrm{Kn}/(5\sqrt{\pi})$.

Figure 9.5 presents the velocity comparison for $\chi = \{0.01, 0.2, 1.0\}$, when $k = 0.1$, or $\mathrm{Kn} = 0.08$. Since the Knudsen number is relatively small, the Navier–Stokes system shows good agreement. The profiles near the rotating wall are magnified to show the Knudsen layers. The R13 results exhibit more curvature than NSF, due to the non–Fourier tangential heat flow effects.

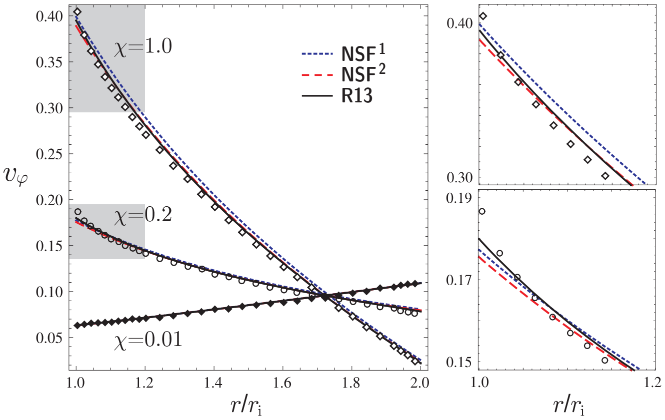

Figure 9.5: Radial velocity distribution for Kn = 0.08 with different accommodation factors. Knudsen number is defined based on the radius of the inner cylinder. Navier–Stokes and R13 results are compared to DSMC data (symbols) from Ref. [8]. Profiles near the rotary wall (shaded areas) are magnified to show the effects of Knudsen layers.

9.6.2 Results for the Temperature Problem

The temperature and velocity problems are independent in the linearized systems. This means coupling between velocity and temperature fields, particularly, viscous heating, is ignored in our analysis. Therefore, the temperature problem is reduced to stationary radial heat conduction between the cylinders. DSMC simulations with isothermal cylinders [8, 116] exhibit small temperature deviation due to viscous dissipation. Tibbs *et al.* [116] reported 1% and 3% density and temperature variations, respectively, while in Ref. [8] effects of viscous heating on density and temperature is about 5% for Kn = 0.13 ($k = 0.1$).

As postulated by Fourier's law, for isothermal walls our numerical results for the linearized equations confirm a homogeneous radial distribution for temperature where,

$$\theta\left(r\right)=\theta^{W},\qquad q_{r}\left(r\right)=\sigma_{\varphi\varphi}\left(r\right)=\sigma_{rr}\left(r\right)=0. \tag{9.24}$$

The above results, with Eq. (9.14), give a constant radial distribution for density $\rho\left(r\right)=\rho_{0}$.

We consider a case where the cylinders are at different temperatures. Then, the linear temperature problem can be characterized by Knudsen number Kn, surface accommodation factor χ, and wall temperatures θ^W. The parameters are chosen similar to the velocity problem, but $v_\varphi^{W,\mathrm{i}} = v_\varphi^{W,\mathrm{o}} = 0$, and we shall define two temperature modes, with $\theta^{W,\mathrm{i}} = 2\theta^{W,\mathrm{o}} = 2$, and $\theta^{W,\mathrm{o}} = 2\theta^{W,\mathrm{i}} = 2$ for mode 1 and 2, respectively.

Profiles of diagonal elements of stress tensor, radial heat flux, and temperature are shown in Fig. 9.6. Plots (a)–(h) are obtained for fully diffusive walls $\chi = 1$, and the effects of Kn variations are shown. Plots (i)–(p) are obtained for $\mathrm{Kn} = 0.1$, while the effects of χ variations are examined.

In the temperature problem, switching between the temperature modes only inverts the process, compare the signs of σ_{rr}, $\sigma_{\varphi\varphi}$, and q_r between the temperature modes.

The first and second row of plots show that diagonal stress components, which are zero in NSF system, grow with Kn and χ. These non–Newtonian stress components can be interpreted as Knudsen layers for the temperature problem. The behavior of the radial heat flux $\tilde{q}_r$ in the temperature problem is similar to that of the shear stress $\tilde{\sigma}_{r\varphi}$ in the velocity problem. So one might conclude that in the linear limit the differences between the NSF and R13 results for $\tilde{q}_r$ only refers to the difference between the boundary conditions. This cannot be proved through the numerical solutions, as we do not have an explicit solution for $\tilde{q}_r$. Heat flow between two cylinders is stronger at rarefied conditions, due to the larger mean free path. Analogously, diffusive walls increase the heat flow since they provide better thermalization for the gas molecules.

The bottom plots in Fig. 9.6 are devoted to the radial temperature distribution. It can be seen that there are larger temperature jumps on the inner cylinder, owing to its higher curvature. Plots (g) and (h) show that the temperature jump increases with Kn, since the number of gas–surface collisions decreases for large Knudsen numbers. On the other hand, temperature jump and χ are in inverse relation. For very small values of χ, temperature jump increases on both cylinders, such that a homogeneous temperature fills the annulus, see plots (o) and (p).

Finally, the proposed second–order jump condition provides better matching between NSF and R13 results.

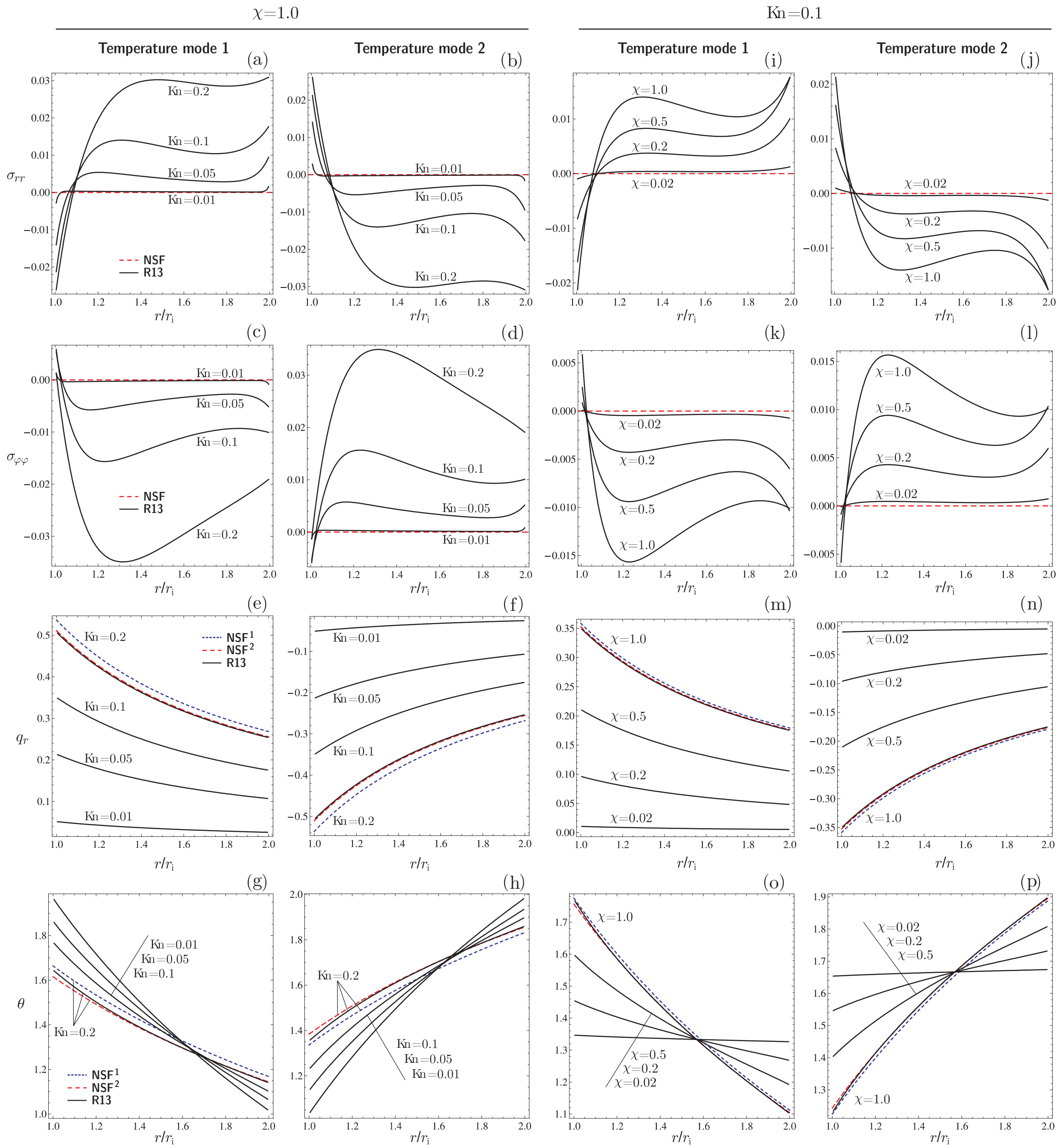

Figure 9.6: Solutions for the linear temperature problem: dashed blue line is NSF with first-order boundary condition; long-dashed red line is NSF with second–order boundary condition; continues black line is R13 with third-order boundary conditions. Radial distribution of non–Newtonian shear stresses (first and second rows), radial heat flux (third row), and temperature (bottom plots) in the annulus are shown. For each temperature mode, effects of different surface accommodation factors and Knudsen numbers are depicted.

Chapter 10

Linear Theory for Flows in Tubes

In this section, linearized Navier–Stokes–Fourier (NSF) and regularized 13–moment (R13) equations along with their corresponding boundary conditions are employed to investigate nonequilibrium effects in Poiseuille and transpiration flows of rarefied gases in tubes.

10.1 Poiseuille and Transpiration Flows in Tubes

Tubes with circular cross section are favored in engineering applications as flow passages. Rarefied gas flows in circular channels under pressure gradients (cylindrical Poiseuille flow), and temperature gradients (cylindrical thermal transpiration/creep flow) are rigorously investigated through kinetic approaches, see Ref. [92] for an extensive bibliography. Kinetic solutions of cylindrical Poiseuille flow were first reported in 1966 by Cercignani and Sernagiotto [23], followed by Ferziger's improvements [29]. They confirmed the presence of a minimum in the flow rate, which was previously observed in experiments by Knudsen [51] (Knudsen paradox).

One year later, Sone and Yamamoto [103], and Loyalka [60] initiated kinetic approaches for thermally–driven flows in tubes. The interesting phenomenon in transpiration flows is the existence of a pumping effect, also known as thermomolecular pressure difference (TPD), which was proved by Knudsen experiments [52].

Nowadays, owing to broad improvements in computational facilities and numerical schemes, the quality of kinetic solutions for cylindrical Poiseuille and transpiration flows is considerably improved. Thus, they provide a reliable benchmark for validating the results of macroscopic approaches, and even for calibrating the experiments.

We investigate steady state flows subject to small longitudinal pressure and temperature gradients, where the linearized R13 equations can be used to analyze the problem with minimum numerical effort. In order to validate our solutions, we compare them with the most recent kinetic data.

An explicit solution for two–way flow pattern, which appears in simultaneous Poiseuille and transpiration flows, is discussed. Furthermore, we examine the validity of Onsager's reciprocity relation for both NSF and R13 equations. Breakdown of Onsager's symmetry is used as a new criterion to determine the range of applicability of macroscopic approaches.

Finally, in order to improve the accuracy of classical NSF hydrodynamics, a new set of velocity slip and temperature jump conditions for NSF system is proposed. These conditions are deduced from the R13 kinetic boundary conditions using a scaling approach [110, 113], see Appendix C for more details. It is shown that these second–order boundary conditions for axial flows in tubes considerably improve the NSF solutions for the considered boundary value problems.

10.2 Flow Setting for Poiseuille and Transpiration Flows in Tubes

We consider a system including two reservoirs containing the same gas, joined by a capillary of length L, as depicted in Fig. 10.1a. The pressure p, temperature T, and mass density ρ of the gas in the cold low–pressure and warm high–pressure reservoirs are denoted by $\{p_1, T_1, \rho_1\}$ and $\{p_2, T_2, \rho_2\}$, respectively, and the valves of reservoirs allow to adjust these conditions.

First, we assume isothermal reservoirs $T_1 = T_2$, while a constant pressure difference is maintained between the reservoirs by adjusting the valves such that $p_2 > p_1$. In this setting a pressure driven Poiseuille flow occurs from the right reservoir to the left one. Quite differently, a thermally–induced flow can be initiated between isobaric reservoirs, $p_1 = p_2$, which are kept at different temperatures $T_1 > T_2$, and a temperature gradient along the capillary wall connects the temperatures of the reservoirs. In this setting the gas flows from the cold reservoir to the hot one. The arising flow is a thermal transpiration flow [98].

Furthermore, we consider simultaneous Poiseuille and transpiration flows in a closed system, i.e., when both valves are closed. Initially, we assume isobaric reservoirs with different temperatures and a temperature gradient along the capillary wall. This setting initiates a thermally–driven flow in the tube in the direction of the temperature gradient. Therefore, a pressure difference between the reservoirs will establish, known as the thermomolecular pressure difference [52, 89]. This, in turn, will induce a pressure–driven Poiseuille flow, in opposite direction of the transpiration flow. We emphasize that in such a flow setting temperature and pressure gradients have the same direction along the tube, while their corresponding flows have opposite directions. There will be a transpiration flow at the walls, and a backward flow in the centre of the pipe. After a sufficiently long time, a steady state condition will establish in which the closed reservoirs have constant pressure and temperature ratios, and the net mass flow in the capillary is zero. The relation between pressure and temperature can be presented by

$$\frac{p_2}{p_1} = \left(\frac{T_2}{T_1}\right)^{\gamma}, \tag{10.1}$$

where γ is the exponent of thermomolecular pressure difference [92], which strongly depends on the degree of gas rarefaction, i.e., the Knudsen number [89, 90].

We investigate steady state flow in a long capillary with circular cross section of radius R, see Fig. 10.1b. Thus, cylindrical coordinates $\mathbf{x} = \{r, \varphi, z\}$ are employed in our analysis, where r and z are the radial and axial coordinates, respectively. The flow is irrotational, $v_\varphi = 0$, and independent of the azimuthal coordinate, i.e., $\partial/\partial\varphi = 0$.

10.3 Flow in Long Tubes

In general, due to compressibility effects, flow in the tube is two–dimensional in the r–z plane, which requires a numerical approach. As discussed in Ref. [92], and similar to what we did for Poiseuille and transpiration flows in parallel–plate channels, in flows through long passages one can safely discard the small compressibility effects and describe the overall flow behavior using a one–dimensional transport field. In this section we use the same approach which is used in Ref. [92] to justify the unidirectional flow assumption in long tubes.

For sufficiently long tubes where $R/L = \epsilon \ll 1$, one can assume that density and temperature variations in the cross section are negligible compared to their longitudinal variation, so that $\rho = \rho(z)$ and $\theta = \theta(z)$. To proceed, we choose the radius of the tube as the reference length scale to define the dimensionless coordinates

$$\tilde{r} = \frac{r}{R}, \quad \text{and} \quad \tilde{z} = \frac{z}{R}. \tag{10.2}$$

Indeed, the reservoirs affect the flow at the capillary ends, but compared to the length of the capillary,

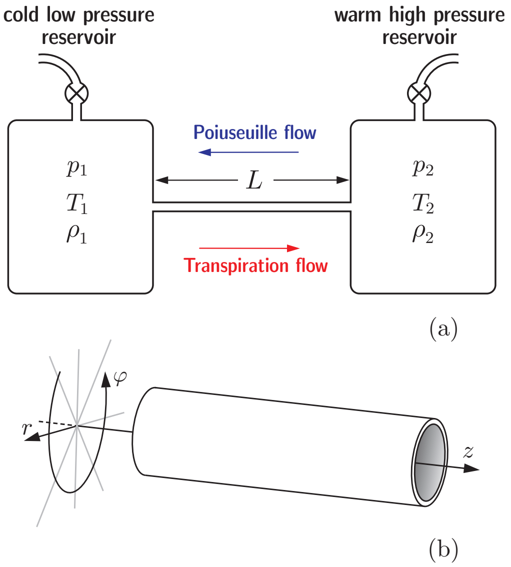

Figure 10.1: Poiseuille flow, thermal transpiration flow, and their combination are illustrated between two vessels (a), which are connected through a long pipe (b). In the case of pressure–driven Poiseuille flow, a constant pressure difference is maintained between the reservoirs by adjusting the valves. In thermal transpiration flow a temperature gradient in axial z–direction is applied on the tube wall which connects the temperatures of two vessels. This longitudinal temperature gradient induces a flow from the cold reservoir to the warm one, while their pressure is the same. When the system is closed and a temperature gradient is applied on the tube wall, Poiseuille and transpiration flows occur simultaneously. In such a setting, temperature and pressure gradients have the same direction along the tube, but their corresponding flows have opposite directions.

the entry/exit effects are limited to very small regions. Then, ignoring these effects [125], we have

$$\rho\left(0\right)=\rho_1, \quad \rho\left(L\right)=\rho_2, \quad \theta\left(0\right)=\theta_1, \quad \theta\left(L\right)=\theta_2. \tag{10.3}$$

At any arbitrary cross section $\tilde{z}=\tilde{z}_0$ along the tube and for $|\tilde{z}-\tilde{z}_0|\lesssim 1$ we can write

$$\begin{aligned} \rho\left(\tilde{z}\right) &= \rho\left(\tilde{z}_0\right)+\left.\frac{\partial\rho}{\partial\tilde{z}}\right|_{\tilde{z}=\tilde{z}_0}\left(\tilde{z}-\tilde{z}_0\right)+\frac{1}{2}\left.\frac{\partial^2\rho}{\partial\tilde{z}^2}\right|_{\tilde{z}=\tilde{z}_0}\left(\tilde{z}'-\tilde{z}_0\right)^2, \\ \theta\left(\tilde{z}\right) &= \theta\left(\tilde{z}_0\right)+\left.\frac{\partial\theta}{\partial\tilde{z}}\right|_{\tilde{z}=\tilde{z}_0}\left(\tilde{z}-\tilde{z}_0\right)+\frac{1}{2}\left.\frac{\partial^2\theta}{\partial\tilde{z}^2}\right|_{\tilde{z}=\tilde{z}_0}\left(\tilde{z}'-\tilde{z}_0\right)^2, \end{aligned} \tag{10.4}$$

where $|\tilde{z}'-\tilde{z}_0|<|\tilde{z}-\tilde{z}_0|$.

The order of derivations can be expressed in terms of the smallness parameter ϵ,

$$\begin{aligned} \frac{\partial \rho}{\partial \tilde{z}} &\sim \epsilon\left(\rho_1-\rho_2\right)=\mathcal{O}(\epsilon), & \frac{\partial^2 \rho}{\partial \tilde{z}^2} &\sim \epsilon^2\left(\rho_1-\rho_2\right)=\mathcal{O}\left(\epsilon^2\right), \\ \frac{\partial \theta}{\partial \tilde{z}} &\sim \epsilon\left(\theta_1-\theta_2\right)=\mathcal{O}(\epsilon), & \frac{\partial^2 \theta}{\partial \tilde{z}^2} &\sim \epsilon^2\left(\theta_1-\theta_2\right)=\mathcal{O}\left(\epsilon^2\right). \end{aligned} \tag{10.5}$$

Since $\epsilon \ll 1$, the second–order derivatives can be neglected, and the expansions in Eq. (10.4) reduce to

$$\rho(\tilde{z})=\rho_0\left[1+\varrho\left(\tilde{z}-\tilde{z}_0\right)\right], \quad \text{and} \quad \theta(\tilde{z})=\theta_0\left[1+\tau\left(\tilde{z}-\tilde{z}_0\right)\right], \tag{10.6}$$

with

$$\rho_0=\rho\left(\tilde{z}_0\right), \quad \varrho=\left.\frac{\partial\left(\rho / \rho_0\right)}{\partial \tilde{z}}\right|_{\tilde{z}=\tilde{z}_0}=\mathcal{O}(\epsilon), \quad \theta_0=\theta\left(\tilde{z}_0\right), \quad \tau=\left.\frac{\partial\left(\theta / \theta_0\right)}{\partial \tilde{z}}\right|_{\tilde{z}=\tilde{z}_0}=\mathcal{O}(\epsilon). \tag{10.7}$$

Accordingly, we can conclude that near a given cross section, $\tilde{z}_0$, on a distance of the order of the tube radius R, density and temperature linearly vary with respect to $\tilde{z}$, and their gradients are small constants of order ϵ. Replacement of density and temperature from Eq. (10.6) into the ideal gas law gives

$$p(\tilde{z})=p_0\left[1+\wp\left(\tilde{z}-\tilde{z}_0\right)\right], \quad \text{with} \quad p_0=\rho_0 \theta_0, \quad \wp=\varrho+\tau=\left.\frac{\partial\left(p / p_0\right)}{\partial \tilde{z}}\right|_{\tilde{z}=\tilde{z}_0}=\mathcal{O}(\epsilon); \tag{10.8}$$

again, all terms of order $\left(\tilde{z}-\tilde{z}_0\right)^2$ are neglected due to linearization.

The constant pressure and temperature gradients are the driving forces for the Poiseuille and transpiration flows, respectively. As will be shown the following sections, our linear analysis discards axial compressibility effects and allows to simplify the problem such that a one–dimensional analysis can be employed to investigate the local transport field across the tube.

The tube walls are impermeable and there is no velocity in the radial direction, $v_r = 0$. Since the flow is assumed to be independent of the φ–direction, the velocity vector $\mathbf{v}$, the heat–flux vector $\mathbf{q}$, and the symmetric and trace–free stress tensor $\boldsymbol{\sigma}$ simplify to

$$\mathbf{v}=\begin{pmatrix} 0 \\ 0 \\ v_z(r) \end{pmatrix}, \quad \mathbf{q}=\begin{pmatrix} q_r(r) \\ 0 \\ q_z(r) \end{pmatrix}, \quad \boldsymbol{\sigma}=\begin{pmatrix} \sigma_{rr}(r) & 0 & \sigma_{rz}(r) \\ 0 & \sigma_{\varphi\varphi}(r) & 0 \\ \sigma_{rz}(r) & 0 & \sigma_{zz}(r) \end{pmatrix}, \tag{10.9}$$

where all components are only functions of the radial coordinate r. Trace–free condition for the stress tensor gives $\sigma_{\varphi\varphi}(r) = -\sigma_{rr}(r) - \sigma_{zz}(r)$.

10.4 Linearized R13 Equations for Axial Flows in Tubes

For steady state and unidirectional axial flows, as illustrated in Fig. 10.1, linearized R13 equations in cylindrical coordinates [Eqs. (4.40)–(4.70)] reduce to the following three sets of differential equations.

■ The velocity problem:

R13 case: In the linear case, to find the gas velocity we need to solve the following subset of equations

$$\left(\frac{\partial}{\partial \tilde{r}} + \frac{1}{\tilde{r}}\right)\tilde{\sigma}_{rz} = -\wp, \tag{10.10a}$$

$$-\wp + \frac{1}{2}\left(\frac{\partial}{\partial \tilde{r}} + \frac{1}{\tilde{r}}\right)\tilde{R}_{rz} = -\frac{\mathrm{Pr}}{\mathrm{Kn}}\tilde{q}_z - \frac{5}{2}\tau, \tag{10.10b}$$

$$\frac{2}{5}\frac{\partial \tilde{q}_z}{\partial \tilde{r}} + \frac{\partial \tilde{m}_{rrz}}{\partial \tilde{r}} + \frac{\tilde{m}_{rrz} - \tilde{m}_{\varphi\varphi z}}{\tilde{r}} = -\frac{1}{\mathrm{Kn}}\tilde{\sigma}_{rz} - \frac{\partial \tilde{v}_z}{\partial \tilde{r}}, \tag{10.10c}$$

with the constitutive relations

$$\tilde{R}_{rz} = \frac{\mathsf{B}_2}{2}\,\mathrm{Kn}\frac{\partial \tilde{q}_z}{\partial \tilde{r}}, \quad \tilde{m}_{rrz} = -\frac{8\,\mathsf{C}}{15}\,\mathrm{Kn}\left(\wp + \frac{5}{4}\frac{\tilde{\sigma}_{rz}}{\tilde{r}}\right), \quad \tilde{m}_{\varphi\varphi z} = \frac{2\,\mathsf{C}}{15}\,\mathrm{Kn}\left(\wp + 5\frac{\tilde{\sigma}_{rz}}{\tilde{r}}\right), \tag{10.11}$$

and the linearized boundary conditions [cf. Eq. (5.39)]

$$\tilde{\sigma}_{rz} = -\frac{\chi}{2-\chi}\sqrt{\frac{2}{\pi}}\left(\tilde{\mathcal{V}}_z + \frac{1}{5}\tilde{q}_z + \frac{1}{2}\tilde{m}_{rrz}\right)n_r, \tag{10.12a}$$

$$\tilde{R}_{rz} = -\frac{\chi}{2-\chi}\sqrt{\frac{2}{\pi}}\left(-\tilde{\mathcal{V}}_z + \frac{11}{5}\tilde{q}_z + \frac{1}{2}\tilde{m}_{rrz}\right)n_r. \tag{10.12b}$$

Equation (10.10a) is the dimensionless and linearized axial momentum balance, $\wp = \partial \tilde{p}/\partial \tilde{z}$ was introduced in Eq. (10.8). Also, Eq. (10.10b) is the dimensionless and linearized axial heat–flux balance with $\tau = \partial \tilde{\theta}/\partial \tilde{z}$, as the constant and dimensionless axial temperature gradient [Eq. (10.6)]. Equation (10.10c) is the dimensionless and linear form of the shear–stress balance.

Classical case: In the hydrodynamic limit, where high–order moments vanish, the velocity problem reduces to

$$\left(\frac{\partial}{\partial \tilde{r}} + \frac{1}{\tilde{r}}\right)\frac{\partial \tilde{v}_z}{\partial \tilde{r}} = \frac{\wp}{\mathrm{Kn}}, \qquad 0 = -\frac{\mathrm{Pr}}{\mathrm{Kn}}\tilde{q}_z - \frac{5}{2}\tau, \tag{10.13}$$

In Eq. $(10.13)_1$ Navier–Stokes law for shear–stress in dimensionless form was used, i.e.,

$$\tilde{\sigma}_{rz}^{\mathrm{NSF}} = -\mathrm{Kn}\frac{\partial \tilde{v}_z}{\partial \tilde{r}}. \tag{10.14}$$

Equation $(10.13)_2$ is Fourier's law for axial heat conduction (applicable only for thermally–driven flows),

$$\tilde{q}_z^{\mathrm{NSF}} = -\frac{5}{2}\frac{\mathrm{Kn}}{\mathrm{Pr}}\,\tau. \tag{10.15}$$

Since σ_{rz} is of $\mathcal{O}\left(\mathrm{Kn}\right)$, it follows from Eq. (10.10a) and also from Eq. $(10.13)_1$, that pressure gradient $\wp$ is first–order in terms of Knudsen number, $\mathcal{O}\left(\wp\right) = \mathcal{O}\left(\mathrm{Kn}\right)$. Hence, $\wp$ in Eq. (10.10b) provides a second–order contribution to the axial heat flow, and as depicted in Eq. $(10.13)_2$ it vanishes in the hydrodynamic limit [98].

The radial velocity distribution can be found by integrating $(10.13)_1$. Depending on the kinetic model, the integrating constants must be evaluated from the linearized form of the approximate slip conditions [cf. Eq. (C.27)] that read

$$\tilde{\mathcal{V}}_z^{\mathrm{NSF}} = \frac{2-\chi}{\chi}\sqrt{\frac{\pi}{2}}\,\frac{\partial \tilde{v}_z}{\partial \tilde{r}}\,\mathrm{Kn}\,n_r + \frac{1}{2}\frac{\mathrm{Kn}}{\mathrm{Pr}}\,\tau - \left(\frac{1}{5\,\mathrm{Pr}} - \frac{4\,\mathsf{C}}{15}\right)\frac{\partial^2 \tilde{v}_z}{\partial \tilde{r}^2}\,\mathrm{Kn}^2 - \left(\frac{1}{5\,\mathrm{Pr}} + \frac{\mathsf{C}}{15}\right)\frac{1}{\tilde{r}}\frac{\partial \tilde{v}_z}{\partial \tilde{r}}\,\mathrm{Kn}^2. \tag{10.16}$$

In Eq. (10.16) both Navier–Stokes and Fourier laws in dimensionless form [Eqs. (10.14) and (10.15)] were used.

■ The temperature problem:

R13 case: The Thermal behavior of the gas is governed by the equations

$$\left(\frac{\partial}{\partial \tilde{r}} + \frac{1}{\tilde{r}}\right)\tilde{q}_r = 0, \tag{10.17a}$$

$$\left(\frac{\partial}{\partial \tilde{r}} + \frac{1}{\tilde{r}}\right)\tilde{m}_{rzz} = -\frac{1}{\mathrm{Kn}}\tilde{\sigma}_{zz}, \tag{10.17b}$$

$$-\frac{4}{5}\frac{\tilde{q}_r}{\tilde{r}} + \frac{\partial \tilde{m}_{rrr}}{\partial \tilde{r}} + \frac{\tilde{m}_{rrr} - 2\tilde{m}_{r\varphi\varphi}}{\tilde{r}} = -\frac{1}{\mathrm{Kn}}\tilde{\sigma}_{rr}, \tag{10.17c}$$

$$\frac{\partial \tilde{\sigma}_{rr}}{\partial \tilde{r}} + \frac{2\tilde{\sigma}_{rr} + \tilde{\sigma}_{zz}}{\tilde{r}} + \frac{1}{2}\left(\frac{\partial \tilde{R}_{rr}}{\partial \tilde{r}} + \frac{2\tilde{R}_{rr} + \tilde{R}_{zz}}{\tilde{r}}\right) + \frac{1}{6}\frac{\partial \tilde{\varDelta}}{\partial \tilde{r}} = -\frac{\mathrm{Pr}}{\mathrm{Kn}}\tilde{q}_r - \frac{5}{2}\frac{\partial \tilde{\theta}}{\partial \tilde{r}}, \tag{10.17d}$$

with the constitutive relations

$$\tilde{\Delta}=\tilde{R}_{zz}=0,\quad \tilde{R}_{rr}=-\mathsf{B}_2\,\mathrm{Kn}\frac{\tilde{q}_r}{\tilde{r}},\quad \tilde{m}_{rrr}=\frac{3\,\mathsf{C}}{5}\,\mathrm{Kn}\left(\frac{\partial\tilde{\sigma}_{rr}}{\partial\tilde{r}}-\frac{2}{3}\frac{2\tilde{\sigma}_{rr}+\tilde{\sigma}_{zz}}{\tilde{r}}\right),$$
$$\tilde{m}_{r\varphi\varphi}=\frac{\mathsf{C}}{3}\,\mathrm{Kn}\left(-\frac{7}{5}\frac{\partial\tilde{\sigma}_{rr}}{\partial\tilde{r}}-\frac{\partial\tilde{\sigma}_{zz}}{\partial\tilde{r}}+\frac{8}{5}\frac{2\tilde{\sigma}_{rr}+\tilde{\sigma}_{zz}}{\tilde{r}}\right),$$
$$\tilde{m}_{rzz}=\frac{\mathsf{C}}{3}\,\mathrm{Kn}\left(\frac{\partial\tilde{\sigma}_{zz}}{\partial\tilde{r}}-\frac{2}{5}\frac{\partial\tilde{\sigma}_{rr}}{\partial\tilde{r}}-\frac{2}{5}\frac{2\tilde{\sigma}_{rr}+\tilde{\sigma}_{zz}}{\tilde{r}}\right), \tag{10.18}$$

and the linearized boundary conditions [Eq. (5.39)]

$$\tilde{q}_r=\frac{\chi}{2-\chi}\sqrt{\frac{2}{\pi}}\left(-2\tilde{\mathcal{T}}-\frac{1}{2}\tilde{\sigma}_{rr}-\frac{1}{15}\tilde{\Delta}-\frac{5}{28}\tilde{R}_{rr}\right)n_r, \tag{10.19a}$$
$$\tilde{m}_{rrr}=\frac{-\chi}{2-\chi}\sqrt{\frac{2}{\pi}}\left(-\frac{2}{5}\tilde{\mathcal{T}}+\frac{7}{5}\tilde{\sigma}_{rr}-\frac{1}{75}\tilde{\Delta}+\frac{1}{14}\tilde{R}_{rr}\right)n_r, \tag{10.19b}$$
$$\tilde{m}_{rzz}=\frac{\chi}{2-\chi}\sqrt{\frac{2}{\pi}}\left(-\frac{1}{5}\tilde{\mathcal{T}}-\tilde{\sigma}_{zz}+\frac{1}{5}\tilde{\sigma}_{rr}-\frac{1}{150}\tilde{\Delta}-\frac{1}{14}\tilde{R}_{zz}\right)n_r. \tag{10.19c}$$

Equation (10.17a) is the linearized energy balance in dimensionless form where the nonlinear viscous heating term, $-\tilde{\sigma}_{rz}\left(\partial\tilde{v}_z/\partial\tilde{r}\right)$, is omitted. The other equations are linearized balance equations for normal components of the stress tensor and heat–flux vector.

Classical case: Fourier's law for the radial direction is given on the right–hand side of Eq. (10.17d), $\tilde{q}_r^{\mathrm{NSF}}=-\left(5\,\mathrm{Kn}/\left(2\,\mathrm{Pr}\right)\right)\partial\tilde{\theta}/\partial\tilde{r}$. Substitution into Eq. (10.17a) gives an explicit equation for temperature,

$$\left(\frac{\partial}{\partial\tilde{r}}+\frac{1}{\tilde{r}}\right)\frac{\partial\tilde{\theta}}{\partial\tilde{r}}=0. \tag{10.20}$$

Integrating the above equation introduces a constant which must be determined from the linearized temperature jump condition [Eq. (C.28)],

$$\tilde{\mathcal{T}}^{\mathrm{NSF}}=\frac{2-\chi}{\chi}\frac{5}{4\,\mathrm{Pr}}\sqrt{\frac{\pi}{2}}\frac{\partial\tilde{\theta}}{\partial\tilde{r}}\mathrm{Kn}\,n_r-\frac{5}{2\,\mathrm{Pr}}\left[\left(\frac{5\,\mathsf{B}_2}{168}-\frac{1}{5}-\frac{\mathsf{A}_2}{30}\right)\frac{1}{\tilde{r}}\frac{\partial\tilde{\theta}}{\partial\tilde{r}}-\left(\frac{\mathsf{A}_2}{30}+\frac{5\,\mathsf{B}_2}{84}\right)\frac{\partial^2\tilde{\theta}}{\partial\tilde{r}^2}\right]\mathrm{Kn}^2. \tag{10.21}$$

■ The density/pressure problem:

R13 case: Once the temperature problem is solved, we can integrate the linear form of the radial momentum balance,

$$\frac{\partial\tilde{p}}{\partial\tilde{r}}+\frac{\partial\tilde{\sigma}_{rr}}{\partial\tilde{r}}+\frac{2\tilde{\sigma}_{rr}+\tilde{\sigma}_{zz}}{\tilde{r}}=0. \tag{10.22}$$

On account of Eq. (4.31) one can recast Eq. (10.22) as

$$\frac{\partial \tilde{\rho}}{\partial \tilde{r}}+\frac{\partial \tilde{\theta}}{\partial \tilde{r}}+\frac{\partial \tilde{\sigma}_{rr}}{\partial \tilde{r}}+\frac{2\tilde{\sigma}_{rr}+\tilde{\sigma}_{zz}}{\tilde{r}}=0, \tag{10.23}$$

in order to find radial density deviations. Integrating the above equation introduces another integrating constant, which must be determined from the auxiliary condition regarding the conservation of mass in the process, that in proper dimensionless form reads

$$\int_0^1 (\tilde{\rho}+1)\, \tilde{r}\, d\tilde{r} = \text{const.} \tag{10.24}$$

Classical case: Based on the Navier–Stokes law the normal stress components, also known as non–Newtonian stresses, vanish in the hydrodynamic limit $\tilde{\sigma}_{rr}=\tilde{\sigma}_{zz}=0$. Then the density/pressure problem simplifies to $\tilde{\rho}+\tilde{\theta}=\text{const}$.

10.5 Solutions for Poiseuille and Transpiration Flows in Tubes

In this section, explicit linear solutions for Poiseuille and thermal transpiration flows in tubes are presented for the velocity problem. Although the temperature problem in Eqs. (10.17a)–(10.18) is linear, due to the coupling between the non–Newtonian components of the stress tensor via the curvature terms, an explicit solution for it is not accessible. This restriction of obtaining analytical solution for the temperature problem is also reported in our discussion of cylindrical Couette flows [113].

As in Ref. [113], the linear temperature problem can be solved numerically with basic finite difference methods, which yield $\tilde{q}_r=\tilde{\sigma}_{zz}=\tilde{\sigma}_{rr}=\tilde{\theta}=0$ for symmetric temperature distributions on the tube. Similarly, trivial solutions for density and pressure can be concluded from the temperature problem solution that are $\tilde{\rho}=\tilde{p}=0$. This trivial solution means that in the linear regime flow is isothermal. Non–zero solutions for $\{\tilde{q}_r,\tilde{\sigma}_{zz},\tilde{\sigma}_{rr},\tilde{\theta},\tilde{\rho},\tilde{p}\}$ can be obtained when a nonsymmetric temperature distribution is defined on the tube wall, however, this is not a conventional setting for tube flows.

10.5.1 Poiseuille Flow in Tubes

In the Poiseuille flow where the process is driven by the pressure gradient $\wp$, the velocity problem [Eqs. (10.10) and (10.11)] reduces further to

$$\left(\frac{\partial}{\partial \tilde{r}} + \frac{1}{\tilde{r}}\right)\tilde{\sigma}_{rz} = -\wp, \tag{10.25a}$$

$$-\wp + \frac{\mathsf{B}_2\,\mathrm{Kn}}{4}\left(\frac{\partial}{\partial \tilde{r}} + \frac{1}{\tilde{r}}\right)\frac{\partial \tilde{q}_z}{\partial \tilde{r}} = -\frac{\mathrm{Pr}}{\mathrm{Kn}}\tilde{q}_z, \tag{10.25b}$$

$$\frac{2}{5}\frac{\partial \tilde{q}_z}{\partial \tilde{r}} = -\frac{1}{\mathrm{Kn}}\tilde{\sigma}_{rz} - \frac{\partial \tilde{v}_z}{\partial \tilde{r}}. \tag{10.25c}$$

The solution for the above system follows by integration as

$$\tilde{\sigma}_{rz} = \underline{\frac{\boldsymbol{\mathsf{C}}_1}{\tilde{r}} - \frac{\wp}{2}\tilde{r}}, \tag{10.26a}$$

$$\tilde{q}_z = \boldsymbol{\mathsf{C}}_2\,\mathcal{J}_0\left(\frac{2}{\mathrm{Kn}}\sqrt{\frac{\mathrm{Pr}}{\mathsf{B}_2}}\,\tilde{r}\right) + \boldsymbol{\mathsf{C}}_3\,\mathcal{Y}_0\left(\frac{2}{\mathrm{Kn}}\sqrt{\frac{\mathrm{Pr}}{\mathsf{B}_2}}\,\tilde{r}\right) + \frac{\mathrm{Kn}}{\mathrm{Pr}}\,\wp, \tag{10.26b}$$

$$\tilde{v}_z = \underline{\boldsymbol{\mathsf{C}}_4 + \frac{\wp}{4\,\mathrm{Kn}}\tilde{r}^2 - \frac{\boldsymbol{\mathsf{C}}_1}{\mathrm{Kn}}\ln(\tilde{r})} - \frac{2}{5}\tilde{q}_z. \tag{10.26c}$$

$\boldsymbol{\mathsf{C}}_1$–$\boldsymbol{\mathsf{C}}_4$ are the integrating constants, which need to be determined from the boundary conditions.

The underlined terms indicate the solution for the NSF equations. Note that both R13 and NSF systems yield the same solution for shear stress. The NSF system predicts heat flux only in the direction of the temperature gradient, thus, it cannot predict the axial heat flux $\tilde{q}_z$ in this isothermal flow. Similar to Poiseuille flows in planar geometry, this streamwise heat flow, is not driven by temperature gradient, and is a pure rarefaction effect. The zeroth–order Bessel functions $\mathcal{J}_0$ and $\mathcal{Y}_0$ in $\tilde{q}_z$ describe Knudsen boundary layers, and $\mathrm{Kn}\,\wp/\mathrm{Pr}$ is a second–order bulk effect. The term $\boldsymbol{\mathsf{C}}_4$ is the macroscopic slip velocity, while the microscopic slip velocity is $-2\tilde{q}_z/5$ (at $\tilde{r} = 1$).

10.5.2 Transpiration Flow in Pipes

The thermal transpiration flow is induced by the axial temperature gradient τ, while $\wp = 0$. Hence, the velocity problem in (10.10) and (10.11) takes the form

$$\left(\frac{\partial}{\partial \tilde{r}} + \frac{1}{\tilde{r}}\right) \tilde{\sigma}_{rz} = 0, \tag{10.27a}$$

$$\frac{\mathsf{B}_2\,\mathrm{Kn}}{4}\left(\frac{\partial}{\partial \tilde{r}} + \frac{1}{\tilde{r}}\right) \frac{\partial \tilde{q}_z}{\partial \tilde{r}} = -\frac{\mathrm{Pr}}{\mathrm{Kn}}\tilde{q}_z - \frac{5}{2}\,\tau, \tag{10.27b}$$

$$\frac{2}{5}\frac{\partial \tilde{q}_z}{\partial \tilde{r}} = -\frac{1}{\mathrm{Kn}}\tilde{\sigma}_{rz} - \frac{\partial \tilde{v}_z}{\partial \tilde{r}}. \tag{10.27c}$$

Integrating Eq. (10.27) gives the general solution as

$$\tilde{\sigma}_{rz} = \underline{\frac{\mathsf{C}_1}{\tilde{r}}}, \tag{10.28a}$$

$$\tilde{q}_z = \mathsf{C}_2\,\mathcal{J}_0\left(\frac{2}{\mathrm{Kn}}\sqrt{\frac{\mathrm{Pr}}{\mathsf{B}_2}}\,\tilde{r}\right) + \mathsf{C}_3\,\mathcal{Y}_0\left(\frac{2}{\mathrm{Kn}}\sqrt{\frac{\mathrm{Pr}}{\mathsf{B}_2}}\,\tilde{r}\right) \underline{- \frac{5\,\mathrm{Kn}}{2\,\mathrm{Pr}}\,\tau}, \tag{10.28b}$$

$$\tilde{v}_z = \underline{\mathsf{C}_4 - \frac{\mathsf{C}_1}{\mathrm{Kn}}\ln\left(\tilde{r}\right) - \frac{2}{5}\tilde{q}_z}, \tag{10.28c}$$

with the underlined terms as hydrodynamic solutions. Similar to Poiseuille flow, the stress solutions for NSF and R13 are identical. The axial heat flux is a superposition of Knudsen boundary layers $\{\mathcal{J}_0, \mathcal{Y}_0\}$, or mechanocaloric heat flows [61, 62], and a Fourier heat conduction that is forced by the axial temperature gradient τ. In the velocity solution, C_4 and the contribution of the Fourier's law represent the slip velocity (temperature–driven plug flow).

10.6 Results and Discussion for Poiseuille and Transpiration Flows in Tubes

This section provides comparison between our theoretical results and kinetic solutions for the Boltzmann equation. Radial distributions of stress, velocity, streamwise heat flux, and Knudsen layers are compared to available kinetic data. Moreover, for both, Poiseuille and transpiration flows, the reduced mass flow rate, M, and the reduced thermal energy flow rate, E, are compared to Boltzmann data. The mass and thermal energy flow rates in tubes are defined as [92, 95, 124]

$$M = 2\sqrt{2}\int_0^1 \left|\tilde{v}_z\right|\,\tilde{r}\,d\tilde{r}, \quad E = 2\sqrt{2}\int_0^1 \left|\tilde{q}_z\right|\,\tilde{r}\,d\tilde{r}, \tag{10.29}$$

where the factor $2\sqrt{2}$ is included to match dimensionless definitions of M and E in the kinetic simulations. The influence of gas rarefaction, kinetic model, and boundary accommodation coefficients will be investigated on mass and energy transport in the axial direction.

Based on the applied kinetic model, we categorize the available kinetic data in two groups, namely, the linearized Boltzmann equation (BE) data and Bhatnagar–Gross–Krook (BGK) data. In comparisons of our solutions with kinetic data we use the coefficients given in Eqs. (4.15) and (4.16) as approximates for the BE and BGK models. Our general solutions in Eqs. (10.26b) and (10.28b) explicitly show that Pr and B_2 affect the thickness of Knudsen layers and bulk values. This observation is one of the advantages of analytical approach, that is not easily achievable in kinetic solutions.

Conventionally, in kinetic approaches a rarefaction parameter δ is defined as [92]

$$\delta = \frac{\sqrt{\pi}}{2} \frac{\mathcal{L}}{\lambda_0}, \tag{10.30}$$

where $\mathcal{L}$ and λ_0 are reference length scale (here, the radius of the tube R) and mean free path in the local equilibrium state, respectively. The kinetic theory of gases gives the mean free path with respect to macroscopic quantities as [16]

$$\lambda_0 = \sqrt{\frac{\pi\theta_0}{2}} \frac{\mu_0}{p_0}. \tag{10.31}$$

Replacement of λ_0 from Eq. (10.31) into Eq. (10.30) and then comparison with Eq. (4.38), gives a relation between Knudsen number and rarefaction parameter

$$\mathrm{Kn} = \frac{1}{\sqrt{2}\,\delta}, \tag{10.32}$$

which has been used to relate our solutions to the kinetic data.

10.6.1 Poiseuille Flow

The solution for Poiseuille flow is given in (10.26), where for the sake of compatibility with the Boltzmann data we shall set $\wp = 1$. Since the solutions must be finite at $\tilde{r} = 0$, then $\mathsf{C}_1 = \mathsf{C}_3 = 0$. The only unknown constant in the Navier–Stokes–Fourier solution is C_4 which can be evaluated from the linearized slip condition (10.16) at $\tilde{r} = 1$. For the R13 solution the constants $\{\mathsf{C}_2, \mathsf{C}_4\}$ follow from the boundary conditions (10.12).

Since $\mathbf{C}_1 = 0$, shear stress in NSF and R13 linearly depends on radial position, and its magnitude is proportional to the constant pressure gradient (or force), i.e., $\tilde{\sigma}_{rz} = -\wp\,\tilde{r}/2$.

In Fig. 10.2 the radial distribution of velocity and heat flux are shown for $\chi = 1$ and $\mathrm{Kn} = \{0.07, 0.14, 0.35\}$, corresponding to $\delta = \{10, 5, 2\}$. For proper scaling the kinetic data are multiplied with the factor $\sqrt{2}/\delta$. Plots (a) and (b) compare the velocity solutions with both BGK and linear Boltzmann equation (BE) data, respectively. In Poiseuille flow the solutions for BGK and BE are very close. As shown in plot (b), for the small Knudsen number $\mathrm{Kn} = 0.07$, all models show fair agreement with the kinetic solution. As the Knudsen number increases the Navier–Stokes–Fourier equations with first–order slip condition yield unsatisfactory bulk solution, however, it provides a better approximation of the slip velocity. By predicting a larger slip, the second–order slip condition shifts the NSF solution towards the R13 and kinetic results. Compared to NSF with second–order slip condition, R13 shows better agreement with kinetic data near the wall. This improvement is the effect of third–order boundary conditions and Knudsen boundary layer.

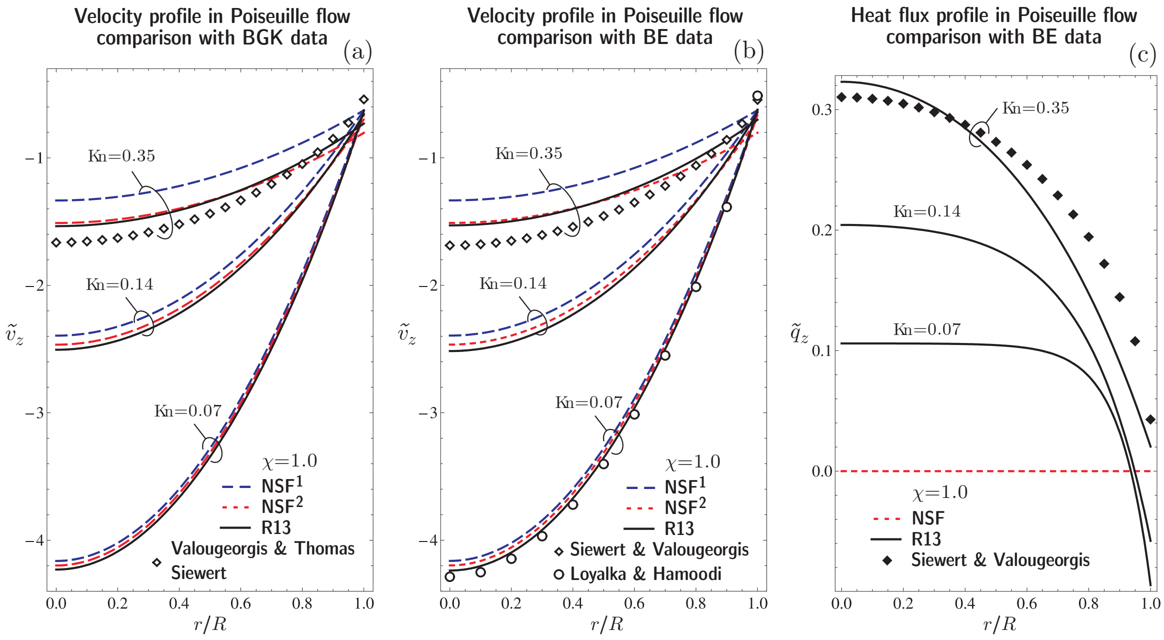

Figure 10.2: Radial distribution of velocity and mechanocaloric heat flux (Knudsen layer) in Poiseuille flow for $\mathrm{Kn} = \{0.07, 0.14, 0.35\}$ and fully diffusive tube surface, $\chi = 1$. Results from Navier–Stokes–Fourier with first–order slip condition (NSF^1; long–dashed blue line), Navier–Stokes–Fourier with second–order slip condition (NSF^2; dotted red line), and regularized 13–moment with third–order boundary conditions (R13; solid black line) are compared to kinetic data (symbols). The BGK data are taken from Refs. [124, 95] and BE data are from [96, 67].

In the velocity profile for Kn $= 0.35$, R13 shows maximum error at $r = 0$, and $r/R = 1$. In plot (b) these errors are 10% and 22% at the center of tubes and on the wall, respectively. These errors are calculated as (Data – R13)/R13.

In plot (c), the Knudsen layer in Poiseuille flow is compared to BE data (BGK data is not available for this case). This high–order nonequilibrium heat flow, which points in opposite direction to mass flow, cannot be predicted by NSF. The magnitude of this heat flux, which is not driven by temperature gradient, is increasing with Knudsen number. As depicted, for small Knudsen numbers, a two–way heat flow occurs; streamwise in a narrow layer near the wall and counter–stream elsewhere. This phenomena is also observed in Poiseuille flow in parallel–plate microchannels [115].

Figure 10.3 shows the reduced mass flow rate in Poiseuille flow M_P for fully diffuse walls $\chi = 1$ in the hydrodynamic regime. It shows that for small Knudsen numbers both NSF and R13 agree with kinetic data, taken from Ref. [56]. Indeed, the agreement between velocity profiles [cf. Fig. 10.2] is the reason for the precise prediction of mass flow rate. The kinetic data in Fig. 10.3 are obtained based on the BGK model, hence we used coefficients in (4.16) to evaluate our results. Similar BGK data were also reported earlier by Cercignani and Sernagiotto [23].

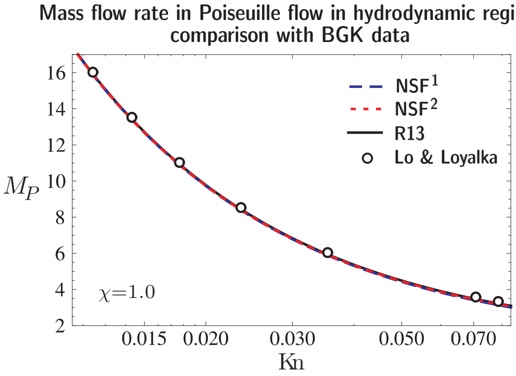

Figure 10.3: The reduced mass flow rate in Poiseuille flow obtained from Navier–Stokes–Fourier with first–order slip condition (NSF^1; long–dashed blue line), Navier–Stokes–Fourier with second–order slip condition (NSF^2; dotted red line), and regularized 13–moment with third–order boundary conditions (R13; solid black line) are compared to BGK kinetic data (symbols) from Ref. [56]. The comparison is presented for small Knudsen numbers and fully diffusive tube surface, $\chi = 1$. The comparison confirms that in the slip flow regime where Kn < 0.1, the results are very close.

Kinetic solutions for Poiseuille flow in the transition regime confirm Knudsen's experimental observation [51], that in low pressure Poiseuille flows the mass flow rate as a function of Knudsen number exhibits a minimum. This phenomenon, which is known as Knudsen minimum paradox, is observed in both parallel–plate channel and tube flows [22, Chap. VII].

Figure 10.4 shows the variations of mass flow rate in Poiseuille flow with respect to Knudsen number and accommodation coefficient of the tube surface. Unlike Fig. 10.3, which is restricted to the hydrodynamic regime, here the Knudsen number varies across the transition regime. NSF solutions with first– and second–order slip conditions are shown in plots (a)–(d), while R13 results are given in plots (e) and (f). Additionally, we compared our solutions with both BGK (left plots) and BE (right plots) data. The symbols present kinetic data for different accommodation coefficients $\chi = \{0.6, 0.8, 1.0\}$. Small values for χ represent smooth walls with less friction that result in larger flow rates. The results in Fig. 10.4 show that for small values of χ the validity of macroscopic models is extended to larger values for Kn. Here, we compare the accuracy of NSF and R13 with kinetic data for $\chi = 1$, which is commonly assumed in engineering applications. NSF with first–order slip condition in plots (a) and (b) does not exhibit any minimum, and is acceptable only for very small Knudsen numbers, $\mathrm{Kn} < 0.1$. The second–order slip condition extends the validity of the NSF system up to $\mathrm{Kn} \lesssim 0.6$, and enables the NSF system to capture a minimum. The R13 solution [cf. plots (e) and (f)] provide acceptable approximation of the flow rate in the transition regime; they are valid for $\mathrm{Kn} < 1.0$ in the BGK model and $\mathrm{Kn} < 1.7$ in the BE model. Our criterion to set these range for Knudsen number is $(\text{Data} - \text{Model})\,/\text{Model} \lesssim 7\%$.

For better comparison, the results for fully diffusive walls are compared in plots (g) and (h). For $\chi = 1$ the kinetic solution gives the minimum around $\mathrm{Kn} = 2.0$, while as our best candidate, i.e., R13, predicts this minimum around $\mathrm{Kn} = 0.7$ and $\mathrm{Kn} = 1.0$ for BGK and BE models.

We emphasize that for proper comparison with the kinetic data our results in Fig. 10.4 are obtained separately with BGK model coefficients (4.16) and linearized Boltzmann model coefficients (4.15).

The reduced thermal energy flow rate in Poiseuille flow, E_P, is discussed in the next section.

10.6.2 Transpiration Flow

The solution for thermal transpiration problem is given in (10.28), where for the sake of compatibility with the kinetic data we set $\tau = 1$. Since these solutions are finite at $\tilde{r} = 0$, then $\mathsf{C}_1 = \mathsf{C}_3 = 0$. The constant C_4 for the NSF system can be evaluated from the linearized slip condition (10.16) at $\tilde{r} = 1$. For the R13 solution the constants $\{\mathsf{C}_2, \mathsf{C}_4\}$ require boundary conditions (10.12).

With $\mathsf{C}_1 = 0$ the shear stress for both NSF and R13 systems vanishes, $\tilde{\sigma}_{rz} = 0$. Accordingly, for

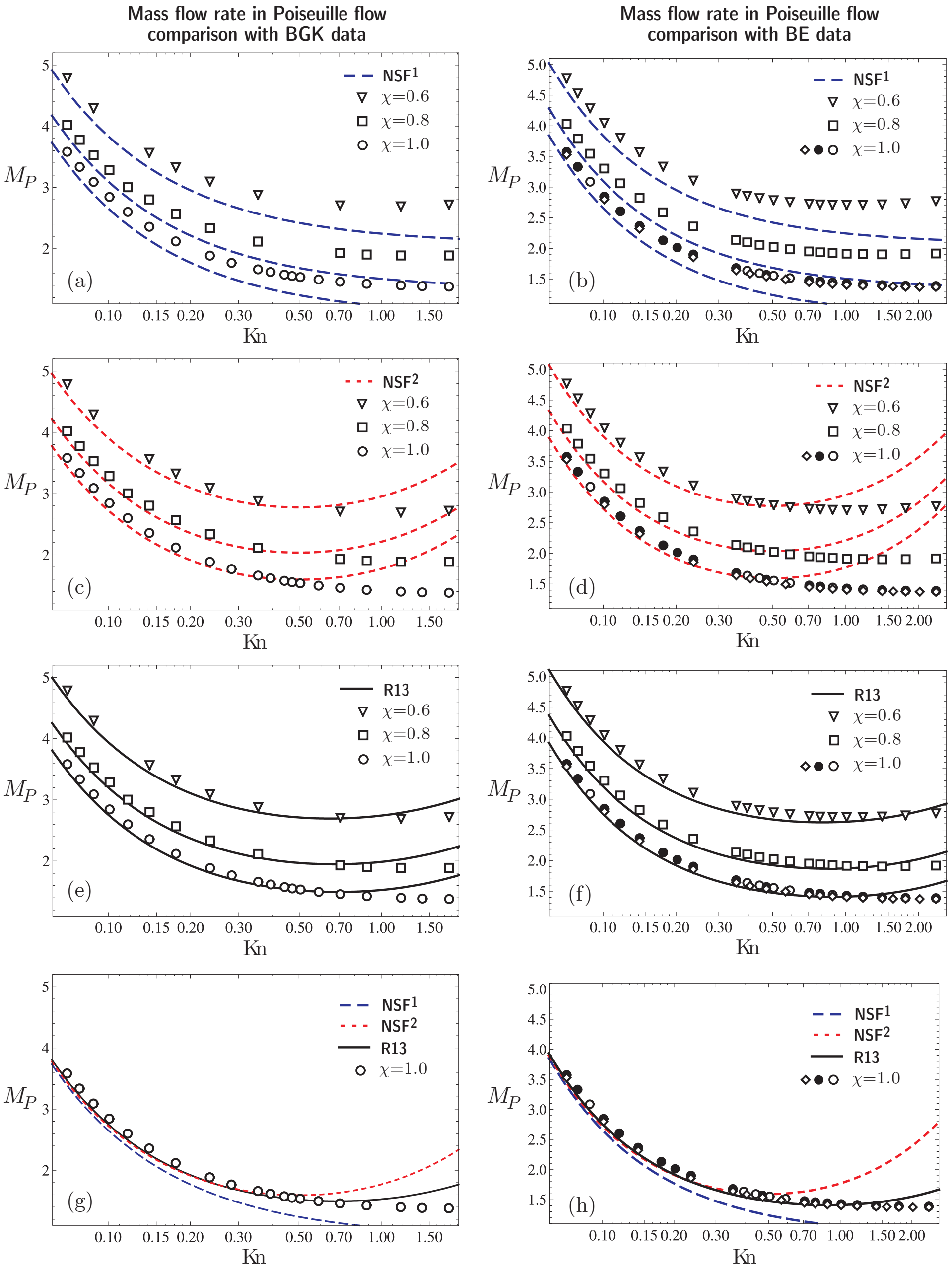

Figure 10.4: The effects of Knudsen number and surface accommodation on the reduced mass flow rate in Poiseuille flow in transition flow regime. Navier–Stokes–Fourier with first–order slip condition (NSF^1; long–dashed blue line), Navier–Stokes–Fourier with second–order slip condition (NSF^2; dashed red line), and regularized 13–moment with third–order boundary conditions (R13; solid black line) are compared to kinetic data (symbols) for $\chi = \{0.6, 0.8, 1.0\}$. Left and right plots correspond to BGK and BE solutions, respectively. BGK data for $\chi = 1$ shown by circles are from Ref. [56], while triangles and cubes are taken from [82, 83]. The BE data for $\chi = 1$ shown by black circles and diamonds are from [96] and [67], respectively. All other data are from Ref. [89]. It is shown that second–order slip condition improves the NSF solution in transition flow regime. In plots (g) and (h) all solutions for $\chi = 1$ are compared.

thermal transpiration flow, the slip condition (10.16) in dimensionless form reduces to

$$\tilde{\mathcal{V}}_z^{\mathrm{NSF}} = \frac{1}{2}\frac{\mathrm{Kn}}{\mathrm{Pr}}\tau,$$

that means in the linear limit the second–order slip condition degrades to a first–order condition. Due to this simplification, the effects of accommodation coefficients do not appear in the slip condition for hydrodynamics.

In Fig. 10.5 profiles of velocity and heat flux in transpiration flow are shown for $\chi = 1$ and $\mathrm{Kn} = \{0.07, 0.14, 0.35\}$, which correspond to $\delta = \{10, 5, 2\}$. Plots (a) and (b) compare the velocity solutions with BGK and linear Boltzmann equation (BE) data, respectively. For proper scaling the kinetic data are multiplied with the factor $\sqrt{2}/\delta$. As depicted, unlike the Poiseuille flow, in transpiration flow the solutions for BGK and BE models are quite different. Our analytical solution shows that this inconsistency roots in the different values for Pr and the coefficient B_2. The results confirm that the magnitude of mass and heat flows increases with the rarefaction degree. Navier–Stokes–Fourier yields a plug flow across the tube cross section, and drastically overestimates the mass and heat fluxes near the wall. In plot (c), the axial heat flux in transpiration flow is compared to BE data. This heat flow is a superposition of Fourier heat flow, i.e., the NSF solution, and the mechanocaloric heat flow [see (10.28b)]. The mechanocaloric heat flow (Knudsen layer), which occurs in mass flow direction competes with the constant Fourier heat flow, and helps the R13 solution to match the kinetic results. For small Knudsen numbers, where the effects of Knudsen boundary layers are limited to the wall neighborhood, NSF and R13 predict the same heat flux at the center of the pipe.

For $\mathrm{Kn} = 0.35$ the R13 solution for velocity shows 18% error with respect to kinetic data at $r/R = 1$. For the heat flux solution the error is around 14% at $r/R = 1$, and 7% at $r/R = 0.65$. These errors are calculated as (Data − R13)/R13.

Figure 10.6 shows the variations of the reduced mass and energy flow rates in thermal transpiration flow with respect to Knudsen number and surface accommodation coefficient. Our analytical results are compared to BGK and BE kinetic data for moderately rarefied flows in the transition regime. The BGK data in plots (a) and (c) are taken from Ref. [57]. BGK data for $\chi = 1$ are also available in [124]. The BE data in plot (b) and (d) are from [89, 96]. Plots (a) and (b) show that for $\mathrm{Kn} < 0.3$ the mass flow rate is a weak function of accommodation coefficients. However, for larger Knudsen numbers the effects of the accommodation coefficient become significant. Linearized NSF

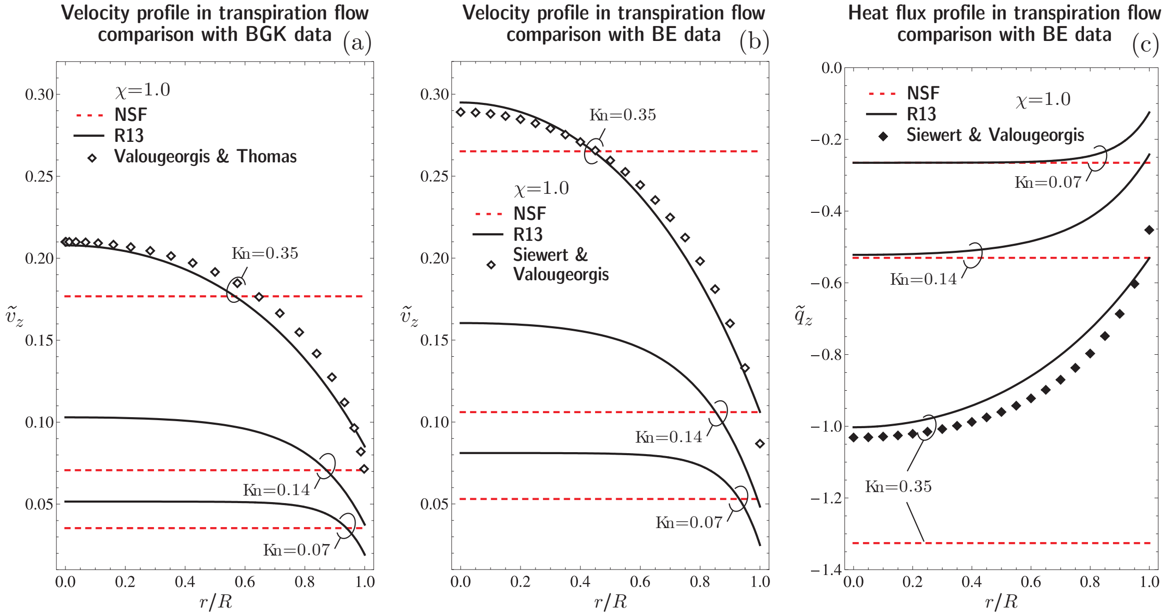

Figure 10.5: Radial distribution of velocity and heat flux in transpiration flow for Kn $= \{0.07, 0.14, 0.35\}$ and fully diffusive tube surface, $\chi = 1$. Results from Navier–Stokes–Fourier (NSF; dotted red line) and regularized 13–moment (R13; solid black line) are compared to Kinetic data (symbols). The BGK data are taken from Refs. [124, 95] and BE data are from [96, 67]. Note that for both velocity and heat flux NSF yields constant solutions. In transpiration flow the first– and second–order slip conditions for NSF are equivalent.

provides a rough approximation of the kinetic data for Kn $\lesssim 0.2$. Nevertheless, it neglects the effects of surface accommodation and drastically overestimates the mass transfer when surface effects come into account, i.e., for Kn > 0.3. The R13 system, on the other hand, yields remarkable agreement with kinetic data up to Kn $= 0.5$. The boundary conditions (10.12) allow the R13 system to take account for the surface effects. For small values of χ this agreement extends to Kn $= 0.7$ for the BGK model, and Kn $= 1.0$ for the BE model. Our criterion to set these range for Knudsen number is $(\text{Data} - \text{Model})/\text{Model} \lesssim 7\%$.

Plots (c) and (d) in Fig. 10.6, show the reduced thermal energy flow rate in transpiration flow. The Navier–Stokes–Fourier system, that only considers Fourier heat flow due to the axial temperature gradient, overestimates the energy flow above Kn $= 0.1$, and fails to capture the surface effects. Similar to the reduced mass flow rate, R13 results are accurate for moderate Knudsen numbers. To the authors' knowledge, there are no linearized Boltzmann kinetic data available for reflective–diffusive surfaces where $\chi < 1$.

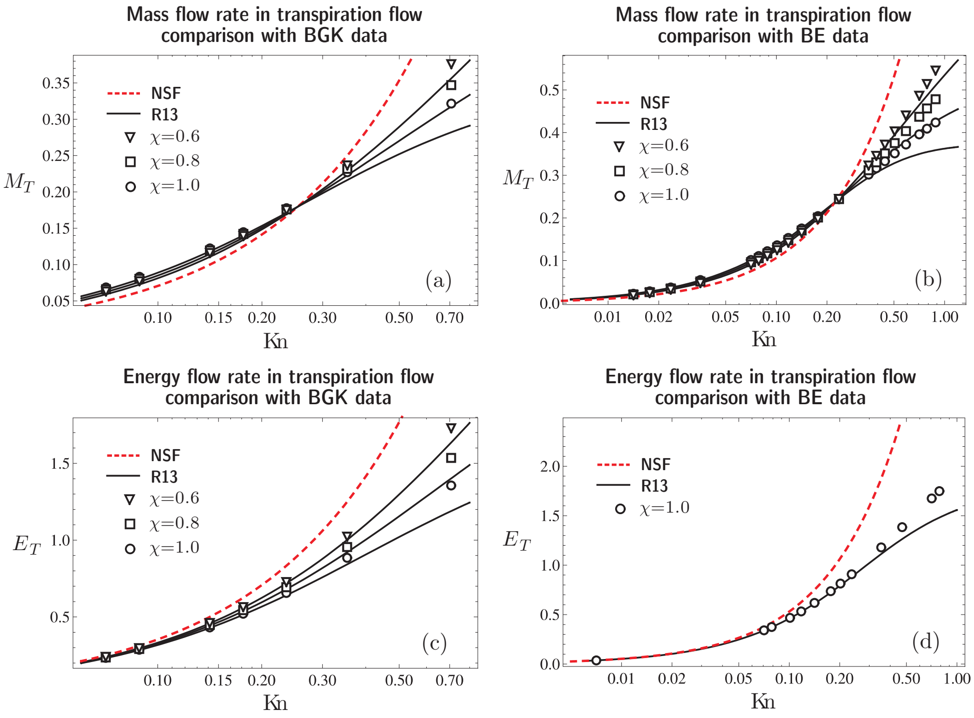

Figure 10.6: The effects of Knudsen number and surface accommodation on the reduced mass and thermal energy flow rates in transpiration flow in the transition regime. Results from Navier–Stokes–Fourier (NSF; dotted red line) and regularized 13–moment (R13; solid black line) are compared to kinetic data (symbols) for $\chi = \{0.6, 0.8, 1.0\}$. Plots (a) and (c) present comparisons with BGK kinetic data taken from Ref. [57]. In plot (b) and (d) our solutions are compared to BE kinetic data from [89] and [96], respectively. In transpiration flow the first– and second–order slip conditions for NSF are equal, and fail to capture the influence of the accommodation coefficient.

10.6.3 Validity of Onsager's Reciprocity Relation

The well–known phenomenological laws of nonequilibrium thermodynamics are derived from the Onsager's theorem which relates thermodynamics forces to thermodynamics fluxes. Despite the independency of thermodynamics forces, they might cause several fluxes, i.e., cross effects [34]. An example for this is coexistence of both mass and energy fluxes due to pressure (or temperature) gradient in Poiseuille (or transpiration) flow, where the pressure (temperature) gradient is considered as the driving thermodynamic force.

For steady state flows in the linear regime the Onsager reciprocity relation can be derived [87, 88] as

$$E_P = M_T. \tag{10.33}$$

Thus, energy flux driven by pressure force should be equal to the mass flux which is driven by temperature force (note that these quantities are defined in dimensionless form).

In Fig. 10.7 our theoretical results for the reduced thermal energy flow rate in Poiseuille flow E_P, and the reduced mass flow rate in transpiration flow M_T, are compared to kinetic data from Refs. [96, 89]. In the kinetic simulations Eq. (10.33) is valid for the entire range of Knudsen numbers, and is usually used to validate the accuracy of computations. As shown, in the absence of a longitudinal temperature gradient, NSF fails to predict the mechanocaloric energy flux in Poiseuille flow, hence, the Onsager reciprocity relation is valid for the NSF system only when $\mathrm{Kn} \to 0$. On the other hand, R13 gives partial agreement, which extends up to $\mathrm{Kn} \lesssim 0.2$, with approximately 7% deviation.

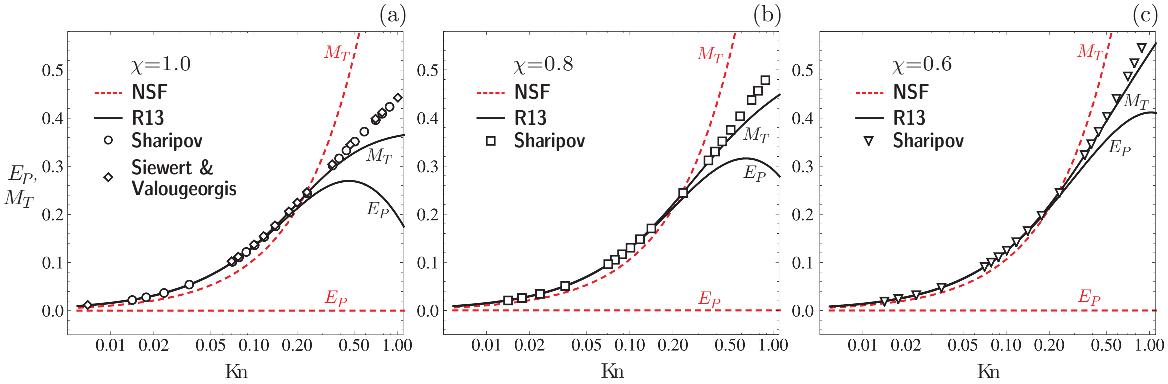

Figure 10.7: Validity of Onsager's reciprocity relation in pipe flows, is examined for Navier–Stokes–Fourier (NSF; dotted red lines) and regularized 13–moment (R13; solid black lines) equations. Our solutions for $\chi = \{1.0, 0.8, 0.6\}$ over moderate Knudsen numbers are compared to LB Kinetic data (symbols) from [89, 96]. It is evident that in NSF system the Onsager's condition holds only for very small Knudsen numbers. However, R13 yields Onsager symmetry for $\mathrm{Kn} < 0.2$.

Here, a question may arise that whether Onsager's reciprocity relation can be used to determine the range of validity of macroscopic transport equations (in terms of Knudsen number)? To answer this question, this criterion is further investigated for planar flows, i.e., the capillary between the reservoirs in Fig. 10.1 is assumed to be a parallel–plate channel. The results are shown in Fig. 10.8. As depicted, in planar internal flows the Onsager's reciprocity relation is valid for $\mathrm{Kn} \lesssim 0.1$, where the Knudsen number is defined based on channel height. If one defines the Knudsen number for pipe flows based on the diameter of the pipe (and not its radius), then for both planar and cylindrical geometries $E_P = M_T$ holds within the same range. Therefore, validity of Onsager's reciprocity relation does not depend on flow geometry, if Knudsen number is defined in a consistent manner.

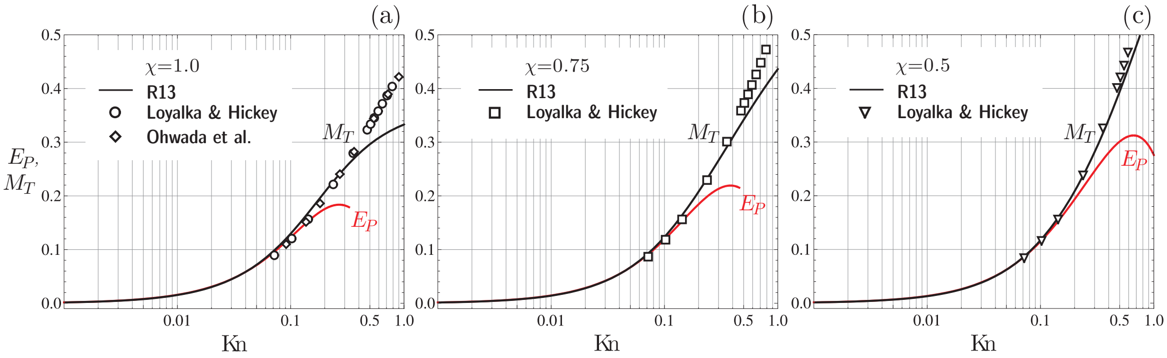

Figure 10.8: Validity of Onsager's reciprocity relation in parallel–plate channel flows, is shown for regularized 13–moment equations. Our solutions for $\chi = \{1.0, 0.75, 0.5\}$ over moderate Knudsen numbers are compared to linear Boltzamnn data (symbols) from [70, 79].

10.6.4 Two–way Poiseuille and Transpiration Flows

In the case of simultaneous Poiseuille and transpiration flows, it is straightforward to show that a superposition of Poiseuille and transpiration solutions satisfies the general velocity problem [Eq. (10.10a)–(10.12b)]. Accordingly, the general solution for the velocity reads

$$\tilde{v}_z = \mathbf{C}_4 + \frac{\wp}{4\,\mathrm{Kn}} r^2 - \frac{2}{5}\left[\mathbf{C}_2\,\mathcal{J}_0\left(\frac{2}{\mathrm{Kn}}\sqrt{\frac{\mathrm{Pr}}{\mathsf{B}_2}}\,\tilde{r}\right) + \frac{\mathrm{Kn}}{\mathrm{Pr}}\,\wp - \frac{5\,\mathrm{Kn}}{2\,\mathrm{Pr}}\,\tau\right]. \tag{10.34}$$

where, again, $\{\mathbf{C}_1,\mathbf{C}_3\} = 0$, and $\{\mathbf{C}_2,\mathbf{C}_4\}$ are superpositions of the corresponding integrating constants for Poiseuille and transpiration flows. In steady state condition, the net mass flow rate is zero,

$$\int_0^1 \tilde{v}_z\,\tilde{r}\,d\tilde{r} = 0. \tag{10.35}$$

Substituting the velocity solution (10.34) into condition (10.35) and then integrating, gives a relation between $\wp$, τ, and Kn, that reads

$$\tau = \wp\left(\frac{2}{5} - \frac{\mathrm{Pr}}{8\,\mathrm{Kn}^2}\right) + \frac{2}{5}\sqrt{\mathrm{Pr}\,\mathsf{B}_2}\,\mathbf{C}_2\,\mathcal{J}_1\left(\frac{2}{\mathrm{Kn}}\sqrt{\frac{\mathrm{Pr}}{\mathsf{B}_2}}\right) - \frac{\mathrm{Pr}\,\mathbf{C}_4}{\mathrm{Kn}}. \tag{10.36}$$

Since the BGK model yields incorrect Prandtl number, it is erroneous in describing isothermal and nonisothermal flows simultaneously [89]. Thus, in this section we use BE coefficients (4.15) in our calculations, that correspond to the correct Prandtl number.

Figure 10.9 shows velocity profiles in simultaneous Poiseuille and transpiration flows for fully diffusive walls, $\chi = 1$. As illustrated, a two–way flow is formed in the tube, in which the pressure–

driven flow is dominant in the center of the tube, and close to the wall thermal creep occurs in the opposite direction. In plot (a) the dimensionless pressure gradient is $\wp = 0.1$, while the values for Knudsen number are $\mathrm{Kn} = \{0.1, 0.15, 0.2\}$, that correspond to $\tau = \{2.05, 1.19, 0.86\}$ according to Eq. (10.36). For a constant pressure gradient, when the Knudsen number increases, the required temperature gradient to satisfy condition (10.35) decreases. In plot (b), the Knudsen number is constant, $\mathrm{Kn} = 0.1$, and different pressure gradients are chosen $\wp = \{0.1, 0.3, 0.5\}$, that yield $\tau = \{2.05, 6.15, 10.25\}$. Indeed, for a given set of $\{\mathrm{Kn}, \mathrm{Pr}, \chi, \mathsf{B}_2\}$, Eq. (10.36) gives a linear relation between $\wp$ and τ.

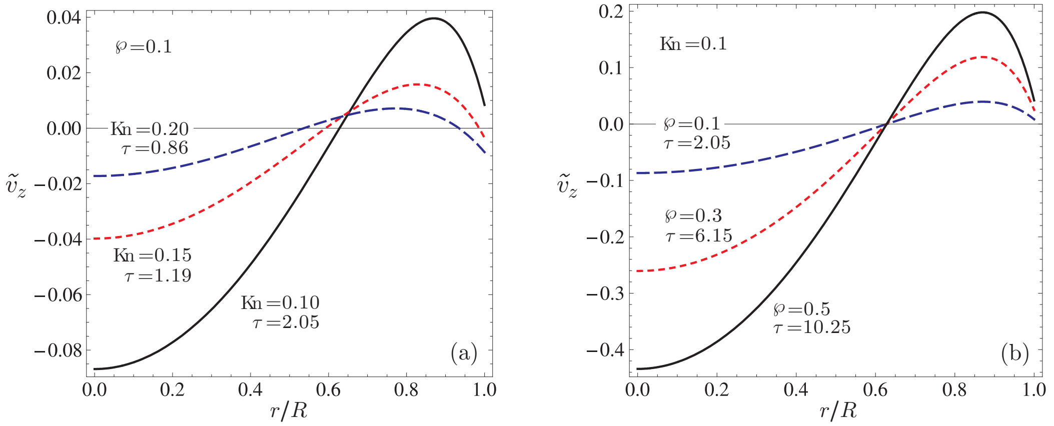

Figure 10.9: Two–way velocity fields in simultaneous Poiseuille and transpiration flows, where pressure–driven flow occurs in the middle of the tube, and temperature–driven flow close to the boundary. The flows have opposite directions, such that the net flow rate is zero. In plot (a) the pressure gradient is constant and the effects of Knudsen number variation are shown. In plot (b) the Knudsen number is fixed, and different pressure gradients are examined. Both plots are shown for fully diffusive walls, $\chi = 1$.

10.6.5 Thermomolecular Pressure Difference

By replacing the integrating constants $\{\mathsf{C}_2, \mathsf{C}_4\}$, into Eq. (10.34) and integrating as in (10.35), the net mass flow rate splits as

$$M_{\text{net}} = \tau M_T - \wp M_P = 0. \tag{10.37}$$

Substitution of τ and $\wp$ from Eqs. (10.7) and (10.8) yields a simple expression for the exponent of thermomolecular pressure difference γ, [cf. Eq. (10.1)]

$$\gamma = \frac{M_T}{M_P}. \tag{10.38}$$

In Fig. 10.10, values for γ obtained from our linear approach are compared to linear kinetic data [89]. Similar to our previous calculations for mass and energy flow rates, we observe consistency between our model and kinetic data for $\mathrm{Kn} < 0.5$. For small accommodation coefficients this consistency extends to $\mathrm{Kn} < 1.0$.

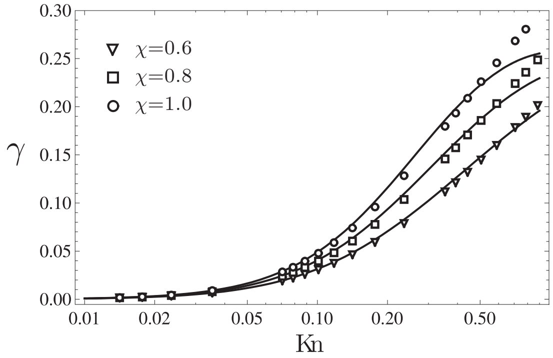

Figure 10.10: The exponent of thermomolecular pressure difference γ, obtained from R13 equations for different accommodation coefficients, is compared to kinetic data (symbols) from Ref. [89].

Chapter 11

Semilinear Theory for Parallel–plate Channel Flows

In this section, we consider semilinearized forms of the R13 system in planar geometry, with semilinearized boundary conditions, which lead to analytical solutions for weakly nonlinear temperature problem for Couette, Poiseuille, and transpiration flows in parallel–plate micro–channels[1]. The nonlinear terms describe the irreversible coupling between the fields of temperature and velocity. We emphasize that for non–planar flows, due to coupling between the stress components through curvature terms, semilinear equations demand numerical approach.

11.1 Semilinear Temperature Problem for Couette and Poiseuille Flows in Parallel–plate Channels

We consider Couette and Poiseuille flows as depicted in Fig. 7.1a, b, with the assumptions in Eq. (6.40).

Velocity and temperature fields are coupled through the nonlinear viscous heating term, $-\sigma_{ij}\left(\partial v_i/\partial x_j\right)$. To retain this coupling in the equations, we considered semilinearization, such that all nonlinear terms are removed except those which introduce quadratic contributions of the shear stress σ_{12}, shear rate $\partial v_1/\partial x_2$, and their combinations (including higher derivatives). Inclusion of these nonlinear terms does not affect the velocity problem [cf. Eqs. (6.46)–(6.43)], however, the temperature

---

[1] The presented material in this chapter are published in Refs. [114, 115].

problem takes the following form,

$$\frac{\partial \tilde{q}_2}{\partial \tilde{x}_2} = \underline{-\,\tilde{\sigma}_{12}\frac{\partial \tilde{v}_1}{\partial \tilde{x}_2}}, \tag{11.1a}$$

$$\frac{8}{15}\frac{\partial \tilde{q}_2}{\partial \tilde{x}_2} \underline{-\frac{2}{3}\tilde{\sigma}_{12}\frac{\partial \tilde{v}_1}{\partial \tilde{x}_2}} + \frac{\partial \tilde{m}_{222}}{\partial \tilde{x}_2} = -\frac{1}{\mathrm{Kn}}\tilde{\sigma}_{22}, \tag{11.1b}$$

$$\underline{-\,\tilde{\sigma}_{12}\frac{\partial \tilde{\sigma}_{12}}{\partial \tilde{x}_2}} + \frac{\partial \tilde{\sigma}_{22}}{\partial \tilde{x}_2} \underline{+\frac{2}{5}\tilde{q}_1\frac{\partial \tilde{v}_1}{\partial \tilde{x}_2}} + \frac{1}{2}\frac{\partial \tilde{R}_{22}}{\partial \tilde{x}_2} + \frac{1}{6}\frac{\partial \tilde{\mathit{\Delta}}}{\partial \tilde{x}_2} \underline{+\tilde{m}_{122}\frac{\partial \tilde{v}_1}{\partial \tilde{x}_2}} = -\frac{5}{2}\frac{\partial \tilde{\theta}}{\partial \tilde{x}_2} - \frac{\mathrm{Pr}}{\mathrm{Kn}}\tilde{q}_2, \tag{11.1c}$$

in which the constitutive parameters read

$$\tilde{\mathit{\Delta}} = \underline{2\,\mathsf{A}_1\,\tilde{\sigma}_{12}^2} + \mathsf{A}_2\,\mathrm{Kn}\left(\frac{\partial \tilde{q}_2}{\partial \tilde{x}_2} \underline{+\tilde{\sigma}_{12}\frac{\partial \tilde{v}_1}{\partial \tilde{x}_2}}\right), \tag{11.2a}$$

$$\tilde{R}_{22} = \underline{\frac{\mathsf{B}_1}{3}\tilde{\sigma}_{12}^2} + \frac{2\,\mathsf{B}_2}{3}\,\mathrm{Kn}\left(\frac{\partial \tilde{q}_2}{\partial \tilde{x}_2} \underline{+\frac{5}{14}\tilde{\sigma}_{12}\frac{\partial \tilde{v}_1}{\partial \tilde{x}_2}}\right), \tag{11.2b}$$

$$\tilde{m}_{222} = \mathsf{C}\,\mathrm{Kn}\left(\frac{3}{5}\frac{\partial \tilde{\sigma}_{22}}{\partial \tilde{x}_2} \underline{-\frac{4}{25}\tilde{q}_1\frac{\partial \tilde{v}_1}{\partial \tilde{x}_2}}\right). \tag{11.2c}$$

In the above equations, the underlined terms denote those nonlinear terms that are quadratic in $\tilde{\sigma}_{12}$ and/or $\partial \tilde{v}_1/\partial \tilde{x}_2$. Indeed, the nonlinear term in the energy balance [Eq. (11.1a)] accounts for viscous heating effects, which we wish to study. Accordingly, all similar terms must be included in the semilinearized equations. For instance, the nonlinear term $\tilde{q}_1\,(\partial \tilde{v}_1/\partial \tilde{x}_2)$, which appears in Eqs. (11.1c) and (11.2c) must be taken into account, because Eq. (6.41c) in the linear velocity problem implies that $\partial \tilde{\sigma}_{12}/\partial \tilde{x}_2$ is the leading term for $\tilde{q}_1$.

To be consistent with the semilinearized R13 equations, we must consider semilinearized boundary conditions,

$$\tilde{q}_2 = \frac{\chi}{2-\chi}\sqrt{\frac{2}{\pi}}\left(\underline{\frac{1}{2}\tilde{\mathcal{V}}_1^2} - 2\tilde{\mathcal{T}} - \frac{1}{2}\tilde{\sigma}_{22} - \frac{1}{15}\tilde{\mathit{\Delta}} - \frac{5}{28}\tilde{R}_{22}\right)n_2, \tag{11.3a}$$

$$\tilde{m}_{222} = \frac{\chi}{2-\chi}\sqrt{\frac{2}{\pi}}\left(\underline{-\frac{3}{5}\tilde{\mathcal{V}}_1^2} + \frac{2}{5}\tilde{\mathcal{T}} - \frac{7}{5}\tilde{\sigma}_{22} + \frac{1}{75}\tilde{\mathit{\Delta}} - \frac{1}{14}\tilde{R}_{22}\right)n_2. \tag{11.3b}$$

The only nonlinear terms left in the above boundary conditions are the underlined quadratic terms in velocity slip (shear). It will be shown that these nonlinear terms correct the temperature jump, and provide a better match with DSMC results.

11.2 General Solution for Semilinear Temperature Problem

For Maxwellian molecules with coefficients (4.15) substitution of constitutive relations (11.2) into (11.1) the semilinear temperature problem reads,

$$\frac{\partial \tilde{q}_2}{\partial \tilde{x}_2} = -\tilde{\sigma}_{12}\frac{\partial \tilde{v}_1}{\partial \tilde{x}_2}, \tag{11.4a}$$

$$-\frac{6}{5}\tilde{\sigma}_{12}\frac{\partial \tilde{v}_1}{\partial \tilde{x}_2} - \frac{6}{5}\,\mathrm{Kn}\frac{\partial^2 \tilde{\sigma}_{22}}{\partial \tilde{x}_2^2} - \frac{12}{25}\,\mathrm{Kn}^2\frac{\partial}{\partial \tilde{x}_2}\left(\frac{\partial \tilde{\sigma}_{12}}{\partial \tilde{x}_2}\frac{\partial \tilde{v}_1}{\partial \tilde{x}_2}\right) = -\frac{1}{\mathrm{Kn}}\tilde{\sigma}_{22}, \tag{11.4b}$$

$$\frac{\partial \tilde{\sigma}_{22}}{\partial \tilde{x}_2} - \frac{13}{7}\tilde{\sigma}_{12}\frac{\partial \tilde{\sigma}_{12}}{\partial \tilde{x}_2} - \frac{67}{105}\,\mathrm{Kn}\frac{\partial \tilde{\sigma}_{12}}{\partial \tilde{x}_2}\frac{\partial \tilde{v}_1}{\partial \tilde{x}_2} + \frac{36}{35}\,\mathrm{Kn}\,\tilde{\sigma}_{12}\frac{\partial^2 \tilde{v}_1}{\partial \tilde{x}_2^2} = -\frac{5}{2}\frac{\partial \tilde{\theta}}{\partial \tilde{x}_2} - \frac{2}{3\,\mathrm{Kn}}\tilde{q}_2. \tag{11.4c}$$

As given in (11.4), the temperature problem requires the solution of the (linear) velocity problem [cf. Eq. (7.1)], where for both Couette and Poiseuille flows $\tau = 0$.

After integrating, with the help of the velocity solution, the solution for (11.4) is obtained as (again, $\mathbf{C}_\alpha$ are the integrating constants)

$$\begin{aligned}\tilde{\theta} = \mathbf{C}_8 &- \frac{\tilde{G}_1^2}{45\,\mathrm{Kn}^2}\tilde{x}_2^4 - \frac{4\,\tilde{G}_1\,\mathbf{C}_1}{45\,\mathrm{Kn}^2}\tilde{x}_2^3 + \left(\frac{488\,\tilde{G}_1^2}{525} - \frac{2\,\mathbf{C}_1^2}{15\,\mathrm{Kn}^2}\right)\tilde{x}_2^2 \\ &+ \left(\frac{976\,\tilde{G}_1\,\mathbf{C}_1}{525} - \frac{4\,\mathbf{C}_5}{15\,\mathrm{Kn}}\right)\tilde{x}_2 + \frac{956\,\tilde{G}_1\,\mathrm{Kn}}{375}A + \frac{96\,\mathrm{Kn}}{175}\tilde{\sigma}_{12}\frac{\partial A}{\partial \tilde{x}_2} - \frac{2}{5}B,\end{aligned}$$

$$\tilde{\sigma}_{22} = -\frac{84\,\tilde{G}_1^2\,\mathrm{Kn}^2}{25} - \frac{6\,\tilde{G}_1^2}{5}\tilde{x}_2^2 - \frac{12\,\tilde{G}_1\,\mathbf{C}_1}{5}\tilde{x}_2 - \frac{6\,\mathbf{C}_1^2}{5} - \frac{152\,\tilde{G}_1\,\mathrm{Kn}}{25}A - \frac{36\,\mathrm{Kn}}{25}\tilde{\sigma}_{12}\frac{\partial A}{\partial \tilde{x}_2} + B,$$

$$\tilde{q}_2 = \mathbf{C}_5 + \frac{\tilde{G}_1^2}{3\,\mathrm{Kn}}\tilde{x}_2^3 + \frac{\tilde{G}_1\,\mathbf{C}_1}{\mathrm{Kn}}\tilde{x}_2^2 + \frac{\mathbf{C}_1^2}{\mathrm{Kn}}\tilde{x}_2 + \frac{2}{5}\tilde{\sigma}_{12}\,A - \frac{18\,\mathrm{Kn}^2\,\tilde{G}_1}{25}\frac{\partial A}{\partial \tilde{x}_2}, \tag{11.5}$$

with the Knudsen layers for the velocity problem A, and temperature problem B,

$$A = \mathbf{C}_2 \sinh\left(\frac{\sqrt{5}}{3\,\mathrm{Kn}}\tilde{x}_2\right) + \mathbf{C}_3 \cosh\left(\frac{\sqrt{5}}{3\,\mathrm{Kn}}\tilde{x}_2\right), \tag{11.6}$$

$$B = \mathbf{C}_6 \cosh\left(\frac{\sqrt{5}}{\sqrt{6}\,\mathrm{Kn}}\tilde{x}_2\right) + \mathbf{C}_7 \sinh\left(\frac{\sqrt{5}}{\sqrt{6}\,\mathrm{Kn}}\tilde{x}_2\right). \tag{11.7}$$

11.2.1 Thermal Solution for Couette Flow

For Couette flow (with $\tilde{G}_1 = 0$), the solution of the velocity problem is presented in Eq. (7.3), in which $\mathbf{C}_3 = 0$ is applied due to symmetry of the solution. Moreover, the symmetry conditions for the temperature distribution, $\tilde{\theta}\left(\tilde{x}_2\right) = \tilde{\theta}\left(-\tilde{x}_2\right)$, yields $\mathbf{C}_5 = \mathbf{C}_7 = 0$, that simplifies the general solution

(11.5) to

$$\begin{aligned}
\tilde{\theta} &= \underline{\mathbf{C}_8 - \frac{2\,\mathbf{C}_1^2}{15\,\mathrm{Kn}^2}\,\tilde{x}_2^2} + \frac{32\,\mathbf{C}_2}{35\sqrt{5}}\,\tilde{\sigma}_{12}\cosh\left(\frac{\sqrt{5}}{3\,\mathrm{Kn}}\tilde{x}_2\right) - \frac{2\,\mathbf{C}_6}{5}\cosh\left(\frac{\sqrt{5}}{\sqrt{6}\,\mathrm{Kn}}\tilde{x}_2\right), \\
\tilde{\sigma}_{22} &= -\frac{6\,\mathbf{C}_1^2}{5} - \frac{12\,\mathbf{C}_2}{5\sqrt{5}}\,\tilde{\sigma}_{12}\cosh\left(\frac{\sqrt{5}}{3\,\mathrm{Kn}}\tilde{x}_2\right) + \mathbf{C}_6\cosh\left(\frac{\sqrt{5}}{\sqrt{6}\,\mathrm{Kn}}\tilde{x}_2\right), \\
\tilde{q}_2 &= \underline{\frac{\mathbf{C}_1^2}{\mathrm{Kn}}\tilde{x}_2} + \frac{2\,\mathbf{C}_2}{5}\,\tilde{\sigma}_{12}\sinh\left(\frac{\sqrt{5}}{3\,\mathrm{Kn}}\tilde{x}_2\right). \qquad (11.8)
\end{aligned}$$

The integrating constants $\mathbf{C}_1$and $\mathbf{C}_2$ are known from the velocity solution, while $\mathbf{C}_6$ and $\mathbf{C}_8$ must be evaluated from semilinear boundary conditions (11.3). The constant $\mathbf{C}_8$ is related to temperature jump. For completeness of the discussion, we mention that the semilinearized R13 equations require the same number of boundary conditions as the linearized R13 equations.

Only the underlined terms in (11.8) would be present in classical hydrodynamics, as solutions of the Navier–Stokes–Fourier equations. All other terms, including the hyperbolic sine and cosine functions of the Knudsen boundary layers, describe rarefaction effects. The normal stress, $\tilde{\sigma}_{22}$, is a superposition of a constant bulk term [107], $-6\,\mathbf{C}_1^2/5$, and Knudsen layers. In classical hydrodynamics, the temperature profile is parabolic, the R13 equations add Knudsen layer contributions.

11.2.2 Thermal Solution for Poiseuille Flow

For Poiseuille flow the solution of the velocity problem is presented in Eq. (7.4), in which $\mathbf{C}_1 = \mathbf{C}_2 = 0$ due to symmetry of the solution. Similar to the Couette flow, the symmetry conditions for the temperature distribution yields $\mathbf{C}_5 = \mathbf{C}_7 = 0$, that simplifies the general solution (11.5) to

$$\begin{aligned}
\tilde{\theta} = \underline{\mathbf{C}_8 - \frac{\tilde{G}_1^2}{45\,\mathrm{Kn}^2}\,\tilde{x}_2^4} &+ \frac{488\,\tilde{G}_1^2}{525}\,\tilde{x}_2^2 + \frac{32\,\mathbf{C}_3}{35\sqrt{5}}\,\tilde{\sigma}_{12}\sinh\left(\frac{\sqrt{5}}{3\,\mathrm{Kn}}\tilde{x}_2\right) \\
&+ \frac{956\,\tilde{G}_1\,\mathrm{Kn}\,\mathbf{C}_3}{375}\cosh\left(\frac{\sqrt{5}}{3\,\mathrm{Kn}}\tilde{x}_2\right) - \frac{2\,\mathbf{C}_6}{5}\cosh\left(\frac{\sqrt{5}}{\sqrt{6}\,\mathrm{Kn}}\tilde{x}_2\right),
\end{aligned}$$

$$\begin{aligned}
\tilde{\sigma}_{22} = -\frac{84\,\tilde{G}_1^2\,\mathrm{Kn}^2}{25} &- \frac{6\,\tilde{G}_1^2}{5}\,\tilde{x}_2^2 - \frac{12\,\mathbf{C}_3}{5\sqrt{5}}\,\tilde{\sigma}_{12}\sinh\left(\frac{\sqrt{5}}{3\,\mathrm{Kn}}\tilde{x}_2\right) \\
&- \frac{152\,\tilde{G}_1\,\mathrm{Kn}\,\mathbf{C}_3}{25}\cosh\left(\frac{\sqrt{5}}{3\,\mathrm{Kn}}\tilde{x}_2\right) + \mathbf{C}_6\cosh\left(\frac{\sqrt{5}}{\sqrt{6}\,\mathrm{Kn}}\tilde{x}_2\right),
\end{aligned}$$

$$\tilde{q}_2 = \underline{\frac{\tilde{G}_1^2}{3\,\mathrm{Kn}}\,\tilde{x}_2^3} + \frac{2\,\mathbf{C}_3}{5}\,\tilde{\sigma}_{12}\cosh\left(\frac{\sqrt{5}}{3\,\mathrm{Kn}}\tilde{x}_2\right) - \frac{6\,\tilde{G}_1\,\mathrm{Kn}\,\mathbf{C}_3}{5\sqrt{5}}\sinh\left(\frac{\sqrt{5}}{3\,\mathrm{Kn}}\tilde{x}_2\right). \tag{11.9}$$

Again, the underlined terms denote the Navier–Stokes–Fourier solutions. All other terms, including the hyperbolic sine and cosine functions of the Knudsen layers, describe rarefaction effects. In Poiseuille flow (like Couette flow) $\tilde{\sigma}_{22}$ does not include Navier–Stokes–Fourier terms, both are superpositions of bulk solutions and Knudsen boundary layers. The temperature profile of classical hydrodynamics is given by the fourth power of $\tilde{x}_2$; the R13 equations correct this value by adding a quadratic term in $\tilde{x}_2$, and Knudsen layer contributions.

11.3 Results and Discussion

11.3.1 Couette Flow

Figure 11.1 shows R13 solutions for the semilinear temperature problem for Couette flow. Semilinear R13 results are compared to DSMC simulations at $\mathrm{Kn} = \{0.05, 0.1, 0.5\}$ for argon. The conditions for DSMC simulation is the same as described for the velocity problem [cf. Fig. (7.2)]. The plots show that for small Knudsen numbers our results are very close to the DSMC data. In plots for $\tilde{q}_2$ the curvature near the walls are Knudsen layers contributions, and since in our theoretical results [Eq. (11.9)] only a few Knudsen layers present, full matching with the DSMC data is not plausible. Additionally, the non–Newtonian heat flux, $\tilde{\sigma}_{22}$, which vanishes in classical hydrodynamics, is predicted with an acceptable accuracy. For $\mathrm{Kn} = 0.5$ we observe deviations from kinetic data, which are more apparent in the temperature results. The main reason for this difference is the independency of viscosity form temperature in our approach. For this problems, numerical solutions for fully nonlinear R13 equations are available in [121], in which a better matching in temperature plots is provided.

11.3.2 Force–driven Poiseuille Flow

Figure 11.2 depicts R13 solutions for the semilinear temperature problem for force–driven Poiseuille flow. Our theoretical results for $\mathrm{Kn} = 0.072$ are compared to DSMC data [129, 133], where the dimensionless external force is $\tilde{G}_1 = 0.2355$, and the walls are stationary at 273 K ($\tilde{\theta}_W = 1$).

An interesting phenomenon observed in force–driven Poiseuille flow is the formation of a characteristic dip in the temperature profile, see the profile for $\tilde{\theta}$ in Fig. 11.2. This minimum was first

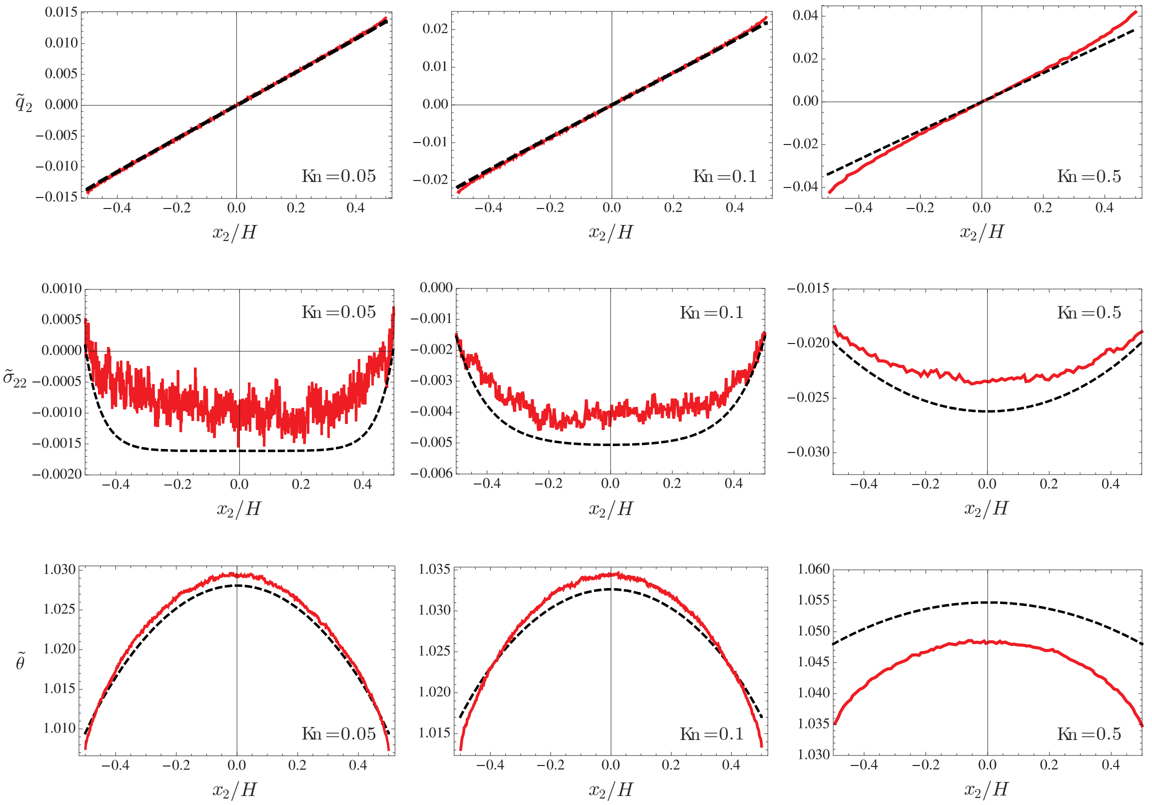

Figure 11.1: Solutions for the semilinearized temperature problem across the channel for Couette flow with argon. Wall temperature and velocities are 273 K and ±100 m/s. Comparison between semilinear R13 (dashed lines) and DSMC (solid lines).

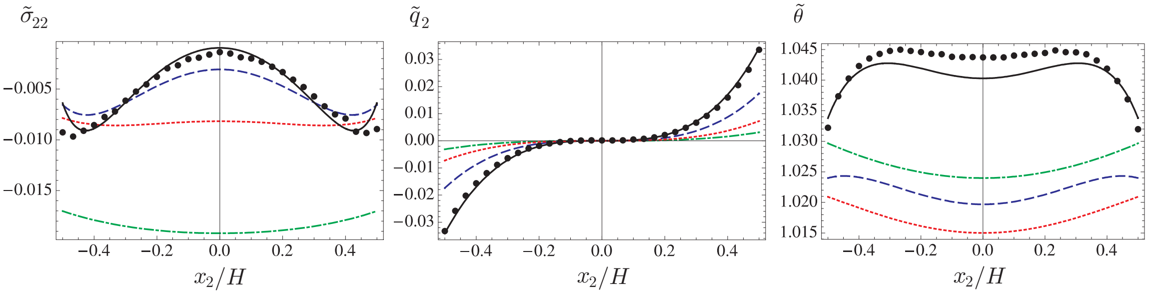

Figure 11.2: Solution of the semilinear temperature problem for force–driven Poiseuille flow with dimensionless force $\tilde{G}_1 = 0.2355$. Profiles are computed for Kn $= 0.072$ (solid line), Kn $= 0.15$ (dashed line), Kn $= 0.4$ (dotted line), and Kn $= 1.0$ (dashed–dotted line). For Kn $= 0.072$ comparison with DSMC simulations (circles) is presented.

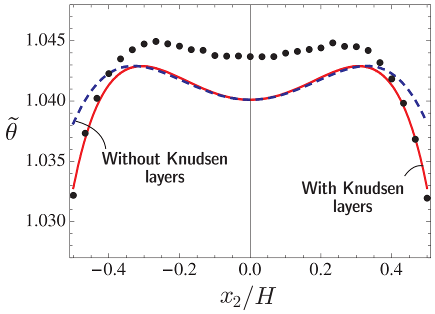

Figure 11.3: Influence of Knudsen boundary layers on temperature profile in force–driven Poiseuille flow. The dashed line represents the superposition of bulk solutions and the temperature jump. The solid line is the full solution including the Knudsen boundary layers. Dots indicate DSMC simulation for $\mathrm{Kn} = 0.072$, and $\tilde{G}_1 = 0.2355$.

reported by Tij and Santos [118], who did not include Knudsen boundary layers in their solution. The analytical solution for $\tilde{\theta}$ in Eq. (11.9), lucidly describes the dip as a result of competition between the bulk contributions, $-\tilde{G}_1^2\,\tilde{x}_2^4/45\,\mathrm{Kn}^2$ and $488\,\tilde{G}_1^2\,\tilde{x}_2^2/525$, while the Knudsen boundary layers contribute to the boundary curvature.

In Fig. 11.3, the dashed line presents the superposition of the bulk terms and the temperature jump for $\mathrm{Kn} = 0.072$, and $\tilde{G}_1 = 0.2355$. The solid line shows the complete solution, which includes the Knudsen boundary layers. As expected, the Knudsen layers strongly affect the temperature (and also other flow parameters) distribution near the boundaries. At small Knudsen numbers, the effect of the Knudsen layers on the temperature dip is negligible. Inclusion of more nonlinear terms yields finer details of the curve, such that better agreement with DSMC results are achieved [36, 118].

11.4 Semilinear Temperature and Density Problems for Transpiration Flow in Parallel–plate Channels

We consider thermal transpiration flow as depicted in Fig. 7.1c, with the assumptions in Eq. (6.40).

In the semilinear approach we include some nonlinear terms within the R13 equations which are of order τ^2, where τ is the dimensionless temperature gradient. Referring to the linear results [cf. Eqs. (7.9a)–(7.8)], $\tilde{q}_1\,(\partial\tilde{v}_1/\partial\tilde{x}_2)$ (and its derivative with respect to $\tilde{x}_2$) is the only nonlinear term in the R13 equations that is certainly of second–order in τ.

Moreover, we consider sufficiently long micro–channels where $\epsilon = H/L \ll 1$ and $\mathcal{O}(\epsilon) = \mathcal{O}(\tau)$. This dimensional assumption leads to neglection of streamwise flow deviations, as they appear to be of third–order (or higher) in τ.

Incorporation of these nonlinear terms does not affect the linear velocity problem [cf. Eqs. (6.46)–(6.43)], however, the semilinearized temperature problem now becomes

$$\begin{aligned}
\frac{\partial \tilde{q}_2}{\partial \tilde{x}_2} &= 0, && \text{(11.10a)}\\
\frac{8}{15}\frac{\partial \tilde{q}_2}{\partial \tilde{x}_2} + \frac{\partial \tilde{m}_{222}}{\partial \tilde{x}_2} &= -\frac{1}{\mathrm{Kn}}\tilde{\sigma}_{22}, && \text{(11.10b)}\\
\frac{\partial \tilde{\sigma}_{22}}{\partial \tilde{x}_2} \underline{+ \frac{2}{5}\tilde{q}_1 \frac{\partial \tilde{v}_1}{\partial \tilde{x}_2}} + \frac{1}{2}\frac{\partial \tilde{R}_{22}}{\partial \tilde{x}_2} + \frac{1}{6}\frac{\partial \tilde{\varDelta}}{\partial \tilde{x}_2} &= -\frac{5}{2}\frac{\partial \tilde{\theta}}{\partial \tilde{x}_2} - \frac{\mathrm{Pr}}{\mathrm{Kn}}\tilde{q}_2, && \text{(11.10c)}
\end{aligned}$$

with

$$\tilde{\varDelta} = \mathsf{A}_2\,\mathrm{Kn}\frac{\partial \tilde{q}_2}{\partial \tilde{x}_2} = 0, \qquad \tilde{R}_{22} = \frac{2\,\mathsf{B}_2}{3}\,\mathrm{Kn}\frac{\partial \tilde{q}_2}{\partial \tilde{x}_2} = 0, \qquad \tilde{m}_{222} = \mathsf{C}\,\mathrm{Kn}\left(\frac{3}{5}\frac{\partial \tilde{\sigma}_{22}}{\partial \tilde{x}_2} \underline{- \frac{4}{25}\tilde{q}_1\frac{\partial \tilde{v}_1}{\partial \tilde{x}_2}}\right). \tag{11.11}$$

Also, the remaining equations for $\tilde{\rho}$ and $\tilde{\sigma}_{11}$ in semilinearized form keep their original form [Eqs. (6.51) and (6.53)], i.e.,

$$\frac{\partial \tilde{\rho}}{\partial \tilde{x}_2} + \frac{\partial \tilde{\theta}}{\partial \tilde{x}_2} + \frac{\partial \tilde{\sigma}_{22}}{\partial \tilde{x}_2} = 0, \qquad -\frac{4}{15}\frac{\partial \tilde{q}_2}{\partial \tilde{x}_2} + \frac{\partial \tilde{m}_{112}}{\partial \tilde{x}_2} = -\frac{1}{\mathrm{Kn}}\tilde{\sigma}_{11}, \tag{11.12}$$

where

$$\tilde{m}_{112} = \frac{\mathsf{C}}{3}\,\mathrm{Kn}\left(\frac{\partial \tilde{\sigma}_{11}}{\partial \tilde{x}_2} - \frac{2}{5}\frac{\partial \tilde{\sigma}_{22}}{\partial \tilde{x}_2} \underline{+ \frac{16}{25}\tilde{q}_1\frac{\partial \tilde{v}_1}{\partial \tilde{x}_2}}\right). \tag{11.13}$$

The underlined terms in Eqs. (11.10) and (11.13) correspond to the nonlinear terms. The semilinear boundary conditions for the above temperature problem are the same as presented in Eq. (11.3). For density problem, the auxiliary condition (6.52) must be used, and for $\tilde{\sigma}_{11}$, boundary condition (6.55) changes to

$$\tilde{m}_{112} = \frac{\chi}{2-\chi}\sqrt{\frac{2}{\pi}}\left(\underline{\frac{4}{5}\tilde{\mathcal{V}}^2} - \frac{1}{5}\tilde{\mathcal{T}} - \tilde{\sigma}_{11} + \frac{1}{5}\tilde{\sigma}_{22} - \frac{1}{150}\tilde{\varDelta} - \frac{1}{14}\tilde{R}_{11}\right) n_2. \tag{11.14}$$

11.5 Solutions for Semilinear Temperature and Density Problems for Transpiration Flow

For Maxwellian molecules with coefficients (4.15) substitution of constitutive relations (11.11) and (11.13) into (11.10) and (11.12) yields

$$\frac{\partial \tilde{q}_2}{\partial \tilde{x}_2} = 0, \tag{11.15a}$$

$$-\frac{6}{5}\mathrm{Kn}\frac{\partial^2 \tilde{\sigma}_{22}}{\partial \tilde{x}_2^2} + \frac{8}{25}\mathrm{Kn}\frac{\partial}{\partial \tilde{x}_2}\left(\tilde{q}_1 \frac{\partial \tilde{v}_1}{\partial \tilde{x}_2}\right) = -\frac{1}{\mathrm{Kn}}\tilde{\sigma}_{22}, \tag{11.15b}$$

$$\frac{\partial \tilde{\sigma}_{22}}{\partial \tilde{x}_2} + \frac{2}{5}\tilde{q}_1 \frac{\partial \tilde{v}_1}{\partial \tilde{x}_2} = -\frac{5}{2}\frac{\partial \tilde{\theta}}{\partial \tilde{x}_2} - \frac{2}{3\,\mathrm{Kn}}\tilde{q}_2, \tag{11.15c}$$

$$-\frac{2}{3}\mathrm{Kn}\frac{\partial^2 \tilde{\sigma}_{11}}{\partial \tilde{x}_2^2} + \frac{4}{15}\mathrm{Kn}\frac{\partial^2 \tilde{\sigma}_{22}}{\partial \tilde{x}_2^2} - \frac{32}{75}\mathrm{Kn}\frac{\partial}{\partial \tilde{x}_2}\left(\tilde{q}_1 \frac{\partial \tilde{v}_1}{\partial \tilde{x}_2}\right) = -\frac{1}{\mathrm{Kn}}\tilde{\sigma}_{11}, \tag{11.15d}$$

$$\frac{d\tilde{\rho}}{d\tilde{x}_2} + \frac{d\tilde{\theta}}{d\tilde{x}_2} + \frac{d\tilde{\sigma}_{22}}{d\tilde{x}_2} = 0, \tag{11.15e}$$

which after integrating lead to the following solutions

$$\tilde{q}_2 = \mathbf{C}_5, \tag{11.16a}$$

$$\begin{aligned}\tilde{\sigma}_{22} = {} & \mathbf{C}_6 \sinh\left(\frac{\sqrt{5}}{\sqrt{6}\,\mathrm{Kn}}\tilde{x}_2\right) + \mathbf{C}_7 \cosh\left(\frac{\sqrt{5}}{\sqrt{6}\,\mathrm{Kn}}\tilde{x}_2\right) \\ & - \frac{4\,\mathbf{C}_3\,\mathrm{Kn}\,\tau}{5}\cosh\left(\frac{\sqrt{5}}{3\,\mathrm{Kn}}\tilde{x}_2\right) - \frac{16\,\mathbf{C}_3^2}{375}\cosh\left(\frac{2\sqrt{5}}{3\,\mathrm{Kn}}\tilde{x}_2\right),\end{aligned} \tag{11.17a}$$

$$\begin{aligned}\tilde{\theta} = {} & \mathbf{C}_8 - \frac{4\,\mathbf{C}_5}{15\,\mathrm{Kn}}\tilde{x}_2 - \frac{2}{5}\left[\mathbf{C}_7 \cosh\left(\frac{\sqrt{5}}{\sqrt{6}\,\mathrm{Kn}}\tilde{x}_2\right) + \mathbf{C}_6 \sinh\left(\frac{\sqrt{5}}{\sqrt{6}\,\mathrm{Kn}}\tilde{x}_2\right)\right] \\ & + \frac{2\,\mathbf{C}_3\,\mathrm{Kn}\,\tau}{25}\cosh\left(\frac{\sqrt{5}}{3\,\mathrm{Kn}}\tilde{x}_2\right) + \frac{62\,\mathbf{C}_3^2}{1875}\cosh\left(\frac{2\sqrt{5}}{3\,\mathrm{Kn}}\tilde{x}_2\right),\end{aligned} \tag{11.18a}$$

$$\begin{aligned}\tilde{\sigma}_{11} = {} & -\frac{1}{2}\left[\mathbf{C}_7 \cosh\left(\frac{\sqrt{5}}{\sqrt{6}\,\mathrm{Kn}}\tilde{x}_2\right) + \mathbf{C}_6 \sinh\left(\frac{\sqrt{5}}{\sqrt{6}\,\mathrm{Kn}}\tilde{x}_2\right)\right] + \frac{64\,\mathbf{C}_3\,\mathrm{Kn}\,\tau}{85}\cosh\left(\frac{\sqrt{5}}{3\,\mathrm{Kn}}\tilde{x}_2\right) \\ & + \frac{704\,\mathbf{C}_3^2}{4875}\cosh\left(\frac{2\sqrt{5}}{3\,\mathrm{Kn}}\tilde{x}_2\right) + \mathbf{C}_9 \sinh\left(\frac{\sqrt{3}}{\sqrt{2}\,\mathrm{Kn}}\tilde{x}_2\right) + \mathbf{C}_{10} \cosh\left(\frac{\sqrt{3}}{\sqrt{2}\,\mathrm{Kn}}\tilde{x}_2\right),\end{aligned} \tag{11.19a}$$

$$\tilde{\rho} = \mathsf{C}_{11} - \tilde{\theta} - \tilde{\sigma}_{22}. \tag{11.20a}$$

In the above solutions, the solution of the linear velocity problem for transpiration flow [Eqs. (7.9a)–(7.8)] is applied. The constant C_3 is available from Eq. (7.9a), and symmetry of the solutions with respect to $\tilde{x}_2 = 0$ gives $\mathsf{C}_5 = \mathsf{C}_6 = \mathsf{C}_9 = 0$. The remaining constants $\{\mathsf{C}_7,\mathsf{C}_8,\mathsf{C}_{10},\mathsf{C}_{11}\}$ turn out to be nonzero and quadratic in τ, however, their lengthy expressions are not presented here.

11.6 Results and Discussion

All terms in Eqs. (11.17a) and (11.20a) are second–order in τ. Moreover, the above solutions are completely constructed by Knudsen layers (all terms include hyperbolic cosine functions), where C_8 is related to the temperature jump. To our knowledge, nonlinear effects in transpiration flow have not been investigated so far. Thus, we were unable to find any previously published data for comparison sake. Figure 11.4 shows the normalized distributions of temperature, density, and non–Newtonian stress components. As shown, when the flow becomes more rarefied, the Knudsen layers extend further into the bulk.

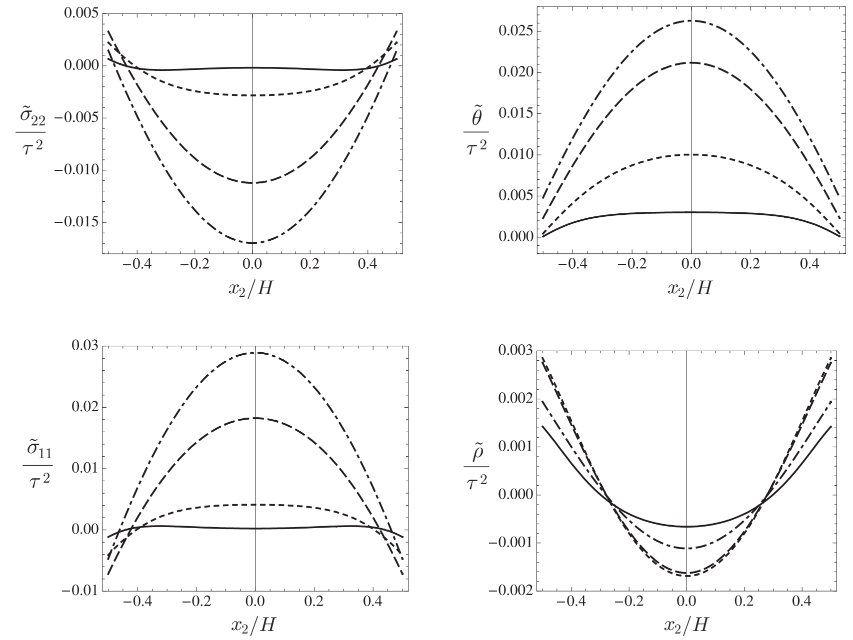

Figure 11.4: Dimensionless distribution of normalized stress components $\{\tilde{\sigma}_{11}/\tau^2, \tilde{\sigma}_{22}/\tau^2\}$, temperature $\tilde{\theta}/\tau^2$, and density $\tilde{\rho}/\tau^2$ across the channel are show for transpiration flow. Semi–linearized R13 results which are obtained for fully diffusive walls $\chi = 1$ in different Knudsen numbers are shown. Note that in the linear theory all these quantities are constant, i.e., remain unchanged with respect to the reference equilibrium state. (Solid line) Kn = 0.088; (dotted line) Kn = 0.177; (dashed line) Kn = 0.353; (dash–dotted line) Kn = 0.530.

Chapter 12

Conclusions and Recommendations

12.1 Conclusions

In this dissertation, we examined the capabilities of classical Navier–Stokes–Fourier (NSF) equations versus an extended set of macroscopic transport equations, referred to as regularized 13–moment (R13) equations, in gas dynamics. NSF equations are well–known in science and engineering applications as the most convenient choice for Computational Fluid Dynamics (CFD) simulations for near–equilibrium processes, when the Knudsen number is sufficiently small, $\mathrm{Kn} \lesssim 0.1$. Similar to NSF, the R13 system represents a set of continuum equations (for gas flows) which are of higher order in the Knudsen number, that means they have increased accuracy over NSF equations to describe nonequilibrium flows. Through our simulation we demonstrated that R13 equations are reliable transport equations for flows in the transition regime, $\mathrm{Kn} \lesssim 0.5$.

Due to their welcoming features, R13 equations deserve to be proposed as a useful CFD tool for micro/rarefied gas flows, nevertheless, they have not been widely accepted by the engineering community as a practical CFD approach. The premier reason for this was the lack of proper boundary conditions for high–order moments. Fortunately, the recent progress in development of kinetic boundary conditions for the moments, as discussed in Chap. 5, has facilitated practical applications of moment equations in advanced engineering and physics.

During the course of this work, both NSF and R13 equations and their corresponding boundary conditions were rigorously studied in the context of kinetic theory to analyze nonequilibrium effects in some fundamental boundary value problems of rarefied gas dynamics. A wide range of rarefaction effects is identified through the investigated problems, which alter the classical flow patterns both in the bulk and near boundary regions. The variety of the selected flow settings allowed to study steady and unsteady rarefaction effects in different processes, i.e., shear–driven, thermally–driven, and force/pressure–driven flows. Moreover, effects of boundary curvature on nonequilibrium flow behavior were studied.

In order to understand the underlying physics, we mostly focused on solutions of the linear transport equations, which offer a clear insight into the nonequilibrium effects at very modest computational expense. Application of the linear equations are limited to microflows (slow flows with small gradients), in which Knudsen boundary layers are the dominant rarefaction phenomena. Our calculations with linearized R13 equations proved that despite their simple structure they can describe the relevant physics, which are missing in the traditional NSF theory.

While the rarefaction effects are known from costly numerical solutions of the Boltzmann equation, they appear in analytical solutions of the R13 equations. In the linear regime where the coupling between velocity and temperature fields are neglected, the transport equations pose independent velocity and temperature problems which can be solved analytically or numerically (with basic numerical approaches). The availability of R13 analytical solutions leads to an increased understanding of linear and nonlinear (semilinear) rarefaction effects.

To conclude, we emphasize that our *inexpensive* analytical solutions are comparable to *expensive* numerical solutions of the Boltzmann equation.

The most significant observations through the linear approach are:

- In both planar and cylindrical geometries and in all processes we observed a heat flow in opposite direction of mass flow that is not driven by temperature gradient. This thermal energy flow, which is not straightforward to conceptualize, is a pure rarefaction effect, known as Knudsen boundary layer. As the degree of flow rarefaction increases the magnitude and thickness of Knudsen boundary layers increase. In thermally–driven flows, superposition of Fourier heat flux and Knudsen boundary layers (mechanocaloric heat flow) constructs the total heat flux. In the force–driven flow, the parallel heat flux includes Knudsen layers and a higher–order bulk term that is absent in NSF solution.

- Based on our simulations, discontinuities of velocity and temperature on the boundary can drastically affect the mass and energy flow rates in the process. Physical and mathematical consistencies of boundary conditions are crucial to correctly evaluate the velocity and temperature jumps in boundary value problems. Our results showed that third–order kinetic boundary conditions for R13 equations yield correct values for velocity slip and temperature jump on the boundaries. Moreover, the second–order velocity slip and temperature jump conditions for NSF system, which are deduced from the R13 boundary conditions, effectively increase the overall accuracy of hydrodynamic results.

- The mass flow rate in Poiseuille flow as a function of Knudsen number demonstrates a minimum at $\mathrm{Kn} \approx 1$ for parallel–plate channel flows, and $\mathrm{Kn} \approx 2$ for pipe flows. We investigated this so–called Knudsen paradox in both planar and circular flow passages, where R13 system exhibited a fair agreement with kinetic data in the transition flow regime. It must be mentioned that the Knudsen paradox cannot be described by NSF with first–order slip condition, but only with second–order slip condition.

- Unlike Poiseuille flow, the mass flow rate in thermal transpiration flow diverges to infinity at the free molecular flow regime, when $\mathrm{Kn} \to \infty$. Through our linear approach we showed that NSF equations over–estimated the mass flow rate in thermally–driven flows (NSF yields a plug flow), but R13 equations match with kinetic data within the transition flow regime. Additionally, the second–order slip condition cannot describe the effects of surface accommodation coefficients in thermally–driven flows.

- For internal flows, the range of applicability for macroscopic transport equations (in terms of Knudsen number) is not uniquely defined. Indeed, depending on the geometry (the choice for the reference length scale) and the process, different ranges for applicability of R13 and NSF equations were observed. To eliminate this inconsistency, we proposed the Onsager's reciprocity relation as a new criterion to determine the range of applicability of macroscopic approaches. Accordingly, NSF equations are applicable to near–equilibrium flows where $\mathrm{Kn} \to 0$, and R13 equations hold for processes in which $0 < \mathrm{Kn} \lesssim 0.2$.

- For unsteady Couette and Poiseuille flows, oscillatory Knudsen layers were identified as characteristic feature of the flows. For pulsating Poiseuille flow NSF and R13 behave quite differently, particularly, in the phase shift.

- The underlying physics of two–way flow patterns in simultaneous Poiseuille and transpiration flows elucidated based on an analytical approach. Moreover, it was shown that R13 equations can accurately predict the exponent of thermomolecular pressure difference for ideal gases when $\mathrm{Kn} \lesssim 0.5$.

The most significant observations through semilinear approach are:

- While in the velocity problem Knudsen boundary layers appear as parallel component of the heat–flux vector, in the semilinear temperature problem Knudsen layers include normal components of the stress tensor.
- The most remarkable feature of semilinear approach is its accuracy and robustness. Semilinear solutions exhibit a rather rich array of rarefaction effects, e.g. multiple Knudsen layers, which were achieved without complicated numerical schemes.

  The characteristic dip in the temperature profile which is observed in kinetic simulation of force–driven Poiseuille flow is known as a nonlinear rarefaction effect. Through semilinear R13 solution, this peculiar temperature distribution was predicted as a consequence on nonlinear bulk effect. We emphasize that some of the nonlinear effects in transpiration flow which are reported in this thesis have not been investigated so far.

12.2 Recommendations for Future Works

During the course of the presented study variety of issues were encountered and several ideas were raised that owing to the limited time some of them have been persisted or remained untouched. This section provides a guideline for potential future works regarding the considered subject in this work.

As an straightforward extension for flows in tubes, force–driven and thermally–driven flows through circular ducts of concentric annular cross sections can be investigated using a similar approach as presented in Chapter 10. While kinetic solution for transpiration flow in annular passages are not reported so far, for force–driven Poiseuille flow in annular ducts kinetic data are available in [14, 20].

As a result of recent advances in microfabrication techniques, micro–channels with different cross sectional geometries are fabricated for both commercial and scientific purposes. To simulate micro gas flows in such geometries, several models have been proposed based on Navier–Stokes–Fourier equations along with velocity slip boundary condition [10, 75], which are valid for small Knudsen numbers (slip flow regime). In order to present a compact and comprehensive general model for all flow geometries, definition of a consistent characteristic length scale is necessary.

A circular duct (tube) is fully described with its diameter, thus the obvious length scale is the diameter or radius. For noncircular cross sections (e.g. elliptical, rectangular, triangular, and trapezoidal) the selection of a characteristic length scale is not as clear. Many textbooks and researchers have conventionally chosen the hydraulic diameter [75], as the characteristic length while other propose the square root of area [10].

In this work we showed that Knudsen layers effectively dominate mass and energy transport in internal micro flows. Since Knudsen layers are absent in the NSF solution, we propose development of a general model for rarefied gas flows in channels with arbitrary cross sections based on R13 equations, which will be valid for moderate Knudsen numbers (transition flow regime).

Developing a strategy to obtain inflow and outflow boundary conditions for moments provides a great potential to use R13 (and other systems of moment equations) in a series of practical engineering applications. One standard application is investigation of compressibility effects in pressure–driven Poiseuille flows, where unlike force–driven flows, the pressure gradient is not constant along the flow [9].

The challenge in deriving inflow and outflow boundary conditions arises from the fact that in contrast to a wall boundary, in inflow and outflow boundaries there is no discontinuity in the velocity distribution function. Hence, a rational approach is required to link the velocity distribution functions before and after entry/exit.

Another ambitious objective for future development is derivation of boundary conditions for diffusive/absorbing walls.

Most flows of interest are multidimensional, and require numerical solutions. Currently, a two–dimensional extension of the numerical method that is proposed in Ref. [121] is developed for micro flows in rectangular cavities. The implicit method solves the steady state R13 equations by avoiding time stepping into the final steady condition, and allows for relatively fast solutions.

An opportunity for future work is to employ a similar numerical approach to solve steady state two–dimensional R13 equations in cylindrical geometry. Such two–dimensional simulations are desired in micro gas flows through bending channels, for instance, circulating thermal creep flow in Knudsen pumps [6], and external flow such as a rarefied gas flow over a bundle of tubes, which has applications in gas–cooled micro heat exchangers.

Finally, we must highlight insufficiency of 13–moment field in describing rarefied gas flows beyond early stages of the transition regime. In highly rarefied situations, larger systems of moment equations are required. Gu and Emerson have developed and solved the regularized 26–moment (R26) equations which give reliable results up to $\mathrm{Kn} \lesssim 1$ [36, 38, 37]. So far, they have only considered shear–driven and force–driven flows in slab geometry. Indeed, transformation of R26 equations into curvilinear coordinates, and also its application to thermally–driven flows is an interesting objective for future studies, which can be observed as an straightforward (but more tedious) extension of the presented work.

Appendix A

Vector and Tensor Analysis in Cylindrical Coordinates

Cylindrical coordinates are a three–dimensional orthogonal curvilinear coordinate system, which are useful in analyzing axisymmetric processes[1], e.g., axisymmetric axial and azimuthal flows in pipes.

Due to curvature effects, vectorial and tensorial operations in cylindrical coordinates are quite different compared to their counterparts in the rectangular Cartesian coordinates. Expressions for gradients of scalars and vectors in cylindrical coordinates are widely available in textbooks. However, for higher order tensors (i.e., square matrix, cubic array, and so on) tensorial operations (gradients and divergences) are not readily available.

R13 equations include gradients and divergences of higher–order tensors (moments). For the purpose of adapting R13 equations for pipe flows, the gradients and divergences of higher–order tensors must be transformed into cylindrical coordinates. In this appendix required transformations to express R13 equations in cylindrical coordinates are collected.

A.1 Transformation Rules

Covariant and contravariant base vectors for any coordinate system are defined as

$$\mathbf{g}_i = \frac{\partial \mathbf{x}}{\partial \eta^i}, \qquad \text{and} \qquad \mathbf{g}^i = \frac{\partial \eta^i}{\partial \mathbf{x}}, \tag{A.1}$$

---

[1] Axisymmetric processes are symmetrical with respect to an axis.

where $\mathbf{x}$ and $\eta^i = \{\eta^1, \eta^2, \eta^3\}$ represent the position vector and coordinates, respectively. Based on *covariant* and *contravariant* basis, a general vector (position vector here) in any arbitrary coordinate system can be written in two different ways

$$\mathbf{x} = x^1\mathbf{g}_1 + x^2\mathbf{g}_2 + x^3\mathbf{g}_3 = x_1\mathbf{g}^1 + x_2\mathbf{g}^2 + x_3\mathbf{g}^3. \tag{A.2}$$

The position vector in any coordinate system is a function of the coordinate itself,

$$\mathbf{x} = \mathbf{x}(\eta^1, \eta^2, \eta^3). \tag{A.3}$$

Accordingly, increment in the position vector, that is displacement, reads

$$d\mathbf{x} = \frac{\partial \mathbf{x}}{\partial \eta^i} d\eta^i. \tag{A.4}$$

Now, we consider the cylindrical coordinate $\{\eta^1 = r, \eta^2 = \varphi, \eta^3 = z\}$ with an underlying Cartesian coordinate $\{\eta^1 = x, \eta^2 = y, \eta^3 = z\}$, where the origin of both coordinates are coincide, see Fig. A.1.

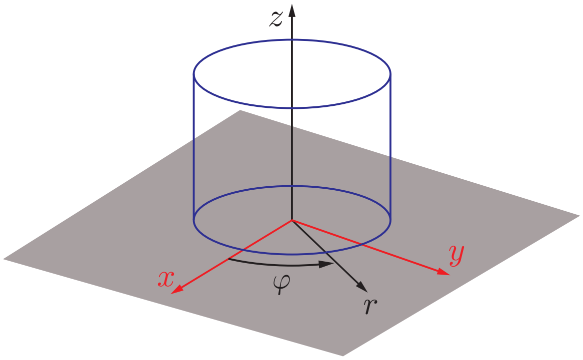

Figure A.1: Rectangular Cartesian coordinates $\{x, y, z\}$, and curvilinear cylindrical coordinates $\{r, \varphi, z\}$.

Cartesian and cylindrical coordinates are related via

$$x = r\cos\varphi, \qquad y = r\sin\varphi, \qquad z = z, \tag{A.5}$$

then, on account of Eq. (A.1), covariant base vectors in cylindrical coordinates are

$$\begin{aligned}
\mathbf{g}_1 &= \frac{\partial \mathbf{x}}{\partial \eta^1} = \left(\frac{\partial \mathbf{x}}{\partial r}\right)_{\varphi,z} = (\cos\varphi, \sin\varphi, 0)^{\mathrm{T}} = \mathbf{e}_r, \\
\mathbf{g}_2 &= \frac{\partial \mathbf{x}}{\partial \eta^2} = \left(\frac{\partial \mathbf{x}}{\partial \varphi}\right)_{r,z} = r\left(-\sin\varphi, \cos\varphi, 0\right)^{\mathrm{T}} = r\mathbf{e}_\varphi, \\
\mathbf{g}_3 &= \frac{\partial \mathbf{x}}{\partial \eta^3} = \left(\frac{\partial \mathbf{x}}{\partial z}\right)_{r,\varphi} = (0, 0, 1)^{\mathrm{T}} = \mathbf{e}_z,
\end{aligned} \tag{A.6}$$

where $\{\mathbf{e}_r, \mathbf{e}_\varphi, \mathbf{e}_z\}$ are *covariant physical basis.*

Moreover, from Eq. (A.5) we have

$$r = \sqrt{x^2 + y^2}, \qquad \varphi = \tan^{-1}\left(\frac{y}{x}\right), \qquad z = z, \tag{A.7}$$

which lead to the contravariant base vectors in cylindrical coordinates

$$\begin{aligned}
\mathbf{g}^1 &= \frac{\partial \eta^1}{\partial \mathbf{x}} = \frac{\partial r}{\partial \mathbf{x}} = (\cos\varphi, \sin\varphi, 0)^{\mathrm{T}} = \mathbf{e}^r, \\
\mathbf{g}^2 &= \frac{\partial \eta^2}{\partial \mathbf{x}} = \frac{\partial \varphi}{\partial \mathbf{x}} = \frac{1}{r}\left(-\sin\varphi, \cos\varphi, 0\right)^{\mathrm{T}} = \frac{1}{r}\mathbf{e}^\varphi, \\
\mathbf{g}^3 &= \frac{\partial \eta^3}{\partial \mathbf{x}} = \frac{\partial z}{\partial \mathbf{x}} = (0, 0, 1)^{\mathrm{T}} = \mathbf{e}^z,
\end{aligned} \tag{A.8}$$

where $\{\mathbf{e}^r, \mathbf{e}^\varphi, \mathbf{e}^z\}$ are *contravariant physical basis.*

For a given coordinate system, both **e** and **g** point in the same direction, however, **e** is dimensionless and **g** is dimensional. Comparison of covariant and contravariant base vectors in cylindrical coordinate system shows that

$$\mathbf{g}_1 = \mathbf{g}^1, \qquad \mathbf{g}_2 = r^2\mathbf{g}^2, \qquad \mathbf{g}_3 = \mathbf{g}^3, \qquad \mathbf{e}^r = \mathbf{e}_r, \qquad \mathbf{e}^\varphi = \mathbf{e}_\varphi, \qquad \mathbf{e}^z = \mathbf{e}_z. \tag{A.9}$$

Alternatively, *physical basis*, denoted by **e**, can be used to express a vector as

$$\mathbf{x} = X^r\mathbf{e}_r + X^\varphi\mathbf{e}_\varphi + X^z\mathbf{e}_z = X_r\mathbf{e}^r + X_\varphi\mathbf{e}^\varphi + X_z\mathbf{e}^z. \tag{A.10}$$

In Eq. (A.10) $\{X^r, X^\varphi, X^z\}$ and $\{X_r, X_\varphi, X_z\}$ are known as *physical components* in covariant and contravariant physical basis, respectively. Equality of covariant and contravariant physical basis in (A.9) implies that the covariant and contravariant physical components in Eq. (A.10) are equal as well,

$$X_r = X^r, \qquad X_\varphi = X^\varphi, \qquad X_z = X^z. \tag{A.11}$$

Now, we define the length of the base vectors as

$$\mathbf{\Lambda}_i = \sqrt{\mathbf{g}_{\underline{i}} \cdot \mathbf{g}_{\underline{i}}} = (1, r, 1)^{\mathrm{T}}, \qquad \text{and} \qquad \mathbf{\Lambda}^i = \sqrt{\mathbf{g}^{\underline{i}} \cdot \mathbf{g}^{\underline{i}}} = (1, \frac{1}{r}, 1)^{\mathrm{T}}. \tag{A.12}$$

Then

$$\mathbf{g}_i = \mathbf{\Lambda}_{\underline{i}} \frac{1}{\mathbf{\Lambda}_{\underline{i}}} \mathbf{g}_i = \mathbf{\Lambda}_{\underline{i}} \mathbf{e}_i, \qquad \text{and} \qquad \mathbf{g}^i = \mathbf{\Lambda}^{\underline{i}} \frac{1}{\mathbf{\Lambda}^{\underline{i}}} \mathbf{g}^i = \mathbf{\Lambda}^{\underline{i}} \mathbf{e}^i, \tag{A.13}$$

where the physical basis are $\frac{1}{\mathbf{\Lambda}_{\underline{i}}} \mathbf{g}_i = \mathbf{e}_i$ and $\frac{1}{\mathbf{\Lambda}^{\underline{i}}} \mathbf{g}^i = \mathbf{e}^i$. Accordingly, a vector can be written in the alternative forms

$$\mathbf{x} = x^i \mathbf{g}_i = x^i \mathbf{\Lambda}_{\underline{i}} \mathbf{e}_i = X^i \mathbf{e}_i, \qquad \text{and} \qquad \mathbf{x} = x_i \mathbf{g}^i = x_i \mathbf{\Lambda}^{\underline{i}} \mathbf{e}^i = X_i \mathbf{e}^i, \tag{A.14}$$

where $x^i \mathbf{\Lambda}_{\underline{i}} = X^i$, and $x_i \mathbf{\Lambda}^{\underline{i}} = X_i$ are the physical components. For cylindrical coordinates we have

$$X^r = x^r, \qquad X^\varphi = r x^\varphi, \qquad X^z = x^z, \qquad X_r = x_r, \qquad X_\varphi = \frac{1}{r} x_\varphi, \qquad X_z = x_z. \tag{A.15}$$

The relation between covariant and contravariant basis is

$$\mathbf{g}_i = g_{ij}\, \mathbf{g}^j, \qquad \text{and} \qquad \mathbf{g}^i = g^{ij}\, \mathbf{g}_j, \tag{A.16}$$

where the components of the *metric tensors*, g_{ij} and g^{ij}, are defined through

$$g_{ij} = \mathbf{g}_i \cdot \mathbf{g}_j, \qquad \text{and} \qquad g^{ij} = \mathbf{g}^i \cdot \mathbf{g}^j. \tag{A.17}$$

Consequently, the metric tensors for cylindrical coordinates are

$$[g_{ij}] = \begin{pmatrix} 1 & 0 & 0 \\ 0 & r^2 & 0 \\ 0 & 0 & 1 \end{pmatrix}, \qquad \text{and} \qquad \left[g^{ij}\right] = \begin{pmatrix} 1 & 0 & 0 \\ 0 & \frac{1}{r^2} & 0 \\ 0 & 0 & 1 \end{pmatrix}. \tag{A.18}$$

The Kronecker delta can be expressed with respect to covariant and contravariant base vectors,

$$\mathbf{g}_i \cdot \mathbf{g}^j = \delta_i^j, \qquad \text{and} \qquad \mathbf{g}^i \cdot \mathbf{g}_j = \delta_j^i. \tag{A.19}$$

Combination of Eqs. (A.1) and (A.4) leads to

$$d\mathbf{x} = \mathbf{g}_i \, d\eta^i, \tag{A.20}$$

and dotting both sides with $\mathbf{g}^j$ yields

$$\mathbf{g}^j \cdot d\mathbf{x} = \mathbf{g}^j \cdot \mathbf{g}_i \, d\eta^i \Longrightarrow$$

$\mathrm{g}^j \cdot d\mathbf{x} = d\eta^j$.(A.21)

Based on the covariant base, the *Christoffel symbol* is defined as

$$\boldsymbol{\Gamma}_{ij} = \frac{\partial \mathbf{g}_i}{\partial \eta^j}, \tag{A.22}$$

and with Eqs. (A.20) and (A.22) it is straightforward to show that

$$\boldsymbol{\Gamma}_{ij} = \frac{\partial^2 \mathbf{x}}{\partial \eta^i \partial \eta^j} = \frac{\partial^2 \mathbf{x}}{\partial \eta^j \partial \eta^i} = \boldsymbol{\Gamma}_{ji}. \tag{A.23}$$

Hence, only six of nine $\boldsymbol{\Gamma}_{ij}$ vectors are independent due to symmetry.

The kth contravariant component of $\boldsymbol{\Gamma}_{ij}$ is obtained by dotting $\mathbf{g}^k$ into $\boldsymbol{\Gamma}_{ij}$,

$$\mathit{\Gamma}_{ij}^k = \mathbf{g}^k \cdot \boldsymbol{\Gamma}_{ij} \tag{A.24}$$

and then

$$\mathit{\Gamma}_{ij}^k \mathbf{g}_k = \frac{\partial \mathbf{g}_i}{\partial \eta^j}. \tag{A.25}$$

The scalar $\mathit{\Gamma}_{ij}^k$ is called the *Christoffel symbol of the second type*, that for cylindrical coordinates reads as

$$\begin{aligned}
&\mathit{\Gamma}_{11}^{1}=0, && \mathit{\Gamma}_{11}^{2}=0, && \mathit{\Gamma}_{11}^{3}=0,\\
&\mathit{\Gamma}_{12}^{1}=0, && \mathit{\Gamma}_{12}^{2}=\tfrac{1}{r}, && \mathit{\Gamma}_{12}^{3}=0,\\
&\mathit{\Gamma}_{13}^{1}=0, && \mathit{\Gamma}_{13}^{2}=0, && \mathit{\Gamma}_{13}^{3}=0,\\
&\mathit{\Gamma}_{21}^{1}=0, && \mathit{\Gamma}_{21}^{2}=\tfrac{1}{r}, && \mathit{\Gamma}_{21}^{3}=0,\\
&\mathit{\Gamma}_{22}^{1}=-r, && \mathit{\Gamma}_{22}^{2}=0, && \mathit{\Gamma}_{22}^{3}=0,\\
&\mathit{\Gamma}_{23}^{1}=0, && \mathit{\Gamma}_{23}^{2}=0, && \mathit{\Gamma}_{23}^{3}=0,\\
&\mathit{\Gamma}_{31}^{1}=0, && \mathit{\Gamma}_{31}^{2}=0, && \mathit{\Gamma}_{31}^{3}=0,\\
&\mathit{\Gamma}_{32}^{1}=0, && \mathit{\Gamma}_{32}^{2}=0, && \mathit{\Gamma}_{32}^{3}=0,\\
&\mathit{\Gamma}_{33}^{1}=0, && \mathit{\Gamma}_{33}^{2}=0, && \mathit{\Gamma}_{33}^{3}=0.
\end{aligned} \tag{A.26}$$

A.2 General form of Tensor Gradient

Based on covariant basis, generic form of a rank–n tensor in any coordinate is

$$\mathbf{T}=T^{i_1\ \cdots\ i_n}\,\mathbf{g}_{i_1}\cdots\mathbf{g}_{i_n}, \tag{A.27}$$

then its differentiation reads

$$\begin{aligned}
d\mathbf{T}&=dT^{i_1\ \cdots\ i_n}\mathbf{g}_{i_1}\cdots\mathbf{g}_{i_n}+T^{i_1\ \cdots\ i_n}d\left(\mathbf{g}_{i_1}\cdots\mathbf{g}_{i_n}\right)\\
&=dT^{i_1\ \cdots\ i_n}\mathbf{g}_{i_1}\cdots\mathbf{g}_{i_n}+T^{i_1\ \cdots\ i_n}\sum_k d\mathbf{g}_{i_k}\prod_{\alpha\neq k}\mathbf{g}_{i_\alpha}.
\end{aligned} \tag{A.28}$$

By using Eq. (A.21) we can write

$$\begin{aligned}
dT^{i_1\ \cdots\ i_n}&=\frac{\partial T^{i_1\ \cdots\ i_n}}{\partial\eta^l}d\eta^l=\frac{\partial T^{i_1\ \cdots\ i_n}}{\partial\eta^l}\left(\mathbf{g}^l\cdot d\mathbf{x}\right),\\
d\mathbf{g}_{i_k}&=\frac{\partial\mathbf{g}_{i_k}}{\partial\eta^l}d\eta^l=\frac{\partial\mathbf{g}_{i_k}}{\partial\eta^l}\left(\mathbf{g}^l\cdot d\mathbf{x}\right).
\end{aligned} \tag{A.29}$$

Replacement of (A.29) into (A.28) yields

$$d\mathbf{T}=\left(\frac{\partial T^{i_1\ \cdots\ i_n}}{\partial\eta^l}\mathbf{g}^l\mathbf{g}_{i_1}\cdots\mathbf{g}_{i_n}+T^{i_1\ \cdots\ i_n}\sum_k\frac{\partial\mathbf{g}_{i_k}}{\partial\eta^l}\mathbf{g}^l\prod_{\alpha\neq k}\mathbf{g}_{i_\alpha}\right)\cdot d\mathbf{x}. \tag{A.30}$$

Furthermore, gradient of a tensor can be presented by

$$d\mathbf{T} = \left(\frac{d\mathbf{T}}{d\mathbf{x}}\right) \cdot d\mathbf{x}. \tag{A.31}$$

Comparison of (A.30) and (A.31) gives

$$\frac{d\mathbf{T}}{d\mathbf{x}} = \frac{\partial T^{i_1 \, \cdots \, i_n}}{\partial \eta^l} \mathbf{g}^l \mathbf{g}_{i_1} \cdots \mathbf{g}_{i_n} + T^{i_1 \, \cdots \, i_n} \sum_k \mathbf{\Gamma}_{i_k l} \mathbf{g}^l \prod_{\alpha \neq k} \mathbf{g}_{i_\alpha}, \tag{A.32}$$

in which the Christoffel symbol is introduced based on Eq. (A.22). Since $\mathbf{\Gamma}_{i_k l} = \mathit{\Gamma}^m_{i_k l} \mathbf{g}_m$, then Eq. (A.32) can be rewritten as

$$\frac{d\mathbf{T}}{d\mathbf{x}} = \left(\frac{\partial T^{i_1 \, \cdots \, i_n}}{\partial \eta^l} \mathbf{g}^l \mathbf{g}_{i_1} \cdots \mathbf{g}_{i_n} + T^{i_1 \, \cdots \, i_n} \sum_k \mathit{\Gamma}^m_{i_k l} \mathbf{g}_m \mathbf{g}^l \prod_{\alpha \neq k} \mathbf{g}_{i_\alpha} \right). \tag{A.33}$$

Keeping the first term unchanged, and changing the dummy index $m \leftrightarrow i_k$ in the second term gives

$$\frac{d\mathbf{T}}{d\mathbf{x}} = \left(\frac{\partial T^{i_1 \, \cdots \, i_n}}{\partial \eta^l} + T^{i_1 \, \cdots \, i_n m} \sum_k \mathit{\Gamma}^{i_k}_{ml} \right) \mathbf{g}^l \mathbf{g}_{i_1} \cdots \mathbf{g}_{i_n}, \tag{A.34}$$

that is the generic form of tensor gradient.

A.3 Gradient of a Scalar

A scalar s is invariant with respect to the coordinate, however, its gradient is coordinate dependent. For scalar quantities Eq. (A.34) reduces to

$$\frac{ds}{d\mathbf{x}} = \frac{\partial s}{\partial \eta^l} \mathbf{g}^l = \frac{\partial s}{\partial \eta^l} \frac{\partial \eta^l}{\partial \mathbf{x}},$$

and its expansion in cylindrical coordinates leads to

$$\operatorname{grad} s = \frac{\partial s}{\partial r} \mathbf{e}_r + \frac{1}{r} \frac{\partial s}{\partial \varphi} \mathbf{e}_\varphi + \frac{\partial s}{\partial z} \mathbf{e}_z = \begin{pmatrix} \frac{\partial s}{\partial r} \mathbf{e}_r \\ \frac{1}{r} \frac{\partial s}{\partial \varphi} \mathbf{e}_\varphi \\ \frac{\partial s}{\partial z} \mathbf{e}_z \end{pmatrix}. \tag{A.35}$$

Note that in the above equation physical contravariant base vectors are replaced with their covariant counterparts base on Eq. (A.9).

A.4 Gradient of a Vector (Rank–1 Tensor)

For a vector (where $k = 1$), denoted by $\mathbf{v}$, Eq. (A.34) reads

$$\frac{d\mathbf{v}}{d\mathbf{x}} = \left(\frac{\partial v^i}{\partial \eta^l} + v^m \mathit{\Gamma}^i_{ml}\right) \mathbf{g}^l \mathbf{g}_i. \tag{A.36}$$

Now, we define a compact notation called *covariant vector differentiation*, as

$$v^i_{/l} = \frac{\partial v^i}{\partial \eta^l} + v^m \mathit{\Gamma}^i_{ml}. \tag{A.37}$$

Accordingly, in cylindrical coordinates, the components of covariant vector differentiation are

$$\begin{aligned}
v^1_{/1} &= \frac{\partial v^1}{\partial r}, & v^1_{/2} &= \frac{\partial v^1}{\partial \varphi} - r v^2, & v^1_{/3} &= \frac{\partial v^1}{\partial z}, \\
v^2_{/1} &= \frac{\partial v^2}{\partial r} + \frac{1}{r} v^2, & v^2_{/2} &= \frac{\partial v^2}{\partial \varphi} + \frac{1}{r} v^1, & v^2_{/3} &= \frac{\partial v^2}{\partial z}, \\
v^3_{/1} &= \frac{\partial v^3}{\partial r}, & v^3_{/2} &= \frac{\partial v^3}{\partial \varphi}, & v^3_{/2} &= \frac{\partial v^3}{\partial z}.
\end{aligned} \tag{A.38}$$

In the above differentiations, Christoffel symbols are replaced from (A.26). Replacement of differentiations from (A.38) into (A.36) gives

$$\begin{aligned}
\frac{d\mathbf{v}}{d\mathbf{x}} = &\left(\frac{\partial v^1}{\partial r}\right) \mathbf{g}_1 \mathbf{g}^1 + \left(\frac{\partial v^1}{\partial \varphi} - r v^2\right) \mathbf{g}_1 \mathbf{g}^2 + \left(\frac{\partial v^1}{\partial z}\right) \mathbf{g}_1 \mathbf{g}^3 \\
&+ \left(\frac{\partial v^2}{\partial r} + \frac{1}{r} v^2\right) \mathbf{g}_2 \mathbf{g}^1 + \left(\frac{\partial v^2}{\partial \varphi} + \frac{1}{r} v^1\right) \mathbf{g}_2 \mathbf{g}^2 + \left(\frac{\partial v^2}{\partial z}\right) \mathbf{g}_2 \mathbf{g}^3 \\
&+ \left(\frac{\partial v^3}{\partial r}\right) \mathbf{g}_3 \mathbf{g}^1 + \left(\frac{\partial v^3}{\partial \varphi}\right) \mathbf{g}_3 \mathbf{g}^2 + \left(\frac{\partial v^3}{\partial z}\right) \mathbf{g}_3 \mathbf{g}^3.
\end{aligned} \tag{A.39}$$

Employment of physical basis [cf. Eqs. (A.6) and (A.8)], physical components [cf. Eq. (A.15)], and some rearrangement yields

$$\begin{aligned}
\operatorname{grad} \mathbf{v} = \frac{\partial \mathbf{v}}{\partial \mathbf{x}} = &\frac{\partial v_r}{\partial r} \mathbf{e}_r \mathbf{e}_r + \frac{1}{r}\left(\frac{\partial v_r}{\partial \varphi} - v_\varphi\right) \mathbf{e}_r \mathbf{e}_\varphi + \frac{\partial v_r}{\partial z} \mathbf{e}_r \mathbf{e}_z \\
&+ \frac{\partial v_\varphi}{\partial r} \mathbf{e}_\varphi \mathbf{e}_r + \frac{1}{r}\left(\frac{\partial v_\varphi}{\partial \varphi} + v_r\right) \mathbf{e}_\varphi \mathbf{e}_\varphi + \frac{\partial v_\varphi}{\partial z} \mathbf{e}_\varphi \mathbf{e}_z \\
&+ \frac{\partial v_z}{\partial r} \mathbf{e}_z \mathbf{e}_r + \frac{1}{r} \frac{\partial v_z}{\partial \varphi} \mathbf{e}_z \mathbf{e}_\varphi + \frac{\partial v_z}{\partial z} \mathbf{e}_z \mathbf{e}_z.
\end{aligned} \tag{A.40}$$

A.5 Divergence of a Vector

Divergence of a vector is the trace of gradient of the vector. Multiplying Eq. (A.36) with δ^i_l gives the divergence of $\mathbf{v}$ as

$$\operatorname{div}\mathbf{v} = \operatorname{tr}\,\operatorname{grad}\mathbf{v} = \frac{\partial v_r}{\partial r} + \frac{1}{r}\frac{\partial v_\varphi}{\partial \varphi} + \frac{v_r}{r} + \frac{\partial v_z}{\partial z}. \tag{A.41}$$

A.6 Gradient of a Square Matrix (Rank–2 Tensor)

For a rank–2 tensor (where $k = 2$), denoted by $\mathbf{T}$, Eq. (A.34) reads

$$\frac{d\mathbf{T}}{d\mathbf{x}} = \left(\frac{\partial T^{ij}}{\partial \eta^l} + T^{im}\mathit{\Gamma}^j_{ml} + T^{jm}\mathit{\Gamma}^i_{ml}\right)\mathbf{g}^l\mathbf{g}_i\mathbf{g}_j. \tag{A.42}$$

Here, we define a compact notation called *covariant rank–2 tensor differentiation*, as

$$T^{ij}_{/l} = \frac{\partial T^{ij}}{\partial \eta^l} + T^{im}\mathit{\Gamma}^j_{ml} + T^{jm}\mathit{\Gamma}^i_{ml}. \tag{A.43}$$

Accordingly, in cylindrical coordinates, the components of covariant rank–2 tensor differentiation are

$$\begin{aligned}
T^{11}_{/1} &= \frac{\partial T^{11}}{\partial r}, & T^{12}_{/1} &= \frac{\partial T^{12}}{\partial r} + \frac{1}{r}T^{12}, & T^{13}_{/1} &= \frac{\partial T^{13}}{\partial r},\\
T^{21}_{/1} &= \frac{\partial T^{21}}{\partial r} + \frac{1}{r}T^{21}, & T^{22}_{/1} &= \frac{\partial T^{22}}{\partial r} + \frac{2}{r}T^{22}, & T^{23}_{/1} &= \frac{\partial T^{23}}{\partial r} + \frac{1}{r}T^{23},\\
T^{31}_{/1} &= \frac{\partial T^{31}}{\partial r}, & T^{32}_{/1} &= \frac{\partial T^{32}}{\partial r} + \frac{1}{r}T^{32}, & T^{33}_{/1} &= \frac{\partial T^{33}}{\partial r},\\
T^{11}_{/2} &= \frac{\partial T^{11}}{\partial \varphi} - r\left(T^{21} + T^{12}\right), & T^{12}_{/2} &= \frac{\partial T^{12}}{\partial \varphi} - rT^{22} + \frac{1}{r}T^{11}, & T^{13}_{/2} &= \frac{\partial T^{13}}{\partial \varphi} - rT^{23},\\
T^{21}_{/2} &= \frac{\partial T^{21}}{\partial \varphi} + \frac{1}{r}T^{11} - rT^{22}, & T^{22}_{/2} &= \frac{\partial T^{22}}{\partial \varphi} + \frac{1}{r}\left(T^{12} + T^{21}\right), & T^{23}_{/2} &= \frac{\partial T^{23}}{\partial \varphi} + \frac{1}{r}T^{13},\\
T^{31}_{/2} &= \frac{\partial T^{31}}{\partial \varphi} - rT^{32}, & T^{32}_{/2} &= \frac{\partial T^{32}}{\partial \varphi} + \frac{1}{r}T^{31}, & T^{33}_{/2} &= \frac{\partial T^{33}}{\partial \varphi},\\
T^{11}_{/3} &= \frac{\partial T^{11}}{\partial z}, & T^{12}_{/3} &= \frac{\partial T^{12}}{\partial z}, & T^{13}_{/3} &= \frac{\partial T^{13}}{\partial z},\\
T^{21}_{/3} &= \frac{\partial T^{21}}{\partial z}, & T^{22}_{/3} &= \frac{\partial T^{22}}{\partial z}, & T^{23}_{/3} &= \frac{\partial T^{23}}{\partial z},\\
T^{31}_{/3} &= \frac{\partial T^{31}}{\partial z}, & T^{32}_{/3} &= \frac{\partial T^{32}}{\partial z}, & T^{33}_{/3} &= \frac{\partial T^{33}}{\partial z}.
\end{aligned} \tag{A.44}$$

In the above differentiations, Christoffel symbols are replaced from (A.26). The final steps are, substituting the above differentiations into (A.42), replacing physical basis from Eq. (A.6) and (A.8) and physical components from (A.15). Finally, the gradient of a rank–2 tensor reads

$$
\begin{aligned}
\frac{d\mathbf{T}}{d\mathbf{x}} = & \left(\begin{array}{l} \dfrac{\partial T_{rr}}{\partial r}\mathbf{e}_r\mathbf{e}_r + \dfrac{\partial T_{r\varphi}}{\partial r}\mathbf{e}_r\mathbf{e}_\varphi + \dfrac{\partial T_{rz}}{\partial r}\mathbf{e}_r\mathbf{e}_z \\ + \dfrac{\partial T_{\varphi r}}{\partial r}\mathbf{e}_\varphi\mathbf{e}_r + \dfrac{\partial T_{\varphi\varphi}}{\partial r}\mathbf{e}_\varphi\mathbf{e}_\varphi + \dfrac{\partial T_{\varphi z}}{\partial r}\mathbf{e}_\varphi\mathbf{e}_z \\ + \dfrac{\partial T_{zr}}{\partial r}\mathbf{e}_z\mathbf{e}_r + \dfrac{\partial T_{z\varphi}}{\partial r}\mathbf{e}_z\mathbf{e}_\varphi + \dfrac{\partial T_{zz}}{\partial r}\mathbf{e}_z\mathbf{e}_z \end{array} \right)\mathbf{e}_r \\
& + \left(\begin{array}{l} \left(\dfrac{\partial T_{rr}}{\partial \varphi} - T_{\varphi r} - T_{r\varphi}\right)\mathbf{e}_r\mathbf{e}_r + \left(\dfrac{\partial T_{r\varphi}}{\partial \varphi} - T_{\varphi\varphi} + T_{rr}\right)\mathbf{e}_r\mathbf{e}_\varphi + \left(\dfrac{\partial T_{rz}}{\partial \varphi} - T_{\varphi z}\right)\mathbf{e}_r\mathbf{e}_z \\ + \left(\dfrac{\partial T_{\varphi r}}{\partial \varphi} + T_{rr} - T_{\varphi\varphi}\right)\mathbf{e}_\varphi\mathbf{e}_r + \left(\dfrac{\partial T_{\varphi\varphi}}{\partial \varphi} + T_{r\varphi} + T_{\varphi r}\right)\mathbf{e}_\varphi\mathbf{e}_\varphi + \left(\dfrac{\partial T_{\varphi z}}{\partial \varphi} + T_{rz}\right)\mathbf{e}_\varphi\mathbf{e}_z \\ + \left(\dfrac{\partial T_{zr}}{\partial \varphi} - T_{z\varphi}\right)\mathbf{e}_z\mathbf{e}_r + \left(\dfrac{\partial T_{z\varphi}}{\partial \varphi} + T_{zr}\right)\mathbf{e}_z\mathbf{e}_\varphi + \dfrac{\partial T_{zz}}{\partial \varphi}\mathbf{e}_z\mathbf{e}_z \end{array} \right)\frac{\mathbf{e}_\varphi}{r} \\
& + \left(\begin{array}{l} \dfrac{\partial T_{rr}}{\partial z}\mathbf{e}_r\mathbf{e}_r + \dfrac{\partial T_{r\varphi}}{\partial z}\mathbf{e}_r\mathbf{e}_\varphi + \dfrac{\partial T_{rz}}{\partial z}\mathbf{e}_r\mathbf{e}_z \\ + \dfrac{\partial T_{\varphi r}}{\partial z}\mathbf{e}_\varphi\mathbf{e}_r + \dfrac{\partial T_{\varphi\varphi}}{\partial z}\mathbf{e}_\varphi\mathbf{e}_\varphi + \dfrac{\partial T_{\varphi z}}{\partial z}\mathbf{e}_\varphi\mathbf{e}_z \\ + \dfrac{\partial T_{zr}}{\partial z}\mathbf{e}_z\mathbf{e}_r + \dfrac{\partial T_{z\varphi}}{\partial z}\mathbf{e}_z\mathbf{e}_\varphi + \dfrac{\partial T_{zz}}{\partial z}\mathbf{e}_z\mathbf{e}_z \end{array} \right)\mathbf{e}_z. \qquad \text{(A.45)}
\end{aligned}
$$

A.7 Divergence of a Square Matrix (Rank–2 Tensor)

Multiplying Eq. (A.42) with δ_l^j gives the divergence of a rank–2 tensor, i.e.,

$$
\begin{aligned}
\operatorname{div}\mathbf{T} = & \left(\frac{\partial T^{1j}}{\partial \eta^j} + T^{1m}\Gamma^j_{mj} + T^{jm}\Gamma^1_{mj}\right)\mathbf{g}_1 \\
& + \left(\frac{\partial T^{2j}}{\partial \eta^j} + T^{2m}\Gamma^j_{mj} + T^{jm}\Gamma^2_{mj}\right)\mathbf{g}_2 \\
& + \left(\frac{\partial T^{3j}}{\partial \eta^j} + T^{3m}\Gamma^j_{mj} + T^{jm}\Gamma^3_{mj}\right)\mathbf{g}_3. \qquad \text{(A.46)}
\end{aligned}
$$

Expansion of the summations over j and m indices, and application of physical basis gives

$$
\begin{aligned}
\operatorname{div}\mathbf{T} = & \left(\frac{\partial T^{11}}{\partial \eta^1} + \frac{\partial T^{12}}{\partial \eta^2} + \frac{\partial T^{13}}{\partial \eta^3} + \frac{1}{r}T^{11} - rT^{22}\right)\mathbf{e}_r \\
& + \left(\frac{\partial T^{21}}{\partial \eta^1} + \frac{\partial T^{22}}{\partial \eta^2} + \frac{\partial T^{23}}{\partial \eta^3} + \frac{2}{r}T^{21} + \frac{1}{r}T^{12}\right)r\mathbf{e}_\varphi \\
& + \left(\frac{\partial T^{31}}{\partial \eta^1} + \frac{\partial T^{32}}{\partial \eta^2} + \frac{\partial T^{33}}{\partial \eta^3} + \frac{1}{r}T^{31}\right)\mathbf{e}_z. \qquad \text{(A.47)}
\end{aligned}
$$

By replacing the physical components, divergence of a rank–2 tensor reads

$$\begin{aligned}\operatorname{div}\mathbf{T} &= \left(\frac{\partial T_{rr}}{\partial r} + \frac{1}{r}\frac{\partial T_{r\varphi}}{\partial \varphi} + \frac{\partial T_{rz}}{\partial z} + \frac{T_{rr} - T_{\varphi\varphi}}{r}\right)\mathbf{e}_r \\ &+ \left(\frac{\partial T_{\varphi r}}{\partial r} + \frac{1}{r}\frac{\partial T_{\varphi\varphi}}{\partial \varphi} + \frac{\partial T_{\varphi z}}{\partial z} + \frac{T_{\varphi r} + T_{r\varphi}}{r}\right)\mathbf{e}_\varphi \\ &+ \left(\frac{\partial T_{zr}}{\partial r} + \frac{1}{r}\frac{\partial T_{z\varphi}}{\partial \varphi} + \frac{\partial T_{zz}}{\partial z} + \frac{T_{zr}}{r}\right)\mathbf{e}_z. \end{aligned} \tag{A.48}$$

A.8 Divergence of a Cubic Array (Rank–3 Tensor)

For a rank–3 tensor (where $k = 3$), denoted by $\mathbf{M}$, Eq. (A.34) reads

$$\frac{d\mathbf{M}}{d\mathbf{x}} = \left(\frac{\partial M^{ijk}}{\partial \eta^l} + M^{ijm}\mathit{\Gamma}^k_{ml} + M^{ikm}\mathit{\Gamma}^j_{ml} + M^{jkm}\mathit{\Gamma}^i_{ml}\right)\mathbf{g}^l\mathbf{g}_i\mathbf{g}_j\mathbf{g}_k, \tag{A.49}$$

Multiplying the above equation with δ^k_l gives the divergence of $\mathbf{M}$ as

$$\begin{aligned}\operatorname{div}\mathbf{M} &= \begin{pmatrix} \dfrac{\partial M^{11k}}{\partial \eta^k} + M^{m1k}\mathit{\Gamma}^1_{mk} \\ + M^{1mk}\mathit{\Gamma}^1_{mk} + M^{11m}\mathit{\Gamma}^k_{mk}\end{pmatrix}\mathbf{g}_1\mathbf{g}_1 + \begin{pmatrix} \dfrac{\partial M^{12k}}{\partial \eta^k} + M^{m2k}\mathit{\Gamma}^1_{mk} \\ + M^{1mk}\mathit{\Gamma}^2_{mk} + M^{12m}\mathit{\Gamma}^k_{mk}\end{pmatrix}\mathbf{g}_1\mathbf{g}_2 \\ &+ \begin{pmatrix} \dfrac{\partial M^{13k}}{\partial \eta^k} + M^{m3k}\mathit{\Gamma}^1_{mk} \\ + M^{1mk}\mathit{\Gamma}^3_{mk} + M^{13m}\mathit{\Gamma}^k_{mk}\end{pmatrix}\mathbf{g}_1\mathbf{g}_3 + \begin{pmatrix} \dfrac{\partial M^{21k}}{\partial \eta^k} + M^{m1k}\mathit{\Gamma}^2_{mk} \\ + M^{2mk}\mathit{\Gamma}^1_{mk} + M^{21m}\mathit{\Gamma}^k_{mk}\end{pmatrix}\mathbf{g}_2\mathbf{g}_1 \\ &+ \begin{pmatrix} \dfrac{\partial M^{22k}}{\partial \eta^k} + M^{m2k}\mathit{\Gamma}^2_{mk} \\ + M^{2mk}\mathit{\Gamma}^2_{mk} + M^{22m}\mathit{\Gamma}^k_{mk}\end{pmatrix}\mathbf{g}_2\mathbf{g}_2 + \begin{pmatrix} \dfrac{\partial M^{23k}}{\partial \eta^k} + M^{m3k}\mathit{\Gamma}^2_{mk} \\ + M^{2mk}\mathit{\Gamma}^3_{mk} + M^{23m}\mathit{\Gamma}^k_{mk}\end{pmatrix}\mathbf{g}_2\mathbf{g}_3 \\ &+ \begin{pmatrix} \dfrac{\partial M^{31k}}{\partial \eta^k} + M^{m1k}\mathit{\Gamma}^3_{mk} \\ + M^{3mk}\mathit{\Gamma}^1_{mk} + M^{31m}\mathit{\Gamma}^k_{mk}\end{pmatrix}\mathbf{g}_3\mathbf{g}_1 + \begin{pmatrix} \dfrac{\partial M^{32k}}{\partial \eta^k} + M^{m2k}\mathit{\Gamma}^3_{mk} \\ + M^{3mk}\mathit{\Gamma}^2_{mk} + M^{32m}\mathit{\Gamma}^k_{mk}\end{pmatrix}\mathbf{g}_3\mathbf{g}_2 \\ &+ \begin{pmatrix} \dfrac{\partial M^{33k}}{\partial \eta^k} + M^{m3k}\mathit{\Gamma}^3_{mk} \\ + M^{3mk}\mathit{\Gamma}^3_{mk} + M^{33m}\mathit{\Gamma}^k_{mk}\end{pmatrix}\mathbf{g}_3\mathbf{g}_3. \end{aligned} \tag{A.50}$$

After replacement of Christoffel symbols, and application of physical components and physical basis, divergence of a cubic array in cylindrical coordinate system reads as

$$
\begin{aligned}
\operatorname{div}\mathbf{M} = {} & \left(\begin{array}{l} \quad \dfrac{\partial M_{rrr}}{\partial r} + \dfrac{1}{r}\dfrac{\partial M_{rr\varphi}}{\partial \varphi} + \dfrac{\partial M_{rrz}}{\partial z} \\ - \dfrac{M_{\varphi r\varphi}}{r} - \dfrac{M_{r\varphi\varphi}}{r} + \dfrac{M_{rrr}}{r} \end{array}\right)\mathbf{e}_r\mathbf{e}_r + \left(\begin{array}{l} \quad \dfrac{\partial M_{r\varphi r}}{\partial r} + \dfrac{1}{r}\dfrac{\partial M_{r\varphi\varphi}}{\partial \varphi} + \dfrac{\partial M_{r\varphi z}}{\partial z} \\ - \dfrac{M_{\varphi\varphi\varphi}}{r} + \dfrac{M_{rr\varphi}}{r} + \dfrac{M_{r\varphi r}}{r} \end{array}\right)\mathbf{e}_r\mathbf{e}_\varphi \\
& + \left(\begin{array}{l} \quad \dfrac{\partial M_{rzr}}{\partial r} + \dfrac{1}{r}\dfrac{\partial M_{rz\varphi}}{\partial \varphi} + \dfrac{\partial M_{rzz}}{\partial z} \\ - \dfrac{M_{\varphi z\varphi}}{r} + \dfrac{M_{rzr}}{r} \end{array}\right)\mathbf{e}_r\mathbf{e}_z + \left(\begin{array}{l} \quad \dfrac{\partial M_{\varphi rr}}{\partial r} + \dfrac{1}{r}\dfrac{\partial M_{\varphi r\varphi}}{\partial \varphi} + \dfrac{\partial M_{\varphi rz}}{\partial z} \\ + \dfrac{M_{rr\varphi}}{r} + \dfrac{M_{\varphi rr}}{r} - \dfrac{M_{\varphi\varphi\varphi}}{r} \end{array}\right)\mathbf{e}_\varphi\mathbf{e}_r \\
& + \left(\begin{array}{l} \quad \dfrac{\partial M_{\varphi\varphi r}}{\partial r} + \dfrac{1}{r}\dfrac{\partial M_{\varphi\varphi\varphi}}{\partial \varphi} + \dfrac{\partial M_{\varphi\varphi z}}{\partial z} \\ + \dfrac{M_{r\varphi\varphi}}{r} + \dfrac{M_{\varphi\varphi r}}{r} + \dfrac{M_{\varphi r\varphi}}{r} \end{array}\right)\mathbf{e}_\varphi\mathbf{e}_\varphi + \left(\begin{array}{l} \quad \dfrac{\partial M_{\varphi zr}}{\partial r} + \dfrac{1}{r}\dfrac{\partial M_{\varphi z\varphi}}{\partial \varphi} \\ + \dfrac{\partial M_{\varphi zz}}{\partial z} + \dfrac{M_{rz\varphi}}{r} + \dfrac{M_{\varphi zr}}{r} \end{array}\right)\mathbf{e}_\varphi\mathbf{e}_z \\
& + \left(\begin{array}{l} \quad \dfrac{\partial M_{zrr}}{\partial r} + \dfrac{1}{r}\dfrac{\partial M_{zr\varphi}}{\partial \varphi} + \dfrac{\partial M_{zrz}}{\partial z} \\ - \dfrac{M_{z\varphi\varphi}}{r} + \dfrac{M_{zrr}}{r} \end{array}\right)\mathbf{e}_z\mathbf{e}_r + \left(\begin{array}{l} \quad \dfrac{\partial M_{z\varphi r}}{\partial r} + \dfrac{1}{r}\dfrac{\partial M_{z\varphi\varphi}}{\partial \varphi} + \dfrac{\partial M_{z\varphi z}}{\partial z} \\ + \dfrac{M_{zr\varphi}}{r} + \dfrac{M_{z\varphi r}}{r} \end{array}\right)\mathbf{e}_z\mathbf{e}_\varphi \\
& + \left(\begin{array}{l} \quad \dfrac{\partial M_{zzr}}{\partial r} + \dfrac{1}{r}\dfrac{\partial M_{zz\varphi}}{\partial \varphi} + \dfrac{\partial M_{zzz}}{\partial z} \\ + \dfrac{M_{zzr}}{r} \end{array}\right)\mathbf{e}_z\mathbf{e}_z. \qquad \text{(A.51)}
\end{aligned}
$$

Appendix B

Regularized 13–moment Equations in Cylindrical Coordinates

In this appendix, moment equations for stress [Eq. (4.20)], heat–flux [Eq. (4.21)], along with R13 constitutive equations [Eq. (4.22)–(4.24)] are presented in cylindrical coordinates, $\{r, \varphi, z\}$. These equations beside transformed conservation laws in (4.25)–(4.27) represent the regularized 13–moment equations in cylindrical geometry. Since all required transformation rules are given in Appendix A, details of transformations are not shown in this appendix.

B.1 Stress Balance in Cylindrical Coordinates

As presented in Eq. (4.20) in the text, the moment equation for stress in symbolic notation is

$$\frac{D\boldsymbol{\sigma}}{Dt} + \frac{4}{5}\left\langle \operatorname{grad}\mathbf{q}\right\rangle + \boldsymbol{\sigma}\operatorname{div}\mathbf{v} + 2\left\langle \boldsymbol{\sigma}\cdot\operatorname{grad}\mathbf{v}\right\rangle + \operatorname{div}\mathbf{m} = -2\rho\theta\left\langle \operatorname{grad}\mathbf{v}\right\rangle - \frac{\rho\theta}{\mu}\boldsymbol{\sigma}. \tag{B.1}$$

Since stress tensor is symmetric, it suffices to obtain balance equations only for $\{\sigma_{rr}, \sigma_{r\varphi}, \sigma_{rz}, \sigma_{\varphi\varphi}, \sigma_{\varphi z}, \sigma_{zz}\}$. Moreover, stress tensor is trace–free, $\sigma_{rr} + \sigma_{\varphi\varphi} + \sigma_{zz} = 0$, thus, any of the diagonal elements can be expressed with respect to the others. This reduces the number of required balance equations for stress tensor to five. However, elimination of one of the diagonal elements depends on the flow setting. For instance, it is preferred to eliminate $\sigma_{\varphi\varphi}$ in cylindrical axial flows, and σ_{zz} in cylindrical azimuthal (rotary) flows. For this reason, and to keep the generality, balance equations for all diagonal elements of the stress tensor are presented in this section.

Balance Equation for σ_{rr}

$$
\begin{aligned}
&\frac{\partial\sigma_{rr}}{\partial t}+v_r\frac{\partial\sigma_{rr}}{\partial r}+\frac{v_\varphi}{r}\frac{\partial\sigma_{rr}}{\partial\varphi}-\frac{10}{3}\frac{v_\varphi\sigma_{r\varphi}}{r}+v_z\frac{\partial\sigma_{rr}}{\partial z}+\frac{8}{15}\frac{\partial q_r}{\partial r}-\frac{4}{15}\frac{\partial q_z}{\partial z}-\frac{4}{15}\frac{1}{r}\frac{\partial q_\varphi}{\partial\varphi}+\frac{7}{3}\sigma_{rr}\frac{\partial v_r}{\partial r}\\
&+\frac{\sigma_{rr}}{r}\frac{\partial v_\varphi}{\partial\varphi}-\frac{4}{15}\frac{q_r}{r}-\frac{2}{3}\sigma_{\varphi z}\frac{\partial v_\varphi}{\partial z}+\frac{4}{3}\frac{\sigma_{r\varphi}}{r}\frac{\partial v_r}{\partial\varphi}+\frac{4}{3}\sigma_{rz}\frac{\partial v_r}{\partial z}-\frac{2}{3}\sigma_{r\varphi}\frac{\partial v_\varphi}{\partial r}-\frac{2}{3}\frac{\sigma_{\varphi\varphi}}{r}\frac{\partial v_\varphi}{\partial\varphi}+\frac{v_r\sigma_{rr}}{r}\\
&+\sigma_{rr}\frac{\partial v_z}{\partial z}-\frac{2}{3}\frac{v_r\sigma_{\varphi\varphi}}{r}-\frac{2}{3}\sigma_{rz}\frac{\partial v_z}{\partial r}-\frac{2}{3}\frac{\sigma_{\varphi z}}{r}\frac{\partial v_z}{\partial\varphi}-\frac{2}{3}\sigma_{zz}\frac{\partial v_z}{\partial z}+\frac{\partial m_{rrr}}{\partial r}+\frac{1}{r}\frac{\partial m_{rr\varphi}}{\partial\varphi}+\frac{\partial m_{rrz}}{\partial z}\\
&+\frac{m_{rrr}-2m_{r\varphi\varphi}}{r}=-\frac{4}{3}\rho\theta\frac{\partial v_r}{\partial r}+\frac{2}{3}\frac{\rho\theta}{r}\frac{\partial v_\varphi}{\partial\varphi}+\frac{2}{3}\frac{\rho\theta v_r}{r}+\frac{2}{3}\rho\theta\frac{\partial v_z}{\partial z}-\frac{\rho\theta}{\mu}\sigma_{rr}.
\end{aligned}
\tag{B.2}
$$

Balance Equation for $\sigma_{r\varphi}$

$$
\begin{aligned}
&\frac{\partial\sigma_{r\varphi}}{\partial t}+v_r\frac{\partial\sigma_{r\varphi}}{\partial r}+\frac{v_\varphi}{r}\frac{\partial\sigma_{r\varphi}}{\partial\varphi}+\frac{v_\varphi\sigma_{rr}}{r}-2\frac{v_\varphi\sigma_{\varphi\varphi}}{r}+v_z\frac{\partial\sigma_{r\varphi}}{\partial z}+\frac{2}{5}\frac{1}{r}\frac{\partial q_r}{\partial\varphi}-\frac{2}{5}\frac{q_\varphi}{r}+\frac{2}{5}\frac{\partial q_\varphi}{\partial r}+2\sigma_{r\varphi}\frac{\partial v_r}{\partial r}\\
&+2\frac{\sigma_{r\varphi}}{r}\frac{\partial v_\varphi}{\partial\varphi}+2\frac{v_r\sigma_{r\varphi}}{r}+\sigma_{r\varphi}\frac{\partial v_z}{\partial z}+\sigma_{rr}\frac{\partial v_\varphi}{\partial r}+\sigma_{rz}\frac{\partial v_\varphi}{\partial z}+\frac{\sigma_{\varphi\varphi}}{r}\frac{\partial v_r}{\partial\varphi}+\sigma_{\varphi z}\frac{\partial v_r}{\partial z}+\frac{1}{r}\frac{\partial m_{r\varphi\varphi}}{\partial\varphi}\\
&+\frac{\partial m_{rr\varphi}}{\partial r}+\frac{\partial m_{r\varphi z}}{\partial z}+\frac{2m_{rr\varphi}-m_{\varphi\varphi\varphi}}{r}=-\frac{\rho\theta}{r}\frac{\partial v_r}{\partial\varphi}+\frac{\rho\theta v_\varphi}{r}-\rho\theta\frac{\partial v_\varphi}{\partial r}-\frac{\rho\theta}{\mu}\sigma_{r\varphi}.
\end{aligned}
\tag{B.3}
$$

Balance Equation for σ_{rz}

$$
\begin{aligned}
&\frac{\partial\sigma_{rz}}{\partial t}+v_r\frac{\partial\sigma_{rz}}{\partial r}+\frac{v_\varphi}{r}\frac{\partial\sigma_{rz}}{\partial\varphi}-2\frac{v_\varphi\sigma_{\varphi z}}{r}+v_z\frac{\partial\sigma_{rz}}{\partial z}+\frac{4}{5}\frac{\partial q_r}{\partial z}+2\sigma_{rz}\frac{\partial v_r}{\partial r}+\frac{\sigma_{rz}}{r}\frac{\partial v_\varphi}{\partial\varphi}+\frac{v_r\sigma_{rz}}{r}\\
&+2\sigma_{rz}\frac{\partial v_z}{\partial z}+\sigma_{rr}\frac{\partial v_z}{\partial r}+\frac{\sigma_{r\varphi}}{r}\frac{\partial v_z}{\partial\varphi}+\frac{\sigma_{\varphi z}}{r}\frac{\partial v_r}{\partial\varphi}+\sigma_{zz}\frac{\partial v_r}{\partial z}+\frac{\partial m_{rrz}}{\partial r}+\frac{\partial m_{rzz}}{\partial z}\\
&+\frac{1}{r}\frac{\partial m_{r\varphi z}}{\partial\varphi}+\frac{m_{rrz}-m_{\varphi\varphi z}}{r}=-2\rho\theta\frac{\partial v_r}{\partial z}-\frac{\rho\theta}{\mu}\sigma_{rz}.
\end{aligned}
\tag{B.4}
$$

Balance Equation for $\sigma_{\varphi\varphi}$

$$
\begin{aligned}
&\frac{\partial\sigma_{\varphi\varphi}}{\partial t}+v_r\frac{\partial\sigma_{\varphi\varphi}}{\partial r}+\frac{v_\varphi}{r}\frac{\partial\sigma_{\varphi\varphi}}{\partial\varphi}+\frac{8}{3}\frac{v_\varphi\sigma_{r\varphi}}{r}+v_z\frac{\partial\sigma_{\varphi\varphi}}{\partial z}+\frac{4}{5}\frac{1}{r}\frac{\partial q_\varphi}{\partial\varphi}+\frac{4}{5}\frac{q_r}{r}-\frac{4}{15}\frac{\partial q_r}{\partial r}-\frac{4}{15}\frac{q_r}{r}-\frac{4}{15}\frac{\partial q_z}{\partial z}\\
&+\sigma_{\varphi\varphi}\frac{\partial v_r}{\partial r}-\frac{4}{15}\frac{1}{r}\frac{\partial q_\varphi}{\partial\varphi}+\frac{7}{3}\frac{\sigma_{\varphi\varphi}}{r}\frac{\partial v_\varphi}{\partial\varphi}+\frac{7}{3}\frac{v_r\sigma_{\varphi\varphi}}{r}+\sigma_{\varphi\varphi}\frac{\partial v_z}{\partial z}+\frac{4}{3}\sigma_{r\varphi}\frac{\partial v_\varphi}{\partial r}+\frac{4}{3}\sigma_{\varphi z}\frac{\partial v_\varphi}{\partial z}-\frac{2}{3}\sigma_{rr}\frac{\partial v_r}{\partial r}\\
&-\frac{2}{3}\frac{\sigma_{r\varphi}}{r}\frac{\partial v_r}{\partial\varphi}-\frac{2}{3}\sigma_{rz}\frac{\partial v_r}{\partial z}-\frac{2}{3}\sigma_{rz}\frac{\partial v_z}{\partial r}-\frac{2}{3}\frac{\sigma_{\varphi z}}{r}\frac{\partial v_z}{\partial\varphi}-\frac{2}{3}\sigma_{zz}\frac{\partial v_z}{\partial z}+\frac{\partial m_{r\varphi\varphi}}{\partial r}+\frac{\partial m_{\varphi\varphi z}}{\partial z}+3\frac{m_{r\varphi\varphi}}{r}\\
&+\frac{1}{r}\frac{\partial m_{\varphi\varphi\varphi}}{\partial\varphi}=-\frac{4}{3}\frac{\rho\theta}{r}\frac{\partial v_\varphi}{\partial\varphi}-\frac{4}{3}\frac{\rho\theta v_r}{r}+\frac{2}{3}\rho\theta\frac{\partial v_r}{\partial r}+\frac{2}{3}\rho\theta\frac{\partial v_z}{\partial z}-\frac{\rho\theta}{\mu}\sigma_{\varphi\varphi}.
\end{aligned}
\tag{B.5}
$$

Balance Equation for $\sigma_{\varphi z}$

$$\begin{aligned}
&\frac{\partial \sigma_{\varphi z}}{\partial t}+v_r\frac{\partial \sigma_{\varphi z}}{\partial r}+\frac{v_\varphi}{r}\frac{\partial \sigma_{\varphi z}}{\partial \varphi}+\frac{v_\varphi \sigma_{rz}}{r}+v_z\frac{\partial \sigma_{\varphi z}}{\partial z}+\frac{2}{5}\frac{\partial q_\varphi}{\partial z}+\frac{2}{5}\frac{1}{r}\frac{\partial q_z}{\partial \varphi}+\sigma_{\varphi z}\frac{\partial v_r}{\partial r}+2\frac{\sigma_{\varphi z}}{r}\frac{\partial v_\varphi}{\partial \varphi}\\
&+2\frac{v_r\sigma_{\varphi z}}{r}+2\sigma_{\varphi z}\frac{\partial v_z}{\partial z}+\sigma_{r\varphi}\frac{\partial v_z}{\partial r}+\frac{\sigma_{\varphi\varphi}}{r}\frac{\partial v_z}{\partial \varphi}+\sigma_{rz}\frac{\partial v_\varphi}{\partial r}+\sigma_{zz}\frac{\partial v_\varphi}{\partial z}+\frac{\partial m_{r\varphi z}}{\partial r}\\
&+\frac{1}{r}\frac{\partial m_{\varphi\varphi z}}{\partial \varphi}+\frac{\partial m_{\varphi zz}}{\partial z}+2\frac{m_{r\varphi z}}{r}=-\rho\theta\frac{\partial v_\varphi}{\partial z}-\frac{\rho\theta}{r}\frac{\partial v_z}{\partial \varphi}-\frac{\rho\theta}{\mu}\sigma_{\varphi z}.
\end{aligned}\tag{B.6}$$

Balance Equation for σ_{zz}

$$\begin{aligned}
&\frac{\partial \sigma_{zz}}{\partial t}+v_r\frac{\partial \sigma_{zz}}{\partial r}+\frac{v_\varphi}{r}\frac{\partial \sigma_{zz}}{\partial \varphi}+v_z\frac{\partial \sigma_{zz}}{\partial z}+\frac{8}{15}\frac{\partial q_z}{\partial z}-\frac{4}{15}\frac{\partial q_r}{\partial r}-\frac{4}{15}\frac{q_r}{r}-\frac{4}{15}\frac{1}{r}\frac{\partial q_\varphi}{\partial \varphi}+\sigma_{zz}\frac{\partial v_r}{\partial r}+\frac{\sigma_{zz}}{r}\frac{\partial v_\varphi}{\partial \varphi}\\
&+\frac{v_r\sigma_{zz}}{r}+\frac{4}{3}\sigma_{rz}\frac{\partial v_z}{\partial r}+\frac{4}{3}\frac{\sigma_{\varphi z}}{r}\frac{\partial v_z}{\partial \varphi}+\frac{7}{3}\sigma_{zz}\frac{\partial v_z}{\partial z}-\frac{2}{3}\sigma_{rr}\frac{\partial v_r}{\partial r}-\frac{2}{3}\frac{\sigma_{r\varphi}}{r}\frac{\partial v_r}{\partial \varphi}+\frac{2}{3}\frac{v_\varphi\sigma_{r\varphi}}{r}-\frac{2}{3}\sigma_{rz}\frac{\partial v_r}{\partial z}\\
&-\frac{2}{3}\sigma_{r\varphi}\frac{\partial v_\varphi}{\partial r}-\frac{2}{3}\frac{\sigma_{\varphi\varphi}}{r}\frac{\partial v_\varphi}{\partial \varphi}-\frac{2}{3}\frac{v_r\sigma_{\varphi\varphi}}{r}-\frac{2}{3}\sigma_{\varphi z}\frac{\partial v_\varphi}{\partial z}+\frac{\partial m_{rzz}}{\partial r}+\frac{1}{r}\frac{\partial m_{\varphi zz}}{\partial \varphi}+\frac{\partial m_{zzz}}{\partial z}\\
&+\frac{m_{rzz}}{r}=-\frac{4}{3}\rho\theta\frac{\partial v_z}{\partial z}+\frac{2}{3}\rho\theta\frac{\partial v_r}{\partial r}+\frac{2}{3}\frac{\rho\theta}{r}\frac{\partial v_\varphi}{\partial \varphi}+\frac{2}{3}\rho\theta\frac{v_r}{r}-\frac{\rho\theta}{\mu}\sigma_{zz}.
\end{aligned}\tag{B.7}$$

B.2 Heat Flux Balance in Cylindrical Coordinates

In symbolic notation, balance equation for the heat flux reads [cf. Eq. (4.21)]

$$\begin{aligned}
&\frac{D\mathbf{q}}{Dt}+\frac{5}{2}\boldsymbol{\sigma}\cdot\operatorname{grad}\theta-\frac{\theta}{\rho}\boldsymbol{\sigma}\cdot\operatorname{grad}\rho-\frac{1}{\rho}\boldsymbol{\sigma}\cdot\operatorname{div}\boldsymbol{\sigma}+\theta\operatorname{div}\boldsymbol{\sigma}+\frac{7}{5}\left(\mathbf{q}\cdot\operatorname{grad}\mathbf{v}+\mathbf{q}\operatorname{div}\mathbf{v}\right)\\
&\qquad+\frac{2}{5}\mathbf{q}\cdot\left(\operatorname{grad}\mathbf{v}\right)^{\mathrm{T}}+\frac{1}{6}\operatorname{grad}\varDelta+\frac{1}{2}\operatorname{div}\mathbf{R}+\mathbf{m}:\operatorname{grad}\mathbf{v}=-\frac{5}{2}\rho\theta\operatorname{grad}\theta-\mathrm{Pr}\frac{\rho\theta}{\mu}\mathbf{q}.
\end{aligned}\tag{B.8}$$

By employing the transformation rules in Appendix A, balance equation for the components of heat flux vector in cylindrical coordinates are obtained.

Balance Equation for q_r

$$\begin{aligned}
&\frac{\partial q_r}{\partial t} + v_r \frac{\partial q_r}{\partial r} + \frac{v_\varphi}{r}\frac{\partial q_r}{\partial \varphi} - \frac{v_\varphi q_\varphi}{r} + v_z \frac{\partial q_r}{\partial z} + \frac{5}{2}\sigma_{rr}\frac{\partial \theta}{\partial r} + \frac{5}{2}\frac{\sigma_{r\varphi}}{r}\frac{\partial \theta}{\partial \varphi} + \frac{5}{2}\sigma_{rz}\frac{\partial \theta}{\partial z} - \frac{\theta\sigma_{rr}}{\rho}\frac{\partial \rho}{\partial r} - \frac{\theta\sigma_{r\varphi}}{\rho r}\frac{\partial \rho}{\partial \varphi} \\
&- \frac{\theta\sigma_{rz}}{\rho}\frac{\partial \rho}{\partial z} - \frac{\sigma_{rr}}{\rho}\frac{\partial \sigma_{rr}}{\partial r} - \frac{\sigma_{rr}}{\rho r}\frac{\partial \sigma_{r\varphi}}{\partial \varphi} - \frac{\sigma_{rr}}{\rho}\frac{\partial \sigma_{rz}}{\partial z} - \frac{\sigma_{rr}^2}{\rho r} + \frac{\sigma_{rr}\sigma_{\varphi\varphi}}{\rho r} - \frac{\sigma_{r\varphi}}{\rho}\frac{\partial \sigma_{r\varphi}}{\partial r} - \frac{\sigma_{r\varphi}}{\rho r}\frac{\partial \sigma_{\varphi\varphi}}{\partial \varphi} - 2\frac{\sigma_{r\varphi}^2}{\rho r} \\
&- \frac{\sigma_{r\varphi}}{\rho}\frac{\partial \sigma_{\varphi z}}{\partial z} - \frac{\sigma_{rz}}{\rho}\frac{\partial \sigma_{rz}}{\partial r} - \frac{\sigma_{rz}}{\rho r}\frac{\partial \sigma_{\varphi z}}{\partial \varphi} - \frac{\sigma_{rz}}{\rho}\frac{\partial \sigma_{zz}}{\partial z} - \frac{\sigma_{rz}^2}{\rho r} + \theta\frac{\partial \sigma_{rr}}{\partial r} + \frac{\theta}{r}\frac{\partial \sigma_{r\varphi}}{\partial \varphi} + \theta\frac{\partial \sigma_{rz}}{\partial z} + \frac{\theta\sigma_{rr}}{r} \\
&- \frac{\theta\sigma_{\varphi\varphi}}{r} + \frac{7}{5}q_r\frac{\partial v_r}{\partial r} + \frac{7}{5}\frac{q_\varphi}{r}\frac{\partial v_r}{\partial \varphi} - \frac{7}{5}\frac{v_\varphi q_\varphi}{r} + \frac{7}{5}q_z\frac{\partial v_r}{\partial z} + \frac{7}{5}q_r\frac{\partial v_r}{\partial r} + \frac{7}{5}\frac{q_r}{r}\frac{\partial v_\varphi}{\partial \varphi} + \frac{7}{5}\frac{v_r q_r}{r} \\
&+ \frac{7}{5}q_r\frac{\partial v_z}{\partial z} + \frac{2}{5}q_r\frac{\partial v_r}{\partial r} + \frac{2}{5}q_\varphi\frac{\partial v_\varphi}{\partial r} + \frac{2}{5}q_z\frac{\partial v_z}{\partial r} + \frac{1}{6}\frac{\partial \varDelta}{\partial r} + \frac{1}{2}\frac{\partial R_{rr}}{\partial r} + \frac{1}{2}\frac{1}{r}\frac{\partial R_{r\varphi}}{\partial \varphi} + \frac{1}{2}\frac{\partial R_{rz}}{\partial z} \\
&+ \frac{1}{2}\frac{R_{rr}}{r} - \frac{1}{2}\frac{R_{\varphi\varphi}}{r} + M_{rrr}\frac{\partial v_r}{\partial r} + \frac{M_{rr\varphi}}{r}\frac{\partial v_r}{\partial \varphi} - \frac{v_\varphi M_{rr\varphi}}{r} + M_{rrz}\frac{\partial v_r}{\partial z} + M_{rr\varphi}\frac{\partial v_\varphi}{\partial r} + \frac{M_{r\varphi\varphi}}{r}\frac{\partial v_\varphi}{\partial \varphi} \\
&+ \frac{v_r M_{r\varphi\varphi}}{r} + M_{r\varphi z}\frac{\partial v_\varphi}{\partial z} + M_{rrz}\frac{\partial v_z}{\partial r} + \frac{M_{r\varphi z}}{r}\frac{\partial v_z}{\partial \varphi} + M_{rzz}\frac{\partial v_z}{\partial z} = -\frac{5}{2}\rho\theta\frac{\partial \theta}{\partial r} - \mathrm{Pr}\frac{\rho\theta}{\mu}q_r.
\end{aligned} \tag{B.9}$$

Balance Equation for q_φ

$$\begin{aligned}
&\frac{\partial q_\varphi}{\partial t} + v_r \frac{\partial q_\varphi}{\partial r} + \frac{v_\varphi}{r}\frac{\partial q_\varphi}{\partial \varphi} + \frac{v_\varphi q_r}{r} + v_z \frac{\partial q_\varphi}{\partial z} + \frac{5}{2}\sigma_{r\varphi}\frac{\partial \theta}{\partial r} + \frac{5}{2}\frac{\sigma_{\varphi\varphi}}{r}\frac{\partial \theta}{\partial \varphi} + \frac{5}{2}\sigma_{\varphi z}\frac{\partial \theta}{\partial z} - \frac{\theta\sigma_{r\varphi}}{\rho}\frac{\partial \rho}{\partial r} \\
&- \frac{\theta\sigma_{\varphi\varphi}}{\rho r}\frac{\partial \rho}{\partial \varphi} - \frac{\theta\sigma_{\varphi z}}{\rho}\frac{\partial \rho}{\partial z} - \frac{\sigma_{r\varphi}}{\rho}\frac{\partial \sigma_{rr}}{\partial r} - \frac{\sigma_{r\varphi}}{\rho r}\frac{\partial \sigma_{r\varphi}}{\partial \varphi} - \frac{\sigma_{r\varphi}}{\rho}\frac{\partial \sigma_{rz}}{\partial z} - \frac{\sigma_{rr}\sigma_{r\varphi}}{\rho r} + \frac{\sigma_{r\varphi}\sigma_{\varphi\varphi}}{\rho r} - \frac{\sigma_{\varphi\varphi}}{\rho}\frac{\partial \sigma_{r\varphi}}{\partial r} \\
&- \frac{\sigma_{\varphi\varphi}}{\rho r}\frac{\partial \sigma_{\varphi\varphi}}{\partial \varphi} - \frac{\sigma_{\varphi\varphi}}{\rho}\frac{\partial \sigma_{\varphi z}}{\partial z} - 2\frac{\sigma_{r\varphi}\sigma_{\varphi\varphi}}{\rho r} - \frac{\sigma_{\varphi z}}{\rho}\frac{\partial \sigma_{rz}}{\partial r} - \frac{\sigma_{\varphi z}}{\rho r}\frac{\partial \sigma_{\varphi z}}{\partial \varphi} - \frac{\sigma_{\varphi z}}{\rho}\frac{\partial \sigma_{zz}}{\partial z} - \frac{\sigma_{rz}\sigma_{\varphi z}}{\rho r} \\
&+ \theta\frac{\partial \sigma_{r\varphi}}{\partial r} + \frac{\theta}{r}\frac{\partial \sigma_{\varphi\varphi}}{\partial \varphi} + \theta\frac{\partial \sigma_{\varphi z}}{\partial z} + 2\frac{\theta\sigma_{r\varphi}}{r} + \frac{7}{5}q_r\frac{\partial v_\varphi}{\partial r} + \frac{7}{5}\frac{q_\varphi}{r}\frac{\partial v_\varphi}{\partial \varphi} + \frac{7}{5}\frac{v_r q_\varphi}{r} + \frac{7}{5}\frac{\partial v_\varphi}{\partial z}q_z \\
&+ \frac{7}{5}q_\varphi\frac{\partial v_r}{\partial r} + \frac{7}{5}\frac{q_\varphi}{r}\frac{\partial v_\varphi}{\partial \varphi} + \frac{7}{5}\frac{v_r q_\varphi}{r} + \frac{7}{5}q_\varphi\frac{\partial v_z}{\partial z} + \frac{2}{5}\frac{q_r}{r}\frac{\partial v_r}{\partial \varphi} - \frac{2}{5}\frac{v_\varphi q_r}{r} + \frac{2}{5}\frac{q_\varphi}{r}\frac{\partial v_\varphi}{\partial \varphi} \\
&+ \frac{2}{5}\frac{v_r q_\varphi}{r} + \frac{2}{5}\frac{q_z}{r}\frac{\partial v_z}{\partial \varphi} + \frac{1}{6}\frac{1}{r}\frac{\partial \varDelta}{\partial \varphi} + \frac{1}{2}\frac{\partial R_{r\varphi}}{\partial r} + \frac{1}{2}\frac{1}{r}\frac{\partial R_{\varphi\varphi}}{\partial \varphi} + \frac{1}{2}\frac{\partial R_{\varphi z}}{\partial z} + \frac{R_{r\varphi}}{r} + M_{rr\varphi}\frac{\partial v_r}{\partial r} \\
&+ \frac{M_{r\varphi\varphi}}{r}\frac{\partial v_r}{\partial \varphi} - \frac{v_\varphi M_{r\varphi\varphi}}{r} + M_{r\varphi z}\frac{\partial v_r}{\partial z} + M_{r\varphi\varphi}\frac{\partial v_\varphi}{\partial r} + \frac{M_{\varphi\varphi\varphi}}{r}\frac{\partial v_\varphi}{\partial \varphi} + \frac{v_r M_{\varphi\varphi\varphi}}{r} + M_{\varphi\varphi z}\frac{\partial v_\varphi}{\partial z} \\
&+ M_{r\varphi z}\frac{\partial v_z}{\partial r} + \frac{M_{\varphi\varphi z}}{r}\frac{\partial v_z}{\partial \varphi} + M_{\varphi zz}\frac{\partial v_z}{\partial z} = -\frac{5}{2}\frac{\rho\theta}{r}\frac{\partial \theta}{\partial \varphi} - \mathrm{Pr}\frac{\rho\theta}{\mu}q_\varphi.
\end{aligned} \tag{B.10}$$

Balance Equation for q_z

$$\begin{aligned}
&\frac{\partial q_z}{\partial t} + v_r \frac{\partial q_z}{\partial r} + \frac{v_\varphi}{r}\frac{\partial q_z}{\partial \varphi} + v_z \frac{\partial q_z}{\partial z} + \frac{5}{2}\sigma_{rz}\frac{\partial \theta}{\partial r} + \frac{5}{2}\frac{\sigma_{\varphi z}}{r}\frac{\partial \theta}{\partial \varphi} + \frac{5}{2}\sigma_{zz}\frac{\partial \theta}{\partial z} - \frac{\theta\sigma_{rz}}{\rho}\frac{\partial \rho}{\partial r} - \frac{\theta\sigma_{\varphi z}}{\rho r}\frac{\partial \rho}{\partial \varphi} - \frac{\theta\sigma_{zz}}{\rho}\frac{\partial \rho}{\partial z} \\
&- \frac{\sigma_{rz}}{\rho}\frac{\partial \sigma_{rr}}{\partial r} - \frac{\sigma_{rz}}{\rho r}\frac{\partial \sigma_{r\varphi}}{\partial \varphi} - \frac{\sigma_{rz}}{\rho}\frac{\partial \sigma_{rz}}{\partial z} - \frac{\sigma_{rr}\sigma_{rz}}{\rho r} + \frac{\sigma_{rz}\sigma_{\varphi\varphi}}{\rho r} - \frac{\sigma_{\varphi z}}{\rho}\frac{\partial \sigma_{r\varphi}}{\partial r} - \frac{\sigma_{\varphi z}}{\rho r}\frac{\partial \sigma_{\varphi\varphi}}{\partial \varphi} - \frac{\sigma_{\varphi z}}{\rho}\frac{\partial \sigma_{\varphi z}}{\partial z} \\
&- 2\frac{\sigma_{r\varphi}\sigma_{\varphi z}}{\rho r} - \frac{\sigma_{zz}}{\rho}\frac{\partial \sigma_{rz}}{\partial r} - \frac{\sigma_{zz}}{\rho r}\frac{\partial \sigma_{\varphi z}}{\partial \varphi} - \frac{\sigma_{zz}}{\rho}\frac{\partial \sigma_{zz}}{\partial z} - \frac{\sigma_{rz}\sigma_{zz}}{\rho r} + \theta\frac{\partial \sigma_{rz}}{\partial r} + \frac{\theta}{r}\frac{\partial \sigma_{\varphi z}}{\partial \varphi} + \theta\frac{\partial \sigma_{zz}}{\partial z} + \theta\frac{\sigma_{rz}}{r} \\
&+ \frac{7}{5}q_r\frac{\partial v_z}{\partial r} + \frac{7}{5}\frac{q_\varphi}{r}\frac{\partial v_z}{\partial \varphi} + \frac{7}{5}q_z\frac{\partial v_z}{\partial z} + \frac{7}{5}q_z\frac{\partial v_r}{\partial r} + \frac{7}{5}\frac{q_z}{r}\frac{\partial v_\varphi}{\partial \varphi} + \frac{7}{5}\frac{v_r q_z}{r} + \frac{7}{5}q_z\frac{\partial v_z}{\partial z} + \frac{2}{5}q_r\frac{\partial v_r}{\partial z} \\
&+ \frac{2}{5}q_\varphi\frac{\partial v_\varphi}{\partial z} + \frac{2}{5}q_z\frac{\partial v_z}{\partial z} + \frac{1}{6}\frac{\partial \varDelta}{\partial z} + \frac{1}{2}\frac{\partial R_{rz}}{\partial r} + \frac{1}{2}\frac{1}{r}\frac{\partial R_{\varphi z}}{\partial \varphi} + \frac{1}{2}\frac{\partial R_{zz}}{\partial z} + \frac{1}{2}\frac{R_{rz}}{r} + M_{rrz}\frac{\partial v_r}{\partial r} \\
&+ \frac{M_{r\varphi z}}{r}\frac{\partial v_r}{\partial \varphi} - \frac{v_\varphi M_{r\varphi z}}{r} + M_{rzz}\frac{\partial v_r}{\partial z} + M_{r\varphi z}\frac{\partial v_\varphi}{\partial r} + \frac{M_{\varphi\varphi z}}{r}\frac{\partial v_\varphi}{\partial \varphi} + \frac{v_r M_{\varphi\varphi z}}{r} + M_{\varphi zz}\frac{\partial v_\varphi}{\partial z} \\
&+ M_{rzz}\frac{\partial v_z}{\partial r} + \frac{M_{\varphi zz}}{r}\frac{\partial v_z}{\partial \varphi} + M_{zzz}\frac{\partial v_z}{\partial z} = -\frac{5}{2}\rho\theta\frac{\partial \theta}{\partial z} - \mathrm{Pr}\frac{\rho\theta}{\mu}q_z.
\end{aligned} \tag{B.11}$$

B.3 R13 Constitutive Equations in Cylindrical Coordinates

B.3.1 $\varDelta$

The quantity $\varDelta$ in symbolic notation reads [Eq. (4.22)]

$$\varDelta = \mathsf{A}_1\frac{\boldsymbol{\sigma}:\boldsymbol{\sigma}}{\rho} + \mathsf{A}_2\frac{\mu}{p}\left(\theta\,\mathrm{div}\,\mathbf{q} + \frac{5}{2}\,\mathbf{q}\cdot\mathrm{grad}\,\theta - \frac{\theta}{\rho}\,\mathbf{q}\cdot\mathrm{grad}\,\rho + \theta\,\boldsymbol{\sigma}:\mathrm{grad}\,\mathbf{v}\right), \tag{B.12}$$

and its expansion in cylindrical coordinates follows as

$$\begin{aligned}
\varDelta = {}& 2\,\mathsf{A}_1\frac{\sigma_{rr}^2 + \sigma_{r\varphi}^2 + \sigma_{rz}^2 + \sigma_{\varphi\varphi}^2 + \sigma_{\varphi z}^2 + \sigma_{rr}\sigma_{\varphi\varphi}}{\rho} + \mathsf{A}_2\frac{\mu}{p}\left[\theta\left(\frac{\partial q_r}{\partial r} + \frac{1}{r}\frac{\partial q_\varphi}{\partial \varphi} + \frac{q_r}{r} + \frac{\partial q_z}{\partial z}\right)\right. \\
&+ \frac{5}{2}\left(q_r\frac{\partial \theta}{\partial r} + \frac{q_\varphi}{r}\frac{\partial \theta}{\partial \varphi} + q_z\frac{\partial \theta}{\partial z}\right) - \frac{\theta}{\rho}\left(q_r\frac{\partial \rho}{\partial r} + \frac{q_\varphi}{r}\frac{\partial \rho}{\partial \varphi} + q_z\frac{\partial \rho}{\partial z}\right) + \theta\left(\sigma_{rr}\frac{\partial v_r}{\partial r}\right. \\
&+ \frac{\sigma_{r\varphi}}{r}\frac{\partial v_r}{\partial \varphi} - \frac{v_\varphi\sigma_{r\varphi}}{r} + \sigma_{rz}\frac{\partial v_r}{\partial z} + \sigma_{r\varphi}\frac{\partial v_\varphi}{\partial r} + \frac{\sigma_{\varphi\varphi}}{r}\frac{\partial v_\varphi}{\partial \varphi} + \frac{v_r\sigma_{\varphi\varphi}}{r} \\
&\left.\left.+ \sigma_{\varphi z}\frac{\partial v_\varphi}{\partial z} + \sigma_{rz}\frac{\partial v_z}{\partial r} + \frac{\sigma_{\varphi z}}{r}\frac{\partial v_z}{\partial \varphi} + \sigma_{zz}\frac{\partial v_z}{\partial z}\right)\right].
\end{aligned} \tag{B.13}$$

B.3.2 R

The quantity $\mathbf{R}$ represents a symmetric and trace–free tensor of rank–2 [Eq. (4.23)],

$$\mathbf{R} = \mathsf{B}_1\frac{\langle\boldsymbol{\sigma}\cdot\boldsymbol{\sigma}\rangle}{\rho} + \mathsf{B}_2\frac{\mu}{p}\left(\theta\,\langle\mathrm{grad}\,\mathbf{q}\rangle + \langle\mathbf{q}\,\mathrm{grad}\,\theta\rangle - \frac{\theta}{\rho}\,\langle\mathbf{q}\,\mathrm{grad}\,\rho\rangle + \frac{10}{7}\,\theta\,\langle\sigma\cdot\langle\mathrm{grad}\,\mathbf{v}\rangle\rangle\right). \tag{B.14}$$

Due to symmetry, it suffices to obtain expressions for $\{R_{rr}, R_{r\varphi}, R_{rz}, R_{\varphi\varphi}, R_{\varphi z}, R_{zz}\}$, where $R_{rr} + R_{\varphi\varphi} + R_{zz} = 0$.

Equation for R_{rr}

$$\begin{aligned} R_{rr} = \frac{\mathsf{B}_1}{3}\frac{2\sigma_{rr}^2 + \sigma_{r\varphi}^2 + \sigma_{rz}^2 - \sigma_{\varphi\varphi}^2 - 2\sigma_{\varphi z}^2 - \sigma_{zz}^2}{\rho} &+ \mathsf{B}_2\frac{\mu}{p}\left[\frac{2}{3}\theta\frac{\partial q_r}{\partial r} - \frac{1}{3}\theta\left(\frac{1}{r}\frac{\partial q_\varphi}{\partial \varphi} + \frac{q_r}{r} + \frac{\partial q_z}{\partial z}\right) + \frac{2}{3}q_r\frac{\partial \theta}{\partial r}\right. \\ &- \frac{1}{3}\left(\frac{q_\varphi}{r}\frac{\partial \theta}{\partial \varphi} + q_z\frac{\partial \theta}{\partial z}\right) - \frac{\theta q_r}{\rho}\frac{\partial \rho}{\partial r} + \frac{1}{3}\frac{\theta}{\rho}\left(q_r\frac{\partial \rho}{\partial r} + \frac{q_\varphi}{r}\frac{\partial \rho}{\partial \varphi} + q_z\frac{\partial \rho}{\partial z}\right) + \frac{10}{7}\theta\left(\frac{2}{3}\sigma_{rr}\frac{\partial v_r}{\partial r} + \frac{1}{3}\sigma_{rz}\frac{\partial v_r}{\partial z}\right. \\ &- \frac{2\sigma_{rr} - \sigma_{\varphi\varphi} - \sigma_{zz}}{9}\left(\frac{\partial v_r}{\partial r} + \frac{1}{r}\frac{\partial v_\varphi}{\partial \varphi} + \frac{v_r}{r} + \frac{\partial v_z}{\partial z}\right) + \frac{1}{6}\frac{\sigma_{r\varphi}}{r}\left(\frac{\partial v_r}{\partial \varphi} - v_\varphi\right) + \frac{1}{6}\sigma_{r\varphi}\frac{\partial v_\varphi}{\partial r} \\ &\left.\left. - \frac{1}{3}\frac{\sigma_{\varphi\varphi}}{r}\frac{\partial v_\varphi}{\partial \varphi} - \frac{1}{3}\frac{v_r\sigma_{\varphi\varphi}}{r} - \frac{1}{3}\sigma_{\varphi z}\left(\frac{\partial v_\varphi}{\partial z} + \frac{1}{r}\frac{\partial v_z}{\partial \varphi}\right) - \frac{1}{3}\sigma_{zz}\frac{\partial v_z}{\partial z}\right)\right]. \end{aligned} \tag{B.15}$$

Equation for $R_{r\varphi}$

$$\begin{aligned} R_{r\varphi} = \mathsf{B}_1\frac{\sigma_{rr}\sigma_{r\varphi} + \sigma_{r\varphi}\sigma_{\varphi\varphi} + \sigma_{rz}\sigma_{\varphi z}}{\rho} &+ \mathsf{B}_2\frac{\mu}{p}\left[\frac{1}{2}\theta\left(\frac{1}{r}\frac{\partial q_r}{\partial \varphi} - \frac{q_\varphi}{r} + \frac{\partial q_\varphi}{\partial r}\right) + \frac{1}{2}\left(\frac{q_r}{r}\frac{\partial \theta}{\partial \varphi} + q_\varphi\frac{\partial \theta}{\partial r}\right)\right. \\ &- \frac{1}{2}\frac{\theta}{\rho}\left(\frac{q_r}{r}\frac{\partial \rho}{\partial \varphi} + q_\varphi\frac{\partial \rho}{\partial r}\right) + \frac{5}{7}\theta\left(\frac{1}{2}\sigma_{rr}\frac{\partial v_\varphi}{\partial r} + \frac{1}{2}\frac{\sigma_{rr}}{r}\left(\frac{\partial v_r}{\partial \varphi} - v_\varphi\right) + \frac{\sigma_{r\varphi}}{r}\left(\frac{\partial v_\varphi}{\partial \varphi} + v_r\right)\right. \\ &- \frac{2}{3}\sigma_{r\varphi}\left(\frac{\partial v_r}{\partial r} + \frac{1}{r}\frac{\partial v_\varphi}{\partial \varphi} + \frac{v_r}{r} + \frac{\partial v_z}{\partial z}\right) + \frac{1}{2}\sigma_{rz}\left(\frac{\partial v_\varphi}{\partial z} + \frac{1}{r}\frac{\partial v_z}{\partial \varphi}\right) + \sigma_{r\varphi}\frac{\partial v_r}{\partial r} \\ &\left.\left. + \frac{1}{2}\frac{\sigma_{\varphi\varphi}}{r}\left(\frac{\partial v_r}{\partial \varphi} - v_\varphi\right) + \frac{1}{2}\sigma_{\varphi\varphi}\frac{\partial v_\varphi}{\partial r} + \sigma_{\varphi z}\frac{\partial v_r}{\partial z}\right)\right]. \end{aligned} \tag{B.16}$$

Equation for R_{rz}

$$\begin{aligned} R_{rz} = \mathsf{B}_1\frac{\sigma_{rr}\sigma_{rz} + \sigma_{r\varphi}\sigma_{\varphi z} + \sigma_{rz}\sigma_{zz}}{\rho} &+ \mathsf{B}_2\frac{\mu}{p}\left[\theta\frac{\partial q_r}{\partial z} + \frac{1}{2}\left(q_r\frac{\partial \theta}{\partial z} + q_z\frac{\partial \theta}{\partial r}\right) - \frac{1}{2}\frac{\theta}{\rho}\left(q_r\frac{\partial \rho}{\partial z} + q_z\frac{\partial \rho}{\partial r}\right)\right. \\ &+ \frac{5}{7}\theta\left(\sigma_{rr}\frac{\partial v_z}{\partial r} + \frac{1}{2}\sigma_{r\varphi}\left(\frac{1}{r}\frac{\partial v_z}{\partial \varphi} + \frac{\partial v_\varphi}{\partial z}\right) + \sigma_{rz}\frac{\partial v_z}{\partial z} - \frac{2}{3}\sigma_{rz}\left(\frac{\partial v_r}{\partial r} + \frac{1}{r}\frac{\partial v_\varphi}{\partial \varphi} + \frac{v_r}{r} + \frac{\partial v_z}{\partial z}\right)\right. \\ &\left.\left. + \sigma_{rz}\frac{\partial v_r}{\partial r} + \frac{1}{2}\frac{\sigma_{\varphi z}}{r}\left(\frac{\partial v_r}{\partial \varphi} - v_\varphi\right) + \frac{1}{2}\sigma_{\varphi z}\frac{\partial v_\varphi}{\partial r} + \sigma_{zz}\frac{\partial v_r}{\partial z}\right)\right]. \end{aligned} \tag{B.17}$$

Equation for $R_{\varphi\varphi}$

$$
\begin{aligned}
R_{\varphi\varphi} = {} & \frac{\mathsf{B}_1}{3}\frac{-\sigma_{rr}^2+\sigma_{r\varphi}^2-2\sigma_{rz}^2+2\sigma_{\varphi\varphi}^2+\sigma_{\varphi z}^2-\sigma_{zz}^2}{\rho}+\mathsf{B}_2\frac{\mu}{p}\Bigg[\frac{1}{3}\theta\left(2\frac{1}{r}\frac{\partial q_\varphi}{\partial\varphi}+2\frac{q_r}{r}-\frac{\partial q_r}{\partial r}-\frac{\partial q_z}{\partial z}\right) \\
& +\frac{q_\varphi}{r}\frac{\partial\theta}{\partial\varphi}-\frac{1}{3}\left(q_r\frac{\partial\theta}{\partial r}+\frac{q_\varphi}{r}\frac{\partial\theta}{\partial\varphi}+q_z\frac{\partial\theta}{\partial z}\right)-\frac{\theta}{\rho}\left(\frac{q_\varphi}{r}\frac{\partial\rho}{\partial\varphi}-\frac{1}{3}q_r\frac{\partial\rho}{\partial r}-\frac{1}{3}\frac{q_\varphi}{r}\frac{\partial\rho}{\partial\varphi}-\frac{1}{3}q_z\frac{\partial\rho}{\partial z}\right) \\
& +\frac{10}{7}\theta\Bigg(\frac{1}{6}\frac{\sigma_{r\varphi}}{r}\left(\frac{\partial v_r}{\partial\varphi}-v_\varphi\right)+\frac{\sigma_{rr}-2\sigma_{\varphi\varphi}+\sigma_{zz}}{9}\left(\frac{\partial v_r}{\partial r}+\frac{1}{r}\frac{\partial v_\varphi}{\partial\varphi}+\frac{v_r}{r}+\frac{\partial v_z}{\partial z}\right) \\
& +\frac{1}{6}\sigma_{r\varphi}\frac{\partial v_\varphi}{\partial r}+\frac{2}{3}\frac{\sigma_{\varphi\varphi}}{r}\left(\frac{\partial v_\varphi}{\partial\varphi}+v_r\right)+\frac{1}{6}\sigma_{\varphi z}\left(\frac{\partial v_\varphi}{\partial z}+\frac{1}{r}\frac{\partial v_z}{\partial\varphi}\right) \\
& -\frac{2}{3}\sigma_{rz}\frac{\partial v_r}{\partial z}-\frac{1}{3}\sigma_{rr}\frac{\partial v_r}{\partial r}-\frac{1}{3}\sigma_{zz}\frac{\partial v_z}{\partial z}\Bigg)\Bigg]. \qquad \text{(B.18)}
\end{aligned}
$$

Equation for $R_{\varphi z}$

$$
\begin{aligned}
R_{\varphi z} = {} & \mathsf{B}_1\frac{\sigma_{rz}\sigma_{r\varphi}+\sigma_{\varphi z}\sigma_{\varphi\varphi}+\sigma_{\varphi z}\sigma_{zz}}{\rho}+\mathsf{B}_2\frac{\mu}{p}\Bigg[\frac{1}{2}\theta\left(\frac{\partial q_\varphi}{\partial z}+\frac{1}{r}\frac{\partial q_z}{\partial\varphi}\right)+\frac{1}{2}\left(q_\varphi\frac{\partial\theta}{\partial z}+\frac{q_z}{r}\frac{\partial\theta}{\partial\varphi}\right) \\
& -\frac{1}{2}\frac{\theta}{\rho}\left(q_\varphi\frac{\partial\rho}{\partial z}+\frac{q_z}{r}\frac{\partial\rho}{\partial\varphi}\right)+\frac{5}{7}\theta\Bigg(\sigma_{r\varphi}\frac{\partial v_z}{\partial r}+\frac{\sigma_{\varphi\varphi}+\sigma_{zz}}{2}\left(\frac{\partial v_\varphi}{\partial z}+\frac{1}{r}\frac{\partial v_z}{\partial\varphi}\right)+\sigma_{\varphi z}\frac{\partial v_z}{\partial z} \\
& -\frac{2}{3}\sigma_{\varphi z}\left(\frac{\partial v_r}{\partial r}+\frac{1}{r}\frac{\partial v_\varphi}{\partial\varphi}+\frac{v_r}{r}+\frac{\partial v_z}{\partial z}\right)+\frac{1}{2}\sigma_{rz}\frac{\partial v_\varphi}{\partial r}+\frac{1}{2}\frac{\sigma_{rz}}{r}\left(\frac{\partial v_r}{\partial\varphi}-v_\varphi\right) \\
& +\frac{\sigma_{\varphi z}}{r}\left(\frac{\partial v_\varphi}{\partial\varphi}+v_r\right)\Bigg)\Bigg]. \qquad \text{(B.19)}
\end{aligned}
$$

Equation for R_{zz}

$$
\begin{aligned}
R_{zz} = {} & \frac{\mathsf{B}_1}{3}\frac{-\sigma_{rr}^2-2\sigma_{r\varphi}^2+\sigma_{rz}^2-\sigma_{\varphi\varphi}^2+\sigma_{\varphi z}^2+2\sigma_{zz}^2}{\rho}+\mathsf{B}_2\frac{\mu}{p}\Bigg[\frac{2}{3}\theta\frac{\partial q_z}{\partial z}-\frac{1}{3}\left(q_r\frac{\partial\theta}{\partial r}+\frac{q_\varphi}{r}\frac{\partial\theta}{\partial\varphi}\right)+\frac{2}{3}q_z\frac{\partial\theta}{\partial z} \\
& -\frac{1}{3}\theta\left(\frac{\partial q_r}{\partial r}+\frac{1}{r}\frac{\partial q_\varphi}{\partial\varphi}+\frac{q_r}{r}\right)-\frac{\theta q_z}{\rho}\frac{\partial\rho}{\partial z}+\frac{1}{3}\frac{\theta}{\rho}\left(q_r\frac{\partial\rho}{\partial r}+\frac{q_\varphi}{r}\frac{\partial\rho}{\partial\varphi}+q_z\frac{\partial\rho}{\partial z}\right)+\frac{10}{7}\theta\Bigg(\sigma_{rz}\frac{\partial v_z}{\partial r} \\
& +\frac{1}{6}\sigma_{\varphi z}\left(\frac{1}{r}\frac{\partial v_z}{\partial\varphi}+\frac{\partial v_\varphi}{\partial z}\right)+\frac{2}{3}\sigma_{zz}\frac{\partial v_z}{\partial z}+\frac{\sigma_{rr}+\sigma_{\varphi\varphi}-2\sigma_{zz}}{9}\left(\frac{\partial v_r}{\partial r}+\frac{1}{r}\frac{\partial v_\varphi}{\partial\varphi}+\frac{v_r}{r}+\frac{\partial v_z}{\partial z}\right) \\
& -\frac{1}{3}\sigma_{rr}\frac{\partial v_r}{\partial r}-\frac{1}{3}\sigma_{r\varphi}\frac{\partial v_\varphi}{\partial r}-\frac{1}{3}\frac{\sigma_{r\varphi}}{r}\left(\frac{\partial v_r}{\partial\varphi}-v_\varphi\right)-\frac{2}{3}\sigma_{rz}\frac{\partial v_r}{\partial z}-\frac{1}{3}\frac{\sigma_{\varphi\varphi}}{r}\left(\frac{\partial v_\varphi}{\partial\varphi}+v_r\right)\Bigg)\Bigg]. \qquad \text{(B.20)}
\end{aligned}
$$

B.3.3 m

The quantity $\mathbf{m}$ represents a symmetric and trace–free tensor of rank–3 [Eq. (4.24)],

$$
\mathbf{m} = \mathsf{C}\,\frac{\mu}{p}\left(\theta\,\langle\operatorname{grad}\boldsymbol{\sigma}\rangle-\frac{\theta}{\rho}\,\langle\boldsymbol{\sigma}\operatorname{grad}\rho\rangle+\frac{4}{5}\,\langle\mathbf{q}\operatorname{grad}\mathbf{v}\rangle\right). \qquad \text{(B.21)}
$$

Owing to symmetry it requires to obtain expressions only for $\{m_{rrr}, m_{rr\varphi}, m_{rrz}, m_{r\varphi\varphi}, m_{r\varphi z}, m_{rzz}, m_{\varphi\varphi\varphi}, m_{\varphi\varphi z}, m_{\varphi zz}, m_{zzz}\}$, where due to the trace–free property

$$m_{rrr} + m_{r\varphi\varphi} + m_{rzz} = m_{rr\varphi} + m_{\varphi\varphi\varphi} + m_{\varphi zz} = m_{rrz} + m_{\varphi\varphi z} + m_{zzz} = 0. \tag{B.22}$$

Equation for m_{rrr}

$$\begin{aligned} m_{rrr} = \mathsf{C}\,\frac{\mu}{p}\Bigg[&\frac{3}{5}\theta\frac{\partial\sigma_{rr}}{\partial r} - \frac{2}{5}\theta\left(\frac{1}{r}\frac{\partial\sigma_{r\varphi}}{\partial\varphi} + \frac{\sigma_{rr}-\sigma_{\varphi\varphi}}{r} + \frac{\partial\sigma_{rz}}{\partial z}\right) - \frac{\theta}{\rho}\left(\frac{3}{5}\sigma_{rr}\frac{\partial\rho}{\partial r} - \frac{2}{5}\frac{\sigma_{r\varphi}}{r}\frac{\partial\rho}{\partial\varphi}\right. \\ &\left. -\frac{2}{5}\sigma_{rz}\frac{\partial\rho}{\partial z}\right) + \frac{4}{5}\left(\frac{2}{5}q_r\frac{\partial v_r}{\partial r} - \frac{1}{5}\left(\frac{q_r}{r}\left(\frac{\partial v_\varphi}{\partial\varphi} + v_r\right) + q_r\frac{\partial v_z}{\partial z} + q_\varphi\frac{\partial v_\varphi}{\partial r}\right.\right. \\ &\left.\left. +\frac{q_\varphi}{r}\left(\frac{\partial v_r}{\partial\varphi} - v_\varphi\right) + q_z\frac{\partial v_z}{\partial r} + q_z\frac{\partial v_r}{\partial z}\right)\right)\Bigg], \end{aligned} \tag{B.23}$$

where for axial flows $\sigma_{\varphi\varphi} = -\sigma_{rr} - \sigma_{zz}$ must be replaced in the above equation.

Equation for $m_{rr\varphi}$

$$\begin{aligned} m_{rr\varphi} = \mathsf{C}\,\frac{\mu}{p}\Bigg[&\frac{1}{3}\theta\left(\frac{1}{r}\frac{\partial\sigma_{rr}}{\partial\varphi} - 2\frac{\sigma_{r\varphi}}{r}\right) - \frac{2}{15}\theta\left(\frac{1}{r}\frac{\partial\sigma_{\varphi\varphi}}{\partial\varphi} - 4\frac{\partial\sigma_{r\varphi}}{\partial r} + \frac{2\sigma_{r\varphi}}{r} + \frac{\partial\sigma_{\varphi z}}{\partial z}\right) - \frac{1}{3}\frac{\theta\sigma_{rr}}{\rho r}\frac{\partial\rho}{\partial\varphi} \\ &+ \frac{2}{15}\frac{\theta}{\rho}\left(\frac{\sigma_{\varphi\varphi}}{r}\frac{\partial\rho}{\partial\varphi} - 4\sigma_{r\varphi}\frac{\partial\rho}{\partial r} + \sigma_{\varphi z}\frac{\partial\rho}{\partial z}\right) + \frac{16}{75}\left(\frac{q_r}{r}\left(\frac{\partial v_r}{\partial\varphi} - v_\varphi\right) + q_\varphi\frac{\partial v_r}{\partial r}\right. \\ &\left. +q_r\frac{\partial v_\varphi}{\partial r}\right) - \frac{4}{75}\left(3\frac{q_\varphi}{r}\left(\frac{\partial v_\varphi}{\partial\varphi} + v_r\right) + q_\varphi\frac{\partial v_z}{\partial z} + \frac{q_z}{r}\frac{\partial v_z}{\partial\varphi} + q_z\frac{\partial v_\varphi}{\partial z}\right)\Bigg]. \end{aligned} \tag{B.24}$$

Equation for m_{rrz}

$$\begin{aligned} m_{rrz} = \mathsf{C}\,\frac{\mu}{p}\Bigg[&\frac{1}{3}\theta\frac{\partial\sigma_{rr}}{\partial z} - \frac{2}{15}\theta\left(\frac{\sigma_{rz}}{r} - 4\frac{\partial\sigma_{rz}}{\partial r} + \frac{1}{r}\frac{\partial\sigma_{\varphi z}}{\partial\varphi} + \frac{\partial\sigma_{zz}}{\partial z}\right) - \frac{1}{3}\frac{\theta\sigma_{rr}}{\rho}\frac{\partial\rho}{\partial z} + \frac{2}{15}\frac{\theta}{\rho}\left(\frac{\sigma_{\varphi z}}{r}\frac{\partial\rho}{\partial\varphi}\right. \\ &\left. -4\sigma_{rz}\frac{\partial\rho}{\partial r} + \sigma_{zz}\frac{\partial\rho}{\partial z}\right) + \frac{16}{75}\left(q_r\frac{\partial v_r}{\partial z} + q_z\frac{\partial v_r}{\partial r} + q_r\frac{\partial v_z}{\partial r}\right) - \frac{4}{75}\left(q_\varphi\frac{\partial v_\varphi}{\partial z}\right. \\ &\left. +\frac{q_\varphi}{r}\frac{\partial v_z}{\partial\varphi} + \frac{q_z}{r}\left(\frac{\partial v_\varphi}{\partial\varphi} + v_r\right) + 3q_z\frac{\partial v_z}{\partial z}\right)\Bigg]. \end{aligned} \tag{B.25}$$

Equation for $m_{r\varphi\varphi}$

$$\begin{aligned} m_{r\varphi\varphi} = \mathsf{C}\,\frac{\mu}{p}\Bigg[&\frac{1}{3}\theta\frac{\partial\sigma_{\varphi\varphi}}{\partial r} - \frac{2}{15}\theta\left(\frac{\partial\sigma_{rr}}{\partial r} - 4\left(\frac{1}{r}\frac{\partial\sigma_{r\varphi}}{\partial\varphi} + \frac{\sigma_{rr}-\sigma_{\varphi\varphi}}{r}\right) + \frac{\partial\sigma_{rz}}{\partial z}\right) - \frac{1}{3}\frac{\theta\sigma_{\varphi\varphi}}{\rho}\frac{\partial\rho}{\partial r} \\ &+ \frac{2}{15}\frac{\theta}{\rho}\left(\sigma_{rr}\frac{\partial\rho}{\partial r} - 4\frac{\sigma_{r\varphi}}{r}\frac{\partial\rho}{\partial\varphi} + \sigma_{rz}\frac{\partial\rho}{\partial z}\right) + \frac{16}{75}\left(\frac{q_r}{r}\left(\frac{\partial v_\varphi}{\partial\varphi} + v_r\right) + q_\varphi\frac{\partial v_\varphi}{\partial r}\right. \\ &\left. +\frac{q_\varphi}{r}\left(\frac{\partial v_r}{\partial\varphi} - v_\varphi\right)\right) - \frac{4}{75}\left(3q_r\frac{\partial v_r}{\partial r} + q_r\frac{\partial v_z}{\partial z} + q_z\frac{\partial v_r}{\partial z} + q_z\frac{\partial v_z}{\partial r}\right)\Bigg], \end{aligned} \tag{B.26}$$

where for axial flows $\sigma_{\varphi\varphi} = -\sigma_{rr} - \sigma_{zz}$ must be replaced in the above equation.

Equation for $m_{r\varphi z}$

$$\begin{aligned} m_{r\varphi z} = \mathsf{C}\,\frac{\mu}{p}\Bigg[&\frac{1}{3}\theta\left(\frac{\partial\sigma_{r\varphi}}{\partial z}+\frac{\partial\sigma_{\varphi z}}{\partial r}+\frac{1}{r}\frac{\partial\sigma_{rz}}{\partial\varphi}-\frac{\sigma_{\varphi z}}{r}\right)-\frac{1}{3}\frac{\theta}{\rho}\left(\sigma_{r\varphi}\frac{\partial\rho}{\partial z}+\frac{\sigma_{rz}}{r}\frac{\partial\rho}{\partial\varphi}+\sigma_{\varphi z}\frac{\partial\rho}{\partial r}\right)\\ &+\frac{4}{15}\left(q_r\frac{\partial v_\varphi}{\partial z}+\frac{q_z}{r}\left(\frac{\partial v_r}{\partial\varphi}-v_\varphi\right)+q_\varphi\frac{\partial v_z}{\partial r}\right)\Bigg]. \end{aligned} \tag{B.27}$$

Equation for m_{rzz}

$$\begin{aligned} m_{rzz} = \mathsf{C}\,\frac{\mu}{p}\Bigg[&\frac{1}{3}\theta\frac{\partial\sigma_{zz}}{\partial r}-\frac{2}{15}\theta\left(\frac{\partial\sigma_{rr}}{\partial r}+\frac{1}{r}\frac{\partial\sigma_{r\varphi}}{\partial\varphi}+\frac{\sigma_{rr}-\sigma_{\varphi\varphi}}{r}-4\frac{\partial\sigma_{rz}}{\partial z}\right)-\frac{1}{3}\frac{\theta\sigma_{zz}}{\rho}\frac{\partial\rho}{\partial r}\\ &+\frac{2}{15}\frac{\theta}{\rho}\left(\sigma_{rr}\frac{\partial\rho}{\partial r}+\frac{\sigma_{r\varphi}}{r}\frac{\partial\rho}{\partial\varphi}-4\sigma_{rz}\frac{\partial\rho}{\partial z}\right)+\frac{16}{75}\left(q_r\frac{\partial v_z}{\partial z}+q_z\frac{\partial v_r}{\partial z}+q_z\frac{\partial v_z}{\partial r}\right)\\ &-\frac{4}{75}\left(3q_r\frac{\partial v_r}{\partial r}+\frac{q_r}{r}\left(\frac{\partial v_\varphi}{\partial\varphi}+v_r\right)+\frac{q_\varphi}{r}\left(\frac{\partial v_r}{\partial\varphi}-v_\varphi\right)+q_\varphi\frac{\partial v_\varphi}{\partial r}\right)\Bigg], \end{aligned} \tag{B.28}$$

where for axial flows $\sigma_{\varphi\varphi} = -\sigma_{rr} - \sigma_{zz}$ must be replaced in the above equation.

Equation for $m_{\varphi\varphi\varphi}$

$$\begin{aligned} m_{\varphi\varphi\varphi} = \mathsf{C}\,\frac{\mu}{p}\Bigg[&\frac{3}{5}\theta\left(\frac{1}{r}\frac{\partial\sigma_{\varphi\varphi}}{\partial\varphi}+\frac{2\sigma_{r\varphi}}{r}\right)-\frac{2}{5}\theta\left(\frac{\partial\sigma_{r\varphi}}{\partial r}+\frac{\partial\sigma_{\varphi z}}{\partial z}\right)+\frac{2}{5}\frac{\theta}{\rho}\left(\sigma_{r\varphi}\frac{\partial\rho}{\partial r}+\sigma_{\varphi z}\frac{\partial\rho}{\partial z}\right)\\ &-\frac{3}{5}\frac{\theta\sigma_{\varphi\varphi}}{\rho r}\frac{\partial\rho}{\partial\varphi}+\frac{8}{25}\frac{q_\varphi}{r}\left(\frac{\partial v_\varphi}{\partial\varphi}+v_r\right)-\frac{4}{25}\left(\frac{q_r}{r}\left(\frac{\partial v_r}{\partial\varphi}-v_\varphi\right)+q_r\frac{\partial v_\varphi}{\partial r}\right.\\ &\left.+q_\varphi\frac{\partial v_r}{\partial r}+q_\varphi\frac{\partial v_z}{\partial z}+\frac{q_z}{r}\frac{\partial v_z}{\partial\varphi}+q_z\frac{\partial v_\varphi}{\partial z}\right)\Bigg]. \end{aligned} \tag{B.29}$$

Equation for $m_{\varphi\varphi z}$

$$\begin{aligned} m_{\varphi\varphi z} = \mathsf{C}\,\frac{\mu}{p}\Bigg[&\frac{1}{3}\theta\frac{\partial\sigma_{\varphi\varphi}}{\partial z}-\frac{2}{15}\theta\left(\frac{\partial\sigma_{rz}}{\partial r}-4\left(\frac{1}{r}\frac{\partial\sigma_{\varphi z}}{\partial\varphi}+\frac{\sigma_{rz}}{r}\right)+\frac{\partial\sigma_{zz}}{\partial z}\right)-\frac{1}{3}\frac{\theta\sigma_{\varphi\varphi}}{\rho}\frac{\partial\rho}{\partial z}\\ &+\frac{2}{15}\frac{\theta}{\rho}\left(\sigma_{rz}\frac{\partial\rho}{\partial r}-4\frac{\sigma_{\varphi z}}{r}\frac{\partial\rho}{\partial\varphi}+\sigma_{zz}\frac{\partial\rho}{\partial z}\right)+\frac{16}{75}\left(q_\varphi\frac{\partial v_\varphi}{\partial z}+\frac{q_\varphi}{r}\frac{\partial v_z}{\partial\varphi}\right.\\ &\left.+\frac{q_z}{r}\left(\frac{\partial v_\varphi}{\partial\varphi}+v_r\right)\right)-\frac{4}{75}\left(q_r\frac{\partial v_r}{\partial z}+q_r\frac{\partial v_z}{\partial r}+q_z\frac{\partial v_r}{\partial r}+3q_z\frac{\partial v_z}{\partial z}\right)\Bigg]. \end{aligned} \tag{B.30}$$

Equation for $m_{\varphi zz}$

$$\begin{aligned} m_{\varphi zz} = \mathsf{C}\,\frac{\mu}{p}\Bigg[& \frac{1}{3}\frac{\theta}{r}\frac{\partial \sigma_{zz}}{\partial \varphi} - \frac{2}{15}\theta\left(\frac{\partial \sigma_{r\varphi}}{\partial r} + \frac{1}{r}\frac{\partial \sigma_{\varphi\varphi}}{\partial \varphi} + \frac{2\sigma_{r\varphi}}{r} - 4\frac{\partial \sigma_{\varphi z}}{\partial z}\right) - \frac{1}{3}\frac{\theta \sigma_{zz}}{\rho r}\frac{\partial \rho}{\partial \varphi} \\ & + \frac{2}{15}\frac{\theta}{\rho}\left(\sigma_{r\varphi}\frac{\partial \rho}{\partial r} + \frac{\sigma_{\varphi\varphi}}{r}\frac{\partial \rho}{\partial \varphi} - 4\sigma_{\varphi z}\frac{\partial \rho}{\partial z}\right) + \frac{16}{75}\left(q_\varphi \frac{\partial v_z}{\partial z} + q_z \frac{\partial v_\varphi}{\partial z} + \frac{q_z}{r}\frac{\partial v_z}{\partial \varphi}\right) \\ & - \frac{4}{75}\left(\frac{q_r}{r}\left(\frac{\partial v_r}{\partial \varphi} - v_\varphi\right) + q_r \frac{\partial v_\varphi}{\partial r} + q_\varphi \frac{\partial v_r}{\partial r} + 3\frac{q_\varphi}{r}\left(\frac{\partial v_\varphi}{\partial \varphi} + v_r\right)\right)\Bigg] . \end{aligned} \tag{B.31}$$

Equation for m_{zzz}

$$\begin{aligned} m_{zzz} = \mathsf{C}\,\frac{\mu}{p}\Bigg[& \frac{3}{5}\theta\frac{\partial \sigma_{zz}}{\partial z} - \frac{2}{5}\theta\left(\frac{\partial \sigma_{rz}}{\partial r} + \frac{1}{r}\frac{\partial \sigma_{\varphi z}}{\partial \varphi} + \frac{\sigma_{rz}}{r}\right) + \frac{2}{5}\frac{\theta}{\rho}\left(\sigma_{rz}\frac{\partial \rho}{\partial r} + \frac{\sigma_{\varphi z}}{r}\frac{\partial \rho}{\partial \varphi}\right) \\ & - \frac{3}{5}\frac{\theta \sigma_{zz}}{\rho}\frac{\partial \rho}{\partial z} + \frac{8}{25} q_z \frac{\partial v_z}{\partial z} - \frac{4}{25}\Bigg(q_r \frac{\partial v_r}{\partial z} + q_r \frac{\partial v_z}{\partial r} + q_\varphi \frac{\partial v_\varphi}{\partial z} \\ & + \frac{q_\varphi}{r}\frac{\partial v_z}{\partial \varphi} + q_z \frac{\partial v_r}{\partial r} + \frac{q_z}{r}\left(\frac{\partial v_\varphi}{\partial \varphi} + v_r\right)\Bigg)\Bigg] . \end{aligned} \tag{B.32}$$

Appendix C

Second–order Velocity Slip and Temperature Jump Conditions

Velocity slip and temperature jump boundary conditions can extend the range of applicability of the Navier–Stokes–Fourier equations around, and in some cases beyond $\mathrm{Kn} \cong 0.1$. Due to simplicity and relatively low cost of Navier–Stokes–Fourier simulations, compared to molecular and extended macroscopic simulations, accurate slip and jump models are very desirable [46].

In this appendix, first– and second–order velocity slip and temperature jump conditions for curved and flat walls are deduced from the R13 boundary conditions, which are of third–order. These conditions are obtained for both hard–sphere and BGK kinetic models.

As shown in Fig. C.1, we assume a curved wall where at any arbitrary azimuthal position φ, the local curvature is $\varsigma\left(\varphi\right)$ and the radius of curvature is $r\left(\varphi\right) = 1/\varsigma\left(\varphi\right)$. Accordingly, the curvature of a plane wall is identically zero, and the curvature of a circle of radius r is a constant, i.e., it does not depend on φ.

In the following sections, slip and jump models for pure rotary, and pure axial flows over curved surfaces (with constant curvature) are derived. These boundary conditions are discussed for different processes, namely, Couette, Poiseuille, and thermal–creep (transpiration) flows. Moreover, by using the asymptotic condition $r \to \infty$, these boundary conditions are adapted to flows in slab geometry.

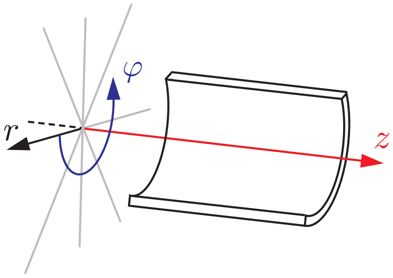

Figure C.1: Schematic presentation of a small segment of a curved surface. The surface is exposed to a gas flow, and, since it is impermeable, $v_r = 0$. In rotary and axial flows we assume $v_z = 0$ and $v_\varphi = 0$, respectively.

C.1 Second–order Slip and Jump Conditions for Rotary Flows

For rotary flows, where φ and r denote azimuthal (tangential) and radial (normal) directions [see Fig. C.1], expressions for slip velocity $\mathcal{V}_\varphi = v_\varphi - v_\varphi^W$, and temperature jump $\mathcal{T} = \theta - \theta_W$, in Eqs. (5.37) and (5.38) read

$$\mathcal{V}_\varphi = \underline{-\frac{2-\chi}{\chi}\sqrt{\frac{\pi\theta}{2}}\frac{\sigma_{r\varphi}}{\mathcal{P}}n_r - \frac{1}{5}\frac{q_\varphi}{\mathcal{P}}} - \frac{1}{2}\frac{m_{rr\varphi}}{\mathcal{P}}, \tag{C.1}$$

and

$$\mathcal{T} = \underline{-\frac{2-\chi}{\chi}\sqrt{\frac{\pi\theta}{2}}\frac{q_r}{2\mathcal{P}}n_r} + \frac{1}{4}\mathcal{V}^2 - \frac{1}{4}\frac{\theta\sigma_{rr}}{\mathcal{P}} - \frac{1}{30}\frac{\mathit{\Delta}}{\mathcal{P}} - \frac{5}{56}\frac{R_{rr}}{\mathcal{P}}. \tag{C.2}$$

The underlined terms correspond to the well–known first–order slip velocity and temperature jump conditions [106], where $\sigma_{r\varphi}$ and q_r require the NSF constitutive relations [Eqs. (9.6) and (9.12)], and $\mathcal{P}^{\mathrm{NSF}} = p$.

We now expand these boundary conditions in the Knudsen number, Kn. Density, temperature, and velocity are equilibrium quantities and are not expanded, since they are of zeroth–order. Heat flux and shear stress are first–order quantities,

$$q_r = \mathrm{Kn}\ \mathring{q}_r, \qquad q_\varphi = \mathrm{Kn}\ \mathring{q}_\varphi, \qquad \sigma_{r\varphi} = \mathrm{Kn}\ \mathring{\sigma}_{r\varphi}, \tag{C.3}$$

while second–order quantities are

$$\begin{gathered} q_\varphi = \mathrm{Kn}^2\ \mathring{q}_\varphi, \qquad \sigma_{rr} = \mathrm{Kn}^2\ \mathring{\sigma}_{rr}, \qquad \sigma_{\varphi\varphi} = \mathrm{Kn}^2\ \mathring{\sigma}_{\varphi\varphi}, \qquad \mathit{\Delta} = \mathrm{Kn}^2\ \mathring{\mathit{\Delta}}, \\ R_{rr} = \mathrm{Kn}^2\ \mathring{R}_{rr}, \qquad R_{\varphi\varphi} = \mathrm{Kn}^2\ \mathring{R}_{\varphi\varphi}, \qquad m_{rr\varphi} = \mathrm{Kn}^2\ \mathring{m}_{rr\varphi}, \qquad m_{\varphi\varphi\varphi} = \mathrm{Kn}^2\ \mathring{m}_{\varphi\varphi\varphi}. \end{gathered} \tag{C.4}$$

Note that the azimuthal heat flux q_φ is of first–order in thermally–driven flow, and second–order in shear–driven and force–driven flows. The remaining quantities, which promote the R13 boundary conditions to be of third–order, are

$$R_{r\varphi} = \mathrm{Kn}^3 \ \mathring{R}_{r\varphi}, \qquad m_{rrr} = \mathrm{Kn}^3 \ \mathring{m}_{rrr}, \qquad m_{r\varphi\varphi} = \mathrm{Kn}^3 \ \mathring{m}_{r\varphi\varphi}. \tag{C.5}$$

For the expansions, all moments in (C.3)–(C.5) are scaled as $M = \mathrm{Kn}^\alpha \mathring{M}$, where the rescaled moment $\mathring{M}$ is of order unity and α is the order of the moment M.

Replacement of the scaled moments into the extended balance equations (4.20)–(4.24) allows to identify their second–order terms. Accordingly, normal heat flux and shear stress balance reduce to the Fourier and Navier–Stokes laws

$$\mathring{q}_r = -\frac{5}{2}\frac{\mu}{\mathrm{Pr}}\frac{\partial\theta}{\partial r}, \qquad \mathring{q}_\varphi = -\frac{5}{2}\frac{\mu}{\mathrm{Pr}}\frac{1}{r}\frac{\partial\theta}{\partial\varphi}, \qquad \mathring{\sigma}_{r\varphi} = -\mu\left(\frac{\partial v_\varphi}{\partial r} - \frac{v_\varphi}{r}\right), \tag{C.6}$$

and the required second–order moments read

$$\mathring{q}_\varphi = \frac{7}{5}\left(1+\frac{1}{\mathrm{Pr}}\right)\frac{\mathring{\sigma}_{r\varphi}\mathring{q}_r}{p} - \frac{\mu}{\rho\,\mathrm{Pr}}\left(\frac{\partial\mathring{\sigma}_{r\varphi}}{\partial r} + 2\frac{\mathring{\sigma}_{r\varphi}}{r}\right) + \frac{\mu}{p\,\mathrm{Pr}}\left(v_\varphi\mathring{\sigma}_{r\varphi} - 2\mathring{q}_r\right)\frac{v_\varphi}{r}, \tag{C.7}$$

$$\mathring{\sigma}_{rr} = 4\frac{\mu}{p}\left(\frac{v_\varphi\mathring{\sigma}_{r\varphi}}{r} + \frac{1}{5}\frac{\mathring{q}_r}{r}\right) - \frac{6}{5}\frac{\mathring{\sigma}_{r\varphi}^2}{p}, \tag{C.8}$$

$$\mathring{\sigma}_{\varphi\varphi} = -4\frac{\mu}{p}\left(\frac{v_\varphi\mathring{\sigma}_{r\varphi}}{r} + \frac{1}{5}\frac{\mathring{q}_r}{r}\right) + \frac{8}{5}\frac{\mathring{\sigma}_{r\varphi}^2}{p}, \tag{C.9}$$

$$\mathring{\varDelta} = \frac{\mathsf{A}_2\,\mu}{\rho}\left(\frac{\partial\mathring{q}_r}{\partial r} + \frac{\mathring{q}_r}{r}\right) - \frac{7\,\mathrm{Pr}\,\mathsf{A}_2}{5}\frac{\mathring{q}_r^2}{p} + \left(2\mathsf{A}_1 - \mathsf{A}_2\right)\frac{\mathring{\sigma}_{r\varphi}^2}{\rho} - \frac{\mathsf{A}_2\,\mu}{p}\frac{\mathring{q}_r v_\varphi^2}{r}, \tag{C.10}$$

$$\mathring{R}_{rr} = \frac{\mathsf{B}_2}{3}\frac{\mu}{\rho}\left(2\frac{\partial\mathring{q}_r}{\partial r} - \frac{\mathring{q}_r}{r}\right) - \frac{8\,\mathrm{Pr}\,\mathsf{B}_2}{15}\frac{\mathring{q}_r^2}{p} + \left(\frac{\mathsf{B}_1}{3} - \frac{5\,\mathsf{B}_2}{21}\right)\frac{\mathring{\sigma}_{r\varphi}^2}{\rho} - \frac{2\,\mathsf{B}_2}{3}\frac{\mu}{p}\frac{\mathring{q}_r v_\varphi^2}{r}, \tag{C.11}$$

$$\mathring{m}_{rr\varphi} = \frac{2\,\mathsf{C}}{15}\frac{\mu}{\rho}\left(4\frac{\partial\mathring{\sigma}_{r\varphi}}{\partial r} - 7\frac{\mathring{\sigma}_{r\varphi}}{r}\right) - \frac{16\,\mathsf{C}\,(1+\mathrm{Pr})}{75}\frac{\mathring{\sigma}_{r\varphi}\mathring{q}_r}{p} - \frac{8\,\mathsf{C}}{15}\frac{\mu}{\rho}\frac{v_\varphi^2\mathring{\sigma}_{r\varphi}}{r}. \tag{C.12}$$

To obtain second–order corrections to slip and jump conditions, the third–order corrections in Eq. (C.5) are dropped.

Subsequent substitution of Eqs. (C.7)–(C.12) into Eq. (C.4) and then into Eqs. (C.1) and (C.2) gives the second–order slip and jump conditions as

$$\begin{aligned}\mathcal{V}_\varphi^{\mathrm{NSF}} &= \underline{-\frac{2-\chi}{\chi}\sqrt{\frac{\pi\theta}{2}}\frac{\sigma_{r\varphi}^{\mathrm{NSF}}}{p}n_r - \frac{1}{5}\frac{q_\varphi^{\mathrm{NSF}}}{p}} + \left[\frac{8\,\mathsf{C}}{75}\left(1+\mathrm{Pr}\right) - \frac{7}{25}\left(1+\frac{1}{\mathrm{Pr}}\right)\right]\frac{q_r^{\mathrm{NSF}}\sigma_{r\varphi}^{\mathrm{NSF}}}{p^2}\\ &\quad + \frac{\mu\theta}{p^2}\left[\left(\frac{1}{5\,\mathrm{Pr}} - \frac{4\,\mathsf{C}}{15}\right)\frac{\partial\sigma_{r\varphi}^{\mathrm{NSF}}}{\partial r} + \left(\frac{2}{5\,\mathrm{Pr}} + \frac{7\,\mathsf{C}}{15}\right)\frac{\sigma_{r\varphi}^{\mathrm{NSF}}}{r}\right]\\ &\quad + \frac{\mu}{p^2}\left[\frac{2}{5\,\mathrm{Pr}}q_r^{\mathrm{NSF}} + \left(\frac{4\,\mathsf{C}}{15} - \frac{1}{5\,\mathrm{Pr}}\right)v_\varphi\sigma_{r\varphi}^{\mathrm{NSF}}\right]\frac{v_\varphi}{r}. \end{aligned} \tag{C.13}$$

and

$$\begin{aligned}\mathcal{T}^{\mathrm{NSF}} &= \underline{-\frac{2-\chi}{\chi}\sqrt{\frac{\pi\theta}{2}}\frac{q_r^{\mathrm{NSF}}}{2p}n_r} + \frac{1}{10}\frac{2-\chi}{\chi}\sqrt{\frac{\pi\theta}{2}}\frac{q_\varphi^{\mathrm{NSF}}\sigma_{r\varphi}^{\mathrm{NSF}}}{p^2}n_r + \mathrm{Pr}\left(\frac{7\,\mathsf{A}_2}{150} + \frac{\mathsf{B}_2}{21}\right)\left(\frac{q_r^{\mathrm{NSF}}}{p}\right)^2\\ &\quad + \left(\frac{q_\varphi^{\mathrm{NSF}}}{10p}\right)^2 + \theta\left[\left(\frac{2-\chi}{\chi}\right)^2\frac{\pi}{8} + \frac{3}{10} - \frac{\mathsf{A}_1}{15} + \frac{\mathsf{A}_2}{30} - \frac{5\,\mathsf{B}_1}{168} + \frac{25\,\mathsf{B}_2}{1176}\right]\left(\frac{\sigma_{r\varphi}^{\mathrm{NSF}}}{p}\right)^2\\ &\quad + \frac{\mu\theta}{p^2}\left[\left(\frac{5\,\mathsf{B}_2}{168} - \frac{1}{5} - \frac{\mathsf{A}_2}{30}\right)\frac{q_r^{\mathrm{NSF}}}{r} - \left(\frac{\mathsf{A}_2}{30} + \frac{5\,\mathsf{B}_2}{84}\right)\frac{\partial q_r^{\mathrm{NSF}}}{\partial r}\right]\\ &\quad + \frac{\mu}{p^2}\left[\left(\frac{\mathsf{A}_2}{30} + \frac{5\,\mathsf{B}_2}{84}\right)v_\varphi q_r^{\mathrm{NSF}} - \theta\sigma_{r\varphi}^{\mathrm{NSF}}\right]\frac{v_\varphi}{r}. \end{aligned} \tag{C.14}$$

The underlined terms indicate the first–order slip velocity and temperature jump contributions, while the rest are second–order corrections. The terms that include q_φ^{NSF} are applicable only for thermal transpiration flow, since they account for azimuthal temperature gradients. Depending on the considered kinetic model constants $\{\mathrm{Pr}, \mathsf{A_i}, \mathsf{B_i}, \mathsf{C}\}$ must be replaced from either (4.15) or (4.16).

C.2 Second–order Slip and Jump Conditions for Axial Flows in Tubes

For axial flows in tubes, where z and r denote axial (tangential) and radial (normal) directions [see Fig. C.1], the expressions for slip velocity, $\mathcal{V}_z = v_z - v_z^W$ and temperature jump, $\mathcal{T} = \theta - \theta_W$ in Eqs. (5.37) and (5.38) read

$$\mathcal{V}_z = \underline{-\frac{2-\chi}{\chi}\sqrt{\frac{\pi\theta}{2}}\frac{\sigma_{rz}}{\mathcal{P}}n_r - \frac{1}{5}\frac{q_z}{\mathcal{P}}} - \frac{1}{2}\frac{m_{rrz}}{\mathcal{P}}, \tag{C.15}$$

and

$$\mathcal{T} = \underline{-\frac{2-\chi}{\chi}\sqrt{\frac{\pi\theta}{2}}\frac{q_r}{2\mathcal{P}}n_r} + \frac{1}{4}\mathcal{V}^2 - \frac{1}{4}\frac{\theta\sigma_{rr}}{\mathcal{P}} - \frac{1}{30}\frac{\varDelta}{\mathcal{P}} - \frac{5}{56}\frac{R_{rr}}{\mathcal{P}}. \tag{C.16}$$

The underlined terms denote the first–order slip velocity and temperature jump conditions [106], where σ_{rz} and q_r must be replaced by the NSF relations, and $\mathcal{P}^{\mathrm{NSF}} = p$.

Again, density, temperature, and velocity are equilibrium quantities and are not expanded, since they are of zeroth–order. Fourier heat flux and shear stress are first–order quantities

$$q_r = \mathrm{Kn}\ \mathring{q}_r, \qquad q_z = \mathrm{Kn}\ \mathring{q}_z, \qquad \sigma_{rz} = \mathrm{Kn}\ \mathring{\sigma}_{rz}, \tag{C.17}$$

while second–order quantities are

$$\begin{gathered} q_z = \mathrm{Kn}^2\ \mathring{q}_z, \qquad \sigma_{rr} = \mathrm{Kn}^2\ \mathring{\sigma}_{rr}, \qquad \sigma_{zz} = \mathrm{Kn}^2\ \mathring{\sigma}_{zz}, \qquad \mathit{\Delta} = \mathrm{Kn}^2\ \mathring{\mathit{\Delta}}, \\ R_{rr} = \mathrm{Kn}^2\ \mathring{R}_{rr}, \qquad R_{zz} = \mathrm{Kn}^2\ \mathring{R}_{zz}, \qquad m_{rrz} = \mathrm{Kn}^2\ \mathring{m}_{rrz}, \qquad m_{\varphi\varphi z} = \mathrm{Kn}^2\ \mathring{m}_{\varphi\varphi z}. \end{gathered} \tag{C.18}$$

Note that the axial heat flux q_z is of first–order in transpiration flow, and second–order for Poiseuille flow. The remaining quantities, which promote the R13 boundary conditions to be of third–order, are

$$R_{rz} = \mathrm{Kn}^3\ \mathring{R}_{rz}, \qquad m_{rrr} = \mathrm{Kn}^3\ \mathring{m}_{rrr}, \qquad m_{r\varphi\varphi} = \mathrm{Kn}^3\ \mathring{m}_{r\varphi\varphi}, \qquad m_{rzz} = \mathrm{Kn}^3\ \mathring{m}_{rzz}. \tag{C.19}$$

The moments in (C.17)–(C.19) are scaled as $M = \mathrm{Kn}^{\alpha}\mathring{M}$, where the rescaled moment $\mathring{M}$ is of order unity and α is the order of the moment M.

Replacement of the scaled moments into the extended balance equations (4.20)–(4.24) allows to identify their second–order terms. Accordingly, normal heat flux and shear stress balance reduce to the Fourier and Navier–Stokes laws

$$\mathring{q}_r = -\frac{5}{2}\frac{\mu}{\mathrm{Pr}}\frac{\partial\theta}{\partial r}, \qquad \mathring{q}_z = -\frac{5}{2}\frac{\mu}{\mathrm{Pr}}\frac{\partial\theta}{\partial z}, \qquad \mathring{\sigma}_{rz} = -\mu\frac{\partial v_z}{\partial r}, \tag{C.20}$$

and the required second–order moments read

$$\mathring{q}_z = \frac{7}{5}\left(1+\frac{1}{\mathrm{Pr}}\right)\frac{\mathring{\sigma}_{rz}\mathring{q}_r}{p} - \frac{\mu}{\rho\,\mathrm{Pr}}\left(\frac{\partial\mathring{\sigma}_{rz}}{\partial r}+\frac{\mathring{\sigma}_{rz}}{r}\right), \tag{C.21}$$

$$\mathring{\sigma}_{rr} = \frac{4}{5}\frac{\mu}{p}\frac{\mathring{q}_r}{r} - \frac{6}{5}\frac{\mathring{\sigma}_{rz}^2}{p}, \tag{C.22}$$

$$\mathring{\sigma}_{zz} = \frac{8}{5}\frac{\mathring{\sigma}_{rz}^2}{p}, \tag{C.23}$$

$$\mathring{\Delta} = \frac{\mathsf{A}_2\,\mu}{\rho}\left(\frac{\partial \mathring{q}_r}{\partial r} + \frac{\mathring{q}_r}{r}\right) - \frac{7\,\mathrm{Pr}\,\mathsf{A}_2}{5}\frac{\mathring{q}_r^2}{p} + (2\mathsf{A}_1 - \mathsf{A}_2)\,\frac{\mathring{\sigma}_{rz}^2}{\rho}, \tag{C.24}$$

$$\mathring{R}_{rr} = \frac{\mathsf{B}_2}{3}\frac{\mu}{\rho}\left(2\frac{\partial \mathring{q}_r}{\partial r} - \frac{\mathring{q}_r}{r}\right) - \frac{8\,\mathrm{Pr}\,\mathsf{B}_2}{15}\frac{\mathring{q}_r^2}{p} + \left(\frac{\mathsf{B}_1}{3} - \frac{5\,\mathsf{B}_2}{21}\right)\frac{\mathring{\sigma}_{rz}^2}{\rho}, \tag{C.25}$$

$$\mathring{m}_{rrz} = \frac{2\,\mathsf{C}}{15}\frac{\mu}{\rho}\left(4\frac{\partial \mathring{\sigma}_{rz}}{\partial r} - \frac{\mathring{\sigma}_{rz}}{r}\right) - \frac{16\,\mathsf{C}\,(1+\mathrm{Pr})}{75}\frac{\mathring{\sigma}_{rz}\mathring{q}_r}{p}. \tag{C.26}$$

To obtain second–order corrections to slip and jump conditions, the third–order corrections in Eq. (C.19) are dropped.

Subsequent substitution of Eqs. (C.21)–(C.26) into Eq. (C.18) and then into Eqs. (C.15) and (C.16) gives the second–order slip and jump conditions as

$$\begin{aligned}\mathcal{V}_z^{\mathrm{NSF}} ={}& \underline{-\frac{2-\chi}{\chi}\sqrt{\frac{\pi\theta}{2}}\frac{\sigma_{rz}^{\mathrm{NSF}}}{p}n_r - \frac{1}{5}\frac{q_z^{\mathrm{NSF}}}{p}} + \left[\frac{8\,\mathsf{C}}{75}(1+\mathrm{Pr}) - \frac{7}{25}\left(1+\frac{1}{\mathrm{Pr}}\right)\right]\frac{q_r^{\mathrm{NSF}}\sigma_{rz}^{\mathrm{NSF}}}{p^2}\\ &+ \frac{\mu\theta}{p^2}\left[\left(\frac{1}{5\,\mathrm{Pr}} - \frac{4\,\mathsf{C}}{15}\right)\frac{\partial\sigma_{rz}^{\mathrm{NSF}}}{\partial r} + \left(\frac{1}{5\,\mathrm{Pr}} + \frac{\mathsf{C}}{15}\right)\frac{\sigma_{rz}^{\mathrm{NSF}}}{r}\right].\end{aligned} \tag{C.27}$$

and

$$\begin{aligned}\mathcal{T}^{\mathrm{NSF}} ={}& \underline{-\frac{2-\chi}{\chi}\sqrt{\frac{\pi\theta}{2}}\frac{q_r^{\mathrm{NSF}}}{2p}n_r} + \frac{1}{10}\frac{2-\chi}{\chi}\sqrt{\frac{\pi\theta}{2}}\frac{q_z^{\mathrm{NSF}}\sigma_{rz}^{\mathrm{NSF}}}{p^2}n_r + \mathrm{Pr}\left(\frac{7\,\mathsf{A}_2}{150} + \frac{\mathsf{B}_2}{21}\right)\left(\frac{q_r^{\mathrm{NSF}}}{p}\right)^2\\ &+ \left(\frac{q_z^{\mathrm{NSF}}}{10p}\right)^2 + \theta\left[\left(\frac{2-\chi}{\chi}\right)^2\frac{\pi}{8} + \frac{3}{10} - \frac{\mathsf{A}_1}{15} + \frac{\mathsf{A}_2}{30} - \frac{5\,\mathsf{B}_1}{168} + \frac{25\,\mathsf{B}_2}{1176}\right]\left(\frac{\sigma_{rz}^{\mathrm{NSF}}}{p}\right)^2\\ &+ \frac{\mu\theta}{p^2}\left[\left(\frac{5\,\mathsf{B}_2}{168} - \frac{1}{5} - \frac{\mathsf{A}_2}{30}\right)\frac{q_r^{\mathrm{NSF}}}{r} - \left(\frac{\mathsf{A}_2}{30} + \frac{5\,\mathsf{B}_2}{84}\right)\frac{\partial q_r^{\mathrm{NSF}}}{\partial r}\right].\end{aligned} \tag{C.28}$$

The underlined terms indicate the first–order slip velocity and temperature jump contributions, while the rest are second–order corrections. The terms that include q_z^{NSF} are applicable only for axial thermal transpiration flow, since they account for axial temperature gradients. Depending on the considered kinetic model constants $\{\mathrm{Pr}, \mathsf{A}_\mathsf{i}, \mathsf{B}_\mathsf{i}, \mathsf{C}\}$ must be replaced from either (4.15) or (4.16).

C.3 Second–order Slip and Jump Conditions for Planar Flows

Since for flat surfaces curvature is zero, $\varsigma = r^{-1} = 0$, then, second–order slip and jump conditions in planar geometry can be obtained from Eqs. (C.13) and (C.14) (or Eqs. (C.27) and (C.28)) in the limit of $r \to \infty$, i.e.,

$$\begin{aligned}\mathcal{V}_t = {} & \underline{-\frac{2-\chi}{\chi}\sqrt{\frac{\pi\theta}{2}}\frac{\sigma_{tn}^{\mathrm{NSF}}}{p}n - \frac{1}{5}\frac{q_t^{\mathrm{NSF}}}{p}} + \left[\frac{8\,\mathsf{C}}{75}\left(1+\mathrm{Pr}\right) - \frac{7}{25}\left(1+\frac{1}{\mathrm{Pr}}\right)\right]\frac{q_n^{\mathrm{NSF}}\sigma_{tn}^{\mathrm{NSF}}}{p^2} \\ & + \frac{\mu\theta}{p^2}\left(\frac{1}{5\,\mathrm{Pr}} - \frac{4\,\mathsf{C}}{15}\right)\frac{\partial \sigma_{tn}^{\mathrm{NSF}}}{\partial x_n},\end{aligned} \tag{C.29}$$

and

$$\begin{aligned}\mathcal{T} = {} & \underline{-\frac{2-\chi}{\chi}\sqrt{\frac{\pi\theta}{2}}\frac{q_n^{\mathrm{NSF}}}{2p}n} + \frac{1}{10}\frac{2-\chi}{\chi}\sqrt{\frac{\pi\theta}{2}}\frac{q_t^{\mathrm{NSF}}\sigma_{tn}^{\mathrm{NSF}}}{p^2}n + \mathrm{Pr}\left(\frac{7\,\mathsf{A}_2}{150} + \frac{\mathsf{B}_2}{21}\right)\left(\frac{q_n^{\mathrm{NSF}}}{p}\right)^2 \\ & + \left(\frac{q_t^{\mathrm{NSF}}}{10p}\right)^2 + \theta\left[\left(\frac{2-\chi}{\chi}\right)^2\frac{\pi}{8} + \frac{3}{10} - \frac{\mathsf{A}_1}{15} + \frac{\mathsf{A}_2}{30} - \frac{5\,\mathsf{B}_1}{168} + \frac{25\,\mathsf{B}_2}{1176}\right]\left(\frac{\sigma_{tn}^{\mathrm{NSF}}}{p}\right)^2 \\ & - \frac{\mu\theta}{p^2}\left(\frac{\mathsf{A}_2}{30} + \frac{5\,\mathsf{B}_2}{84}\right)\frac{\partial q_n^{\mathrm{NSF}}}{\partial x_n},\end{aligned} \tag{C.30}$$

where n and t denote normal and tangential directions with respect to the wall surface.

Bibliography

[1] M. Alaoui and A. Santos. Poiseuille flow driven by an external force. *Phys. Fluids A*, 4:1273, 1992.

[2] Darryl J. Alofs and George S. Springer. Rotating cylinder apparatus for rarefied gas flow studies. *Rev. Sci. Instruments*, 41:1161, 1970.

[3] Darryl J. Alofs and George S. Springer. Cylindrical Couette flow experiments in the transition regime. *Phys. Fluids*, 14:298, 1971.

[4] C. D. Andereck, S. S. Liu, and H. L. Swinney. Flow regimes in a circular Couette system with independently rotating cylinders. *J. Fluid Mech.*, 164:155, 1986.

[5] S. Ansumali, I. V. Karlin, S. Arcidiacono, A. Abbas, and N. I. Prasianakis. Hydrodynamics beyond Navier–Stokes: Exact solution to the lattice Boltzmann hierarchy. *Phys. Rev. Lett.*, 98:124502, 2007.

[6] K. Aoki, P. Degond, and L. Mieussens. Numerical simulations of rarefied gases in curved channels: Thermal creep, circulating flow, and pumping effect. *Commun. Comput. Phys.*, 6:919, 2009.

[7] K. Aoki, Sh. Takata, and T. Nakanishi. Poiseuille–type flow of a rarefied gas between two parallel plates driven by a uniform external force. *Phys. Rev. E*, 65:026315, 2002.

[8] K. Aoki, H. Yoshida, T. Nakanishi, and A. L. Garcia. Inverted velocity profile in the cylindrical Couette flow of a rarefied gas. *Phys. Rev. E*, 68:016302, 2003.

[9] E. B. Arkilic, M. A. Schmidt, and K. S. Breuer. Gaseous slip flow in long microchannels. *J. Microelectromechanical Systems*, 6:167, 1997.

[10] M. Bahrami, A. Tamayol, and P. Taheri. Slip–flow pressure drop in microchannels of general cross section. *J. Fluid Eng.*, 131:031201, 2009.

[11] P. Bahukudumbi, J. H. Park, and A. Beskok. A unified engineering model for steady and quasi–steady shear–driven gas microflows. *Microscale Thermophys. Eng.*, 7:291, 2003.

[12] A. Baranyai, D. J. Evans, and P. J. Daivis. Isothermal shear–induced heat flow. *Phys. Rev. A*, 46:7593, 1992.

[13] L. B. Barichello, M. Camargo, P. Rodrigues, and C. E. Siewert. Unified solutions to classical flow problems based on the BGK model. *J. Appl. Math. Phys. (ZAMP)*, 52:517, 2001.

[14] P. Bassanini, C. Cercignani, and F. Sernagiotto. Flow of a rarefied gas in a tube of annular section. *Phys. Fluids*, 9:1174, 1966.

[15] P. L. Bhatnagar and E. P. Gross M. Krook. A model for collision processes in gases. i. Small amplitude processes in charged and neutral one–component systems. *Phys. Rev.*, 94:511, 1954.

[16] G. A. Bird. Definition of mean free path for ideal gases. *Phys. Fluids*, 26:3222, 1983.

[17] G. A. Bird. *Molecular gas dynamics and the direct simulation of gas flows.* Oxford University Press, 1998.

[18] A. V. Bobylev. The Chapman–Enskog and Grad methods for solving the Boltzmann equation. *Soviet Phys. Dolk.*, 27:29, 1982.

[19] A. V. Bobylev. Instabilities in the Chapman–Enskog expansion and hyperbolic Burnett equations. *J. Stat. Phys.*, 124:371, 2006.

[20] G. Breyiannis, S. Varoutis, and D. Valougeorgis. Rarefied gas flow in concentric annular tube: Estimation of the Poiseuille number and the exact hydraulic diameter. *European J. Mechanics – B/Fluids*, 27:609, 2008.

[21] C. Cercignani. *Mathematical methods in kinetic theory.* Plenum Press, 1969.

[22] C. Cercignani. *Theory and application of the Boltzmann equation.* Scottish Academic Press, 1975.

[23] C. Cercignani and F. Sernagiotto. Cylindrical Poiseuille flow of rarefied gas. *Phys. Fluids*, 9:40, 1966.

[24] C. Cercignani and F. Sernagiotto. Cylindrical Couette flow of a rarefied gas. *Phys. Fluids*, 10:1200, 1967.

[25] S. Chapman and T. G. Cowling. *The mathematical theory of non–uniform gases.* Cambridge University Press, 1970.

[26] H. Chen, S. Chen, and W. H. Matthaeus. Recovery of the Navier–Stokes equations using a lattice–gas Boltzmann method. *Phys. Rev. A*, 45:R5339, 1992.

[27] S. L. Dixon. *Fluid mechanics and thermodynamics of turbomachinery.* Elsevier BH, Oxford, 1998.

[28] D. Einzel, P. Panzer, and M. Liu. Boundary condition for fluid flow: Curved or rough surfaces. *Phys. Rev. Lett.*, 64:2269, 1990.

[29] J. H. Ferziger. Flow of a rarefied gas through a cylindrical tube. *Phys. Fluids*, 10:1448, 1967.

[30] M. Gad–el–Hak. *The MEMS handbook:Iintroduction and fundamentals.*

[31] R. Gohar and H. Rahnejat. *Fundamentals of tribology.* Imperial College Press, London, 2008.

[32] H. Grad. On the kinetic theory of rarefied gases. *Commun. Pure Appl. Math.*, 2:331, 1949.

[33] H. Grad. *Principles of the kinetic theory of gases*, volume 12 of *Handbuch der Physik.* Springer, Berlin, 1958.

[34] S. R. De Groot and P. Mazur. *Non–equilibrium thermodynamics.* Dover, New York, 1984.

[35] X. Gu and D. R. Emerson. A computational strategy for the regularized 13 moment equations with enhanced wall–boundary conditions. *J. Comput. Phys.*, 225:263, 2007.

[36] X. Gu and D. R. Emerson. A high–order moment approach for capturing non–equilibrium phenomena in the transition regime. *J. Fluid Mech.*, 636:177, 2009.

[37] X. Gu, D. R. Emerson, and G. Tang. KramersŠ problem and the Knudsen minimum: a theoretical analysis using a linearized 26–moment approach. *Cont. Mech. Thermodyn.*, 21:345, 2009.

[38] X. Gu, D. R. Emerson, and G. Tang. Analysis of the slip coefficient and defect velocity in the Knudsen layer of a rarefied gas using the linearized moment equations. *Phys. Rev. E*, 81:016313, 2010.

[39] N. G. Hadjiconstantinou. Comment on Cercignani's second–order slip coefficient. *Phys. Fluids*, 15:2352, 2003.

[40] N. G. Hadjiconstantinou. Oscillatory shear–driven gas flow in the transition and free–molecular–flow regimes. *Phys. Fluids*, 17:100611, 2005.

[41] Y.–L. Han, E. P. Muntz, A. Alexeenko, and M. Young. Experimental and computational studies of temperature gradient–driven molecular transport in gas flows through nano/microscale channels. *Nano. Microscale Thermophys. Eng.*, 11:151, 2007.

[42] K. A. Hickey and S. K. Loyalka. Plane Poiseuille flow: Rigid sphere gas. *J. Vac. Sci. Technol. A*, 8:957, 1990.

[43] L. H. Holway. Kinetic theory of shock structure using an ellipsoidal distribution function. In *Rarefied Gas Dynamics, (Proceedings of the Fourth International Symposium, University of Toronto, 1964)*, volume I, page 193. Academic Press, New York, 1966.

[44] S. Jin and M. Slemrod. Regularization of the Burnett equations via relaxation. *J. Stat. Phys.*, 103:1009, 2001.

[45] I. V. Karlin, A. N. Gorban, G. Dukek, and T. F. Nonnenmacher. Dynamic correction to moment approximations. *Phys. Rev. E*, 57:1668, 1998.

[46] G. M. Karniadakis and A. Beskok. *Micro flows: Fundamentals and simulation.* Springer, 2002.

[47] R. E. Khayat and B. C. Eu. Nonlinear transport processes and fluid dynamics: Cylindrical Couette flow of Lennard–Jones fluids. *Phys. Rev. A*, 38:2492, 1988.

[48] R. E. Khayat and B. C. Eu. Generalized hydrodynamics, normal–stress effects, and velocity slips in the cylindrical Couette flow of Lennard–Jones fluids. *Phys. Rev. A*, 39:728, 1989.

[49] S. H. Kim and H. Pitsch. Analytic solution for a higher–order lattice Boltzmann method: Slip velocity and Knudsen layer. *Phys. Rev. E*, 78:016702, 2008.

[50] S. H. Kim, H. Pitsch, and D. Boyd. Slip velocity and Knudsen layer in the lattice Boltzmann method for microscale flows. *Phys. Rev. E*, 77:026704, 2008.

[51] M. Knudsen. Eine Revision der Gleichgewichtsbedingung der Gase. Thermische Molekularströmung. *Ann. Phys.*, 31:205, 1910.

[52] M. Knudsen. Thermischer Molekulardruck der Gase in Röhren. *Ann. Phys.*, 33:1435, 1910.

[53] M. N. Kogan. *Rarefied gas dynamics.* Plenum Press, 1969.

[54] L. D. Landau and E. M. Lifshitz. *Fluid mechanics.* Pergamon, Oxford, 1987.

[55] C. R. Lilley and J. E. Sader. Velocity gradient singularity and structure of the velocity profile in the Knudsen layer according to the Boltzmann equation. *Phys. Rev. E*, 76:026315, 2007.

[56] S. S. Lo and S. K. Loyalka. An efficient computation of near–continuum rarefied gas flows. *J. Appl. Math. Phys. (ZAMP)*, 33:419, 1982.

[57] S. S. Lo, S. K. Loyalka, and T. S. Storvick. Kinetic theory of thermal transpiration and mechanocaloric effect. V. Flow of polyatomic gases in a cylindrical tube with arbitrary accommodation at the surface. *J. Chem. Phys.*, 81:2439, 1984.

[58] D. A. Lockerby, J. M. Reese, D. R. Emerson, and R. W. Barber. Velocity boundary condition at solid walls in rarefied gas calculations. *Phys. Rev. E*, 70:017303, 2004.

[59] D. A. Lockerby, J. M. Reese, and M. A. Gallis. The usefulness of higher–order constitutive relations for describing the Knudsen layer. *Phys. Fluids*, 17:100609, 2005.

[60] S. K. Loyalka. Thermal transpiration in a cylindrical tube. *Phys. Fluids*, 12:2301, 1969.

[61] S. K. Loyalka. Kinetic theory of thermal transpiration and mechanocaloric effect. I. *J. Chem. Phys.*, 55:4497, 1971.

[62] S. K. Loyalka. Kinetic theory of thermal transpiration and mechanocaloric effect. II. *J. Chem. Phys.*, 63:4054, 1975.

[63] S. K. Loyalka. Velocity profile in the Knudsen layer for the Kramer's problem. *Phys. Fluids*, 18:1666, 1975.

[64] S. K. Loyalka. Temperature jump and thermal creep slip: Rigid sphere gas. *Phys. Fluids A*, 1:403, 1989.

[65] S. K. Loyalka and J. W. Cipolla. Thermal creep slip with arbitrary accommodation at the surface. *Phys. Fluids*, 14:1656, 1971.

[66] S. K. Loyalka and J. H. Ferziger. Model dependence of the slip coefficient. *Phys. Fluids*, 10:1833, 1967.

[67] S. K. Loyalka and S. A. Hamoodi. Poiseuille flow of a rarefied gas in a cylindrical tube: Solution of linearized Boltzmann equation. *Phys. Fluids A*, 2:2061, 1990.

[68] S. K. Loyalka and K. A. Hickey. Velocity slip and defect: Hard sphere gas. *Phys. Fluids A*, 1:612, 1989.

[69] S. K. Loyalka and K. A. Hickey. The Kramers problem: Velocity slip and defect for a hard sphere gas with arbitrary accommodation. *J. Appl. Math. Phys. (ZAMP)*, 41:245, 1990.

[70] S. K. Loyalka and K. A. Hickey. Kinetic theory of thermal transpiration and the mechanocaloric effect: Planar flow a rigid sphere gas with arbitrary accommodation at the surface. *J. Vac. Sci. Tech. A*, 9:158, 1991.

[71] S. K. Loyalka and H. Lang. Linearized Poiseuille flow between parallel plates. *J. Appl. Math. Phys. (ZAMP)*, 21:690, 1970.

[72] S. K. Loyalka, N. Petrellis, and T. S. Storvick. Some numerical results for the BGK model: Thermal creep and viscous slip problems with arbitrary accomodation at the surface. *Phys. Fluids*, 18:1094, 1975.

[73] M. Malek Mansour, F. Baras, and A. L. Garcia. On the validity of hydrodynamics in plane poiseuille flows. *Physica A*, 240:255, 1997.

[74] C. Maxwell. On stress in rarefied gases arising from inequalities of temperature. *Phil. Trans. Roy. Soc. Lon.*, 170:231, 1879.

[75] G. L. Morini, M. Spiga, and P. Tartarini. The rarefaction effect on the friction factor of gas flow in microchannels. *Superlattices and Microstructures*, 35:587, 2004.

[76] I. Müller, D. Reitebuch, and W. Weiss. Extended thermodynamics – Consistent in order of magnitude. *Cont. Mech. Thermodyn.*, 15:113, 2003.

[77] R. S. Myong, J. M. Reese, R. W. Barber, and D. R. Emerson. Velocity slip in microscale cylindrical Couette flow: The Langmuir model. *Phys. Fluids*, 17:087105, 2005.

[78] K. Nanbu. Analysis of cylindrical Couette flows by use of the direction simulation method. *Phys. Fluids*, 27:2632, 1984.

[79] T. Ohwada, Y. Sone, and K. Aoki. Numerical analysis of the Poiseuille and thermal transpiration flows between two parallel plates on the basis of the Boltzmann equation for hard–sphere molecules. *Phys. Fluids A*, 1:2042, 1989.

[80] T. Ohwada, Y. Sone, and K. Aoki. Numerical analysis of the shear and thermal creep flows of a rarefied gas over a plane wall on the basis of the linearized Boltzmann equation for hard–sphere molecules. *Phys. Fluids A*, 1:1588, 1989.

[81] J. H. Park, P. Bahukudumbi, and A. Beskok. Rarefaction effects on shear driven oscillatory gas flows: A direct simulation Monte Carlo study in the entire Knudsen regime. *Phys. Fluids*, 16:317, 2004.

[82] B. T. Porodnov, A. N. Kulev, and F. T. Tukhvetov. Thermal transpiration in a circular capillary with a small temperature difference. *J. Fluid Mech.*, 88:609, 1978.

[83] B. T. Porodnov and F. T. Tukhvetov. Theoretical investigation of nonisothermal flow of a rarefied gas in a cylindrical capillary. *J. Eng. Phys. Thermophys.*, 36:61, 1979.

[84] O. Reynolds. Experimental researches on thermal transpiration of gases through porous plates and on the law of transpiration and impulsion. *Phil. Trans. Roy. Soc. Lon.*, 170:727, 1879.

[85] D. Risso and P. Cordero. Generalized hydrodynamics for a Poiseuille flow: Theory and simulations. *Phys. Rev. E*, 58:546, 1998.

[86] P. Rosenau. Extending hydrodynamics via the regularization of the Chapman–Enskog expansion. *Phys. Rev. A*, 40:7193, 1989.

[87] F. Sharipov. Onsager–Casimir reciprocity relations for open gaseous systems at arbitrary rarefaction : I. General theory for single gas. *Physica A*, 203:437, 1994.

[88] F. Sharipov. Onsager–Casimir reciprocity relations for open gaseous systems at arbitrary rarefaction : II. Application of the theory for single gas. *Physica A*, 203:457, 1994.

[89] F. Sharipov. Rarefied gas flow through a long tube at any temperature ratio. *J. Vac. Sci. Technol. A*, 14:2627, 1996.

[90] F. Sharipov. Application of the Cercignani-ŨLampis scattering kernel to calculations of rarefied gas flows. III. Poiseuille flow and thermal creep through a long tube. *Eurp. J. Mech. B/Fluids*, 22:145, 2003.

[91] F. Sharipov and D. Kalempa. Oscillatory Couette flow at arbitrary oscillation frequency over the whole range of the Knudsen number. 4:363, 2008.

[92] F. Sharipov and V. Seleznev. Data on internal rarefied gas flows. *J. Phys. Chem. Ref. Data*, 27:657, 1998.

[93] F. M. Sharipov and G. M. Kremer. Nonlinear Couette flow between two rotating cylinders. *Transp. Theory Stat. Phys.*, 25:217, 1996.

[94] F. M. Sharipov and G. M. Kremer. Non–isothermal couette flow of a rarefied gas between two rotating cylinders. *European J. Mechanics – B/Fluids*, 18:121, 1999.

[95] C. E. Siewert. Poiseuille and thermal–creep flow in a cylindrical tube. *J. Compu. Phys.*, 160:470, 2000.

[96] C. E. Siewert and D. Valougeorgis. An analytical discrete–ordinates solution of the S–model kinetic equations for flow in a cylindrical tube. *J. Quant. Spectrosc. Radiat. Transf.*, 72:531, 2002.

[97] L. H. Söderholm. Hybrid Burnett equations: A new method of stabilizing. *Trans. Theory and Stat. Phys.*, 36:495, 2007.

[98] Y. Sone. *Kinetic theory and fluid dynamics*. Birkhäuser, 2002.

[99] Y. Sone and T. Doi. Ghost effect of infinitesimal curvature in the plane Couette flow of a gas in the continuum limit. *Phys. Fluids*, 16:952, 2004.

[100] Y. Sone, H. Sugimoto, and K. Aoki. Cylindrical Couette flows of a rarefied gas with evaporation and condensation: Reversal and bifurcation of flows. *Phys. Fluids*, 11:476, 1999.

[101] Y. Sone, Sh. Takata, and H. Sugimoto. The behavior of a gas in the continuum limit in the light of kinetic theory: The case of cylindrical Couette flows with evaporation and condensation. *Phys. Fluids*, 8:3403, 1996.

[102] Y. Sone, Y. Waniguchi, and K. Aoki. One–way flow of a rarefied gas induced in a channel with a periodic temperature distribution. *Phys. Fluids*, 8:227, 1996.

[103] Y. Sone and K. Yamamoto. Flow of rarefied gas through a circular pipe. *Phys. Fluids*, 11:1672, 1968.

[104] S. Stefanov and C. Cercignani. Monte Carlo simulation of the TaylorŨ-Couette flow of a rarefied gas. *J. Fluid Mech.*, 256:199, 1993.

[105] H. Struchtrup. Stable transport equations for rarefied gases at high orders in the Knudsen number. *Phys. Fluids*, 16:3921, 2004.

[106] H. Struchtrup. *Macroscopic transport equations for rarefied gas flows: Approximation methods in kinetic theory.* Springer, 2005.

[107] H. Struchtrup and T. Thatcher. Bulk equations and Knudsen layers for the regularized 13 moment equations. *Cont. Mech. Thermodyn.*, 19:177, 2007.

[108] H. Struchtrup and M. Torrilhon. Regularization of Grad's 13–moment equations: Derivation and linear analysis. *Phys. Fluids*, 15:2668, 2003.

[109] H. Struchtrup and M. Torrilhon. H theorem, regularization, and boundary conditions for linearized 13–moment equations. *Phys. Rev. Lett.*, 99:014502, 2007.

[110] H. Struchtrup and M. Torrilhon. Higher–order effects in rarefied channel flows. *Phys. Rev. E*, 78:046301, 2008.

[111] S. Succi. *The Lattice Boltzmann equation for fluid dynamics and beyond.* Oxford University Press, 2004.

[112] P. Taheri, A. S. Rana, H. Struchtrup, and M. Torrilhon. Macroscopic description of steady and unsteady rarefaction effects in boundary value problems of gas dynamics. *Cont. Mech. Thermodyn.*, 21:423, 2009.

[113] P. Taheri and H. Struchtrup. Effects of rarefaction in microflows between coaxial cylinders. *Phys. Rev. E*, 80:066317, 2009.

[114] P. Taheri and H. Struchtrup. Rarefaction effects in thermally–driven microflows. *Physica A*, 2010.

[115] P. Taheri, M. Torrilhon, and H. Struchtrup. Couette and Poiseuille microflows: Analytical solutions for regularized 13–moment equations. *Phys. Fluids*, 21:017102, 2009.

[116] K. W. Tibbs, F. Baras, and A. L. Garcia. Anomalous flow profile due to the curvature effect on slip length. *Phys. Rev. E*, 56:2282, 1997.

[117] M. Tij, M. Sabbane, and A. Santos. Nonlinear Poiseuille flow in a gas. *Phys. Fluids*, 10:1021, 1998.

[118] M. Tij and A. Santos. Perturbation analysis of a stationary nonequilibrium flow generated by an external force. *J. Stat. Phys.*, 76:1399, 1994.

[119] B. D. Todd and D. J. Evans. Temperature profile for Poiseuille flow. *Phys. Rev. E*, 55:2800, 1997.

[120] B. D. Todd and Denis J. Evans. The heat flux vector for highly inhomogeneous nonequilibrium fluids in very narrow pores. *J. Chem. Phys.*, 103:9804, 1995.

[121] M. Torrilhon and H. Struchtrup. Boundary conditions for regularized 13–moment–equations for micro–channel flows. *J. Comp. Phys.*, 227:1982, 2008.

[122] C. Truesdell and R. G. Muncaster. *Fundamentals of Maxwell's kinetic theory of a simple monatomic gas.* Academic Press, 1980.

[123] F. J. Uribe and A. L. Garcia. Burnett description for plane Poiseuille flow. *Phys. Rev. E*, 60:4063, 1999.

[124] D. Valougeorgis and J. R. Thomas. Exact numerical results for Poiseuille and thermal creep flow in a cylindrical tube. *Phys. Fluids*, 29:423, 1986.

[125] S. Varoutis, D. Valougeorgis, O. Sazhin, and F. Sharipov. Rarefied gas flow through short tubes into vacuum. *J. Vac. Sci. Technol. A*, 26:228, 2008.

[126] W. G. Vincenti and C. H. Kruger. *Introduction to physical gas dynamics.* John Wiley & Sons, 1965.

[127] W. Weiss. Continuous shock structure in extended thermodynamics. *Phys. Rev. E*, 52:5760, 1995.

[128] D. A. Wolf–Gladrow. *Lattice–Gas Cellular Automata and Lattice Boltzmann models.* Oxford University Press, 2004.

[129] K. Xu. Super–Burnett solutions for Poiseuille flow. *Phys. Fluids*, 15:2077, 2003.

[130] K. Xu and Z. Li. Microchannel flow in the slip regime: Gas–kinetic BGK-ŨBurnett solutions. *J. Fluid Mech.*, 513:87, 2004.

[131] H. Yoshida and K. Aoki. Linear stability of the cylindrical Couette flow of a rarefied gas. *Phys. Rev. E*, 73:021201, 2006.

[132] S. Yuhong, R. W. Barber, and D. R. Emerson. Inverted velocity profiles in rarefied cylindrical Couette gas flow and the impact of the accommodation coefficient. *Phys. Fluids*, 17:047102, 2005.

[133] Y. Zheng, A. L. Garcia, and B. J. Alder. Comparison of kinetic theory and hydrodynamics for Poiseuille flow. *J. Stat. Phys.*, 109:495, 2002.

[134] X. Zhong, R. W. MacCormack, and D. R. Chapman. Stabilization of the Burnett equations and applications to hypersonic flows. *AIAA Journal*, 31:1036, 1993.